

THE FORMATION OF EXCIMER MOLECULES IN  
MICROWAVE DISCHARGES

Timothy Graham Frank

A Thesis Submitted for the Degree of PhD  
at the  
University of St Andrews



1984

Full metadata for this item is available in  
St Andrews Research Repository  
at:

<http://research-repository.st-andrews.ac.uk/>

Please use this identifier to cite or link to this item:

<http://hdl.handle.net/10023/13616>

This item is protected by original copyright

THE FORMATION OF EXCIMER MOLECULES IN  
MICROWAVE DISCHARGES

Thesis presented by

T.G.Frank MSc

to the

University of St. Andrews

in application for the degree of

Doctor of Philosophy

February 1984





ProQuest Number: 10166274

All rights reserved

INFORMATION TO ALL USERS

The quality of this reproduction is dependent upon the quality of the copy submitted.

In the unlikely event that the author did not send a complete manuscript and there are missing pages, these will be noted. Also, if material had to be removed, a note will indicate the deletion.



ProQuest 10166274

Published by ProQuest LLC (2017). Copyright of the Dissertation is held by the Author.

All rights reserved.

This work is protected against unauthorized copying under Title 17, United States Code  
Microform Edition © ProQuest LLC.

ProQuest LLC.  
789 East Eisenhower Parkway  
P.O. Box 1346  
Ann Arbor, MI 48106 – 1346

Tu A138

#### DECLARATION

I hereby certify that this thesis has been composed by me, and is a record of work done by me, and has not previously been presented for a higher degree.

This research was carried out in the Physical Sciences Laboratory of St. Salvator's College, in the University of St. Andrews, under the supervision of Dr. Maitland.

T.G.Frank

CERTIFICATE

I certify that T.G.Frank has spent nine terms at research work in the Physical Science Laboratory of St. Salvator's College, in the University of St. Andrews, under my direction, that he fulfilled the conditions of Ordinance No.16 (St. Andrews) and that he is qualified to submit the following thesis in application for the Degree of Doctor of Philosophy.

A. Maitland

Research Supervisor

#### AUTHOR'S CAREER

Born in 1946 in Paignton, Devon. Secondary education at Paignton County Secondary Modern School and South Devon Technical College, Torquay. Studied for first degree, in Physics, at Lancaster University (1965-1968). Various employment in the London area, including a period as a development engineer with Rank Precision Industries, up to 1973. Post Graduate Certificate in Education obtained at Leeds University (1972-1973). From 1973 to 1978 employed as a physics teacher at Morgan Academy, Dundee. Obtained an MSc. in The Principles of Instrument Design at Aberdeen University in 1979. This one year course included the preparation of a thesis. The thesis reported on the design, construction, and testing by the author of an instrument for plotting very small variations in refractive index in glass samples. From 1979 to the present the author has studied excimer lasers at St. Andrews University.

#### ACKNOWLEDGEMENTS

I would like to thank Dr. Maitland for his assistance throughout this work. His enthusiasm especially is very much appreciated. The technical assistance received is gratefully acknowledged with thanks to R. McRaw, M. Robertson, J. Spark, B. McAndie, and F. Akerboom. Outwith the University of St. Andrews, thanks are due to the Director of The Admiralty Surface Weapons Establishment and Dr. Lacey of the Establishment for the loan of the radar set. I would also like to thank Dr. McKeague of UKAEA Dounreay for the loan of the optical spectrum analyser.

I am grateful for my financial support which was in the form of a case studentship from the SRC in collaboration with Barr and Stroud Ltd.. Finally, I would to thank Sally Frank for her encouragement and support throughout the period of this work.

ABSTRACTThe Formation of Excimer Molecules in Microwave Discharges

Experimental and theoretical aspects of the formation of excimer molecules in gas discharges are described. Experimental studies are of the emission spectrum of rare-gas halide molecules, produced in a microwave discharge, and cover aspects relevant to rare-gas halide lasers and to the possibility of pumping these lasers by microwave discharge. There is a particular emphasis on gas lifetime recording. The apparatus consists of an adapted 3cm radar set, producing 50kW pulses of 320ns duration at 1100pps, a halogen compatible gas handling system, and an optical spectrum analyser with a recording facility. This provides a very flexible system with widespread potential for spectral studies.

Reaction kinetics are described using rate equations, and these involve competing formation and loss processes. The equations are evaluated to provide upper limits for the partial pressures of constituent gases under the condition that formation is dominant. The loss of free halogens by diffusion is compared with loss by recombination and gives the delineation of diffusion and recombination dominated regions of the operating conditions. It is shown that the threshold pump power density in a laser is proportional to linewidth/ $\lambda^5$  and that for a typical excimer laser this requirement is at least  $10\text{kW cm}^{-3}$ .

Diffusion loss of halogens in the experimental apparatus is expected to be high due to the use of a small diameter (2mm) discharge tube and a strong reaction between the tube material (quartz) and free halogens. Detailed calculations of the loss of halogens by diffusion to the tube wall under the pulsed conditions of the experiment are provided. The thermal behaviour is evaluated and permits the use of a temperature dependent diffusion coefficient. It is shown that the excess gas temperature, at equilibrium, above the wall temperature is independent of the gas pressure, but that direct proportionality to the diffusivity means that this excess temperature is proportional to the mean absolute gas temperature. Forced convection cooling of the outside of the discharge tube can be very effective in cooling the discharge gas within. At the experimental pulse rate, and for the lowest pressures (0.1At) the temperature and concentration contributions of a pulse disappear well before the end of the inter-pulse period. At the highest pressures (2At) the temperature and concentration fall by about 25% in the inter-pulse period. At equilibrium, the mean concentration of free halogen that results from effective cooling (forced convection) is approximately twice that achieved without effective cooling (free convection).

The design criteria for suitable microwave discharge couplers are developed from a consideration of microwave discharges, microwave propagation, and the absorption skin depth. It is shown that multi-element directional couplers may be particularly suitable if the coupling elements are graded along the coupling region. A calculation scheme is derived for the coupling factors of each



element necessary to give uniform excitation of the discharge volume. This approach is applied to a Schwinger directional coupler, chosen because it permits a demountable structure, and details of construction and performance are provided.

The experimental work consists mainly of an extensive programme testing mixtures of a rare-gas (Xe, Kr, or Ar) with a halogen donor ( $\text{SF}_6$ ,  $\text{NF}_3$ , or HCl) and a buffer gas (He, Ne, or Ar). The majority of work concerns KrF and XeF but some results are also presented for ArF, XeCl, and KrCl. The spectrum of XeO is observed. The main variables are mixture ratio and total pressure and the principal measurements are available either from integrated spectra or from temporal records of the intensity at the spectrum peak. The results form an empirical optimisation study. One of the aims of this study was to find the mixture ratios and total pressures for which the fluorescent emission, for any given excimer system, was a maximum. These ratios and pressures could then be used as a starting point in attempts to obtain lasing. Considerable use was made of  $\text{SF}_6$  as the donor because it is a cheap alternative to  $\text{NF}_3$  and has not been studied in detail as a donor elsewhere. Results are extracted from the main body of results in order to compare the performance of these two donors and to compare the performance of the three buffers. It is shown conclusively that greater lifetimes are obtainable with  $\text{SF}_6$  but at the cost of lower intensities. In the buffer comparison much lower fluorescent emission is observed when Ar is used, in both XeF and KrF mixtures, and that discharges are only formed below about 100Torr. Below the optimum dilutions the results for He and Ne are similar. However, at higher dilutions in XeF and KrF mixtures,

fluorescent intensities are significantly greater, and discharges may be obtained at greater total pressure, with Ne buffer. In XeF mixtures it is found that gas lives are 4 to 8 times as long with Ne buffer as they are with He buffer.

The temporal records provide gas life information on a scale ranging from 300 to  $10^6$  pulses. To reveal behaviour over fewer pulses and within single pulses a high speed system (5ns response time) was developed using a monochromator, fast photomultiplier, and storage oscilloscope. Because of the very small ratio of the pulse width to the inter-pulse period a blanking system was devised to remove the over-bright base line occurring during the inter-pulse period. The high repetition rate of 1100pps and much reduced volume enabled gas life studies to be carried out in times which are orders of magnitude smaller than those required using the 10pps of a conventional excimer laser system with much greater volume.

## CONTENTS

1	INTRODUCTION . . . . .	5
2	RARE-GAS HALIDE EXCIMER LASERS . . . . .	11
2.1	Molecular Structure and Spectroscopy . . . . .	11
2.1.1	Excimer Molecules . . . . .	11
2.1.2	Rare-Gas Halide Molecules . . . . .	14
2.1.3	Rare-Gas Halide B - X Emission Features . . . . .	19
2.2	Excimer Kinetics . . . . .	23
2.2.1	Formation Kinetics . . . . .	23
2.2.2	Quenching Kinetics . . . . .	27
2.2.3	Halide Kinetics . . . . .	33
2.2.4	Buffer Gas Kinetics . . . . .	40
2.3	Laser Operation . . . . .	46
3	HALOGEN LOSS BY DIFFUSION TO THE WALL . . . . .	52
3.1	Derivation of the Calculation Method . . . . .	52
3.1.1	Basic Equations . . . . .	53
3.1.2	Heat Transport . . . . .	55
3.1.3	Diffusion . . . . .	63
3.2	Application to the Experimental Situation . . . . .	65
3.2.1	Heat Transport . . . . .	65
3.2.2	Diffusion . . . . .	73
3.2.3	Conclusions . . . . .	75
4	MICROWAVE DISCHARGE EXCITATION . . . . .	77
4.1	Comparison of Microwave and DC Discharges . . . . .	78
4.1.1	Discharge Excitation by DC Pulses . . . . .	78
4.1.2	Microwave Discharge Excitation . . . . .	80
4.2	Microwave Discharge Couplers . . . . .	89
4.2.1	The Coupling Problem . . . . .	89
4.2.2	Microwave Discharge Coupler Design . . . . .	94
4.2.3	Preionisation Methods . . . . .	98
4.3	Comparison of Microwave and DC Discharge Apparatus . . . . .	100
5	MICROWAVE APPARATUS . . . . .	104
5.1	The Radar Set . . . . .	104
5.1.1	General Description . . . . .	104
5.1.2	Safety . . . . .	107
5.1.3	Details of the Magnetron Circuitry . . . . .	109

5.2	Radar Set Adaptation . . . . .	.111
5.2.1	Alterations and Additions . . . . .	.111
5.2.2	Waveguide Assembly . . . . .	.113
5.3	Microwave Discharge Couplers . . . . .	.113
5.3.1	Transverse-Tube Coupler . . . . .	.114
5.3.2	Longitudinal-tube Coupler . . . . .	.116
5.3.3	Schwinger Coupler . . . . .	.119
6	OTHER APPARATUS . . . . .	.122
6.1	Optical Spectrum Analyser . . . . .	.122
6.2	Gas Handling System . . . . .	.125
6.3	Pulse Recording System . . . . .	.127
7	EXPERIMENTS . . . . .	.130
7.1	Experimental Methods . . . . .	.131
7.1.1	Intensity vs Time Recording . . . . .	.131
7.1.2	Spectrum Recording . . . . .	.134
7.1.3	Pulse Recording . . . . .	.135
7.2	Experimental Programme . . . . .	.137
8	RESULTS . . . . .	.138
8.1	Empirical Presentation of Results . . . . .	.138
8.2	Excimer Spectra . . . . .	.140
8.3	Mixture Ratios and Total Pressure . . . . .	.141
8.3.1	XeF Mixtures . . . . .	.141
8.3.2	KrF Mixtures . . . . .	.142
8.3.3	XeCl Mixtures . . . . .	.143
8.3.4	Lasing Attempts . . . . .	.144
8.3.5	Mixtures With No Buffer Gas . . . . .	.145
8.4	Temporal Behaviour . . . . .	.146
8.4.1	Single Pulse Behaviour . . . . .	.147
8.4.2	Pulse Envelope Records . . . . .	.150
8.4.3	Temporal Records . . . . .	.150
8.4.4	Constant Intensity . . . . .	.151
8.4.5	Three Process behaviour . . . . .	.152
8.4.6	Intensity During Early Pulses . . . . .	.153
8.4.7	Unbuffered Mixtures of Nitrogen-Trifluoride and Krypton . . . . .	.155
8.5	Donor Comparison . . . . .	.156
8.6	Buffer Gas Type . . . . .	.158
8.6.1	Buffers in XeF Mixtures . . . . .	.158
8.6.2	Buffers in KrF Mixtures . . . . .	.159
8.7	Collisional Relaxation . . . . .	.161
	REFERENCES . . . . .	.167

## 1 INTRODUCTION

Excimer lasers were first introduced in 1975 and subsequent intense interest has brought these lasers to the forefront of the laser field when the requirement is for efficient production of pulsed radiation in the UV spectrum at high pulse powers and energies. The first suggestion for a laser system using emission from the bound - free electronic transition of an excimer molecule was made in 1960 by Houtermans (1960). Of the many possible excimer systems, the rare-gas halides are outstanding as efficient emitters of u-v radiation. This was first demonstrated with ArCl by Golde and Thrush (1974) and with several xenon monohalides by Velazco and Setser (1975). Laser action from XeBr was demonstrated soon after this by Searles and Hart (1974), from XeF, XeCl, and KrF by Ewing and Brau (1975) and Brau and Ewing (1975 a). Following these early experiments the development of excimer lasers has been such that commercial systems are now available from at least seven major manufacturers, reflecting the current interest in these widely applicable devices.

The earlier rare-gas halide lasers were pumped by high intensity relativistic electron beams but now the most commonly used method is the transverse DC discharge. A new and challenging alternative to these pumping methods exists in the utilisation of a microwave discharge. Microwave excitation has been achieved by Mendelsohn et. al.(1981) for a XeCl laser and further development of the same system is reported by Wisoff et. al.(1982). Microwave excitation is also reported by Christensen and Waynant (1982) for a XeF laser. These

are the outstanding reports of microwave excitation of excimer lasers to date. In the discussions of Chapter 4, it is suggested that many real advantages may result from the use of this method of excitation. In particular the lack of electrodes in contact with the laser gases may give much longer lifetimes, the discharge apparatus may be very compact, and greater pulse durations and pulse repetition rates may be feasible. Accordingly this thesis concerns an investigation of the formation of rare-gas halide molecules in a microwave discharge and permits an assessment of the microwave discharge pumping scheme.

Outside the field of excimer lasers, the applications for microwave discharges have been widespread and their fundamental properties have been investigated in depth. Interest in microwave discharges developed after 1945 with pioneering work by Professors S.C.Brown and W.P.Allis at the Massachusetts Institute of Technology. The earlier work was concerned mainly with the conditions for the initiation of breakdown and with the interaction of low power microwaves with gases ionised by an alternative source. Many texts are available covering these topics. For example, the breakdown process is described in detail by MacDonald (1966) and the interaction of microwaves with plasma is covered by Heald and Wharton(1965). However, much current interest in microwave discharges concerns applications such as spectrum sources and plasma chemistry where maintenance of a stable, uniform, discharge is the requirement.

It is shown in Section 2.3 that to achieve threshold lasing conditions in typical rare-gas halide excimer lasers, pump power densities of at least  $10\text{kW cm}^{-3}$  are required and that values of around  $1\text{MW cm}^{-3}$  would be desirable for a microwave apparatus of wide ranging excimer laser application. Clearly operation at these power levels is limited to fairly short pulses (probably below a micro-second). It is fortunate that pulsed microwave sources of sufficient power have been developed for use in radar systems. This means that magnetrons capable of providing the pulse power necessary for excimer laser operation are commercially available. In addition, government surplus radar sets may be available at low cost. For the purposes of the work of this thesis a naval X-band radar set was obtained and adapted as described in Chapter 5. While this provided an apparatus that was convenient, reliable and cheap, the pulse power of  $50\text{kW}$  proved to be insufficient to obtain lasing from any of the excimer molecules investigated.

The high efficiency of excimer lasers derives from the utilisation of a bound-free transition and from favourable kinetics. This is explained in Chapter 2 where rare-gas halide molecules are described in detail and related to the molecular spectrum. Formation and quenching kinetics are also discussed and contrasted. The available kinetic rate constants enable limiting values for the partial pressures of the gas components to be derived such that the quenching remains negligible.



A major problem in the operation of rare-gas halide lasers is the limited gas life that occurs. The gases involved are expensive and flexible gas handling systems are required to enable gas replacement. The great convenience afforded by a sealed system is at present impracticable. The limited lifetime is mainly due to the loss of the halogen donor. This was expected to be rapid in the experimental apparatus described herein where discharges are established in a 2mm diameter quartz tube. Thus a strong wall reaction for free halogens and a small lifetime against wall collisions result in the rapid accumulation of stable halides. Chapter 3 discusses the diffusive transport of particles to the tube wall and allows for the temperature dependency of the diffusion coefficient.

Microwave discharges are compared with DC discharges in Chapter 4. It is pointed out that the rapid field reversal and lack of electrodes in the microwave case prevent the decay into highly ionised and non-uniform discharge modes that occur in the later stages of a DC discharge pulse. However, a more powerful argument in favour of microwave discharges arises from the very convenient apparatus that waveguide transmission allows. The discharge is obtained by means of a microwave discharge coupler. The problem of coupler design replaces the multiple problem, in DC discharges, of designing the electrode geometry and maintaining very low impedance loops in a structure containing a large high voltage insulator. Chapter 4 considers coupler design in detail and it is shown that the Schwinger directional coupler, redesigned with graded coupling



elements, provides an attractive possibility for a discharge coupler. Details of the construction and testing are provided.

The experimental work described in Chapter 7 involved the use of an optical spectrum analyser (OSA), which is described in Chapter 6, to give plots of emission intensity (at band centre) against time and to provide a spectrum plot of excimer emission. The OSA range of operation extended from the UV to the IR giving a recorded spectrum  $160\text{\AA}$  in width. In most cases a spectrum record was obtained by collecting the output from 1000 pulses. In order to study single pulses or the first few pulses of a burst of pulses further apparatus was developed and is described in Chapter 5. The rare-gas halides XeF, XeCl, KrF, KrCl, and ArF were studied during the experimental work and XeO emission was also observed. The molecules were formed in discharges in mixtures of the rare-gas (Xe, Kr, or Ar), a halogen donor ( $\text{NF}_3$ ,  $\text{SF}_6$ , or HCl), and a buffer gas (He, Ne, or Ar). Excimer emission intensities were recorded for the different buffers and halogen donors over a wide range of mixture ratios. Whenever a particular gas mixture was being tested, spectra and time plots were recorded for each of about 8 total pressures surrounding the pressure at which maximum output occurred.

The raw data from the experimental work consisted of over 400 sheets of graph paper obtained from the OSA and could not be included directly in the thesis. However, some of the data was copied by tracing and photo-reduced to enable it to be presented in Chapter 8. The trends in intensity and gas life-time in response to changes in the principal variables (gas type, mixture ratio, and total pressure)

are discussed in conjunction with the presentation of the results.

The volume of data generated by this work is an indication of how useful the microwave apparatus could be for this kind of investigation. This was a direct result of the compact and flexible coupling arrangement of the waveguide and small volume discharge tube, and the use of the OSA. Another outstanding feature is that the system allowed gas life-time studies to be carried out in half a minute (at 1100 pps) where many hours would be required in a DC discharge pumped excimer laser where pulse rates are usually about 1 pulse per second. The microwave apparatus proved to be simple, safe, and completely reliable with no particular engineering difficulties in connecting the microwave source to the discharge coupler or in construction of the complete system. In the light of these observations, the use of a microwave system of the type described can be highly recommended for creation and studies of rare-gas halide molecules. The indications are that expansion of the system (in terms of power) could indeed provide a valuable alternative as an excimer laser pump source.

## 2 RARE-GAS HALIDE EXCIMER LASERS

### 2.1 Molecular Structure and Spectroscopy

#### 2.1.1 Excimer Molecules

The excimer molecule will be considered here in terms of molecular binding and the curve of potential energy against nuclear separation. Molecular potential energy consists of both a Coulombic interaction with the nuclei as charge centres and the electronic potential energy which is a function of the molecular states. A continuous adiabatic Coulomb potential curve can be drawn for each molecular state. Figure 2.1(a) shows a representation of curves for three such molecular states, the upper giving a purely repulsive potential and the middle and lower curves giving weak and strong binding respectively. It is usual to take the lowest point of the lowest curve as zero for the potential energy of the system and this also gives the ground state equilibrium inter-nuclear separation.

A potential diagram such as that shown in Fig 2.1(a) is typical of a stable molecule where binding is strong in the ground a state. In an excited state, however, the molecule may be weakly bound and dissociate in collisions or may be unbound. For certain molecules

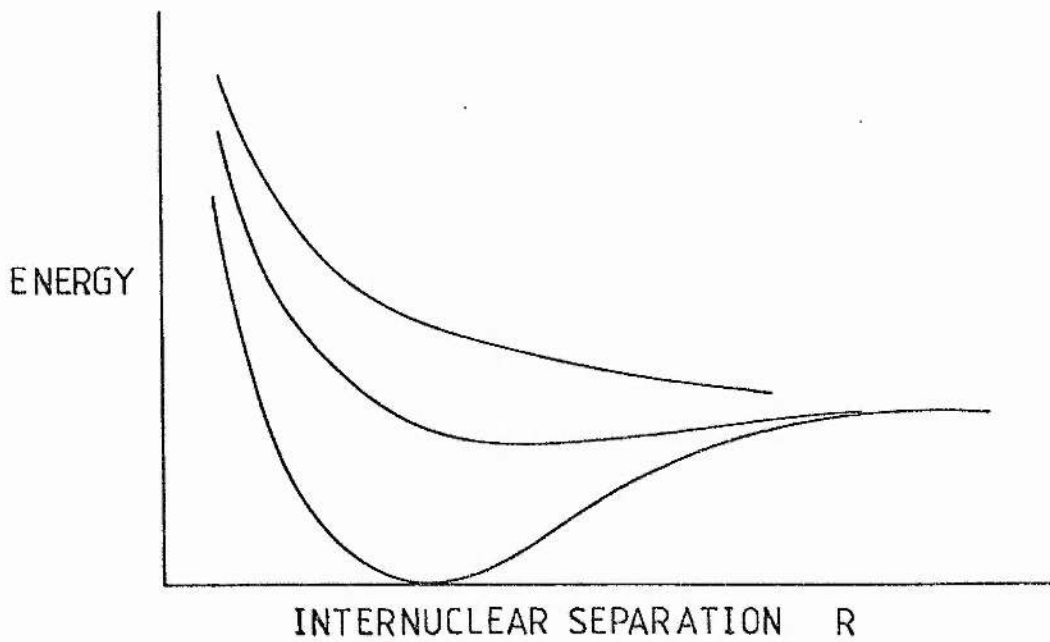


Figure 2.1(a) Molecular potential

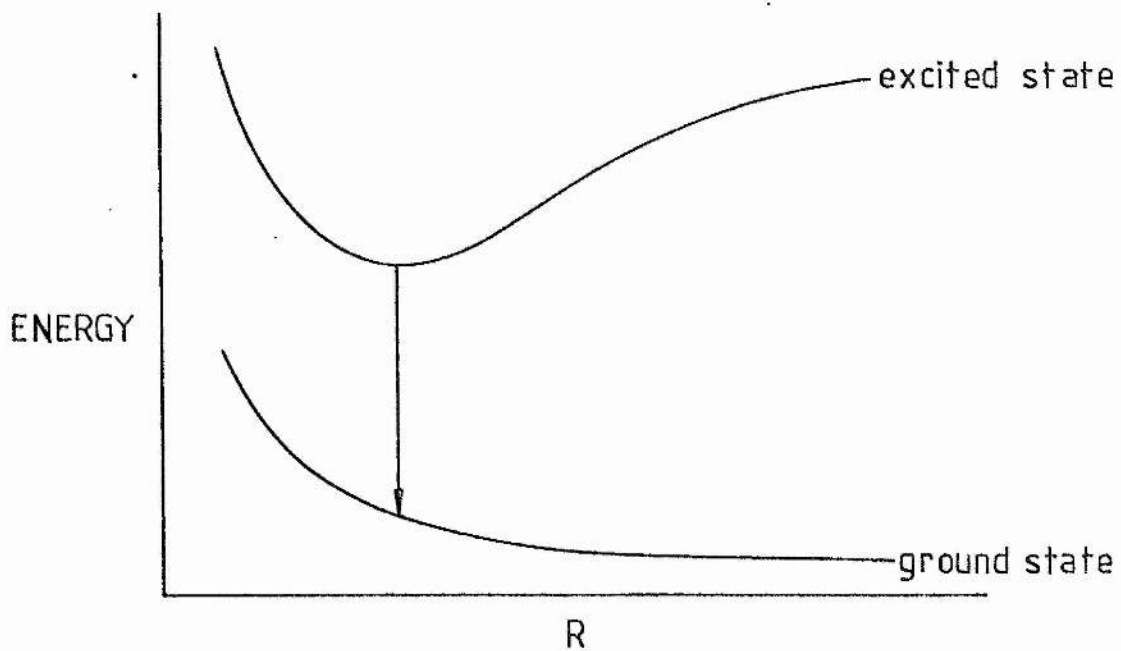


Figure 2.1(b) Excimer potential

the ordering of the binding strengths may be reversed with respect to the lower molecular states giving a potential diagram of the type shown in Fig 2.1(b). Here the molecule is unbound in the ground state but is strongly bound in an excited state. Molecules exhibiting this kind of behaviour have become widely known as excimers. In the chemical literature, however, the term 'excimer' is restricted to homopolar molecules (also known as dimers) whereas the term 'exiplex' is used where heteropolar molecules are concerned. It should also be noted that, in practice, 'excimer' molecules will be present if lower levels are sufficiently weakly bound to ensure rapid collisional removal with the consequence that the molecular population is primarily in the form of the strongly bound excited state. It is clear that electronic transitions from a strongly bound excited state to a dissociative ground state provide good candidates for lasers since the problem of absorption by the reverse transition is removed.

An ideal excimer molecule for a laser system would have a single, strongly bound excited state that can be pumped with high efficiency and a single electronic transition to a repulsive ground state. This ideal is most likely to be approached by a simple diatomic molecule. Unfortunately the molecular bound-free electronic transition has a drawback for laser operation in that the spontaneous emission bandwidth is very wide due to the rotational-vibrational manifold of the bound excited state. This wide bandwidth results in a high threshold pump power density for lasing (as demonstrated by calculation in Section 2.3). In the ideal molecule relaxation of vibrational and rotational levels to their ground states must be

possible on a time-scale that is short compared with the spontaneous emission lifetime and this again is predictive of simple diatomic molecules as likely laser candidates. The rare-gas monohalides, especially XeF, XeCl, KrF, and KrCl, give a very near approach to the ideal molecule with the result that rare-gas halide lasers are the excimer lasers that have received the most widespread interest and development to date. The other rare-gas halides where lasing has been produced are XeBr and ArF. Fluorescent emission has been observed from NeF, ArCl, KrBr, and XeI but not from ArBr and KrI where predissociation probably takes place. In all of the excimers that have been studied in relationship to laser operation, radiation is by means of an electric dipole transition so that typical excited state lifetimes are around 10 ns. Since the dissociative ground state lifetime will be about one molecular vibration period (around  $10^{-14}$  ns), population inversion is assured. For the case of a weakly bound ground state, collisional dissociation takes place. Since excimer lasers are generally operated at pressures of well over 1 atmosphere, where collision frequencies will be greater than  $10^{10} \text{ s}^{-1}$ , lifetimes of around  $10^{-1}$  ns can be expected and population inversion is still maintained. The nature of the rare-gas halide molecules, from which their suitability as laser media stem, is described in the following subsections.

### 2.1.2 Rare-Gas Halide Molecules

The electronic transition in rare-gas halides responsible for their utilisation in lasers is closely allied to the behaviour of the isolated rare-gas fragment. In their ground states, rare-gases are unreactive due to a full outer electron shell ( $p^6$ ). The first excited state of a rare-gas atom has an outer electron configuration  $p^5s^1$  and, because there is always a particularly large energy difference between a p shell and the next s shell, this excited state is closer to the ionisation potential than to the ground state. In argon, for example, the first excited state is 11.5 eV above the ground state which is 73% of the ionisation energy. Ionisation of the excited argon atom then takes 4.3 eV. An important observation can be made here in that potassium, the next element in the periodic table, also has an isolated, single, outer s electron and has an ionisation potential of 4.3 eV. It can therefore be expected that excited argon atoms will behave like potassium atoms especially when forming ionic bonds with other atoms to form molecules. Such a comparison can be made between each rare-gas in its first excited state and the alkali-metal that follows it in the periodic table. Since the alkali-metals form stable molecules with the halogens by ionic binding, it is possible to gain understanding of rare-gas halides and make predictions for their behaviour by comparison with the corresponding alkali-halide. This analogy was usefully applied by Brau and Ewing (1975 b) in early studies of rare-gas halides and gave reasonably accurate predictions of rare-gas halide emission spectra.

Despite the apparent simplicity of rare-gas halide molecules, a full understanding of their emission spectra has still to be achieved. One reason for this is the general difficulty of quantifying molecular spectra where vibrational and rotational energy states add to the electronic state. In general, these states cannot be regarded as independent. For example each electronic state has its own potential curve, as previously mentioned, with various degrees of well depth and well asymmetry. This means that the intervals of the vibrational states vary considerably between electronic states and, within a given electronic state, the intervals will be unequal due to the anharmonic vibration of the atoms in the asymmetric potential. These vibrational and rotational features are described in more detail in Section 2.1.3. Another difficulty in understanding rare-gas halide spectra arises from the existence of many electronic molecular states. While a good theoretical framework exists for the description of molecular states, problems of identification and energy ordering have frequently arisen. The lower states in the bound-bound transition of XeF and XeCl give examples where these problems have occurred.

Calculations of the rare-gas halide electronic states have been carried out by many authors and, in particular detail, by Dunning and Hay (1978) and Hay, et. al. (1979). Rhodes (1979) also gives much information on rare-gas halide molecular states and cites many references. As reflected in these works, the first step in a full description of excimer molecules is to establish the electronic configuration and term symbols for the ground state and the excited



states. The nature and strength of the binding in each state can then be characterised. Though many problems still remain, it could be said that the rare-gas halides have become well understood by using this general approach. In the following description of rare-gas halide molecular states, use is made of a fortuitous simplification that can be applied if accurate numerical predictions are not required. The simplification is to base the analysis on the possible states of the atomic fragments at infinite separation. This is justified by the dominant role of the excited rare-gas atom in the molecule with its interactive outer electron being well removed from the atom itself.

Consider first the case where spin-orbit interactions are not taken into account. Ground state rare-gases with their full subshells have  $S=0$  and  $L=0$  giving the term symbol  $^1S$ . (Note. The spectroscopic nomenclature follows Herzberg (1950) throughout.) Ground state halogens on the other hand have  $S=1/2$  and  $L=1$  giving symbols  $^2P_{3/2,1/2}$ . For positive rare-gas and negative halogen ions these term symbols are simply interchanged. In close proximity, the neutral ground state pair will be subject to covalent bonding (usually repulsive) while the ion pair will be subject to strong ionic bonding. This ionic bond description is directly applicable to the halogen-excited rare-gas bond by virtue of the high energy (near ionisation) of the rare-gas excited state and the high electronegativity of the halogen. The projection of the total angular momentum vector on the molecular axis ( $\Lambda$ ) can have values 0 to  $L$ . Therefore there are two states,  $\Lambda=0$  and  $\Lambda=1$  for both the upper (ionically bound) level and the lower (covalently bound) level.

These states are labelled,  $2^2\Sigma^+$ ,  $2^2\Pi$ ,  $1^2\Sigma^+$ , and  $1^2\Pi$ , respectively.

Spin-orbit effects are primarily present for the halogen in the covalent manifold and the rare-gas ions in the ionic manifold. The largest effect, where rare-gas halides are concerned, is due to the  $^2P_{3/2} - ^2P_{1/2}$  splitting in the heavier of the rare-gas ions. In  $\text{Xe}^+$ , for example, this splitting amounts to 1.3eV. In the molecule this results in a splitting of the  $\Pi$  state into  $2^2\Pi_{1/2}$  and  $2^2\Pi_{3/2}$  states with an energy difference that has been generally shown to be close to the  $^2P_{3/2} - ^2P_{1/2}$  splitting of the rare-gas ion (eg, see Rhodes 1979, P.91). The corresponding splitting due to the neutral halogen in the covalent bond increases with the atomic number of the halogen but is generally smaller than the rare-gas contribution in the ionic bond. All six molecular states are shown schematically in Fig 2.2. It should be noted here that while the simple ionic upper level and covalent lower level bonding model successfully predicts the near degenerate 3-fold splitting of the ground state and first excited state of the rare-gas halide molecule, more detailed models of the binding are required to correlate observations with the details of this splitting. A clear example of this is given by the bound lower level in  $\text{XeF}$  which was not predicted by earlier theory. Krauss and Liu (1976) found that the binding could only be predicted if some ionic bonding was mixed with the lower covalent bond in the presence of a weak van der Waal's attraction.

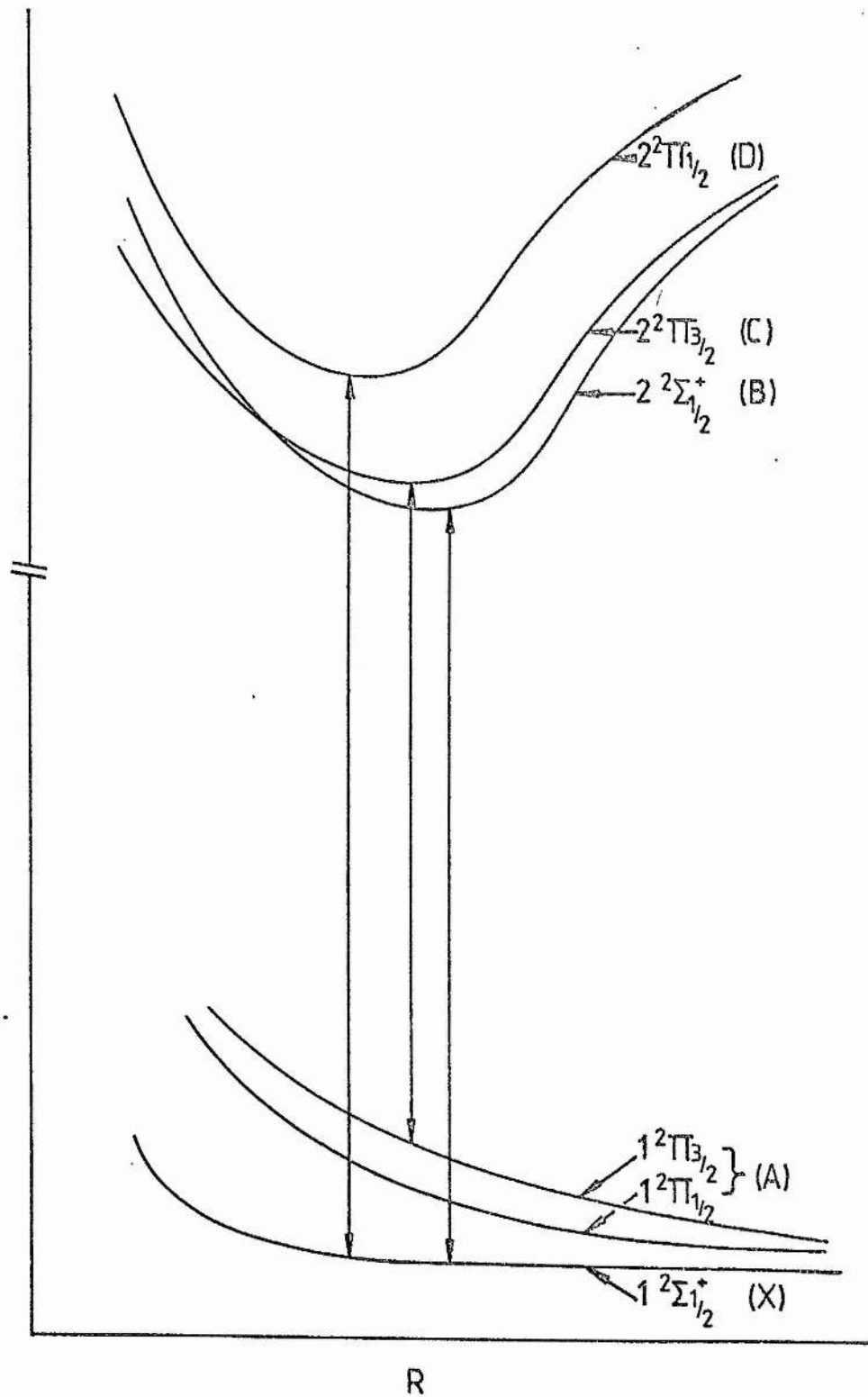


Figure 2.2 Rare-gas halide molecular states and transitions

Of the nine connections between the three upper and three lower states described above, there are five transitions allowed by the  $\Delta\Omega=0$  rule. (Hay et. al. 1979). The states involved in observed transitions are labelled in spectroscopic notation using X for the lowest state and A, B, C etc. for the other states in ascending order of energy. These are shown in Fig 2.2 where the near degenerate  $2^2\Sigma$  states are included in the single A state. The strongest rare-gas halide excimer emission is due to the B - X,  $\Sigma - \Sigma$  transition. This transition also gives the narrowest emission band and is consequently of greatest interest for laser operation. The reason for this narrow band width is that the lower  $\Sigma$  curve is relatively flat at the inter-nuclear separation at which the transition occurs. Thus when transitions occur from higher vibrational levels in the upper electronic state, and therefore from a range in the inter-nuclear separation, the terminating point (X state) is of more or less constant energy over the range of internuclear separations involved. The C - A transition has received considerable attention mainly because there is a lack of high power lasers in the blue-green spectrum. However, this emission band is very broad, due to a steep lower potential curve, with the result that lasing has been achieved for a C - A transition in XeF only. The remaining transition of interest is the D - X band. Due to the closeness of the B and C states, the D - X band is shorter in wavelength than the B - X band by an amount that corresponds approximately to the spin-orbit splitting of the rare-gas  $2P$  state. Unfortunately this transition is unlikely to be useful for laser operation as it appears to be rather easily quenched (Rhodes 1979,

P.92).

### 2.1.3 Rare-Gas Halide B - X Emission Features

The finer details of the B - X rare-gas halide emission bands are explained in terms of molecular vibration and rotation in the B state and also in the X state for the cases of a bound lower level. These features have important consequences for laser operation. Firstly, they effect the width of the spontaneous emission band and consequently the threshold pump power density, and secondly, they influence the frequency distribution of the laser emission. To illustrate the important details in the B - X emission spectra, the spectra of a few representative cases will be described. (The spectra shown below were obtained from the experimental work described later in the thesis).

XeF The spectrum of XeF is distinguished from the other rare-gas halides by having sharp details on both the blue and red sides of the emission peak. This is due to the significant binding ( $1100 \text{ cm}^{-1}$ ) in the lower level, as shown in the approximate potential diagram of Fig 2.3(a). The position of the curves is such that transitions from all the lower vibration levels of the upper state terminate on a vibrational level in the lower state below the dissociation limit. It can be seen in Fig 2.3(a) that the lower curve departs strongly from the symmetric parabolic shape of the upper curve. The molecular vibration in the lower state is therefore anharmonic and the vibrational intervals get closer with increasing vibrational energy.

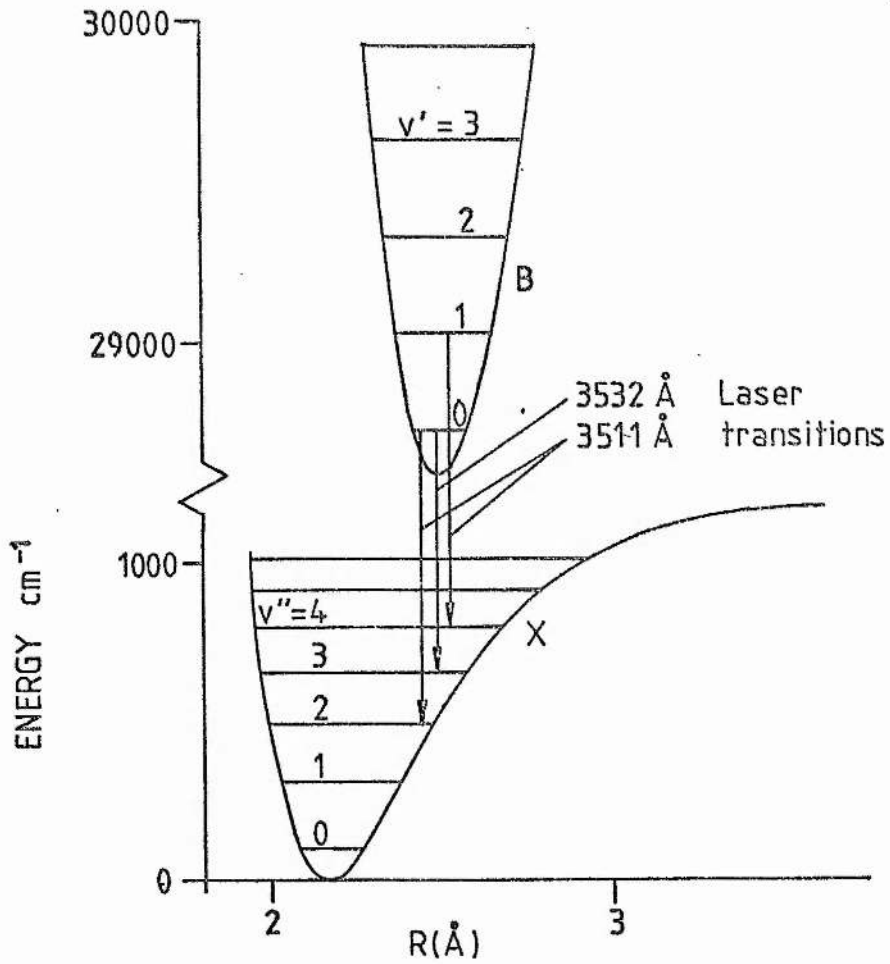


Figure 2.3(a). Xe F potentials and vibrational levels

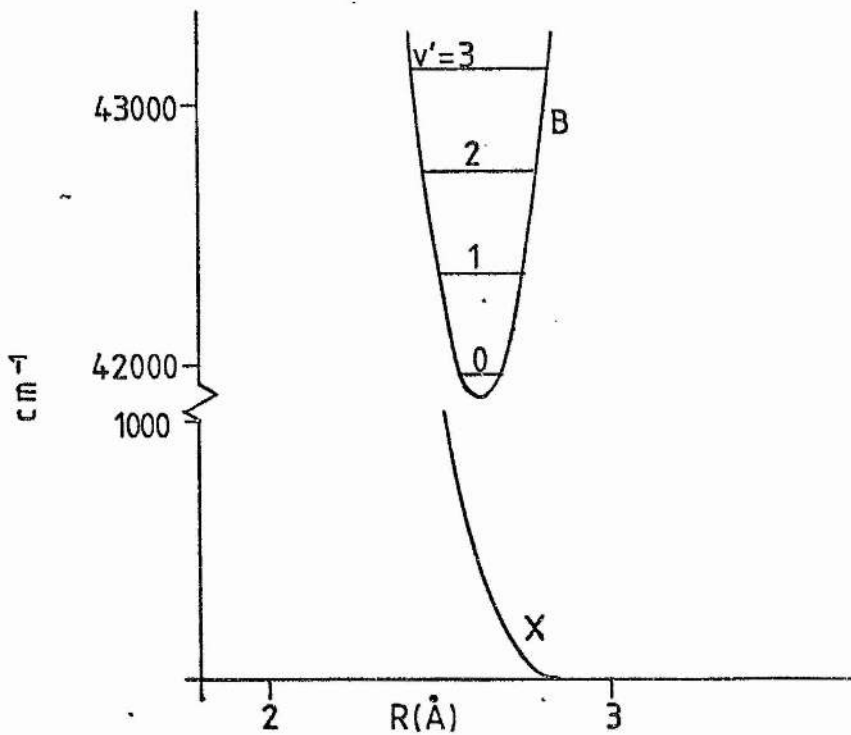


Figure 2.3(b). Kr F potentials

The result of this is that the spacing of the vibrational features in the spectrum is somewhat complicated as can be seen in the XeF B - X spectrum of Fig 2.4. Tellinghuisen, J. et. al. (1978) have analysed this spectrum and given the vibrational assignment shown in Fig 2.4. The additional peaks and the blue or red (or both) degrading of the assigned peaks arise from molecular rotation. The fine structure of rotational bands is not generally resolvable in this spectrum due to pressure and isotopic broadening. However, rotational states affect the spectrum markedly, the greatest influence being on the vibrational frequencies in the weakly bound lower state that are altered by the 'centrifugal distortion' of the molecular potential.

Generally, the B states of the rare-gas halide will be formed with a non-thermal distribution of vibrational states due to conversion of the excess energy of the precursors to vibrational energy. However, the relative probabilities for transitions between different pairs of vibrational states in the upper and lower electronic levels, respectively, are shown, by evaluation of the Frank-Condon factors (Tellinghuisen, P.C. et. al. 1978), to be greatest for transitions from the lowest vibrational level of the upper state. The extent to which the gain for transitions from this level is homogeneously broadened is a determinant of the lasing efficiency and depends on the extent to which high lying vibrational states can relax to the lowest state. Such relaxation must be induced by collision processes if it is to compete with spontaneous decay from the B state. Consequently both the spontaneous emission spectrum and the lasing spectrum are affected by the pressure and

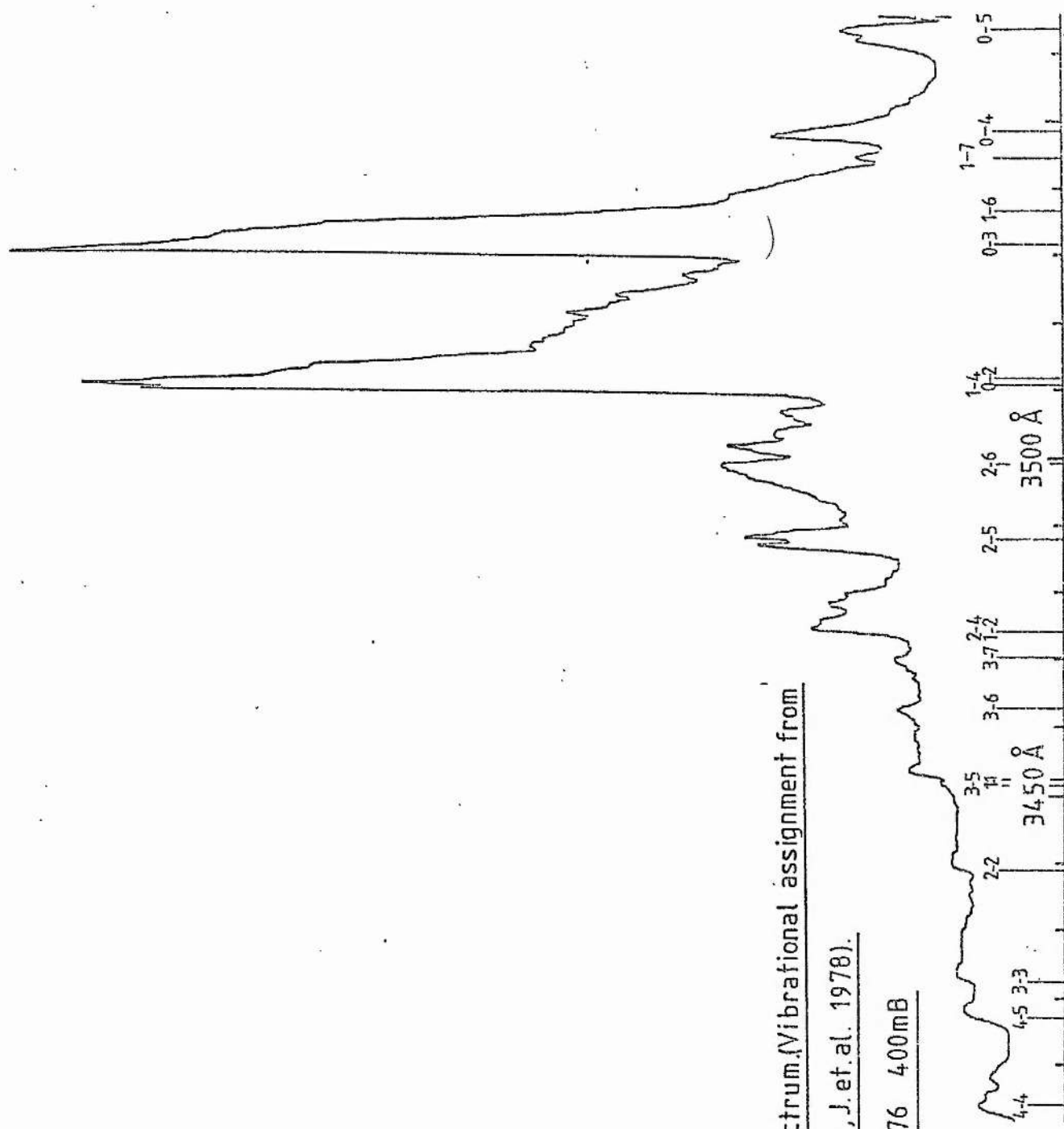
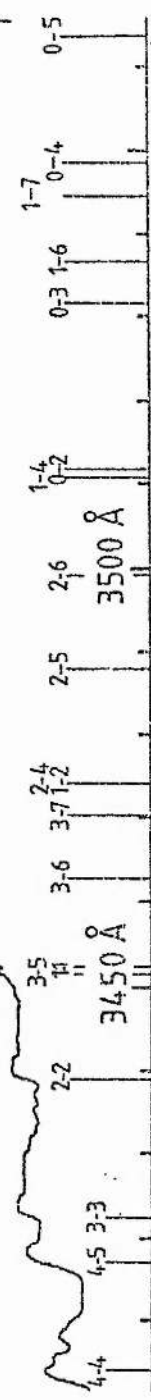


Figure 2.4 Xe F B-X spectrum.(Vibrational assignment from

Tellinghuisen, J.et.al. 1978).

SF<sub>6</sub>:Xe:He 1:3:76 400mB





temperature of the gas mixture and the type of buffer gas used. For example, complete relaxation to a thermal distribution in the B state is achieved at 0.5 atm with Ar buffer and at about 3 atm with Ne buffer, (Rokni 1978). Hsia et. al. (1979) report raised temperature experiments in a XeF laser and show a transition from the 3530 Å lasing wavelength (0 - 3) to the 3510 Å lasing wavelength (0 - 2, 1 - 4) for a temperature change from 300K to 450K.

If the lower laser level in XeF, namely the  $v''=2, 3,$  and 4 levels of the X state, were not removed, laser action would be self terminating. However, the shallow well depth of the X state allows rapid dissociation by collisional processes. Fulgham et. al. (1980) have investigated the lower level dissociation and give a lifetime of 4 - 6 ns.atm with He as buffer. Since the upper state lifetime is around 15 ns, some improvement may be expected by increasing pressure above 1 atm and by increasing the gas temperature. Absorption experiments capable of indicating the lower level population were not carried out in the experimental work to be reported. The fluorescent spectra, however, will reflect the distribution in the upper level vibrational manifold.

XeCl A spectrum of XeCl is shown Fig 2.5 where the vibrational assignments have been taken from Tellinghuisen et. al. (1976). The presence of lower level vibrational states indicates lower level binding which is given by Tellinghuisen et. al. (1976) as  $255 \text{ cm}^{-1}$ . Thus XeCl joins XeF in being the only excimers with bound lower levels, though in the case of XeCl, the binding is so weak that under usual operating conditions collisional processes will keep the

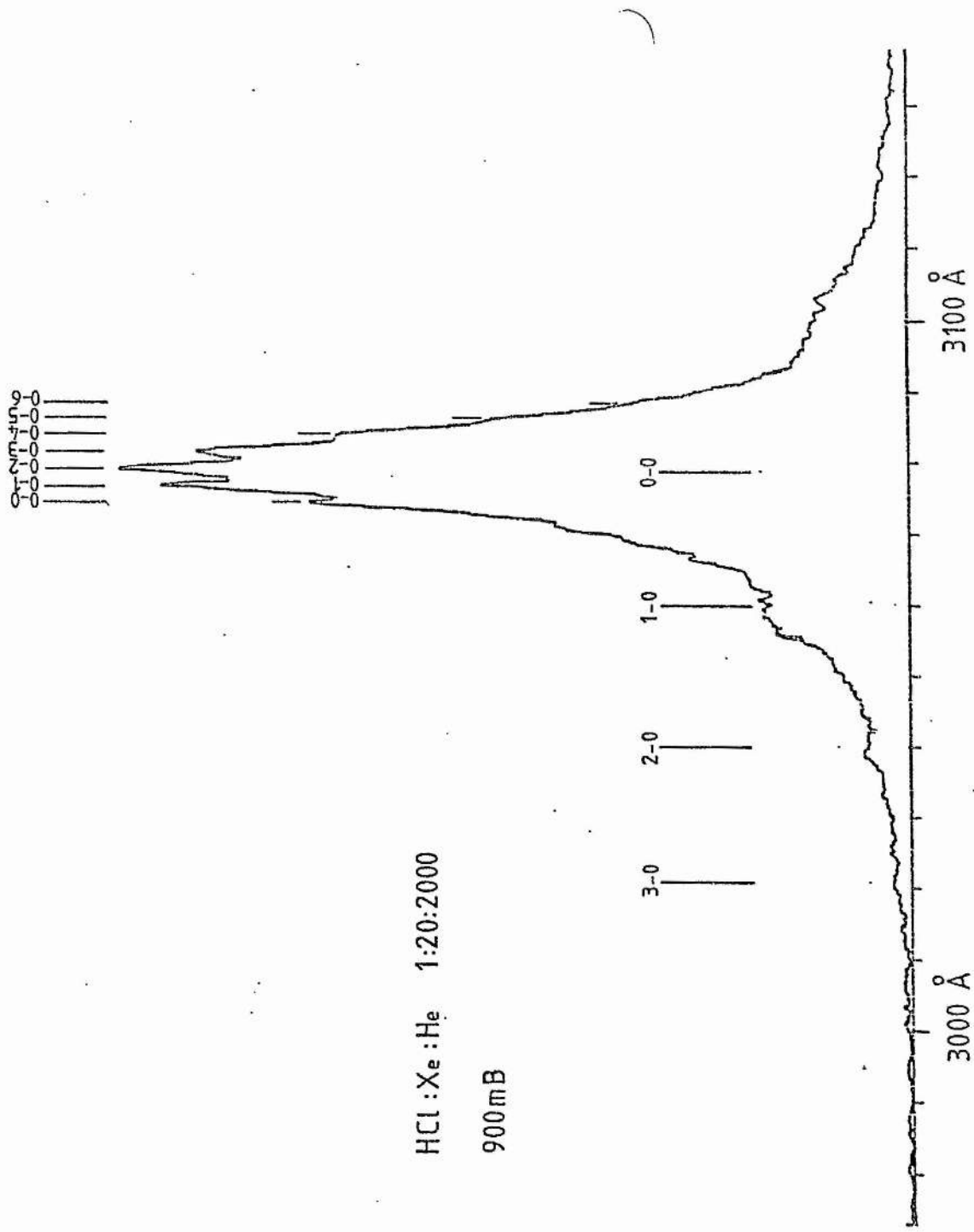


Figure 2.5 XeCl B-X spectrum. (Vibrational assignments from Tellinghuisen et al. 1976)

lower population negligibly small. The Frank-Condon factors for the B - X potential curves of XeCl give the three strongest transitions as 0 - 2, 0 - 1, 0 - 3 in order of strength. Under lasing conditions, which generally give lasing on all three transitions, rapid vibrational transfer is required to channel the upper state population energy through the laser transitions.

KrCl and KrF The nature of a bound - free B - X transition spectrum is shown clearly in Figs 2.6 and 2.7 for KrF and KrCl respectively. The undulations due to vibrational states in the upper electronic state are smoothed out by the continuum deriving from the repulsive lower state. The corresponding potential diagram for KrF is shown in Fig 2.3(b).

ArF The ArF spectrum of Fig 2.8 is included here as an example of spurious features in the spectrum. It seems likely that all the detail of this spectrum is due to strong absorption. Burnam and Djeu (1976), for example, attribute similar detail in the ArF lasing spectrum to the Schumann-Runge system of O<sub>2</sub>.

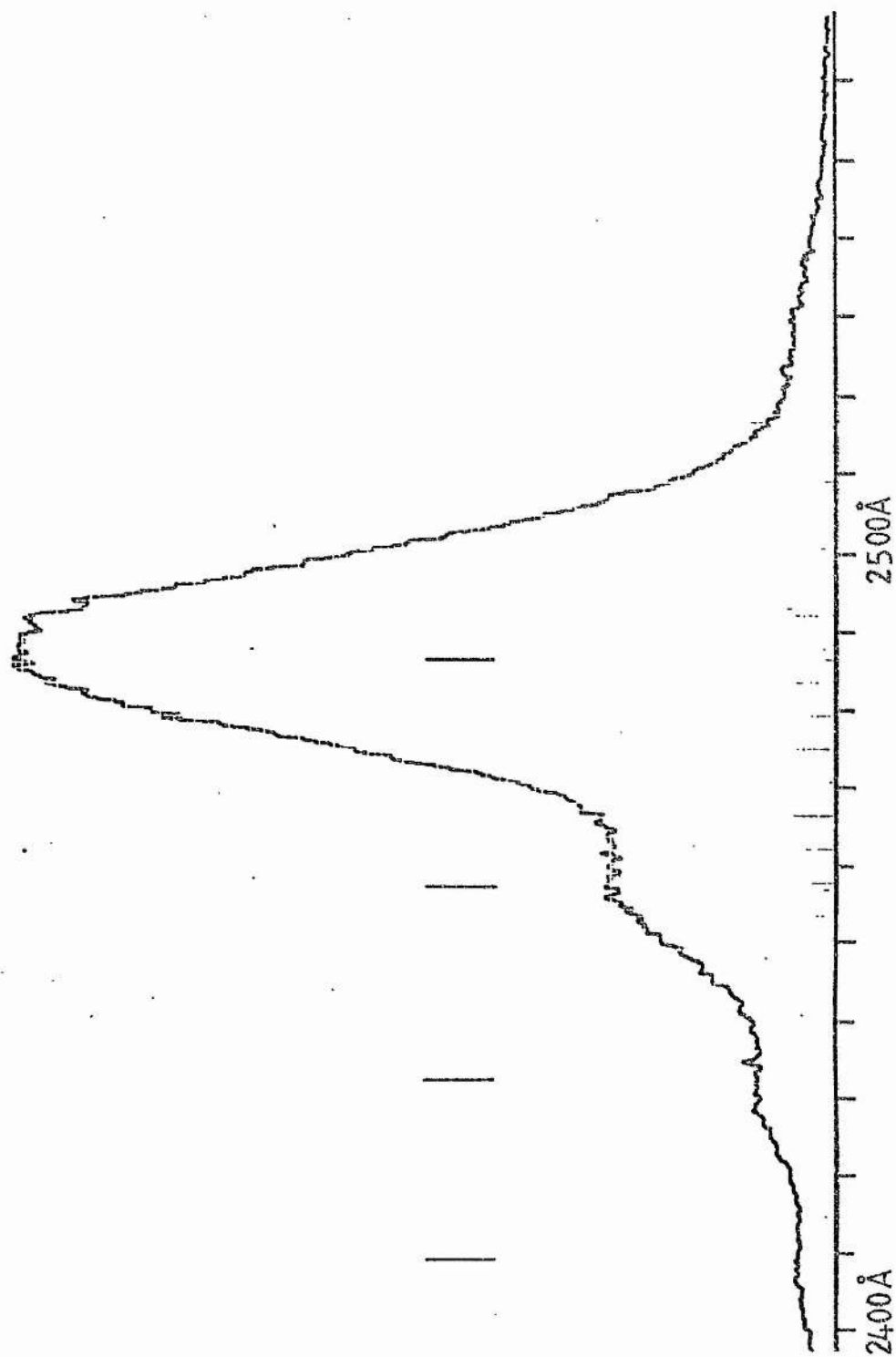


Figure 2.6 KrF B-X spectrum. SF<sub>6</sub>:Kr:He 1:3:100 400mB

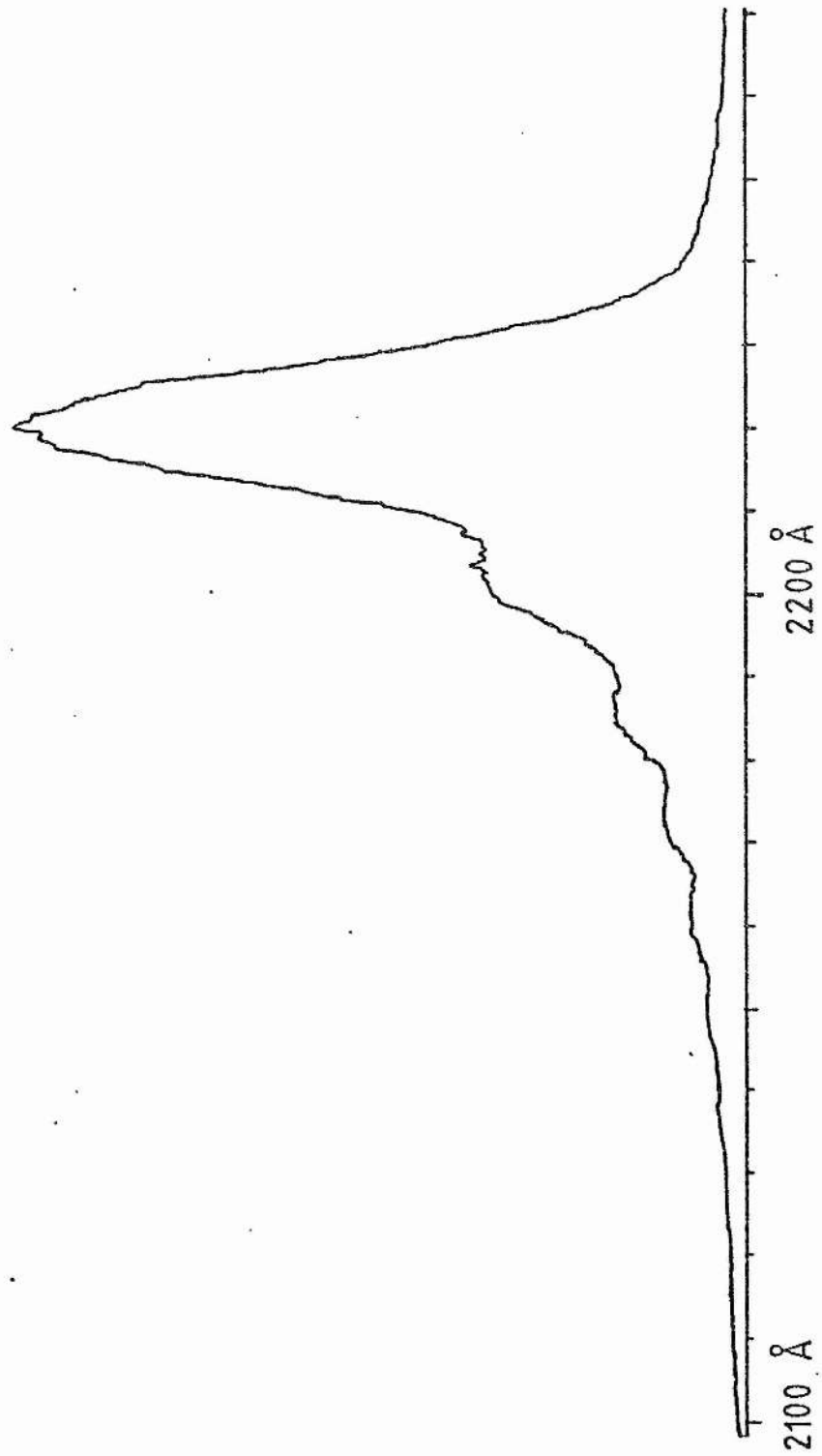


Figure 2.7 KCl B-X spectrum. HCl:Kr:He 1:50:1000 500mB

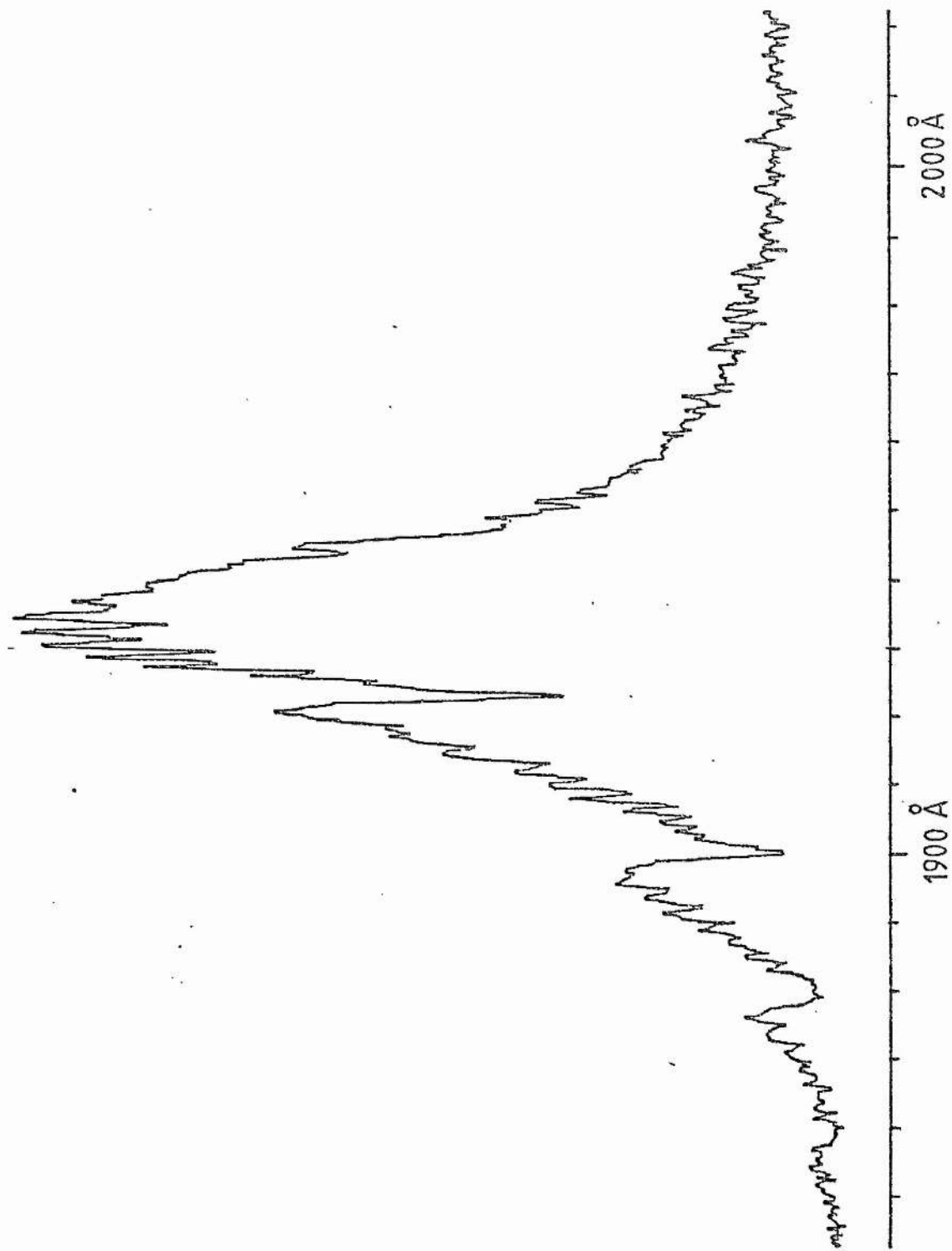


Figure 2.8 ArF B-X spectrum.  $S_{\text{F}}:\text{Ar}$  1:30 20mB

## 2.2 Excimer Kinetics

The high efficiency of excimer lasers is due not only to the bound-free nature of the lasing transition but also to some particularly favourable kinetic processes by which the excimer molecules are formed. Even so, there are many loss processes that compete with the formation reaction and reduce the upper state population. It is the purpose of this chapter to outline the important formation and loss processes and their dependency on pressure, gas mixture ratio, and the kind of halogen donor and buffer gas used.

### 2.2.1 Formation Kinetics

Gas mixtures for rare-gas halide excimer lasers generally consist of three components: a halogen bearing molecule, the rare-gas that forms the excimer, and a buffer gas (also a rare-gas) that usually constitutes over 95% of the mixture. The use of tripartite mixtures results in quite complicated kinetic processes in the discharge with the generation of a large variety of excited and ionised species. Table 2.1 shows, in general terms, the species and reactions that are considered to be important in excimer lasers. The species consist of monatomic and diatomic ionised and excited rare-gases, excited triatomic species with a halogen component, and various ionised and excited states of the halogen molecule and its dissociation products. The reactions in Table 2.1 are shown in three principal sections: initial electron impact excitation and ionisation

REACTION SPECIES	INITIAL SPECIES BY ELECTRON IMPACT	INTERMEDIATE AND 2ND. STEP REACTIONS
(1) R <sup>+</sup>	1. (1,2)e+R → R <sup>+</sup> +2e	15. (2) B <sup>*</sup> + R → B+R <sup>+</sup> +e
(1) R <sup>*</sup>	2. (1) → R <sup>*</sup> +e	16. (2) → BR <sup>+</sup> +E
(1) R <sub>2</sub> <sup>+</sup>	3. (2)e+M(X) → M(X) <sup>-</sup>	17. → R <sup>*</sup> +B
(1) R <sub>2</sub> <sup>*</sup>	4. → M(X) <sup>-*</sup>	18. (1,2) R <sup>*</sup> +e → R <sup>+</sup> +2e
BR <sup>+</sup>	5. → N(X)+X+e	19. (1,2) R <sup>*</sup> +R <sup>*</sup> → R <sup>+</sup> +R+e
BR <sup>*</sup>	6. → N(X)+X <sup>-</sup>	20. (1,2) R <sup>*</sup> +R <sub>2</sub> <sup>*</sup> → R <sub>2</sub> <sup>+</sup> +R+e
TRIAMOMIC	7. → N(X)+X <sup>*</sup> +e	21. (1,2) R <sub>2</sub> <sup>*</sup> +R <sub>2</sub> <sup>*</sup> → R <sub>2</sub> <sup>+</sup> +2R+e
R <sub>2</sub> X <sup>*</sup>	RARE-GAS HALIDE FORMATION	22. (1) R <sub>2</sub> <sup>+</sup> +R → R <sub>2</sub> <sup>+</sup> +R
BRX <sup>*</sup>		23. (1) R <sup>+</sup> +R → R <sub>2</sub> <sup>+</sup> +R
HALIDE	METASTABLE CHANNEL	24. R <sup>*</sup> +B+B → BR <sup>*</sup> +B
M(X) <sup>-</sup>	8. R <sup>*</sup> +M(X) → RX <sup>*</sup> +N(X)	25. R <sup>+</sup> +B+B → BR <sup>+</sup> +B
M(X) <sup>-*</sup>	9. BR <sup>*</sup> +M(X) → RX <sup>*</sup> +N(X)+B	26. B <sub>2</sub> <sup>+</sup> +R → R <sup>+</sup> +2B
X	10. R <sub>2</sub> <sup>*</sup> +M(X) → RX <sup>*</sup> +N(X)+R	27. (1) R <sub>2</sub> <sup>+</sup> +e → R <sup>*</sup> +R
X <sup>-</sup>	11. X <sub>2</sub> <sup>*</sup> +R → RX <sup>*</sup> +X	HALIDE
X <sup>*</sup>	IONIC CHANNEL	28. M(X) <sup>-*</sup> → M(X) <sup>-</sup>
X <sub>2</sub> <sup>*</sup>	12. R <sup>+</sup> +X <sup>-</sup> +M → RX <sup>*</sup> +M	29. → N(X) <sup>-</sup> +X
BX <sup>*</sup>	13. R <sub>2</sub> <sup>+</sup> +X <sup>-</sup> +M → RX <sup>*</sup> +R+M	30. (1) M(X)+R <sup>*</sup> → X+N(X)+R
	EXCHANGE REACTION	31. M(X)+X <sup>*</sup> → X <sub>2</sub> <sup>*</sup>
	14. BX <sup>*</sup> +R → RX <sup>*</sup> +B	32. B <sup>+</sup> +X <sup>-</sup> → BX <sup>*</sup>
		33. B <sup>*</sup> +M(X) → BX <sup>*</sup> +N(X)
		34. B <sub>2</sub> <sup>+</sup> +X <sup>-</sup> → BX <sup>*</sup> +B
		35. BX <sup>*</sup> → B+X <sup>*</sup>
		36. BX <sup>*</sup> +R → R <sup>*</sup> +B+X

R - rare-gas, B - buffer gas, M(X) and N(X) - halides,  
X - halogen, M - third body

(1) Reactions involving R or B. (2) Electron reactions

#### Notes

1. Buffer gas always lighter than excimer rare-gas.
2. Ionic reaction third body omitted in most cases.
3. N(X) usually subject to further dissociation.
4. Impurity reactions may be important.

Table 2.1 General formation reactions and reaction species.



of the rare-gases and the halogen donor and its products, the final rare-gas halide forming reaction, and the many intermediate reactions including transfer of excitation and charge from one component to another.

The efficiency of excimer reaction kinetics is determined by the quantum efficiency, branching in the reaction chain and branching within single reactions. The quantum efficiency, defined as the ratio of the laser photon energy to the initial precursor energy, plus any additional quantities to account for intermediate excitations, can be assessed from the energy values given in Table 2.2. It can be seen that the upper limit for quantum efficiency is around 50%. Branching in the reaction chain represents a loss, or partial loss, of energy to the system and is present in the simplest and most efficient reaction chains in the form of quenching reactions. The degree to which any branch is favoured will depend on particle densities and reaction rates. Some important rates are given in Table 2.3 and it is noteworthy that these are fast reactions resulting in free lifetimes, for reactants in typical lasers, of less than 10 ns. Branching within a single reaction is indicated by the branching ratio which is the ratio of the probability of producing the rare-gas halide to the probability of an alternative outcome. It is an outstanding feature of rare-gas halides that the branching ratios for the formation reactions (8 - 14 in Table 2.1) can be high and are effectively unity for XeF(F<sub>2</sub> and NF<sub>3</sub> donor), KrF(F<sub>2</sub>), XeCl(Cl<sub>2</sub>), and XeBr(Br<sub>2</sub>). The overall laser efficiency will be influenced by these kinetic efficiencies and also by quenching of the rare-gas halide, discharge inefficiency, and optical absorption at

Rare -Gases

R	R <sup>+</sup>	R <sup>**+</sup>	R <sup>**</sup>	R <sub>2</sub> <sup>+</sup>	R <sub>2</sub> <sup>**</sup>	mass	n-1 x10 <sup>6</sup>	ρ	K	d
He	24.6		19.8	2.47	2.55	4	36	0.18	1.4	2.0
Ne	21.6	41.1	16.7	1.16	0.5	20	67	0.90	0.49	2.3
Ar	15.8	27.6	11.5	1.23	0.68	40	281	1.79	0.21	2.9
Kr	14.0	24.6	9.9	1.15		84	427	3.76	0.15	3.2
Xe	12.1	21.2	8.3	1.03		131	702	5.86	0.08	3.5

Halogens

REACTION	ENERGY - eV
F <sub>2</sub> → F + F	1.6
F <sup>-</sup> → F + e	3.5
F → F <sup>+</sup> + e	17.4
SF <sub>6</sub> → SF <sub>5</sub> + F	3.7
SF <sub>6</sub> <sup>-</sup> → SF <sub>5</sub> <sup>-</sup> + F	1.5
SF <sub>6</sub> <sup>-</sup> → SF <sub>6</sub> + e	1.4
SF <sub>5</sub> <sup>-</sup> → SF <sub>5</sub> + e	3.6
SF <sub>6</sub> → SF <sub>6</sub> <sup>+</sup> + e	16.6
NF <sub>3</sub> → NF <sub>2</sub> + F	2.35
Cl <sub>2</sub> → Cl + Cl	2.5
HCl → H + Cl	4.43

R - Rare -gas  
R<sup>\*\*</sup> - <sup>3</sup>P<sub>2</sub> metastable state  
n - Refractive index at STP  
ρ - kg m<sup>-3</sup> at STP  
K - Diffusivity cm<sup>2</sup>s<sup>-1</sup> [31.2 (26)]  
d - Diameter - Å (Moore 1972)

Rare -gas halides

RX <sup>**</sup>	λ Å	E <sub>hv</sub>	T <sub>ns</sub>	σ
NeF	1080	11.5	2.6	
ArCl	1750	7.1		
ArF	1930	6.5	4.2	3x10 <sup>-16</sup>
KrCl	2220	5.6		
KrF	2490	5.0	6.8	2x10 <sup>-16</sup>
XeCl	3080	4.0	11.0	5x10 <sup>-16</sup>
XeF	3510	3.5	15.0	4x10 <sup>-16</sup>

λ - B-X wavelength  
E<sub>hv</sub> - Energy (eV)  
T - B state lifetime  
σ - Stimulated emission cross section (cm<sup>2</sup>)  
0.032 eV X state bond  
0.14 eV " "

Quantum efficiency

RX <sup>**</sup>	R <sup>+</sup>	R <sup>**</sup>
NeF	0.53	0.69
ArCl	0.45	0.62
ArF	0.41	0.56
KrCl	0.40	0.57
KrF	0.36	0.51
XeCl	0.33	0.48
XeF	0.29	0.42

R<sup>+</sup> - Ionic channel  
R<sup>\*\*</sup> - Metastable channel

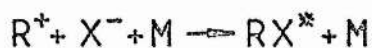
Table 2.2 Rare-Gas Halide Data

### Metastable Channel

Reaction	Rate cm <sup>3</sup> s <sup>-1</sup>	Branching ratio
Xe <sup>**</sup> + F <sub>2</sub> → XeF <sup>**</sup> + F	75 × 10 <sup>-11</sup>	1
Xe <sup>**</sup> + NF <sub>3</sub> → XeF <sup>**</sup> + NF <sub>2</sub>	9 × 10 <sup>-11</sup>	1
Xe <sup>**</sup> + Cl <sub>2</sub> → XeCl <sup>**</sup> + Cl	72 × 10 <sup>-11</sup>	1
Xe <sup>**</sup> + HCl → XeCl <sup>**</sup> + H	56 × 10 <sup>-11</sup>	
Kr <sup>**</sup> + F <sub>2</sub> → KrF <sup>**</sup> + F	66 × 10 <sup>-11</sup>	
Kr <sup>**</sup> + NF <sub>3</sub> → KrF <sup>**</sup> + NF <sub>2</sub>	8.9 × 10 <sup>-11</sup>	0.6
Kr <sup>**</sup> + Cl <sub>2</sub> → KrCl <sup>**</sup> + Cl	73 × 10 <sup>-11</sup>	0.9
Ar <sup>**</sup> + F <sub>2</sub> → ArF <sup>**</sup> + F	75 × 10 <sup>-11</sup>	

(values from Rhodes 1979)

### Ionic Channel



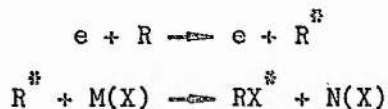
Rare gas	Rate constant cm <sup>6</sup> s <sup>-1</sup>	Max. eff. 2-body constant cm <sup>3</sup> s <sup>-1</sup>
Xe	6.7 × 10 <sup>-26</sup> (<1 At.)	2.0 × 10 <sup>-6</sup> (at 1 At)
Kr	8.9 × 10 <sup>-26</sup> ..	2.5 × 10 <sup>-6</sup> ..
Ar	1.2 × 10 <sup>-25</sup> ..	3.4 × 10 <sup>-6</sup> ..
Ne	5.6 × 10 <sup>-26</sup> (<2 At.)	3.4 × 10 <sup>-6</sup> (at 2 At)
He	6.1 × 10 <sup>-26</sup> ..	6.9 × 10 <sup>-6</sup> ..

(approximated from Flannery 1978)

Table 2.3 Excimer Formation Rates

the laser wavelength.

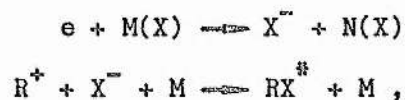
Of the possible rare-gas halide formation channels, the following is outstanding in simplicity and efficiency:-



where R is the rare-gas, M(X) and N(X) are halogen bearing molecules, and X is the halogen atom. For any given rare-gas halide, the metastable channel has the highest quantum efficiency, the metastable rare-gas being the precursor of lowest energy. In addition to this, the formation reaction is fast, with a rate coefficient in the range  $10^{-10}$  to  $10^{-9}$   $\text{cm}^3 \text{s}^{-1}$  as shown in Table 2.3. This is because the excited rare-gas is near ionisation and an electron can transfer to a halogen atom in the halogen bearing molecule and remove the atom to form the ionically bound rare-gas halide. Such reactions are described as 'harpooning' due to the quite large separations (5 - 10 Å) at which they can take place. It is clearly desirable to design discharge pumped rare-gas halide lasers to promote this formation channel (if it is possible to simultaneously maintain discharge efficiency and minimise optical absorption and excited state quenching).

In electron-beam pumped devices the fraction of rare-gas halide formation that takes place through the metastable channel is unavoidably small. This is because the electron beam energy is usually above 100 keV with the result that high densities of ionic species are produced. A typical ionic reaction channel is





where M is a third body, most probably the buffer gas. The recombination of  $R^+$  and  $X^-$  in this reaction can only occur if the kinetic energy generated by the particles' approach is removed. This happens when the orbiting pair collide with a neutral background gas atom (M). Therefore, at low pressure, the three-body rate constant can be expressed as the product of a two-body rate constant and the third-body particle density. At high pressure, however, the approach of the ions is impeded by the mobility of the ions. In this regime, the effective two-body rate constant will vary inversely as the third-body particle density. Therefore, it follows that there will be a maximum in the effective two-body rate constant at an intermediate pressure. This is demonstrated in the theoretical calculations of Flannery and Yang (1978) for excimer formation in mixtures of a single rare-gas with a fluorine donor. Their graphical results, showing variation of the rate constant against background number density (on two scale ranges), are shown in Fig 2.9. Corresponding approximate rate constants are given in Table 2.3.

Although the ionic formation reactions may have high branching ratios and fast rates, in the presence of adequate third-body pressure, the attainable kinetic efficiencies are lower than in the metastable channel. The energy levels shown in Table 2.2 indicate that the ionic quantum efficiency is limited to about 70% of the metastable quantum efficiency. In addition a much greater variety of reactions take place when the initial formation is ionic rather than metastable with a resulting loss of energy. Despite these

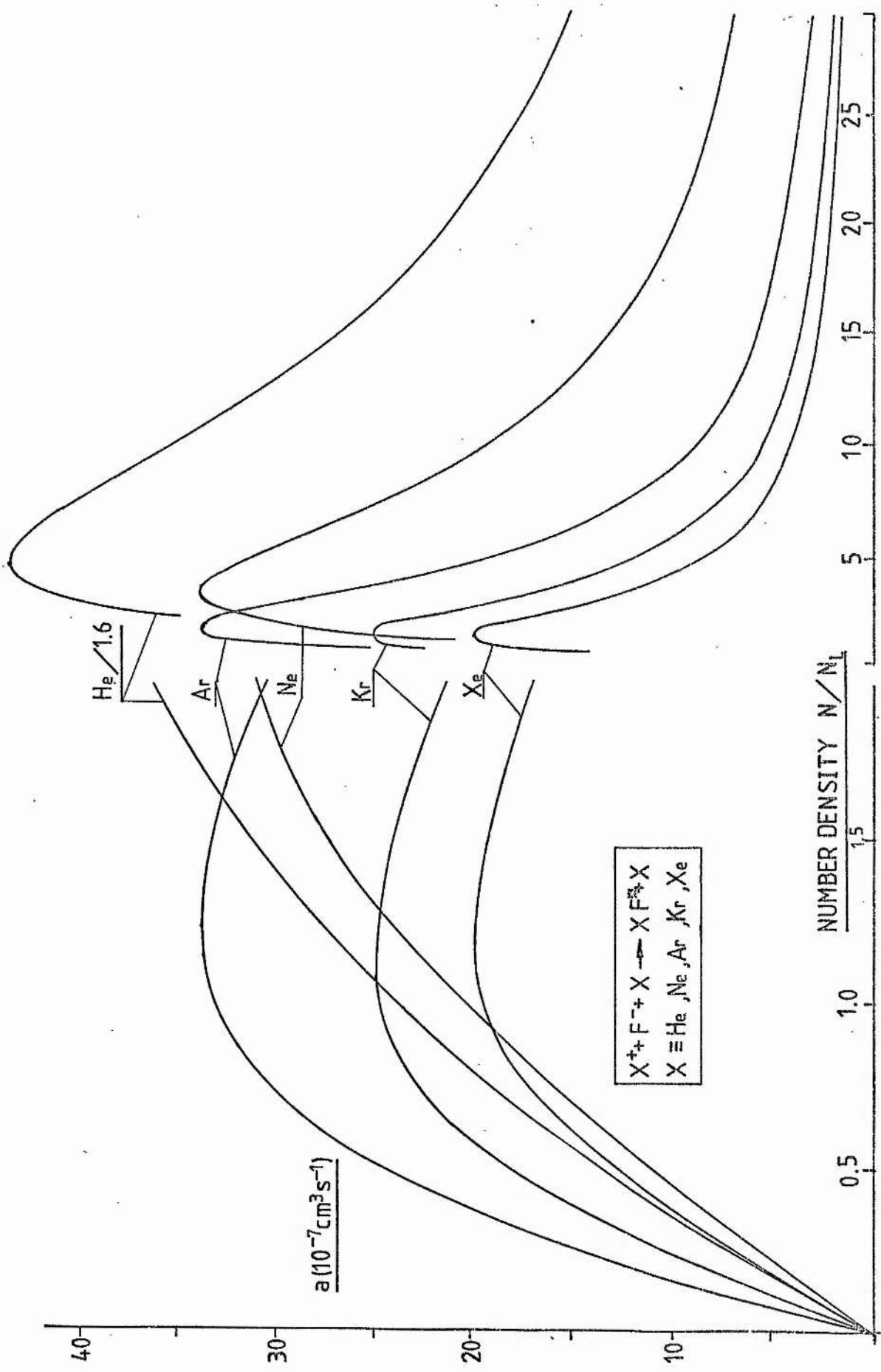


Figure 2.9 Recombination coefficient - a - vs. gas density. (From Flannery 1978)

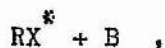
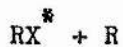
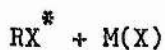
inefficiencies, electron beam pumping still yields higher efficiencies than does discharge pumping. The reasons for this stem largely from the discharge instabilities which develop in DC pulsed discharges. Highest efficiencies for excimer lasers have been achieved by combining e-beam and discharge pumping.

The role of the halogen donor and buffer gas in the kinetics of rare-gas halide lasers is important and complicated. Their quenching activity will be apparent in the following section and the remaining details of their behaviour is presented in sections 2.2.3 and 2.2.4.

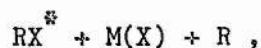
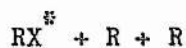
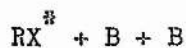
### 2.2.2 Quenching Kinetics

In rare-gas halide lasers, various reactions take place which remove the excimer molecule and also the ionic and metastable precursors in direct competition with formation reactions. Energy may consequently be lost via a radiative transition. Such reactions are very important and partly determine the pressure and ratios of the constituent gases. Despite this, much of the necessary quantitative information on quenching reactions is not available, most of the published data being confined to XeF and KrF lasers.

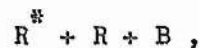
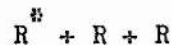
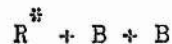
The general reactions, where published information exists, are for excimer quenching by two-body reactions,



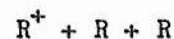
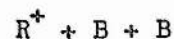
excimer quenching in three-body reactions,



metastable quenching in three-body reactions,



and ion quenching in three-body reactions,



A collection of quenching rate constants for some particular cases of these reactions is given in Table 2.4 and although this does not represent an exhaustive summary of the literature it is fairly representative of the fact that quenching studies have been carried out for only a small fraction of the gas combinations that have been used for excimer lasers. It is noted, in particular, that no studies have been carried out using  $SF_6$ , the donor used in the majority of the experimental work described in this thesis. Despite these reservations the significance of the available data is considerable and may be related to the trends demonstrated in the experiments described in Chapters 7 and 8.



Values from Rhodes(1979) and:-

- (2) Rokni (1978)
- (3) Johnson (1980)
- (4) Rokni (1977)
- (5) Trainor (1980)
- (6) Fisher (1978)

	XeF <sup>+</sup>	KrF <sup>+</sup>	ArF <sup>+</sup>	He <sup>+</sup>	Ar <sup>+</sup>	Kr <sup>+</sup>	Xe <sup>+</sup>	He <sup>+</sup>	Ne <sup>+</sup>	Ar <sup>+</sup>	Kr <sup>+</sup>	Xe <sup>+</sup>
F <sub>2</sub>	35	55	190								20	
NF <sub>3</sub>	1.6											
He	0.01 (6)											
Ne	0.03 (6)											
Ar	0.13	0.13	0.86									
Kr		0.16 (2)										
Xe	2.9 (2)							9				
2He				0.02								
2Ne	0.45 (5)								8			
2Ar	1.5 (4)	7 (2)			1	1	0.1			25		
2Kr		67 (2)				3					25 (3)	
2Xe	2.6						4					20
Xe+He							1.4					11
Xe+Ne	80 (5)											
Xe+Ar	30 (4)						2					
Xe+F <sub>2</sub>	1500 (5)											
Kr+He											6.1	
Kr+Ar											25 (3)	
Ar+He										10		
e	4x10 <sup>4</sup> (5)											

Units 2-body : 10<sup>-11</sup> cm<sup>3</sup>s<sup>-1</sup>  
 3-body : 10<sup>-32</sup> cm<sup>6</sup>s<sup>-1</sup>

Table 2.4 Quenching Reaction Rates

The net formation rate of excimer molecules via the 2-body metastable channel with loss by spontaneous decay and 2-body quenching, and with no other process effective, is given by

$$dn_1/dt = k_1 n_2 n_3 - k_2 n_1 n_4 - n_1/t_s \quad (1)$$

where the symbols are as follows :

- $n_1$  - excimer number density in  $\text{cm}^{-3}$
- $n_2$  - metastable rare-gas density in  $\text{cm}^{-3}$
- $n_3$  - donor molecule density in  $\text{cm}^{-3}$
- $n_4$  - quenching particle density in  $\text{cm}^{-3}$
- $k_1$  - formation (harpoon reaction) rate constant in  $\text{cm}^3 \text{s}^{-1}$
- $k_2$  - 2-body quenching rate constant in  $\text{cm}^3 \text{s}^{-1}$
- $t_s$  - excimer spontaneous emission lifetime in s .

Assuming that the constituent gas densities stay constant on the timescale of interest and that stimulated emission is negligible, the solution to (1) is

$$n_1 = k_1 n_2 n_3 (1 - \text{expt}(-k_2 n_4 - 1/t_s)) / (k_2 n_4 + 1/t_s) \quad (2)$$

This has the maximum value

$$n_1 = k_1 n_2 n_3 / (k_2 n_4 + 1/t_s) \quad (3)$$

with a characteristic rise time given by

$$t(\text{rise}) = -(\ln(1 - 1/e))/(k_2 n_4 + 1/t_s) \quad (4)$$

Equation (4) has a maximum value when the quenching is small and for a typical excimer life-time of 10 ns is about 5 ns. This maximum rise time is shorter than the usual pumping pulse durations (50 ns) and much shorter than the microwave pulses of the experimental apparatus (320 ns) used in this study so that the excimer density given by (3) may be used in most cases.

For 2-body quenching of the excimer by the halogen donor, equation (3) becomes

$$n_1 = k_1 n_2 n_3 / (k_2 n_3 + 1/t_s) \quad (5)$$

This expression has a maximum value, at high donor concentrations, given by

$$n_1 = k_1 n_2 / k_2 \quad (6)$$

where we have assumed that the metastable density,  $n_2$ , remains constant. To achieve say 90% of this value, the required donor density is given by

$$n_3 = 9/t_s k_2 \quad (7)$$

This value could be interpreted as the minimum donor density required for the excimer density to have a value that is not limited by the

donor density. On this basis, the minimum partial pressures for  $F_2$  and  $NF_3$  corresponding to the constants in Table 2.4 are 0.06 atm ( $F_2, XeF$ ), 0.09 atm ( $F_2, KrF$ ), 0.04 atm ( $F_2, ArF$ ), and 1.4 atm ( $NF_3, XeF$ ).

If 2-body quenching by a rare-gas is considered, a useful criterion would be that the quenching should be less than the spontaneous loss which is unavoidable. The quenching loss is equal to the spontaneous loss when the following is satisfied;

$$k_3 n_4 = 1/t_s, \quad (8)$$

where  $n_4$  is the rare-gas number density and  $k_3$  is the quenching rate constant for the rare-gas acting on the excimer molecule. The number density  $n_4$  can now be regarded as the maximum rare-gas density and converted to a partial pressure. Maximum partial pressures calculated on this basis for 2-body rare-gas quenching of excimers are shown in Table 2.5(a).

Some values of the 3-body quenching rate constants are shown in Table 2.4. If 3-body quenching and spontaneous decay are regarded as the only losses, equation (1) can be written to give

$$dn_1/dt = k_1 n_2 n_3 - k_3 n_1 n_5 n_6 - n_1/t_s \quad (9)$$

where  $k_3$  is the 3-body quenching rate constant and  $n_5$  and  $n_6$  are the rare-gas densities. If a single rare-gas is involved,  $n_5$  and  $n_6$  will be equal to the total rare-gas density. In this case a partial

Quenchant	X <sub>e</sub> F <sup>**</sup>	K <sub>r</sub> F <sup>**</sup>
He	25	
Ne	8.3	
Kr		3.4
Xe	0.086	
Ar	1.9	3.2

Table 2.5(a) 2-body Excimer Quenching

Quenchant and 3rd.-body	X <sub>e</sub> F <sup>**</sup>	K <sub>r</sub> F <sup>**</sup>	Product of 2-body maximum pressures
Ne + Ne	4.5		
Ar + Ar	2.5	1.5	
Kr + Kr		0.48	
Xe + Xe	0.6		
Xe + Ne	0.12 At <sup>2</sup>		0.71 At <sup>2</sup>
Xe + Ar	0.31 //		0.16 //
Xe + F <sub>2</sub>	0.006 //		0.0006 //
Kr + Ar		0.24At <sup>2</sup>	11 //

Table 2.5 (b) 3-body Excimer Quenching

Quenchant and 3rd.-body	K <sub>r</sub> <sup>**</sup> (F <sub>2</sub> )	K <sub>r</sub> <sup>**</sup> (NF <sub>3</sub> )	X <sub>e</sub> <sup>**</sup> (F <sub>2</sub> )	X <sub>e</sub> <sup>**</sup> (NF <sub>3</sub> )	Product of 2-body maximum pressures
Ar + Ar	4.5	8	14	23	
Kr + Kr	2.5	4.7			
Xe + Xe			2.2	3.6	
Xe + He			14At <sup>2</sup>	38At <sup>2</sup>	2.2 At <sup>2</sup>
Xe + Ar			9.8//	27 //	0.16 //

Table 2.5 (c) 3-body Metastable Quenching

Table 2.5 Quenching—Maximum Partial Pressures (At)

pressure can be found for the rare-gas where the quenching loss and spontaneous loss of the excimer are equal. As before, this pressure could be regarded as a useful maximum and values for cases with rate constants in Table 2.4 are given in Table 2.5(b). If, however, the 3-body quenching is due to two rare-gases, a maximum value can only be found for the product of the partial pressures of the two gases. Such values are also shown in Table 2.5(b) along with values for the product of the maximum pressures of the two gases from the 2-body quenching data for comparison.

Some data is available on the quenching of metastable precursors in 2-body and 3-body reactions. In the absence of other effects the rate of change of the metastable density is given by

$$dn_2/dt = M - k_1 n_2 n_3 - k_4 n_2 n_5 n_6, \quad (10)$$

where the symbols retain their previous meaning and where  $k_4$  is the 3-body metastable quenching rate constant and  $M$  is the metastable production rate. Since it is desirable that quenching should not compete with excimer formation, maximum quenchant and third-body partial pressures are taken as those required to make the quenching loss rate equal to the excimer formation rate using

$$k_1 n_3 = k_4 n_5 n_6. \quad (11)$$

Values of maximum quenchant and third-body partial pressures can be obtained if a value for  $n_3$  is assumed. Minimum values for  $n_3$ , the donor density, were calculated above (in terms of partial pressure).

By using these and metastable quenching rate constants from Table 2.4 we get the values shown in Table 2.5(c). As before, the cases of a single rare-gas and two rare-gases are dealt with.

Quenching of ionic rare-gas precursors will be analogous to metastable quenching. However, the complexity of the ionic formation rate coefficient and lack of knowledge of ion densities mean that the simplified analysis of quenching presented above cannot be applied and no other analysis will be attempted here.

### 2.2.3 Halide Kinetics

The roles of the halogen donor and its products in discharges in rare-gas halide gas mixtures are varied and crucial in determining the fluorescent efficiency. The electro-negativity of the halides result in their having a large influence on discharge stability; they also have fast reaction rates in both formation and quenching reactions. Of special importance in the present study is the reactive nature of the halogens which result in the eventual loss of usable donor molecules. As this happens, the stabilising effect of the electron attaching halogens is lost, resulting in a runaway discharge current in DC discharges or large reflections in microwave discharges. The halogens are lost by the formation of highly stable compounds formed from the original donor constituent atoms or, more importantly, by reaction with wall materials. In the present study, discharge tubes of small diameter were used so that the loss of halogens in wall reactions was fast; consequently, effective gas life

measurements constituted a large proportion of the experimental work. In active lasers the halogen donor and its products may reduce the laser performance by absorbing at the laser wavelength. This and other considerations result in there being very few halogen compounds which are suitable donors. The most frequently used donors are the diatomic halogens,  $\text{NF}_3$ , and  $\text{HCl}$ . In the present work  $\text{SF}_6$  was used extensively because it is cheap, stable, and relatively unstudied in an excimer context. In a few cases  $\text{NF}_3$  was used for comparison with  $\text{SF}_6$ . The donor used for  $\text{XeCl}$  and  $\text{KrCl}$  was  $\text{HCl}$ . In the following discussion,  $\text{F}_2$  is included because of its widespread use and because it will be formed when the other fluorine donors,  $\text{NF}_3$  and  $\text{SF}_6$  dissociate in the discharge.

Fluorine Molecular fluorine is probably the best donor for  $\text{KrF}$  and  $\text{ArF}$  lasers though slightly inferior to  $\text{NF}_3$  for use in  $\text{XeF}$  lasers. It gives rapid formation rates both by the metastable channel (reaction 8, Table 2.1) and the ionic channel (reaction 12, Table 2.1). The ionic channel formation rate is actually determined by the slower electron dissociative attachment rate which is about  $7 \times 10^{-10} \text{ cm}^3 \text{ s}^{-1}$  for 5 eV thermal electrons. The rapid formation rates with  $\text{F}_2$  as donor are matched by rapid quenching of the excimer by  $\text{F}_2$  as shown in Table 2.4. If donor concentrations are high enough for equation (6) of Section 2.2.2 to apply, the ratio of the excimer density to the metastable density is limited to 2.1 : 1 for  $\text{XeF}$ , 1.2 : 1 for  $\text{KrF}$ , and 0.4 : 1 for  $\text{ArF}$ .



For each rare-gas fluoride molecule, two fluorine atoms are generated with the result that the density of free fluorine is highest when  $F_2$  is used as the donor. Since fluorine, and the other halogens, are effectively lost via reactions involving the free atoms, the gas life with  $F_2$  as donor is likely to be poor. The major consideration concerning gas life is the comparison of the wall collision rate with the  $F + F$  recombination rate. The recombination rate is quite slow. For example, Johnson and Hunter (1980) give an estimated value of  $10^{-33} \text{ cm}^6 \text{ s}^{-1}$  for the reaction



where  $M$  is a third-body. The fluorine loss rate will be twice the recombination rate of formation of  $F_2$  and is therefore given by

$$dn_7/dt = 2k_5(n_7)^2 n_6 , \quad (1)$$

where  $n_7(\text{cm}^{-3})$  is the fluorine number density,  $n_6(\text{cm}^{-3})$  is the buffer gas density, and  $k_5$  is the rate constant. Substitution of the above value for  $k_5$  gives

$$dn_7/dt = 2 \times 10^{-33} (n_7)^2 n_6 \text{ cm}^{-3} \text{ s}^{-1} . \quad (2)$$

If it is assumed that each fluorine atom that collides with the container wall is lost there, the diffusion loss rate is given by

$$v_D = Dn_7/\Lambda^2 , \quad (3)$$

where  $v_D$  ( $\text{cm}^{-3}\text{s}^{-1}$ ) is the diffusion loss rate,  $D$  the diffusion coefficient and  $\Lambda$  the characteristic diffusion length. For a cylindrical volume with negligible end areas (a long thin tube for example),  $\Lambda$  is given by

$$\Lambda^2 = (r/2.405)^2, \quad (4)$$

where  $r$  is the tube radius and 2.405 comes from the Bessel function. (The derivations of equations (3) and (4) are given by McDaniel and Mason 1973). The diffusion coefficient for fluorine can be found from the equation

$$D = 3(8kT/\pi m_2)^{1/2}/32n_2\sigma_{12}^2, \quad (5)$$

which is equation (28) of Section 3.1.1. Here,  $n_2$  is the buffer gas density,  $m_2$  the buffer gas molecular mass, and  $\sigma_{12}$  the buffer gas - halogen collision diameter. Using values from Table 3.1 for fluorine with helium as buffer at 300K gives

$$D = 2.7 \times 10^{19}/n_6 \text{ cm}^2\text{s}^{-1} \quad (6)$$

with  $n_6$  in  $\text{cm}^{-3}$ . Substituting equations (4) and (6) into (3) gives

$$v_D = 1.6 \times 10^{20} n_7/r^2 n_6 \text{ cm}^{-3}\text{s}^{-1}, \quad (7)$$

where  $r$  is in cm and  $n_7$  is in  $\text{cm}^{-3}$ . The diffusion loss rate can now be compared with the recombination loss rate by comparing equations

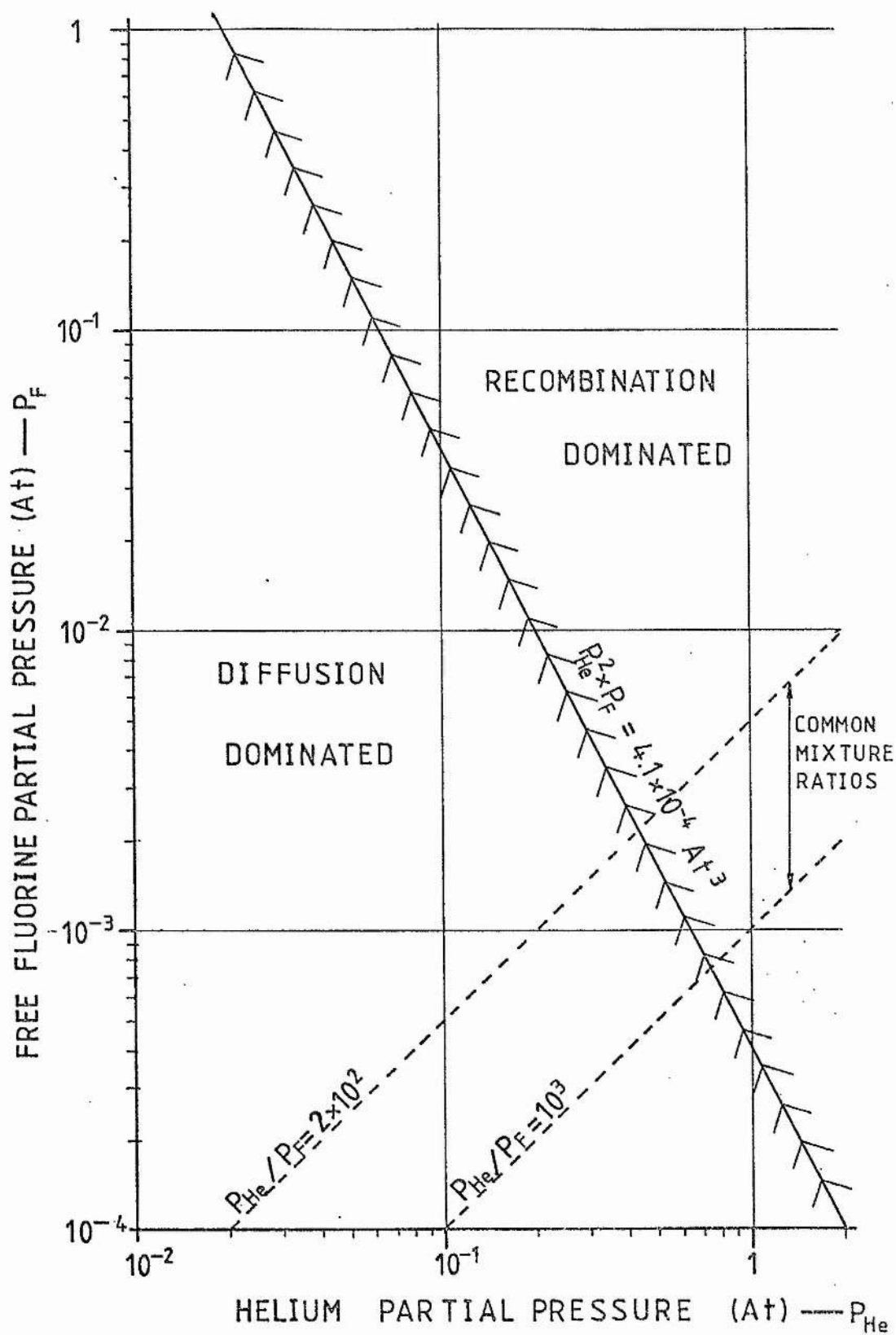
(7) and (2). Equating these and using the experimental tube radius of 0.1 cm and converting to partial pressure gives

$$P_{\text{He}}^2 P_{\text{F}} = 4.1 \times 10^{-4} \text{ atm}^3 \quad (8)$$

where  $P_{\text{He}}$  and  $P_{\text{F}}$  are the helium and fluorine partial pressures respectively. This function is plotted in Fig. 2.10 where the straight line delineates the recombination and diffusion dominated regions. Also shown on this graph is a region that covers the range of buffer gas -  $\text{F}_2$  mixture ratios commonly used in excimer lasers.

The experimental work was conducted over ranges of pressures and mixtures that fall in both the recombination dominated and diffusion dominated regions of Fig 2.10. However, in the long term, after a large number of pulses, the halogen population will be depleted by diffusion even if the diffusion rate is slow. The details of the diffusion process in the short term are discussed in Chapter 3.

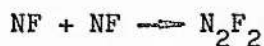
Nitrogen Trifluoride The removal of a fluorine atom from  $\text{NF}_3$  takes 2.5 eV compared with 1.6 eV for  $\text{F}_2$  (Table 2.2). Possibly as a result of this, the metastable excimer formation reactions are slower for  $\text{NF}_3$  as donor than for  $\text{F}_2$ . However, for XeF at least, the quenching by  $\text{NF}_3$  is also considerably slower than quenching by  $\text{F}_2$ . Thus the ratio of the excimer density to the metastable density, calculated from (6) of Section 2.2.2, is 5.6 for XeF with  $\text{NF}_3$  donor compared to the ratio 2.1 with  $\text{F}_2$  as donor. This predicts a higher formation efficiency for  $\text{NF}_3$  and it seems likely that this is the reason for higher lasing efficiencies that are reported when it is used to



• FIGURE 2.10 Fluorine recombination and diffusion

replace  $F_2$  in XeF lasers.

Nitrogen trifluoride has been used in KrF lasers, as well as XeF lasers, and reaction kinetics have been studied by Chow et. al. (1977), Shaw and Jones (1977), Smith and Huestis (1981), and Tang et. al. (1981). In Chow (1977) it is suggested that the formation reaction of  $Kr^*$  with  $NF_2$  is twice as fast as the reaction with  $NF_3$  and that the increase in laser output that occurs during the first 100 shots is due to the initial increase in  $NF_2$  density. From this it follows that the recombination reaction



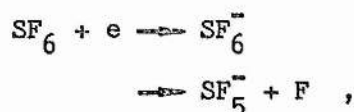
will be important as well as the reaction



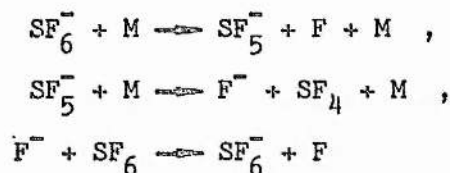
Although the reaction rate for  $NF + NF$  is not known, it is suggested in Chow (1977) that the above reaction is the most likely and removes most of the  $NF$  between laser pulses. The 3-body recombination rate has been found to be  $2.3 \times 10^{-31} \text{ cm}^6 \text{ s}^{-1}$  with 1 Atm of Ne as buffer (Tang 1981), decreasing to about half this value with 4 Atm of Ne. This is about 200 times faster than the  $F + F$  recombination rate with the result that the free fluorine density, and hence the diffusion loss, will be less when  $NF_3$  is used instead of  $F_2$  as the donor. This correlates with the increased gas lives that are reported for  $NF_3$ .

Sulphur Hexafluoride Sulphur hexafluoride is seldom used as a

fluorine donor in excimer lasers and consequently the kinetics of  $SF_6$  in this context have received little attention. The stability of  $SF_6$  is greater than that of  $NF_3$ ; energies greater than 3.7 eV are required to remove a fluorine atom from  $SF_6$ . For this reason  $SF_6$  is unlikely to give good branching ratios for excimer formation in the metastable channel. The reaction rate of  $Kr^{\#}$  with  $SF_6$ , for example, is shown by Velazco et. al. (1976) to be negligibly small. However, strong lasing with  $SF_6$  as a donor has been observed by Rothe and Gibson (1977) with the implication that formation must take place via ionic species. This seems reasonable in view of the strong electron affinity of  $SF_6$  (1.4 eV) and F (3.5 eV). Electrical breakdown in  $SF_6$  has been studied extensively due to its use as an electrical insulator. Important reactions are given by



as discussed by Fehsenfeld (1970), and



as discussed by McGeehan et. al. (1975). These reactions, coupled with the observation that six fluorine atoms are available from each donor molecule, suggest that F and  $F^-$  densities will be high when  $SF_6$  is used as a donor. Generally however there is little information available to suggest which of the possible reactions and species will

be present in rare-gas halide gas discharges with  $SF_6$  as donor.

#### 2.2.4 Buffer Gas Kinetics

Buffer gases have generally been found to be necessary in rare-gas halide laser gas mixtures with optimum quantities often exceeding 95% of the total gas content. The type of buffer gas (He, Ne or Ar) has been found to be important for discharge stability, fluorescence efficiency, and lasing efficiency. In the following discussion of the important functions of the buffer gas, Xe and Kr will be included because in some of the experimental work no buffer gas was used and, since Xe or Kr are then the majority gas, they must perform the functions of the buffer gas. A collection of data for rare-gases is given in Table 2.2.

Electron Energy Distribution The buffer gas type and its pressure determine the E/N value (ratio of electric field to number density) of the discharge which is a determinant of the electron energy distribution. The distribution in turn affects the rate at which the various excitations and ionisations take place. In the experimental microwave apparatus the pulse power, P, was 50 kW and this is related to the electric field at the waveguide centre, E, by

$$P = Eab(1-(f_c/f)^2)^{1/2}/4(\mu_0/\epsilon_0)^{1/2}$$

where a and b are the waveguide dimensions,  $\mu_0$  and  $\epsilon_0$  are the permeability and permittivity of free space,  $f_c$  is the cut-off

frequency, and  $f$  is the guide frequency (see Harvey 1963). This gives an electric field of  $6.7\text{kVcm}^{-1}$  for the waveguide (WG 16) used in our experiments. The discharge coupling structure reduces this value by a factor of about 7 and the pressure range used for the majority of experiments was 0.1 to 2 atm. The resultant range of  $E/N$  values was  $1.8 \times 10^{-17}$  to  $3.6 \times 10^{-16} \text{Vcm}^2$  for the cases of good microwave to discharge coupling. For cases of poor coupling, lower  $E/N$  values result. Electron energy distribution for various  $E/N$  values in discharges in helium, argon, and neon are given by Sze (1979) and reproduced in Fig 2.11. The metastable and ionic energies of the rare-gases are indicated on this diagram and this enables certain qualitative observations to be made with respect to discharge stability and metastable excitation efficiency. Discharge instability in the form of a runaway growth of electron density and current is a major limitation in excimer laser discharges. In DC discharge devices, the result is secondary emission at the electrodes accompanied by arc formation which results in a low impedance that is not matched to the supply network. The decay of the discharge to localised arcs both terminates its use as a medium giving useful optical gain and causes electrode damage at the arcing points. In a microwave discharge this problem is not as severe owing to the containment of the discharge in a dielectric tube. However, high electron densities again result in an unmatched load with the result that a large proportion of the incident microwave power is reflected back from a discharge that is localised within a small portion of the discharge tube. Clearly, if the high energy wing of the electron distribution is too far past the ionisation energy of the heavy rare-gas present, then the tendency to ionisation instability will be



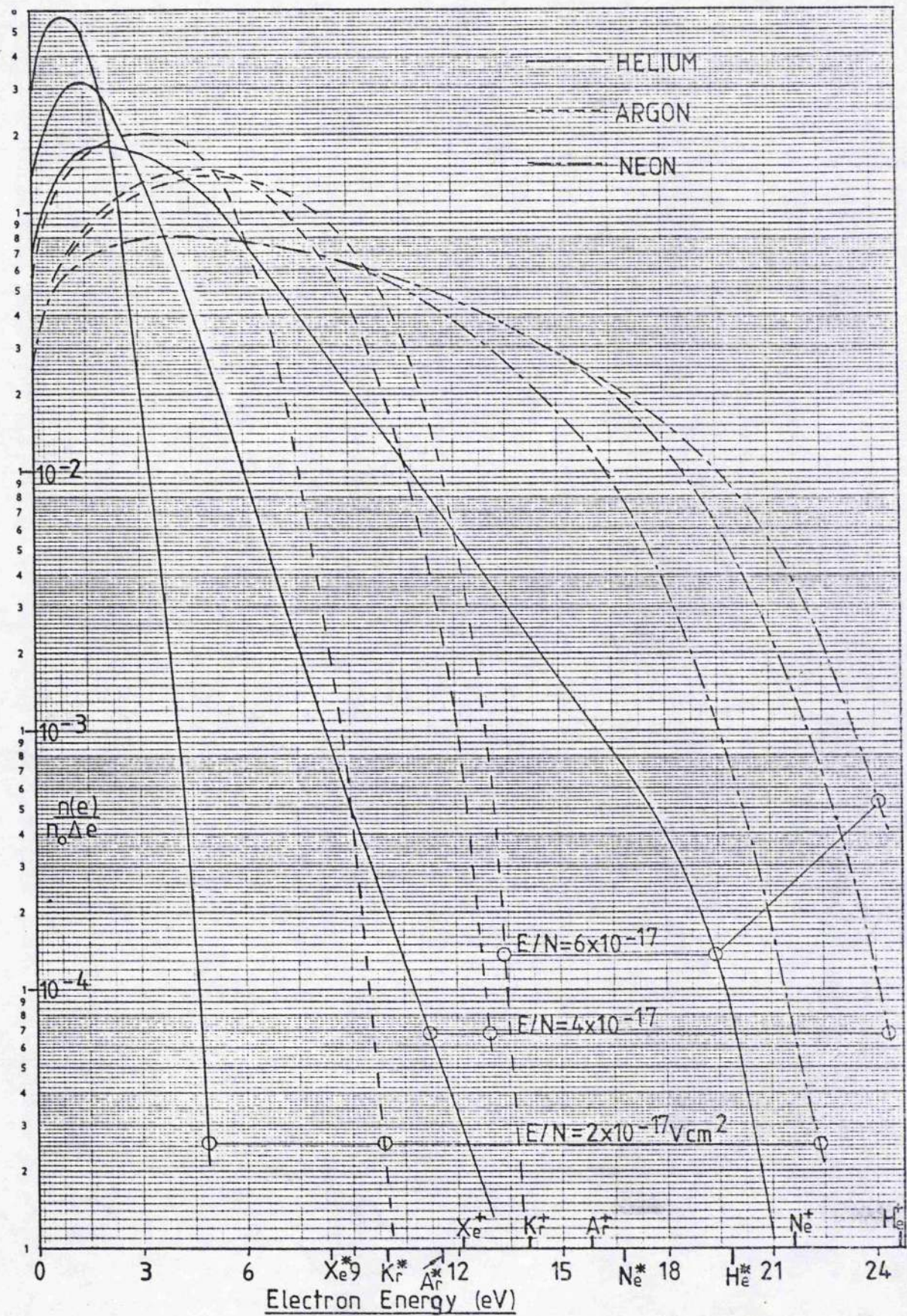


Figure 2.11 Electron Energy Distribution (from Sze 1979)



increased. In practice, however, the presence of attaching species, namely halogens, or easily ionised impurities will alter the relationship between E/N and the onset of instability. Under these circumstances the curves of Fig 2.11 may not be very relevant and a more detailed analysis, like that given in Johnson(1980) for example, may be required.

Thermal Effects The high pump powers used in excimer lasers mean that high gas temperatures are possible. In practice, temperature rises are limited by short pulse operation, low pulse repetition rates, and, in some cases, fast gas circulation. Although moderate temperature rises may be favourable in some cases, large rises will ultimately give unwanted thermal populations. Also, large temperature rises during the discharge will disturb the refractive index in the optical path and affect the beam quality.

Gas heating occurs through elastic collisions between energetic electrons and neutrals. The relaxation time,  $t_e$ , for electrons (see Haydon 1964) is given by the approximation

$$t_e = M/2mv_c ,$$

where M is the molecular mass of the background gas, m is the electron mass, and  $v_c$  the electron - background gas collision frequency per electron. This gives the characteristic time for electrons to come to thermal equilibrium with the background gas in the absence of an external field. The mean collision frequency can be found from the relation

$$v_c = NQV ,$$

where  $N$  is the background gas particle density,  $Q$  is the electron - background gas atom collision cross - section, and  $V$  is the mean electron speed. To obtain an order of magnitude estimate for the value of  $t_e$ , a cross - section of  $3 \times 10^{-20} \text{ m}^2$  is used (Haydon 1964) with an electron energy of 5 eV. With 1 atm of buffer gas, this gives the following values;

$$\text{for helium } t_e = 3 \times 10^{-9} \text{ sec ,}$$

$$\text{for neon } t_e = 2 \times 10^{-8} \text{ sec , and}$$

$$\text{for argon } t_e = 3 \times 10^{-8} \text{ sec .}$$

This indicates that gas heating, with a consequential loss of efficiency, may take place even during a short discharge pulse, particularly with helium as buffer. In addition, it seems likely that long pulses (>100 ns) will result in optical disturbances caused by spatial irregularities of gas heating which result in irregularities in refractive index. For a gas the density is related to the refractive index by the Gladstone-Dale law

$$n-1/\rho = \text{constant} = \Delta n/\Delta \rho .$$

Since for a small heating irregularity the change in density will be proportional to the density itself, the resultant change in refractive index will be proportional to  $(n - 1)$ . Values of  $(n - 1)$  are shown in Table 2.2 and indicate that optical disturbances may be expected to increase with increasing rare-gas atomic mass.

The values of diffusivity for rare-gases are given in Table 2.2 and exhibit considerable variation. Since the diffusivity gives the rate of heat transport per unit temperature gradient, it indicates the rate at which heating irregularities will disappear. The high value for helium may be beneficial for two reasons. Firstly, it will add to the advantage that helium already has for maintaining beam quality in a long discharge pulse. Secondly, use of this gas will aid inter-pulse cooling. This is particularly important in the experiments described in this thesis because of the small tube diameters and the high repetition rates used (1100 pps).

Redistribution of Vibrational Levels As has been described in Section 2.1.3, the lasing efficiency of excimer lasers will have some dependence on the rate of redistribution of vibrational states in the upper state manifold. It is required that this process be fast enough to prevent a non-equilibrium distribution with a deficiency in the upper laser level. In XeF, rapid removal of the bound lower level is also required. Both of these processes are promoted by collisions between the excimer molecule and buffer gas atoms. The collision frequency per excimer molecule (using the approximate theory given in Moore 1972) is given by

$$z = N \pi d^2 (8kT/\mu\pi)^{1/2},$$

where  $z$  is the collision frequency,  $N$  is the buffer gas number density,  $d$  is the collision diameter, and  $\mu$  the reduced mass. For 1 atm of buffer gas at 300K, and using  $3\text{\AA}$  for  $d$ , and the buffer gas

atomic mass for  $\mu$  as rough approximations, the collision frequencies for He, Ne, and Ar buffers are  $9.5 \times 10^{10}$ ,  $4.3 \times 10^{10}$ , and  $3.0 \times 10^{10} \text{ s}^{-1}$ , respectively. These correspond to lifetimes between collisions that are 50 times less than excimer spontaneous decay lifetimes. However, the collision rate just given will be larger than the vibrational transition rate induced. This is because the excimer vibrational energy levels are separated by 0.037 eV in XeF, 0.05 eV in KrF, and 0.026 eV in XeCl, while the characteristic energy at 300K is 0.026 eV. While these data could be used to predict the buffer pressures required for adequate upper state relaxation, there are outstanding uncertainties in the collision process. An example of this is the fast relaxation reported for Ar buffer on XeF (Hsia 1979) which is thought to be due to the formation of the intermediate specie  $\text{ArXeF}^*$ .

Quenching Activity Information on the quenching activity of the rare-gas is given in Table 2.4 which has been used to calculate the partial pressure limits shown in Table 2.5. For 2-body quenching, He and Ne apparently pose no problems but Ar may quench XeF, and KrF to a lesser extent. The high quenching rate of Xe on XeF indicates that Xe pressure has to be considerably less than 0.1 atm for a low quenching rate. In gas mixtures with no buffer gas, this becomes the total gas pressure limit. Quenching of KrF by Kr is very much slower, however, and therefore KrF operation will not have the same limitations imposed by quenching that XeF has.

From the information on 3-body quenching, only two examples occur giving more stringent conditions than the 2-body limitations. Firstly, Kr partial pressure in a KrF mixture has to be less than 0.48 atm for low quenching. Secondly, if Ne buffer is used with XeF mixtures, the product of the Xe and Ne partial pressure must be less than  $0.12 \text{ atm}^2$ . For example, if the Ne pressure is 1 atm the Xe pressure limit is about the same as that required by the 2-body quenching limit; ie. it must be below about 0.1 atm.

### 2.3 Laser Operation

The pump power density required to obtain excimer fluorescent emission has merely to be sufficient to maintain the discharge with an E/N value high enough for metastable production. For laser operation, however, the population inversion has to be sufficient to give a small signal gain that will give a net gain against the optical losses due to absorption in the laser gas and reflection and transmission losses at the mirrors and/or windows. It is shown below that the relatively high optical loss, coupled with the short wavelength, and broad band emission of rare-gas halide excimers, results in a very high threshold value for the pump power density which will result in laser oscillation. This high power requirement has important consequences for the design of the pumping system.

The important absorption processes in rare-gas halide lasers are probably photodissociation of halides and rare-gas dimer positive ions, photodetachment of negative halogen ions, and photoionisation of excited rare-gas atoms and molecules (Rhodes 1979). Due to the difficulty in detecting absorbing species and measuring absorption during short high power pulses there is considerable uncertainty and lack of information concerning absorption. Brau (in Rhodes 1979) gives a summary of photoabsorption cross sections that have been found from experimental work or calculated on theoretical grounds. Gower et. al. (1978) gives values of 1 - 2%  $\text{cm}^{-1}$  for transient absorption in a XeF laser using  $\text{F}_2$  as donor and He as buffer. Although a careful selection of donor and rare-gases and their pressures can lead to much smaller absorption (Rhodes 1979), the kinetic efficiency is reduced. It seems likely, therefore, that a value of 1%  $\text{cm}^{-1}$  absorption will be a useful lower limit to apply. For a common excimer laser of about 1m length this gives a round trip loss of 200%. This clearly is much greater than any reasonable mirror losses which would therefore have a subordinate role in this case. In the discharge tube of this work, the discharge length was around 10 cm so that a round trip absorption loss of 20% might be expected. By using a small output coupling fraction, mirror losses are kept well below this loss value and may still be ignored.

Threshold lasing may be approached by increasing the pump power and hence both the upper state population and the spontaneous emission intensity. Laser oscillation begins when the spontaneous emission intensity along the cavity axis causes sufficient stimulated

emission to compensate for the optical losses. The fraction of the spontaneous emission that travels sufficiently parallel to the optical axis to complete a round trip of the cavity is very small. The stimulated emission at threshold is also very small as this merely replaces the fraction of the spontaneous intensity lost in a round trip of the cavity. Therefore, the threshold pump power is that required to feed the total spontaneous emission that occurs when the round trip loss from the cavity is equal to the round trip gain. Regarding the lower laser population as effectively zero, the small signal gain coefficient is given by

$$\gamma_0(\nu) = N\sigma(\nu) ,$$

where  $\gamma_0(\nu)$  is the frequency dependent small signal gain coefficient,  $N$  is the upper state population density and  $\sigma(\nu)$  is the frequency dependent stimulated emission cross-section. Equating the small signal gain to the loss,  $l(\nu)$ , gives the threshold population

$$N = l(\nu)/\sigma(\nu) .$$

This population is lost to spontaneous emission at the rate

$$dN/dt = l(\nu)/t\sigma(\nu)$$

where  $t$  is the upper state lifetime.



If the pump power is converted to spontaneous emission with an efficiency  $e$ , the threshold pump power density is given by

$$P = (dN/dt)hv/e = h\nu l(\nu)/et\sigma(\nu) \quad (1)$$

where  $h\nu$  is the photon energy. Values of the product  $t\sigma(\nu)$  have been measured for some of the excimers. For example, values for XeF, KrF, and XeCl are given in Rhodes(1979) as 64, 17, and  $50 \text{ \AA}^2 \text{ ns}$  respectively. Alternatively,  $\sigma t$  values may be calculated in the following way. The stimulated emission rate may be expressed in terms of the stimulated emission cross-section or in terms of the Einstein B coefficient (the stimulated emission rate coefficient). This yields the relationship

$$B = \sigma(\nu)c/h\nu g(\nu)$$

where  $g(\nu)$  is the line shape function. The B coefficient is related to the A coefficient (spontaneous emission rate coefficient) by

$$A = B8\pi h\nu^3/c^3,$$

(see for example Verdeyen 1981). Since the A coefficient is the reciprocal of the spontaneous emission lifetime, these two equations can be combined to give

$$\sigma(\nu)t = \lambda^2 g(\nu)/8\pi.$$

The approximate linewidth is given by

$$\Delta\nu = 1/g(\nu) = c\Delta\lambda/\lambda^2$$

which gives

$$\sigma(\nu)t = \lambda^4/8\pi c\Delta\lambda \quad (2)$$

Substitution in (1) yields

$$P = 8\pi I(\nu)hc^2\Delta\lambda/e\lambda^5 \quad (3)$$

The linewidth for XeF is difficult to assess but the spectra of Figs 2.6 and 2.5 for KrF and XeCl indicate FWHM linewidths of about 30Å and 20Å respectively. This gives values for  $\sigma t$  of 17Å<sup>2</sup> ns for KrF and 60Å<sup>2</sup> ns for XeCl which compare well with the values above. The highest pump power density required is for ArF ( $\sigma t = 12\text{Å}^2 \text{ ns}$ ) while the lowest is for XeF ( $\sigma t = 64\text{Å}^2 \text{ ns}$ ). Using these values in (1) with 1% cm<sup>-1</sup> loss gives threshold pump power densities of  $8.8 \times 10^8 / e \text{ Wm}^{-3}$  and  $8.5 \times 10^9 / e \text{ Wm}^{-3}$  for XeF and ArF respectively.

The efficiency used above is the product of the efficiency of metastable precursor production by the discharge and the quantum efficiency, if perfect excimer formation kinetics are assumed. For XeF the quantum efficiency is 0.42 and metastables may be produced with an efficiency of around 20% (Rhodes 1979). This gives a threshold pump power density for XeF of around  $10^{10} \text{ Wm}^{-3}$  ( $10 \text{ kWcm}^{-3}$ ) as a minimum value. A practical laser design would need to allow for

high output coupling and the likely occurrence of non-optimum conditions such as high optical absorption in impure gases. A pump power density of perhaps  $100\text{kWcm}^{-3}$  may then be required. If, in addition, operation with a short wavelength excimer, such as ArF, was a desired option, pump power densities a factor of 10 larger ( $1\text{MWcm}^{-3}$ ) would be desirable. Thus while continuous operation of excimer lasers is not precluded by any intrinsic property, it is clearly prevented by the power requirement and the attendant heat disposal problem.

To summarise, it has been shown above that the laser pump power requirement is a function of the linewidth/ $\lambda^5$ . This indicates the dramatic increase in difficulty of laser operation that accompanies the development of short wavelength lasers. In addition, broad linewidth and high optical absorption of excimer emission results in high pump power density requirements of at least  $10\text{kWcm}^{-3}$ . It follows that development of systems with smaller power supply requirements would involve efforts to give high efficiencies in very small active volumes.

### 3 HALOGEN LOSS BY DIFFUSION TO THE WALL

In the microwave discharge apparatus a small bore tube, 2 mm internal diameter, was used to contain the discharge volume. Since a strong reaction is to be expected between a free halogen atom and silicon from the quartz tube, it is important to consider the loss of halogen resulting from diffusion to the wall. This diffusion is described in the following with the diffusant produced in repetitive short pulses accompanied by heat production. The thermal behaviour is treated first to allow calculation of temperature dependent diffusion.

#### 3.1 Derivation of the Calculation Method

The primary simplifications are that the pulse duration is assumed to be negligible compared with the period between the pulses, and that the thermal capacity of the containing tube is much greater than that of the gas. The latter simplification permits the tube heating to be treated separately from the gas heating.

Two heat loss processes are described: free convection and forced convection. Under free convection, heat is lost from the outer surface of the tube at a rate proportional to  $T^{5/4}$ , while forced convection is regarded as holding the outer surface of the tube at room temperature.

### 3.1.1 Basic Equations

The fundamental equations governing diffusion in isotropic media are

$$f = -D \text{ grad } C \quad (1)$$

and

$$\partial C / \partial t = \text{div}(D \text{ grad } C), \quad (2)$$

where  $C$  is the particle concentration,  $D$  the diffusion coefficient and  $f$  the normal particle flow in number per unit time per unit area. For heat transport by conduction in both the gas and the tube wall we can write

$$C = \rho h T,$$

and

$$D = K / \rho h,$$

where  $T$  is the temperature,  $\rho$  the density,  $h$  the specific heat capacity, and  $K$  the thermal conductivity of the gas (or the wall).

It is usual to write

$$k = K / \rho h$$

where  $k$  is known as the diffusivity. The solution of the diffusion equation (2) is discussed in depth by Crank (1956) and, for heat conduction, by Carslaw and Jaeger (1959).

The particular solution of (2) required here is for cylindrical geometry with variation for the radial coordinate only. The temperature dependence of the diffusion and diffusivity will be treated by separating the time behaviour into small elements with constant diffusion and diffusivity. The necessary changes due to temperature will be in steps providing an average value to assign to each time element. This means that a solution of (2) for constant diffusion coefficient can be used, thus avoiding considerable mathematical complexity.

For the case of a constant diffusion coefficient and by using cylindrical coordinates with radial variation only, equation (2) becomes

$$\frac{\partial C}{\partial t} = D \left( \frac{\partial^2 C}{\partial r^2} + \frac{1}{r} \frac{\partial C}{\partial r} \right) . \quad (3)$$

It will be useful to use the following dimensionless variables in this equation;

$$\bar{r} = r/a$$

$$\bar{t} = Dt/a^2, \quad \bar{C} = C/C_0 \text{ for diffusion, and}$$

$$\bar{t} = kt/a^2 \quad \text{and} \quad \bar{T} = T/T_0 \text{ for heat transport,}$$

where  $a$  is the inner tube wall radius,  $C_0$  is the concentration of diffusant resulting from a single excitation pulse, and  $T_0$  is the room temperature (293K).

### 3.1.2 Heat Transport

The appropriate dimensionless form of (3) is

$$\partial \bar{T} / \partial \bar{t} = \partial^2 \bar{T} / \partial \bar{r}^2 + (1/\bar{r}) \partial \bar{T} / \partial \bar{r} \quad (4)$$

For typical boundary conditions the analytic solution of this equation involves lengthy summations. Solutions are therefore obtained using the finite difference method (Crank 1956) with  $\bar{r}$  divided into a number of intervals. In the following, the integer variables  $i$  and  $j$  give the number of spatial increments,  $\delta \bar{r}$ , and temporal increments,  $\delta \bar{t}$ , respectively. The finite difference representations of the derivatives approximate to the following,

$$(\partial^2 \bar{T} / \partial \bar{r}^2)_{i,j} = (\bar{T}_{i+1,j} - 2\bar{T}_{i,j} + \bar{T}_{i-1,j}) / (\delta \bar{r})^2, \quad (5)$$

$$(\partial \bar{T} / \partial \bar{r})_{i,j} = (\bar{T}_{i+1,j} - \bar{T}_{i-1,j}) / 2\delta \bar{r}, \quad (6)$$

$$(\partial \bar{T} / \partial \bar{t})_{i,j} = (\bar{T}_{i,j+1} - \bar{T}_{i,j}) / \delta \bar{t}. \quad (7)$$

Also, we have

$$\bar{r} = i\delta\bar{r} \quad (8)$$

Substituting these into (5) gives

$$\bar{T}_{i,j+1} = \bar{T}_{i,j} + \delta\bar{t}[(2i+1)\bar{T}_{i+1,j} - 4i\bar{T}_{i,j} + (2i-1)\bar{T}_{i-1,j}]/2i(\delta\bar{r})^2 \quad \dots(9)$$

This equation gives a formula whereby the radial distribution of the dimensionless temperature can be calculated for successive time intervals starting from an initial distribution. It can be seen that the value of the main variable at a given point is calculated from three spatial values one time increment previously. These three spatial points are the current point and its neighbours at smaller and larger radius. This formula cannot be used, therefore, for the two end points of the radius variable. In addition, these end points may be in contact with heat sources or sinks. Since, in general, a great variety of conditions may occur, it will be necessary to elaborate the model used here to permit calculation of these terminal values.

For the tube, the large thermal capacity means that conditions in the gas will have stabilised before the tube temperature starts to rise. As a consequence, the heat flowing into the inner tube wall can be regarded as constant, smooth, and equal to the average rate at which the gas is heated. For the present circumstances equation (1) can be written



$$f = -D\partial C/\partial r \quad ,$$

which in dimensionless variables of heat transport is

$$\dot{q} = (-KT_0/a)\partial\bar{T}/\partial\bar{r} \quad , \quad (10)$$

where  $\dot{q}$  is energy per unit area per unit time. The finite difference representation of (10) is

$$(\bar{T}_{i+1,j} - \bar{T}_{i-1,j})/2\delta\bar{r} = -a\dot{q}/KT_0 \quad . \quad (11)$$

For the inner tube wall, the term  $T_{i-1}$  in (11) and (9) will be fictitious and must be eliminated from (9) and (11) to give

$$\bar{T}_{i,j+1} = \bar{T}_{i,j} + (2\delta\bar{t}/(\delta\bar{r})^2)[\bar{T}_{i+1,j} - \bar{T}_{i,j} + (2i-1)\delta\bar{r}a\dot{q}/2iKT_0] \quad . \quad \dots(12)$$

For the outer tube wall,  $\dot{q}$  is the heat loss rate and  $\bar{T}_{i+1}$  is eliminated to give

$$\bar{T}_{i,j+1} = \bar{T}_{i,j} + (2\delta\bar{t}/(\delta\bar{r})^2)[\bar{T}_{i-1,j} - \bar{T}_{i,j} - (2i+1)\delta\bar{r}a\dot{q}/2iKT_0] \quad . \quad \dots(13)$$

Under forced convection, the outer wall temperature is constant at  $T_0$  and (13) is not used. For free convection from a horizontal tube of diameter  $d$ ,  $\dot{q}$  is given by

$$\dot{q} = H(\Delta T)^{5/4}/d^{1/4} \quad , \quad (14)$$

where  $\Delta T$  is the difference between the surface temperature and room temperature and  $H$  is a constant. If  $d$  is in cm and  $\dot{q}$  is in  $\text{Wcm}^{-2}$  the value of  $H$ , given by Zemansky (1957), is  $4.2 \times 10^{-4}$ . In (13) we can now replace  $\dot{q}$  using (14) and then by writing

$$\Delta T = T_{i,j} - T_0 \quad ,$$

we get

$$\begin{aligned} \bar{T}_{i,j+1} = \bar{T}_{i,j} + (2\delta\bar{r}/(\delta\bar{r})^2)[\bar{T}_{i-1,j} - \bar{T}_{i,j} - \\ (2i+1)\delta\bar{r}aHT_0^{1/4}(\bar{T}_{i,j} - 1)^{5/4}10^{-4}Kd^{1/4}] \quad . \quad (15) \end{aligned}$$

If fairly high temperatures are expected on the tube surface, radiative heat loss will become important. In that case the Stefan-Boltzmann radiation law

$$\dot{q} = \sigma E(T^4 - T_0^4)$$

will replace equation (14) or, for intermediate temperatures, be added to it.

We now consider the thermal behaviour of the gas. Initially the gas cooling between pulses is less than the temperature rise caused by the pulses. The mean temperature therefore rises up to a constant value where the inter-pulse cooling and the pulse heating are equal. It is assumed that, due to the large thermal capacity of the tube, the temperature rise of the tube is negligible in the time taken for the mean temperature to become constant. Therefore, in the short term, the gas temperature at the inner tube wall is constant and equal to room temperature. In the long term, the equilibrium gas temperature behaviour can simply be superimposed on the slowly rising wall temperature. However, for large rises in temperature, particularly when cooling is by free convection, the change in diffusivity with temperature will alter the equilibrium behaviour of the gas. This can be taken into account by recalculating the equilibrium behaviour at a few discrete intervals during the temperature rise of the tube.

By symmetry, the temperature gradient at the tube axis is zero so the term  $(1/\bar{r})\partial\bar{T}/\partial\bar{r}$  in equation (4) is indeterminate. The finite difference representation on the axis is given by Crank(1956) but without a derivation; we shall now derive it. The temperature gradient is represented by Taylor's series as

$$\left(\frac{\partial\bar{T}}{\partial\bar{r}}\right)_{\bar{r}} = \left(\frac{\partial\bar{T}}{\partial\bar{r}}\right)_{\text{axis}} + \bar{r}\left(\frac{\partial^2\bar{T}}{\partial\bar{r}^2}\right)_{\text{axis}} + \dots\text{etc} \quad (16)$$

For small  $\bar{r}$ ,  $\partial\bar{T}/\partial\bar{r} = 0$  and (16) approximates to

$$\frac{1}{\bar{r}} \left( \frac{\partial \bar{T}}{\partial \bar{r}} \right)_{\bar{r}} = \left( \frac{\partial^2 \bar{T}}{\partial \bar{r}^2} \right)_{\text{axis}} \quad (17)$$

From (17) and (4) we get

$$\frac{\partial \bar{T}}{\partial \bar{t}} = 2 \frac{\partial^2 \bar{T}}{\partial \bar{r}^2} \quad (18)$$

when  $\bar{r}$  is small. Using  $i = 0$  on the axis, the finite difference representations (4) and (6) give, after rearranging,

$$\bar{T}_{0,j+1} = \bar{T}_{0,j} + 4(\delta \bar{t} / (\delta \bar{r})^2) [\bar{T}_{1,j} - \bar{T}_{0,j}] \quad (19)$$

If detailed time behaviour is not required for the tube, a simple equilibrium analysis can be used by setting

$$\frac{\partial \bar{T}}{\partial \bar{t}} = 0$$

in equation (4) to get

$$\frac{\partial^2 \bar{T}}{\partial \bar{r}^2} + (1/\bar{r}) \frac{\partial \bar{T}}{\partial \bar{r}} = 0 \quad (20)$$

This equation has the general solution

$$\bar{T} = A + B \ln \bar{r} \quad .$$

Using  $\bar{T} = \bar{T}_b$ ,  $\bar{r} = b/a$  at the outer wall, and equation (10), the radial variation of  $\bar{T}$  at equilibrium is given by

$$\bar{T} = \bar{T}_b - (q_a / K T_0) \ln(\bar{r} a / b) \quad (21)$$

The equilibrium temperature difference between the inner and outer tube wall is then given by

$$\bar{T}_a - \bar{T}_b = -(\dot{q}a/KT_0)\ln(a/b) \quad (22)$$

Alternatively, we can calculate the variation of tube temperature with time by treating the tube as a mass with uniform temperature. This approximation is appropriate when the rise in mean temperature is large compared with the temperature drop across the tube wall. The rate at which the mean tube temperature rises is given by

$$dT_m/dt = (P - A_b\dot{q})/mc \quad (23)$$

where  $P$  is the heat supply rate,  $A_b$  is the tube outer surface area,  $\dot{q}$  is the heat loss rate given by (14),  $m$  is the tube mass, and  $c$  is the specific heat capacity of the tube material. Substituting for  $\dot{q}$  from (14) with  $\Delta T = T_m - T_0$  and separating the variables gives

$$\int_0^t dt = \int_0^{T_m} [mcd^{1/4}/(Pd^{1/4} - A_bH(T_m - T_0)^{5/4})] dt_m \quad (24)$$

This integral can be evaluated using standard integral tables. However, having regard to the approximations involved in deriving the equation, numerical integration of (24) is adequate.

The variation of diffusivity with temperature will be considered for the case of pressure being independent of temperature which is the appropriate approximation for a tube of gas connected to a reservoir. The thermal conductivity of a gas varies with the mean molecular speed and is therefore proportional to  $T^{1/2}$ . The gas density is proportional to  $P/T$  and therefore the diffusivity is given by

$$k = K/\rho c = \text{constant} \times T^{3/2}/P \quad (25)$$

From gas kinetic theory (Moore 1972), we have

$$K = m\bar{c}C_p/8^{1/2} \pi d^2, \text{ and}$$

$$\bar{c} = (8k_B T/\pi m)^{1/2},$$

where  $m$  is the particle mass,  $\bar{c}$  is the mean thermal speed,  $C_p$  is the specific heat capacity,  $d$  is the collision diameter,  $k_B$  is Boltzmann's constant, and  $T$  the absolute temperature. In addition, the density of a gas is given by

$$\rho = N_L m P 273/T,$$

where  $N_L$  is Loschmidt's number and  $P$  the pressure in atmospheres. Combining these equations, (25) becomes

$$k = k_B^{1/2} T^{3/2} / 273 P \pi^{3/2} d^2 N_L m^{1/2} \quad (26)$$

As stated previously, the temperature used in this equation will be a mean value and subject to piece-wise variation only. It is important to note that the diffusivity and the temperature rise due to a single heating pulse are both inversely proportional to pressure. Since these determine the heat gain and loss rates for the gas, the equilibrium mean gas temperature will be independent of pressure. This is demonstrated in equation (37) below.

### 3.1.3 Diffusion

In obtaining solutions to the diffusion problem three simplifications are made: (a) each excitation pulse adds a constant quantity to the diffusant particle concentration, (b) the diffusant concentration is zero at the wall due to a strong wall reaction, and (c) the wall reaction is the only loss process. The diffusion process is then described by equations (9) and (19) with  $\bar{c}$  replacing  $\bar{T}$  and with

$$\bar{t} = Dt/a^2 .$$

An approximate expression for the diffusion coefficient  $D$  can be derived using kinetic theory. Jost(1952) gives

$$D = (3/32(n_1 + n_2)\sigma_{12}^2)(8kT/\pi\mu)^{1/2} , \quad (27)$$

where  $n_1$  and  $n_2$  are the number densities of the diffusant and

background gas,  $\sigma_{12}$  is the collision diameter for the two gas species and  $\mu$  is the reduced mass defined by

$$\mu = m_1 m_2 / (m_1 + m_2) .$$

When the diffusant is in small concentrations and the background gas is light such that  $n_2 \gg n_1$  and  $m_2 \ll m_1$  equation (27) becomes

$$D = (3/32 n_2 \sigma_{12}^2) (8kT/\pi m_2)^{1/2} . \quad (28)$$

This equation can be rewritten in more convenient form using

$$n_2 = n_L P^{2/3} / T ,$$

where  $n_L$  is Loschmidt's number, and substituting the value for Boltzmann's constant using MKS units. We get

$$D = (T^{3/2}/P) (7.6 \times 10^{-41} / \sigma_{12}^2 m^{1/2}) m^2 s^{-1} . \quad (29)$$

The equivalence of particle and thermal diffusion allows equation (26) for the diffusivity, obtained following Moore(1972), to be compared with (29). Substituting values for  $n_L$  and  $k_B$  in (26) gives the expression

$$k = (T^{3/2}/P) (9.1 \times 10^{-41} / d^2 m^{1/2}) m^2 s^{-1} ,$$

which compares favourably with (29). Equation (29) will, therefore, be used to calculate  $D$  for the case of fluorine diffusing in helium



that is considered in Section 3.2.2.

### 3.2 Application to the Experimental Situation

#### 3.2.1 Heat Transport

The tube used in the experimental work was of fused quartz and Table 3.1 gives the data required by the calculation to follow. The microwave apparatus delivered 17.6 W average power. The power absorbed by the gas is estimated to be at least 10 W so this is the value we shall use.

For forced convection, equations (9) and (12) are required. The initial dimensionless temperature at these points is 1 and the temperature at  $i = 20$  remains at 1. The value of  $\delta\bar{r}$  is 0.1 and it was found that the calculation was stable when  $\delta\bar{t}/(\delta\bar{r})^2$  was 0.4 which leads to  $4.0 \times 10^{-3}$  for  $\delta\bar{t}$ . In equation (12) the value of the term

$$((2i - 1)/2i)(\delta\bar{r}a_j/KT_0)$$

becomes  $1.716 \times 10^{-3}$  when  $i = 10$ . The temperature distribution can now be found at successive time intervals, each corresponding to a certain number of time increments,  $j$ . Dimensionless time is converted to actual time by using

### Microwave Pulses

Pulse duration	320 ns
Pulse interval	0.909 ms
Pulse power	50 kW
Mean power	17.6 W
Pulse energy	16.0 mJ

### Tube (fused quartz)

ID	2.0 mm
OD	4.0 mm
Length	200 mm
Inner wall area	12.6 cm <sup>2</sup>
Outer wall area	25.1 cm <sup>2</sup>
Volume	0.628 cm <sup>3</sup>
Quartz volume	1.89 cm <sup>3</sup>
Mass	4.15 g
Density	2204 kg m <sup>-3</sup>
Thermal conductivity	1.5 W m <sup>-1</sup> K <sup>-1</sup>
Specific heat capacity	780 J kg <sup>-1</sup> K <sup>-1</sup>
Diffusivity	8.7 × 10 <sup>-7</sup> m <sup>2</sup> s <sup>-1</sup>

### Helium

Collision diameter [from Moore 1972]	0.2 nm
Mass	6.68 × 10 <sup>-27</sup> kg
Specific heat capacity (C <sub>p</sub> )	5254 J kg <sup>-1</sup> K <sup>-1</sup>
Density (STP)	0.179 kg m <sup>-3</sup>

### Fluorine

Collision diameter	~0.23 nm
Mass	3.17 × 10 <sup>-26</sup> kg

Table 3.1 Values for diffusion calculation

$$\bar{t} = kt/a^2 = 0.87t$$

and temperature in degrees Kelvin is obtained from the equation

$$T = \bar{T}T_0 .$$

This calculation and all ensuing calculations were completed using a Hewlett-Packard HP41CV programmable calculator. The results for various time intervals and in the long term limit are shown in Fig 3.1(a). The temperature drop across the tube is  $3.7^{\circ}\text{C}$  at equilibrium. A plot of the inner wall temperature against time is shown in Fig 3.2(a) which shows that 90% of the total rise takes place in 0.7s (770 microwave pulses).

When the tube is cooled by free convection, equation (15) must be used when  $i = 20$ . The last term in this equation has the coefficient,

$$((2i + 1)/2i)(\delta\bar{r}aHT_0^{1/4}/Kd^{1/4}10^{-4} ,$$

which has the value  $1.49 \times 10^{-3}$ . The temperature distributions at various time intervals, and the equilibrium distribution, are shown in Fig 3.1(b)(with discontinuities in the temperature axis). The temperature drop across the tube at equilibrium is still  $3.7^{\circ}\text{C}$ . The finite difference method is quite slow for this calculation so instead of calculating the detailed time behaviour of the whole spatial temperature distribution the time behaviour of the spatial



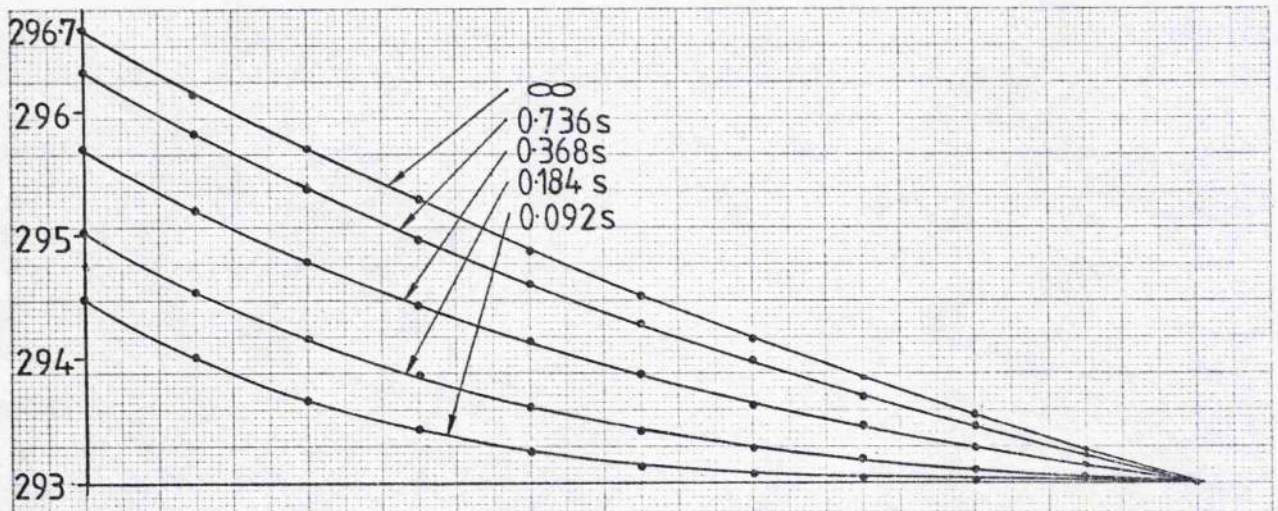


Figure 3.1(a) Tube temperature - forced convection

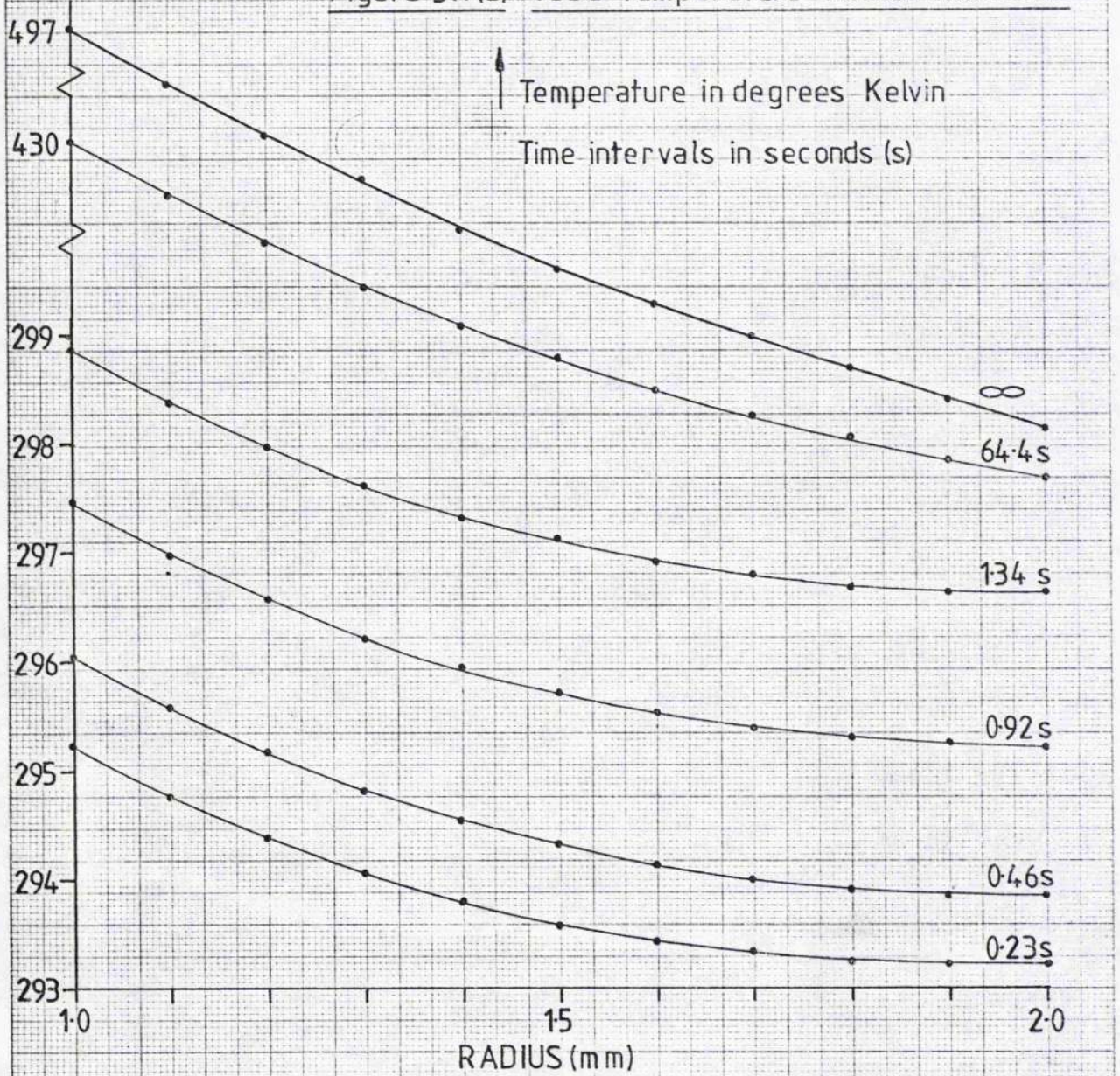


Figure 3.1(b) Tube temperature - free convection



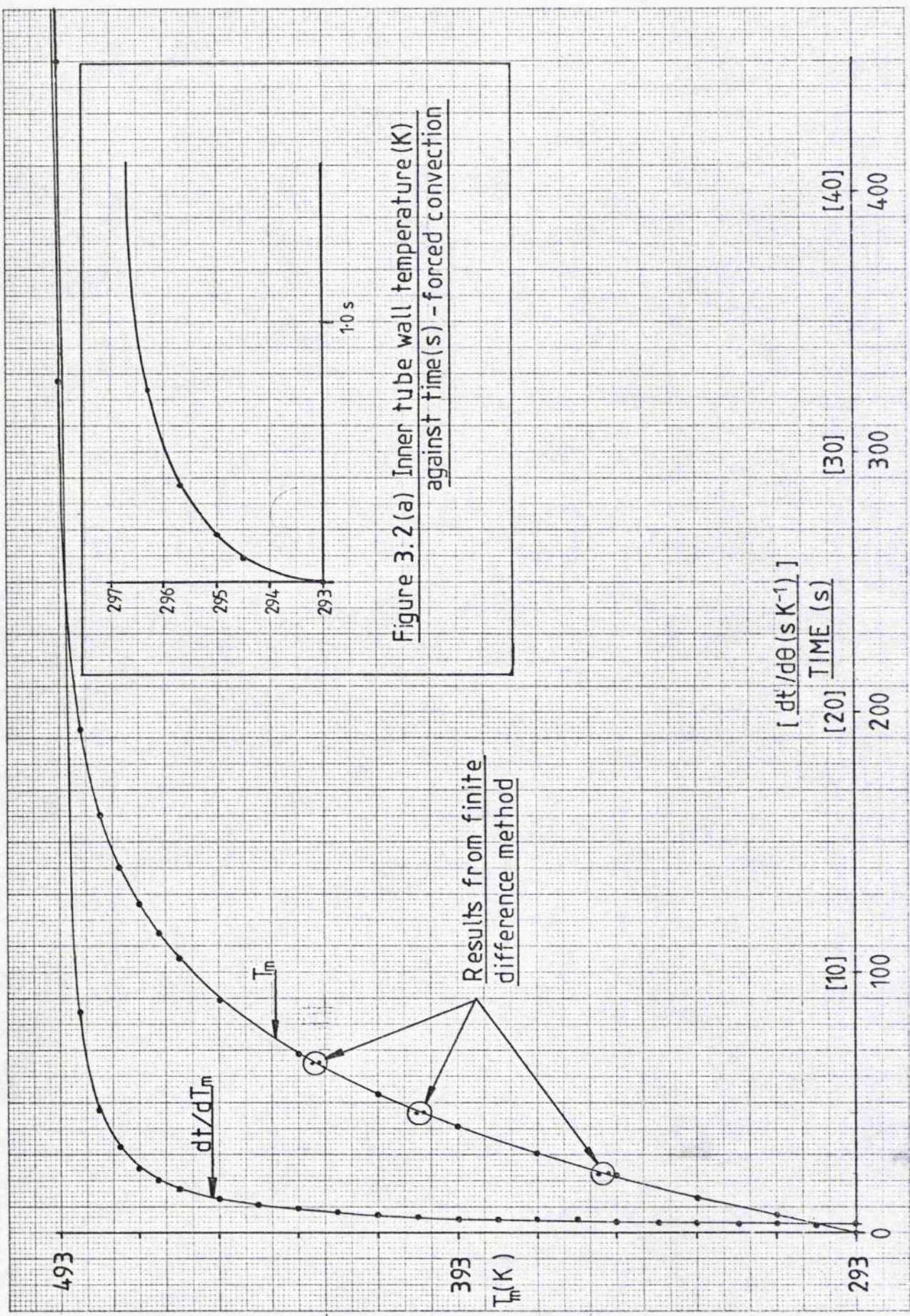


Figure 3.2(b) Tube spatial mean temperature (and  $dt/d\theta$ ) vs. time - free convection

mean temperature is found from (23) and (24). The results are shown in Fig 3.2(b) which shows that 90% of the total rise of  $200^{\circ}\text{C}$  takes place in 130 seconds. In order to demonstrate that the calculation based on spatial mean temperature is adequate, calculations using the finite difference method for the inner and outer wall temperatures at three representative times are also shown in Fig 3.2(b).

To summarise, the temperature of the inner wall rises by  $3.7^{\circ}\text{C}$  to equilibrium in about 1 second with forced convection cooling and by  $200^{\circ}\text{C}$  to equilibrium in about 200 seconds with free convection cooling when the heat input is 10 W.

In the experimental work, gas mixtures were most frequently diluted with helium, this gas often constituting over 90% of the mixture. Consequently, a reasonable approximation is to consider the thermal behaviour to be that of pure helium. For an average absorbed power of 10 W, each pulse deposits  $9.1 \times 10^{-3} \text{ J}$  into the helium. In the following, results will be obtained for 2 atm, 1 atm, 0.5 atm, and 0.1 atm total pressure. The temperature rise for a single microwave pulse at each of these pressures is  $8.3^{\circ}\text{C}$ ,  $16.5^{\circ}\text{C}$ ,  $33.1^{\circ}\text{C}$ , and  $165^{\circ}\text{C}$ , respectively. During the heating pulse, gas will be lost from that part of the tube in which the discharge occurs by expansion and will return during the inter-pulse cooling. This effect is ignored here because of the difficulty in determining the thermal history of the gas that leaves and returns to the tube during a pulse cycle. Consequently, the calculation for the lower pressures, particularly at 0.1 atm, will probably underestimate the resulting temperatures.



In calculating the gas temperature resulting from a pulse sequence, we use the superposition principle. The temperature behaviour over many pulses can be found by adding sections of the behaviour that would follow a single pulse as described below. Also, the results at a given pressure can be rescaled to give the results at other pressures and to allow for changes in diffusivity and density.

Results using equations (9) and (19) are obtained with a constant inner tube wall temperature of 293K (which is 1.0 in dimensionless form), a single heating pulse which gives an initial uniform distribution of 2.0 (dimensionless temperature), and with  $\delta\bar{t}/(\delta\bar{r})^2 = 0.25$ . The distribution is calculated for a total of 400 increments and results extracted at a selection of intermediate values are shown in Fig 3.3. For each distribution selected from the calculation sequence, the spatial mean temperature  $\bar{T}_m$  is found by applying Simpson's Rule to the spatial distribution. These values are plotted in Fig 3.4 which provides the basic temperature behaviour that will be used in our subsequent discussions and calculations. The 'least squares' best approximation to an exponential curve for this data is

$$\bar{T}_m = 0.973e^{-0.0145j} \quad (30)$$

where  $\bar{T}_m$  is the dimensionless spatial mean temperature on the scale of 0 to 1, and  $j$  is the number of increments of dimensionless time. Calculations using this equation deviate by no more than 2.5% from

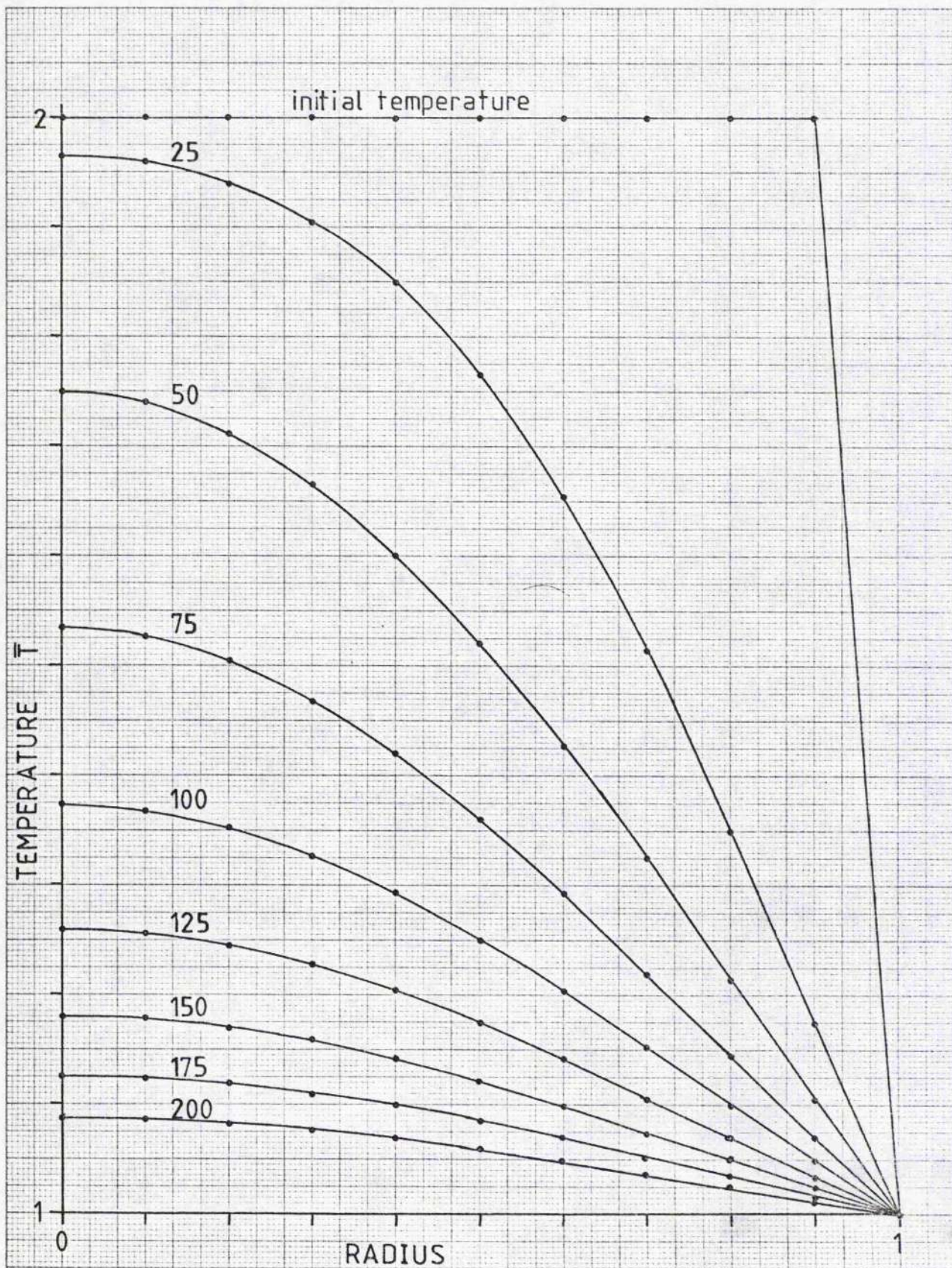


Figure 3.3 Gas temperature vs Radius. Time intervals in 25 calculation increment steps.



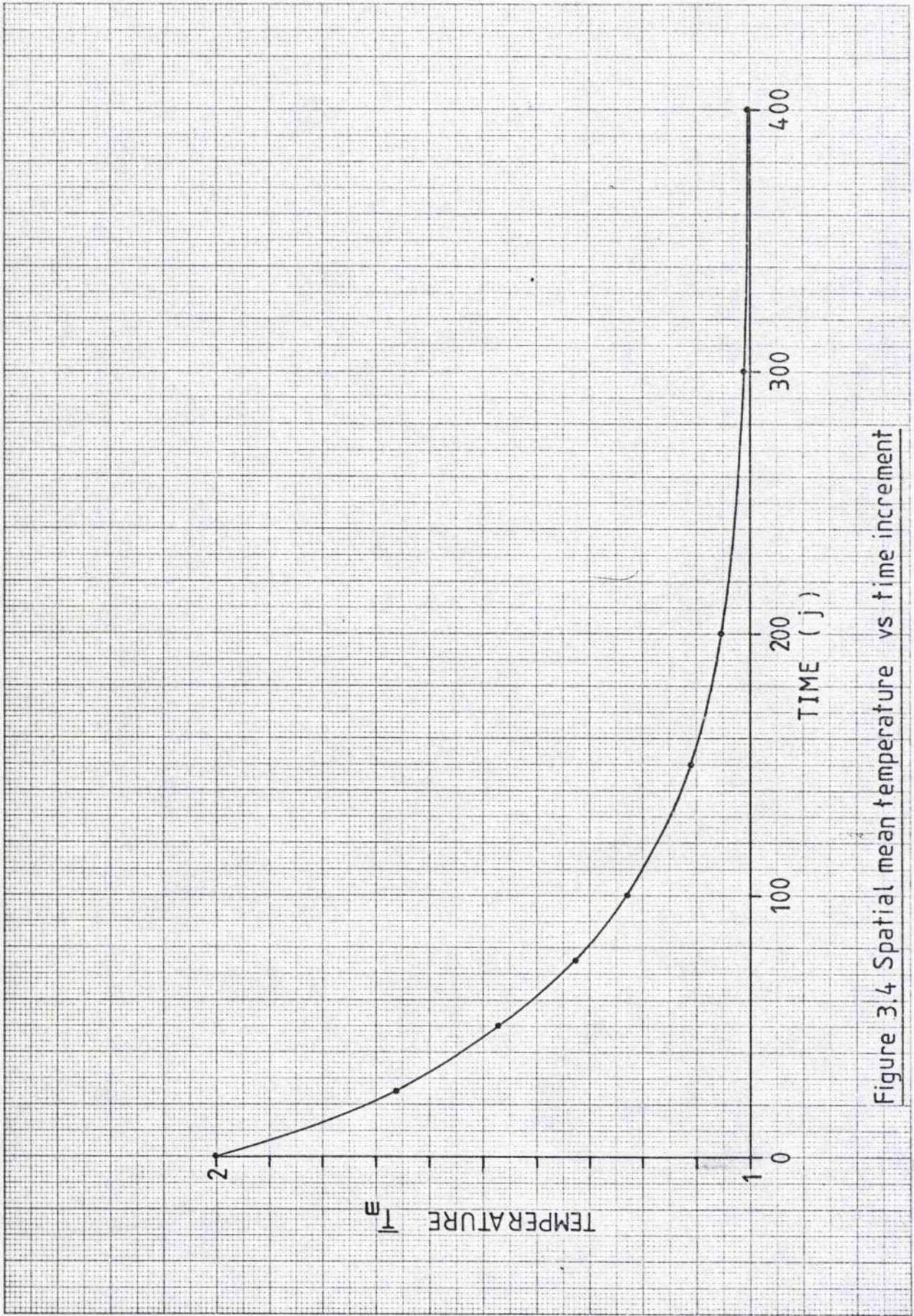


Figure 3.4 Spatial mean temperature vs time increment

the data in Fig 3.4. By the superposition principle, the mean temperature after many pulses ( $\bar{T}_a$ ) can be regarded as the sum of the residual temperatures of each individual pulse. This is obtained from the area under the curve in Fig 3.4 (by integration of (30)) divided by the number of calculation increments,  $n$ , in a microwave inter-pulse period; we get

$$\bar{T}_a = 67.1(1 - e^{-0.0145j})/n \quad (31)$$

Here the temperature is an average both spatially and temporally in the sense that the pulse effects have been smoothed out. Also it is noted that this is a dimensionless value on a scale of 0 to 1 where 1 represents the temperature rise per pulse. For large values of  $j$  this becomes the equilibrium value,  $\bar{T}_e$  given by

$$\bar{T}_e = 67.1/n \quad (32)$$

The temperature rise,  $T_p$ , due to a microwave pulse of energy  $E$  is

$$T_p = EK/v\rho C_p \quad (33)$$

For helium we get

$$\rho = 0.179 \times 273P/T \quad ,$$

and using data from Table 3.1 we get

$$T_p = 5.64 \times 10^{-2} T/P \quad , \quad (34)$$

where  $T$  is the mean absolute temperature. Values for  $T_p$ , at a range of pressures, with  $T = 293\text{K}$  are shown in Table 3.2. Recalling previous equations

$$\delta t = a^2 \delta \bar{t} / k, \quad \delta \bar{t} = 2.5 \times 10^{-3}, \quad \text{and}$$

$$k = 2.78 \times 10^{-8} T^{3/2} / P,$$

(equation (26) with values from Table 3.1) the time per calculation increment is given by

$$\delta t = 0.090 P / T^{3/2} \text{ s} .$$

The increments in a microwave inter-pulse period are then given by

$$n = 1.01 \times 10^{-2} T^{3/2} / P , \quad (35)$$

and values for a mean temperature of  $293\text{K}$  are given in Table 3.2. Combining (35) and (32) gives

$$\bar{T}_e = 6.64 \times 10^3 P / T^{3/2} . \quad (36)$$

To convert this temperature  $\bar{T}_e$  to temperature in degrees centigrade above the wall temperature we use (34) to get

$$T_e = 375 / T^{1/2} \text{ } ^\circ\text{C} . \quad (37)$$



Pressure (Atmospheres)				mean gas tempera- ture -K	wall tempera- ture -K	cooling convection type
0.1	0.5	1.0	2.0			
Mean gas temperature rise per pulse $T_p$ (K) from equation (34)						
165	33.1	16.5	8.3	293	293	forced
177	35.4	17.7	8.9	314	293	
232	46.4	23.3	11.6	411.5	393	free
287	57.5	28.7	14.4	509.6	493	
Gas temperature calculation increments - n from equation (35)						
507	101	50.7	25.3	293	293	forced
562	112	56.2	28.1	314	293	
843	169	84.3	42.2	411.5	393	free
1160	232	116	58.1	509.6	493	
Diffusion calculation increments per pulse. - n from equation (42)						
366	73.2	36.6	18.3	293	293	forced
406	81.2	40.6	20.3	314	293	
609	122	60.9	30.5	411.5	393	free
840	168	84.0	42.0	509.6	493	
Equilibrium mean concentration $C_e/C_o$ ( $=\bar{C}_e$ ) from equation (43)						
0.17	0.83	1.65	3.31	314	293	forced
0.11	0.55	1.10	2.20	411.5	393	free
0.08	0.40	0.80	1.60	509.6	493	

Table 3.2 Summary of temperature and diffusion calculation results.

This important result shows that the temperature of the gas at equilibrium (with spatial averaging and temporal smoothing) is independent of the gas pressure but dependent on the mean absolute temperature of the gas. For a wall temperature of 293K, this equation is satisfied by the value

$$T_e = 21^{\circ}\text{C} .$$

Using a new value for the mean temperature of 314K, new values from equations (34) and (35) are found and appear in Table 3.2.

Equation (31) can be used, with values of  $n$  and  $T_p$  from Table 3.2, to plot the spatial-temporal mean temperature against time (or number of microwave pulses) and these results are shown in Fig 3.5. Figure 3.4 can be adapted to give the temperature behaviour in a single inter-pulse period after equilibrium and this is shown in Fig 3.6. To obtain the long term forced convection behaviour, the equilibrium temperature rise of  $21^{\circ}\text{C}$  has to be added to the curve of Fig 3.2(a) for the inner tube wall temperature and gives the curve shown in Fig 3.7(a). The correction required for the additional  $3.7^{\circ}\text{C}$  due to the wall temperature is negligible.

Under conditions of free convection, where the inner wall temperature rises to 493K, corrections will be substantial. Using an intermediate temperature of 393K, equation (37) is satisfied by the value

$$T_e = 18.5^{\circ}\text{C} ,$$



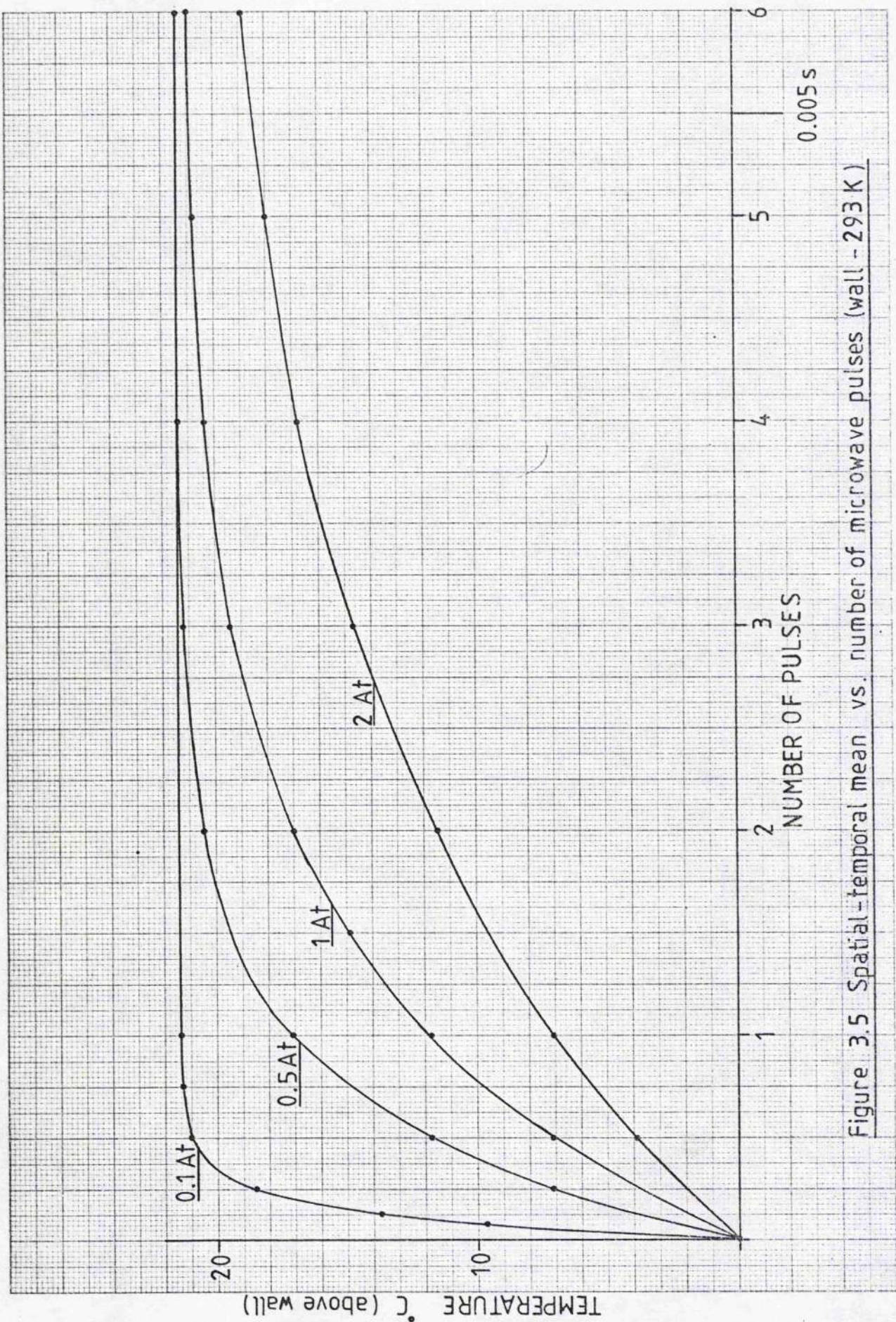


Figure 3.5 Spatial-temporal mean vs. number of microwave pulses (wall - 293 K)



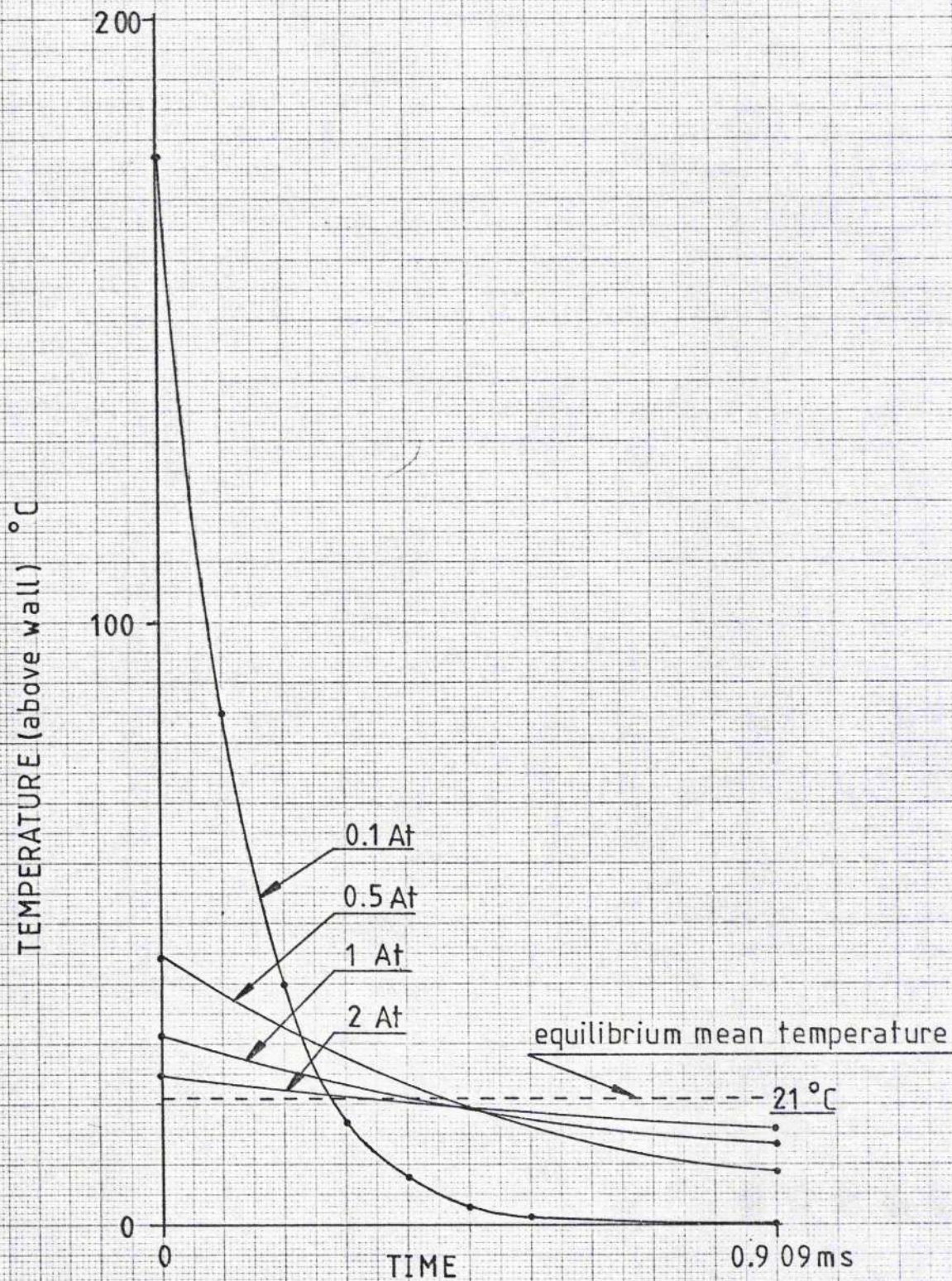


Figure 3.6 Mean temperature vs. time during an inter-pulse period at equilibrium (wall -293 K).



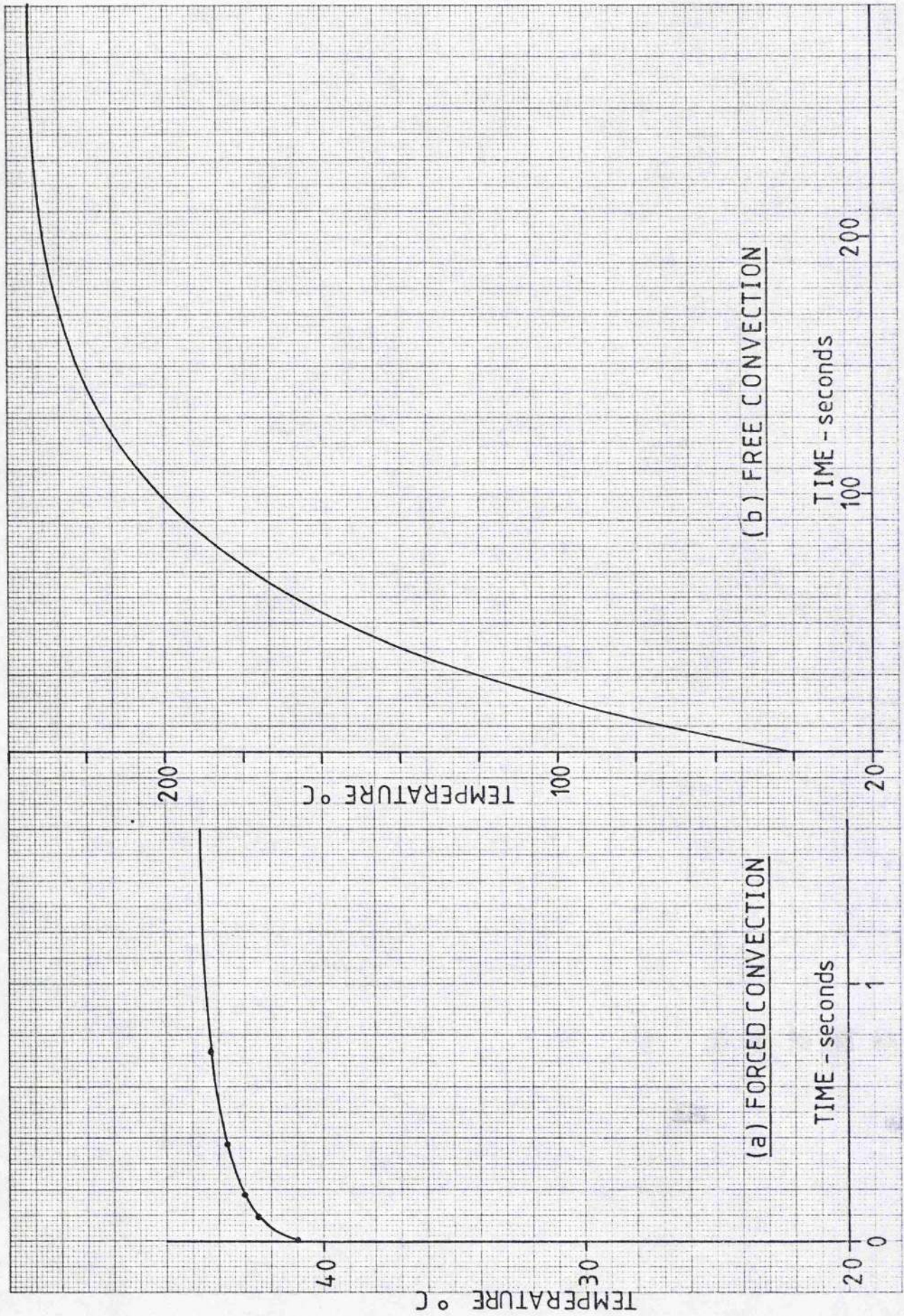


Figure 3.7 Mean gas temperature vs. time (room temperature - 20°C)



while for 493K it is satisfied by

$$T_e = 16.6^\circ\text{C} .$$

The mean absolute temperatures of the gas at wall temperatures of 393K and 493K are 411.5K and 509.6K, respectively. These values can now be used in (34) and (35) to provide further values of  $n$  and  $T_p$  for Table 3.2. The temperature behaviour in a single inter-pulse period with a wall temperature of 493 is shown Fig 3.8. Finally, by adding  $21^\circ\text{C}$ ,  $18.5^\circ\text{C}$ , and  $16.6^\circ\text{C}$  to the curve of Fig 3.2(b) at 293K, 393K, and 493K, respectively, the curve for the mean gas temperature, in the long term, with free convection cooling is obtained in Fig 3.7(b).

The gas temperature behaviour can now be summarised. The difference in thermal capacity between the tube and the gas it contains means that the gas reaches a quasi-equilibrium in the short term during which the tube temperature remains approximately constant. For room temperature gas the temperature rise to equilibrium is about  $21^\circ\text{C}$  while gas at  $200^\circ\text{C}$  rises by only  $16.5^\circ\text{C}$  to equilibrium. The number of microwave pulses to reach equilibrium goes from 1 to 10 as the pressure increases from 0.1 atm to 2 atm. The temperature rise per pulse and the rate of cooling between pulses is greater for both lower pressures and higher temperatures. With forced convection the inner tube wall temperature rises by about  $40^\circ\text{C}$  to equilibrium in about 1 second while under free convection the rise to equilibrium is about  $216^\circ\text{C}$  and this takes

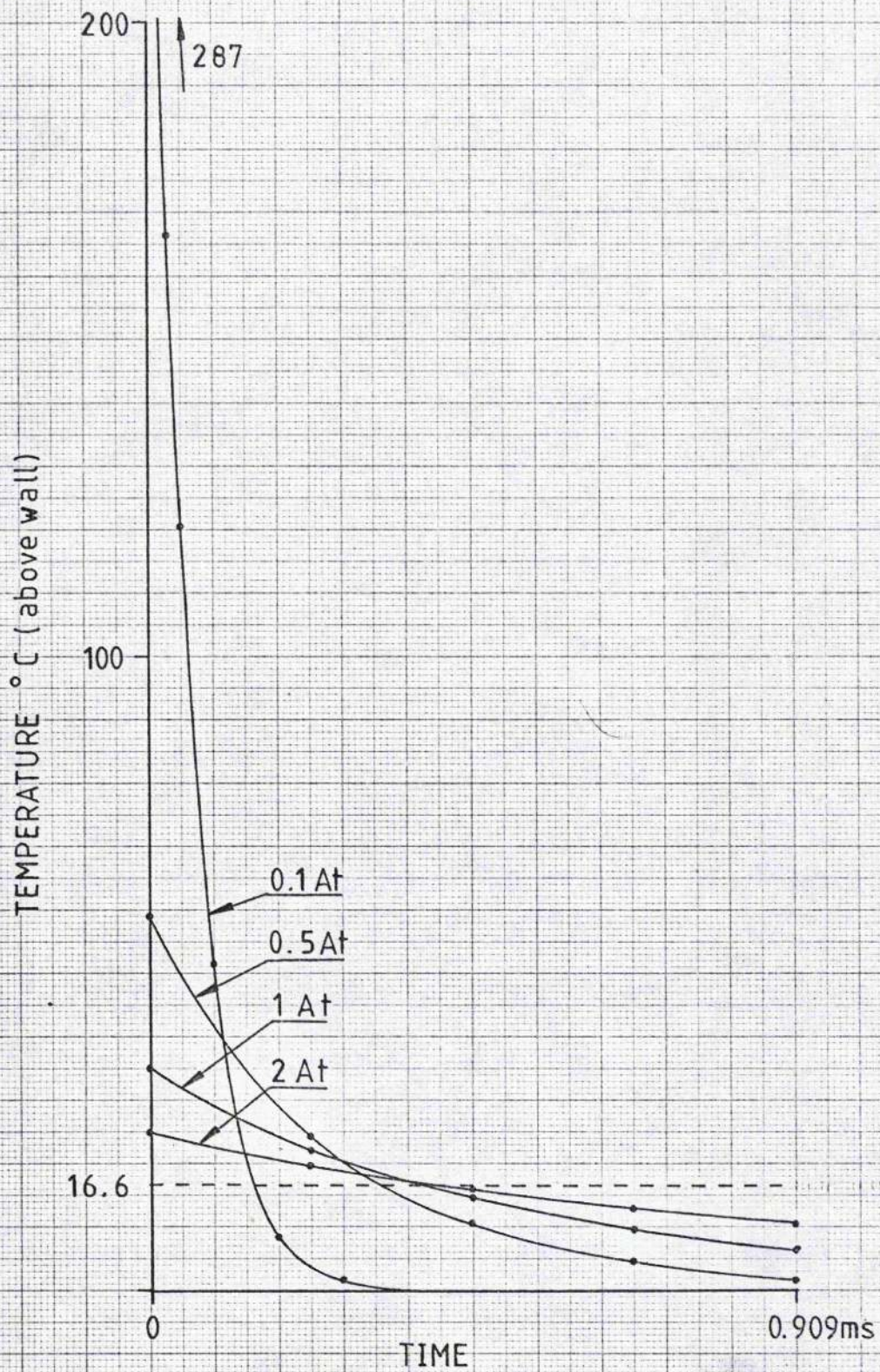


Figure 3.8 Mean temperature vs. time during an inter-pulse period (wall - 493 K)



about 200 seconds. Therefore the final mean gas temperatures are about 25°C and 235°C for forced and free convection cooling respectively. Finally, the heat loss by radiation at 235°C from the tube outer wall is, by Stefan's Law, about 0.3W and is therefore not an important loss process in this case.

### 3.2.2 Diffusion

Having determined the temperature conditions prevailing in the system we can now consider the diffusion of fluorine, through the helium-fluorine donor mixture, to the tube walls. It will be assumed that each microwave pulse contributes a constant concentration  $C_0$  of fluorine by dissociation of a donor molecule. The time behaviour of the spatial distribution following a single microwave pulse is given directly by equations (9) and (19) as shown in Fig 3.3 where the temperature scale (1 - 2) is replaced by the concentration scale  $0 - \bar{C}_0$ . Similarly, Fig 3.4 gives the spatial mean concentration against dimensionless time on a scale  $0 - \bar{C}_0$  following a single pulse. The mean concentration after many pulses is found by re-writing (31) in the form

$$\bar{C}_a = 67.1(1 - e^{0.0145j})/n \quad (38)$$

The equilibrium value from (32) is

$$\bar{C}_e = 67.1/n \quad (39)$$

Equation (29) for the diffusion coefficient is evaluated with  $m_2$  as the helium atomic mass and  $\sigma_{12}$  as the mean fluorine-helium diameter, using values from Table 3.1, to give

$$D = 2.01 \times 10^{-8} T^{3/2} / P \text{ m}^2 \text{ s}^{-1} . \quad (40)$$

Using  $\delta \bar{t} = 2.5 \times 10^{-3}$ , we get

$$\delta t = a^2 \delta \bar{t} / D = 0.12 P / T^{3/2} \text{ s} , \quad (41)$$

and the number of calculation increments per microwave inter-pulse period becomes

$$n = 7.3 \times 10^{-3} T^{3/2} / P . \quad (42)$$

Values of  $n$  when  $T = 293\text{K}$  are given in Table 3.2. Combining (39) and (42) gives the equilibrium concentration as

$$\bar{c}_e = 9.2 \times 10^3 P / T^{3/2} . \quad (43)$$

The equilibrium temperature rise when the wall temperature is 293K is 21°C. Using  $T = 314\text{K}$  in (43) at the four pressures of interest gives the equilibrium concentrations for the 293K wall temperature. These appear in Table 3.2. To obtain the temporal-spatial mean concentration increase with pulse number, a mean temperature of 314K is used in (42) (the corresponding values of  $n$  are given in Table 3.2) and equation (38) is then used. These results are plotted in Fig 3.9. With forced convection, the equilibrium mean gas

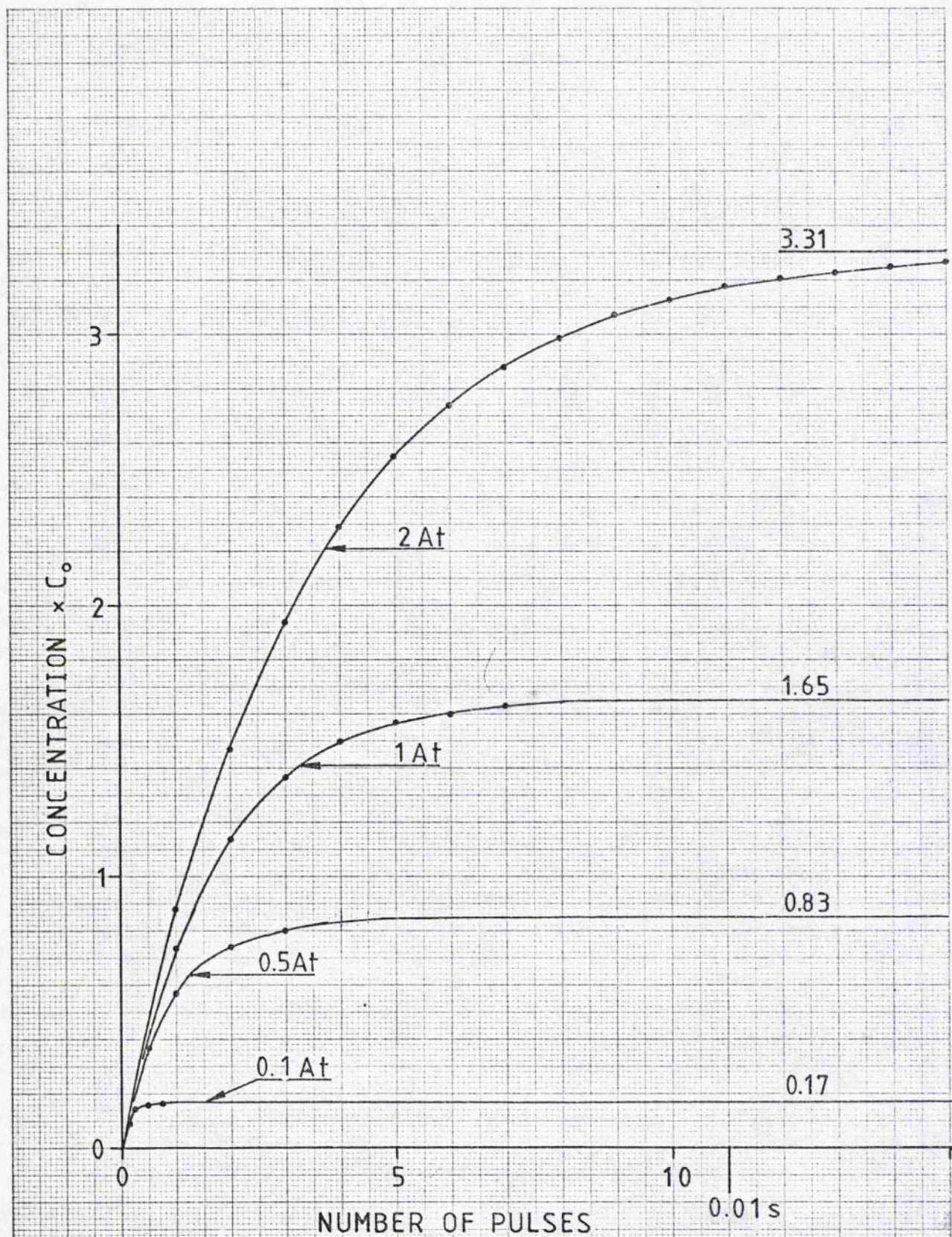


Figure 3.9 Temporal-spatial mean concentration vs. number of pulses (wall -293K, gas -314K)



temperature rises by a further  $3.7^{\circ}\text{C}$ . The effect of this rise on the diffusion is small and consequently it is neglected. Under free convection, however, the mean gas temperature rises to 509.6K which has a considerable effect on the diffusion. The calculation increments per microwave inter-pulse period and the long term equilibrium mean concentration are calculated for this temperature, and the intermediate temperature 411.5K, and recorded in Table 3.2. The (mean) concentration behaviour in a single inter-pulse period after long term equilibrium is shown for forced and free convection cooling in Fig 3.10. Finally, Fig 3.11 shows the mean concentration, in the long term, against time for free and forced convective cooling.

### 3.2.3 Conclusions

In the preceding sections, diffusion theory is applied to a specific experimental situation under various approximations and limitations. Within this context several clear trends emerge and these are listed below.

1. Forced convection cooling of the outer wall of the discharge tube can be very effective in keeping the temperature of the gas within the tube low.
2. The mean gas temperature after long term equilibrium has been established is insensitive to pressures within the range considered. This is demonstrated by equation (37), derived above, which indicates that the equilibrium mean temperature of the gas above the mean wall

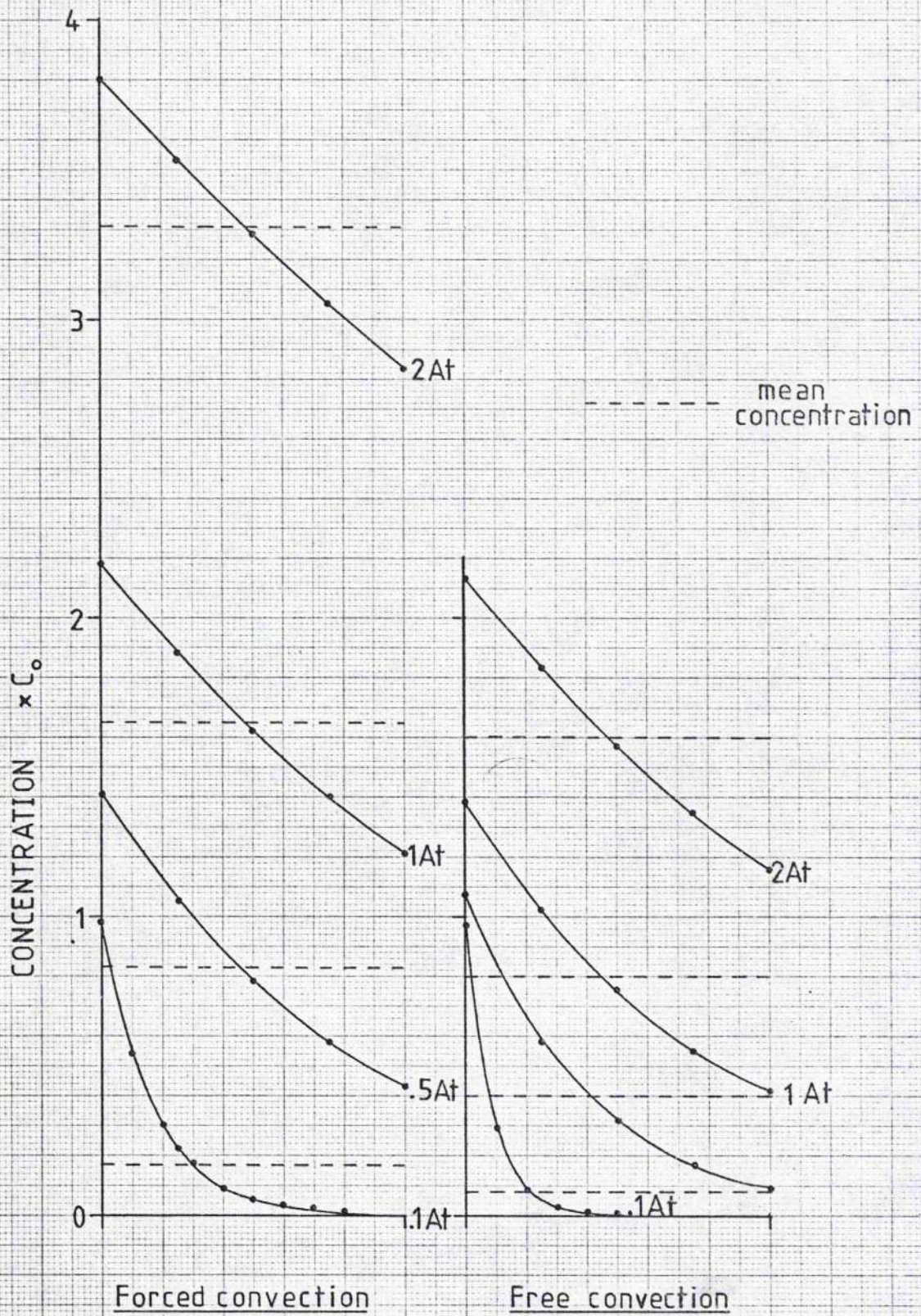


Figure 3.10 Mean concentration vs time during a microwave inter-pulse period.



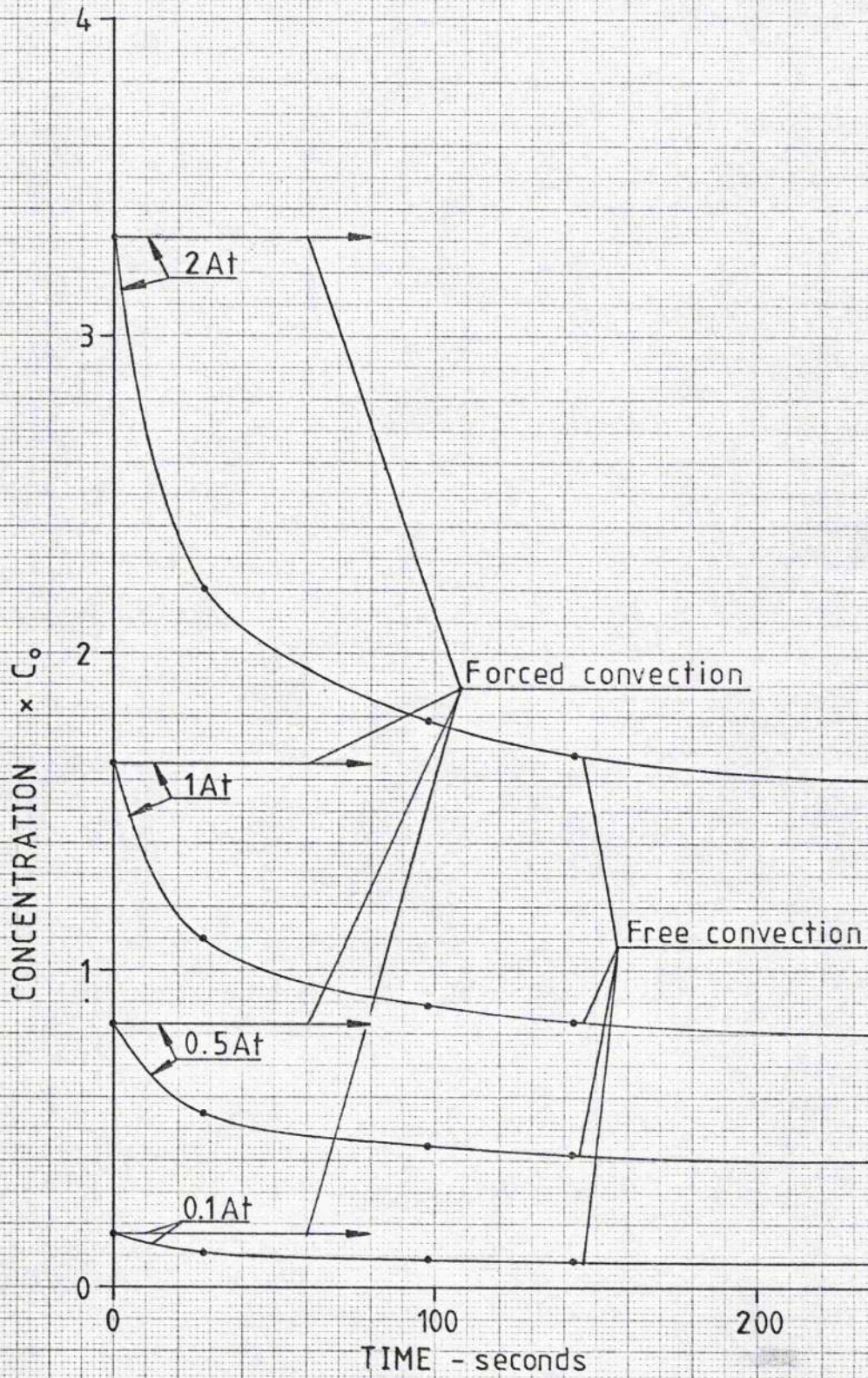


Figure 3.11 Temporal-spatial mean concentration vs time.



temperature is dependent only on the mean absolute temperature of the gas.

3. The temperature and particle concentrations show a marked difference between the behaviour at 0.1 atm and the behaviour at 2 atm during the inter-pulse period. In particular, at 0.1 atm the mean temperature and concentration increments imparted by each pulse have been removed by the end of the inter-pulse period. However, at 2 atm the mean temperature and concentration only fall by about 25% during the inter-pulse period. This aspect is shown in Figs 3.6, 3.8, and 3.10.

4. The mean equilibrium concentration depends strongly on pressure and temperature and is therefore dependent on cooling. This is shown clearly in Fig 3.11 where the mean concentration at 2 atm is 20 times the mean concentration at 0.1 atm for both forced convection (cooling) and free convection (no cooling). At all pressures, the mean concentration with forced convection is approximately twice the mean concentration that occurs after thermal equilibrium is established with free convection.

#### 4 MICROWAVE DISCHARGE EXCITATION

Microwave discharges in gases have found widespread use in such applications as the excitation of spectral sources and chemical reaction chambers. However, the microwave discharge represents a radical departure from the more usual methods (such as e-beam or fast discharge) used to pump rare-gas halide excimer lasers. Previous reports of gas lasers excited by microwave discharge include CO<sub>2</sub> (Handy and Brandelik 1978), Ar (Paik and Creedon 1978), He - Ne (Ahmed and Kocher 1964), CS<sub>2</sub> and O<sub>2</sub> (Suart et. al. 1972), Br, C, Cl, S, Si (Brandelik and Smith 1980), and microwave driven dissociation of the fluorine donor in the chemical HF laser (Bertrand et. al. 1978). The first successful application of a microwave discharge to pump an excimer laser (XeCl) was achieved in 1981 by Mendelsohn et. al. (1981). The advantages and disadvantages of microwaves for providing the high pump power density required for excimer lasers are discussed below.

## 4.1 Comparison of Microwave and DC Discharges

### 4.1.1 Discharge Excitation by DC Pulses

In pumping by DC pulses, a capacitor bank is discharged rapidly through the active medium. This is currently the most frequently used method for pumping excimer lasers. Electron-beam and electron-beam stabilised DC discharge systems are larger, and more expensive. However, even though DC discharge systems are preferred for small scale experiments, such lasers still have considerable design problems which largely stem from the high pump power densities required (about  $1\text{MWcm}^{-3}$ ). The plasma impedance during the uniform glow phase of a high power pulsed discharge is around  $0.5\Omega$ . Thus, for typical laser active volumes (about  $10^3\text{cm}^3$ ) voltages of around 20kV are required. (Typical values of E/N of rare-gas halide lasers are about  $10^{-5}\text{Vcm}^2$ ). It has been found that, because of the high pressures involved, the spatial and temporal uniformity required for efficient laser excitation can only be achieved under carefully controlled and rather limited circumstances. The problems of discharge uniformity and stability are discussed in detail by Levatter and Lin (1980) where the requirements for very short voltage rise times and homogeneous preionisation are emphasised. The formation of a filamentary (streamer) discharge following the application of a high voltage pulse is a natural consequence of the low density of seed electrons and the low level of diffusive spreading that results from the high gas pressure. In the electron

avalanches that follow the application of an electric field at high E/N values a point is reached where the magnitude of the space charge field at the head of the avalanche approaches the magnitude of the applied field ('Raether criterion', see Raether 1940). This spacecharge field accelerates the development of the avalanche so that streamer formation times are very much less than the time for a single electron to travel across the interelectrode gap (transit time). In He at 1atm and a typical E/N value of  $1.5 \times 10^{-16} \text{ Vcm}^2$  the electron drift velocity is about  $2 \times 10^6 \text{ cm s}^{-1}$  giving a transit time of  $1 \mu\text{s}$  for a 2 cm gap. Streamer formation, however, may take place in times as short as  $10^{-9} \text{ s}$ . This suggests that short voltage rise times will be required if the discharge is to be uniform at high pressure. Experience has shown that a uniform glow discharge can only be obtained at high pressure if preionisation produces adequate, uniform seed electron densities and only if the voltage risetime is less than about 20ns.

Unless the voltage pulse is kept deliberately short (<50ns), discharge instability will only be forestalled by the preceding measures. Thus, a relatively stable discharge will eventually decay by runaway current growth, a fall in plasma impedance and hence a fall in the E/N value. Ultimately, arcs will form which will cause electrode damage. Current stability on these short time scales is due almost entirely to balance between electron production by ionisation and electron loss by attachment. Therefore, the current growth accompanies a fall in the attachment rate due, for example, to a fall in  $\text{F}_2$  density. In addition to current instability, slight spatial irregularities will cause heating irregularities which will

eventually cause the spatial homogeneity to be lost, thus encouraging the development of arcs. Thermal instability is discussed by Jacob and Mani (1975) who give references to other aspects of high pressure discharge instabilities.

To summarise, DC discharge pumping of excimer lasers requires homogeneous preionisation and voltage pulses in excess of 20kV with risetimes below about 20ns and durations of less than about 100ns. In addition to this, gas mixture ratios must be limited to the proportions that permit an electron avalanche yet give attachment controlled stability. It should be noted however that improvement in one of these conditions may allow a relaxation in another.

#### 4.1.2 Microwave Discharge Excitation

As with DC discharge excitation, microwave excitation has to perform the dual task of driving electron avalanches and maintaining the electron temperature while inelastic collisions (particularly metastable production) are taking place. The problems of maintaining the best E/N value for metastable production while maintaining stability, uniformity and efficiency are still present but there are important differences which will be discussed below. However, it will be useful first to consider whether a microwave system can provide the E/N values and power density required for excimer laser pumping. The power which can be transmitted by a waveguide is limited by breakdown of the gas within the waveguide. In the  $TE_{01}$  mode of a rectangular guide, the electric field is parallel to the

narrow wall and is maximum at the guide centre. It is generally recommended that waveguide electric fields are limited to a quarter of that value at which breakdown occurs in air at STP. However, greater fields are obtained if the waveguide surface is smooth and if the guide is pressurised. Adding gases such as  $\text{SF}_6$  to the gas of the waveguide also gives increased breakdown fields. Thus the breakdown field for air ( $30\text{kVcm}^{-1}$ ) may be approached or exceeded. Field values of around  $10\text{kVcm}^{-1}$  are typical in DC systems but such a value will be difficult to achieve using microwaves. This is because the guide electric field is reduced by the coupling structure which distributes the field over the length of the discharge tube. For a discharge tube of length 20cm and X-band (3cm) microwaves, the reduction in field is at least a factor of 10. It therefore seems that successful lasing can only be achieved when the waveguide has its power handling capability improved.

It will be recalled that a pump power density of  $2\text{MWcm}^{-3}$  is a realistic aim for an excimer laser. Therefore, since it is unlikely that discharge tube volumes will be much below  $1\text{cm}^3$ , the magnetron power will have to be 10kW in the most optimistic case and probably 1MW more realistically. Magnetrons operating at X-band frequencies are available up to 600kW with  $\text{SF}_6$  internal insulation. Higher powers can be obtained at lower frequencies but here the benefits of a larger waveguide will have to be weighed against the cheaper and more compact X-band systems.

The obvious difference between a microwave and a DC discharge is that the electric field of the latter is modulated at high frequency in the former. An immediate and most significant result of this is that the streamer breakdown which is so difficult to prevent in high power DC discharges cannot occur in the equivalent microwave discharge. This is because the field reversal time (about  $10^{-10}$  s) is much less than the streamer formation time ( $<10^{-9}$  s). This removes the stringent demands for short pulse rise times and homogeneous preionisation. However, it will remain necessary to expect fairly short risetimes since the overall pulse will be of short duration. In addition some level of preionisation may be desirable for reasons given below. Another result of the high frequency modulation is that the discharge may be contained in a dielectric tube. This prevents the long term decay into arcs that occurs in a DC discharge and may lead to lower levels of contamination.

The main difficulties of operating a microwave discharge for laser excitation at high pressure are those of obtaining a uniform discharge of sufficient length with efficient coupling of the microwave power into the discharge. A further problem arises in that the optimum excitation conditions for reliable initiation of the discharge. An insight into these difficulties can be gained by a simplified consideration of the propagation of microwaves in a plasma in terms of electron density, electron - atom collision frequency and the microwave frequency.

The microwave field can be represented as a plane electromagnetic wave travelling in the z-direction as

$$E = E_0 e^{j\omega t - \gamma z}$$

where  $\gamma$  is the complex propagation coefficient and is given by

$$\gamma = \alpha + j\beta$$

where  $\alpha$  and  $\beta$  are the attenuation and phase coefficients. These can be expressed in terms of the attenuation index and refractive index,  $\chi$  and  $\mu$ , by

$$\alpha = \chi\omega/c$$

and

$$\beta = \mu\omega/c .$$

In the absence of collisions, free electrons oscillate at a phase of  $90^\circ$  to the applied field and therefore do not gain energy in the steady state. When collisions do occur the electron motion is randomised by the collisions and the electrons gain kinetic energy continuously. As the collision frequency increases the electron oscillation in the driving field is increasingly damped as the in-phase drift velocity increases. The equation of motion for an electron in the driving field  $E$  with collisional damping is



$$m\ddot{x} = -eE - \nu m\dot{x}$$

where  $x$  is the displacement,  $\nu m\dot{x}$  the damping term and  $\nu$  is the collision frequency for momentum transfer. This has the steady state solution

$$x = eE/m\omega(\omega - j\nu) \quad (1)$$

where the substitution of  $j\omega$  for  $\partial/\partial t$  has been used. The complex conductivity is then given by

$$\sigma = J/E = -ne\dot{x}/E = ne^2(\nu - j\omega)/m(\omega^2 + \nu^2) \quad (2)$$

where  $J$  is the current density and  $n$  the electron density. The frequency of oscillation of free electrons in a plasma, the plasma frequency  $\omega_p$ , is given by

$$\omega_p = (ne^2/m\epsilon_0)^{1/2} \quad (3)$$

(The electron density obtained from this equation is the critical or plasma density). Substitution in (2) then gives

$$\sigma = \epsilon_0 \omega_p^2 (\nu - j\omega) / (\omega^2 + \nu^2) \quad (4)$$

It is shown in Heald and Wharton (1965) that the conductivity and dielectric constant may be combined in a single complex conductivity or a complex dielectric constant. The same process may also be applied to the refractive index and absorption index. By a process of substitution and extraction of real and imaginary parts (not repeated here) the refractive index and attenuation index can be expressed as follows:

$$\mu = \frac{c\beta}{\omega} = \left[ \frac{1}{2} \left( 1 - \frac{\omega_p^2}{\omega^2 + v^2} \right) + \frac{1}{2} \left[ \left( 1 - \frac{\omega_p^2}{\omega^2 + v^2} \right)^2 + \left( \frac{\omega_p^2}{\omega^2 + v^2} \frac{v}{\omega} \right)^2 \right]^{\frac{1}{2}} \right]^{\frac{1}{2}} \quad (5)$$

$$\chi = \frac{c\alpha}{\omega} = \left[ -\frac{1}{2} \left( 1 - \frac{\omega_p^2}{\omega^2 + v^2} \right) + \frac{1}{2} \left[ \left( 1 - \frac{\omega_p^2}{\omega^2 + v^2} \right)^2 + \left( \frac{\omega_p^2}{\omega^2 + v^2} \frac{v}{\omega} \right)^2 \right]^{\frac{1}{2}} \right]^{\frac{1}{2}} \quad (6)$$

The attenuation coefficient can be used to give a skin depth defined as the distance travelled in the plasma for a  $1/e$  reduction in the electric field strength by

$$\delta = 1/\alpha = c/\chi\omega \quad (7)$$

This equation is applicable for microwaves incident on a well defined plasma boundary and for a homogeneous electron density within the plasma. Under these conditions the power reflection and transmission coefficients are

$$r = ((1 - \mu)^2 + \chi^2) / ((1 + \mu)^2 + \chi^2) \quad (8)$$

and

$$t = 1 - r = 4\mu / ((1 + \mu)^2 + \chi^2) \quad (9)$$

respectively. Finally, the power absorption is given by

$$P = \sigma_r E_0^2 \quad (10)$$

where  $\sigma_r$  is the real part of the conductivity and  $E_0$  is the local field amplitude.

Equations (7) - (10) can now be evaluated using typical values of  $\omega_p$  (or electron density) and with a microwave frequency of  $9 \times 10^9$  Hz ( $5.7 \times 10^{10}$  rad s<sup>-1</sup>). To estimate the experimental range of collision frequency  $\nu$  the range of E/N values has to be found. The field at the waveguide centre can be found from the field-power relation for a waveguide (Harvey 1963) which is

$$P = E_m^2 ab (1 - f_c/f)^{1/2} / 1510$$

where  $P$  is the transmitted power,  $E_m$  is the spatial maximum of the field amplitude in the TE<sub>01</sub> mode,  $a$  and  $b$  are the guide dimensions,  $f_c$  is the cutoff frequency, and  $f$  is the transmission frequency. This gives about  $7 \text{ kVcm}^{-1}$  for  $E_m$  in the apparatus which will be reduced by the coupler to perhaps  $0.7 \text{ kVcm}^{-1}$ . For the experimental pressure range 0.01 - 2.0 atm the range of E/N values will then be  $2.6 \times 10^{-15}$  -  $1.3 \times 10^{-17} \text{ Vcm}^{-1}$ . Mean electron energies at these E/N values can be gauged from the electron distributions given in Fig 2.11. These range from about 2eV (He) to about 12eV (Ne). Curves of

collision frequency against electron energy are given by MacDonald(1966) and reproduced in Fig 4.1. Taking the required collision frequency for momentum transfer to be reasonably near the total collision frequency given in Fig 4.1, the range corresponding to the above electron energy range is  $7 \times 10^{11} - 1 \times 10^{13} \text{ s}^{-1}$ .

Taking intervals of  $\nu$  in powers of 10, values of  $\chi$ ,  $\mu$ , and  $\delta$  are plotted against electron density in Fig 4.2 using logarithmic scales. The reflection coefficient  $r$  is plotted in Fig 4.3(a). Figure 4.3(b) shows a plot of  $\mu$ ,  $\chi$ ,  $\delta$ , and  $r$  for the particular case  $\nu = 5.7 \times 10^{11} \text{ s}^{-1}$  which is the microwave frequency in  $\text{rad s}^{-1}$ . On all of these graphs a dashed line is drawn to indicate the electron density at which the plasma frequency is equal to the microwave frequency.

Inspection of the graphs and preceding equations reveals the change in the propagation characteristics that occur when either the collision frequency or the plasma frequency passes through the microwave frequency. In particular it can be seen that for any given collision frequency above the microwave frequency, as the electron density increases the plasma changes from being relatively transparent to being opaque with high reflection and small skin depth. These changes are more abrupt at or below the collision frequency which is equal to the microwave frequency. If the case is considered where a strong microwave field is incident on a gas and causes the gas to breakdown, it can be seen that the discharge will be localised in a shallow skin depth where the microwaves meet the gas and that the remaining volume will be shielded. Even if the

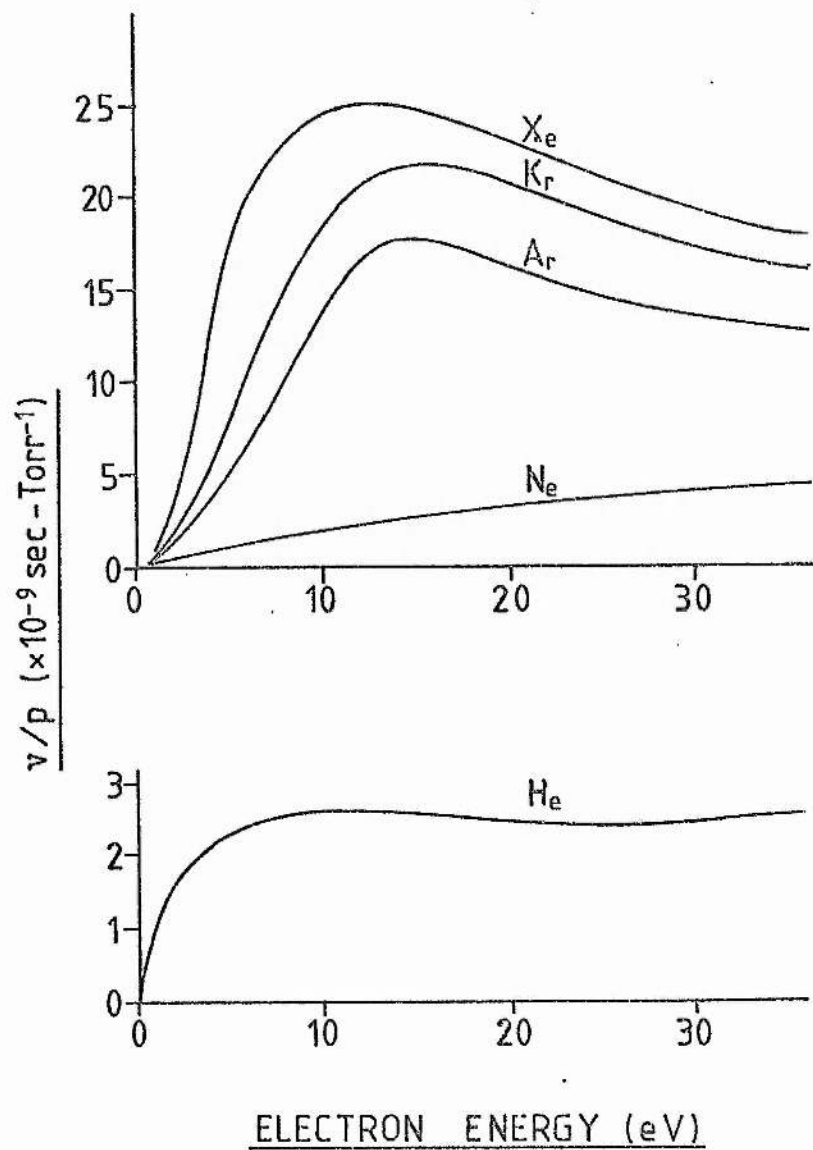


Figure 4.1 Ratio of electron collision frequency to pressure vs electron energy in rare gases (Tellinghuisen 1976)

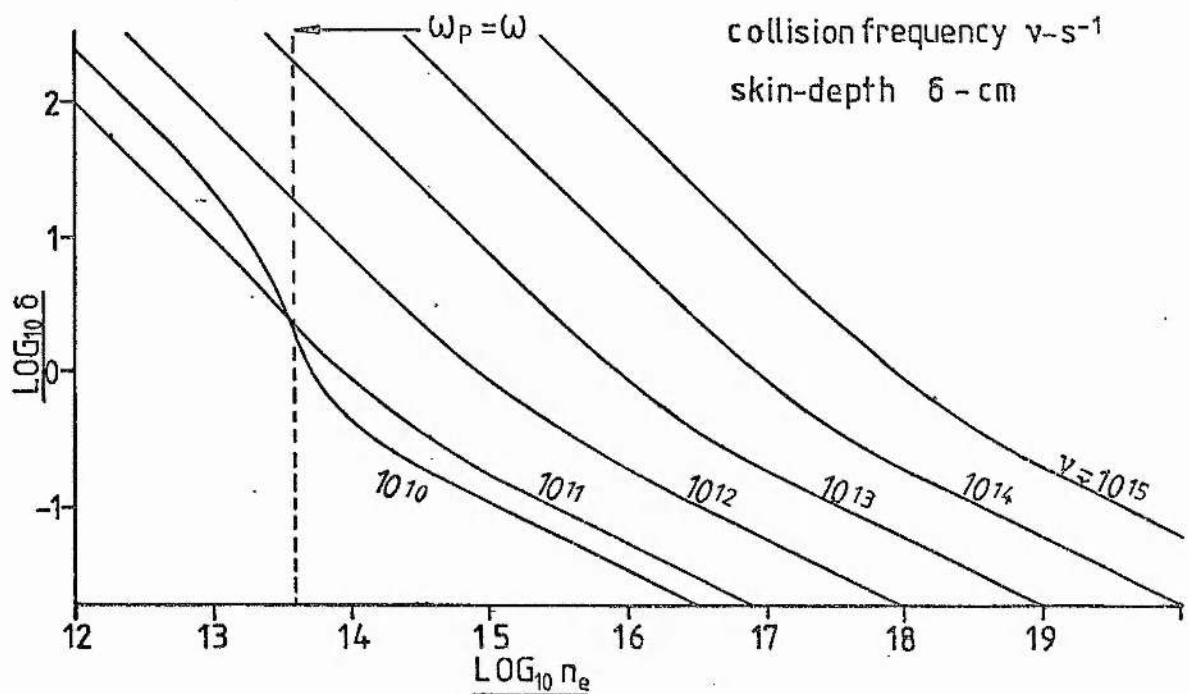
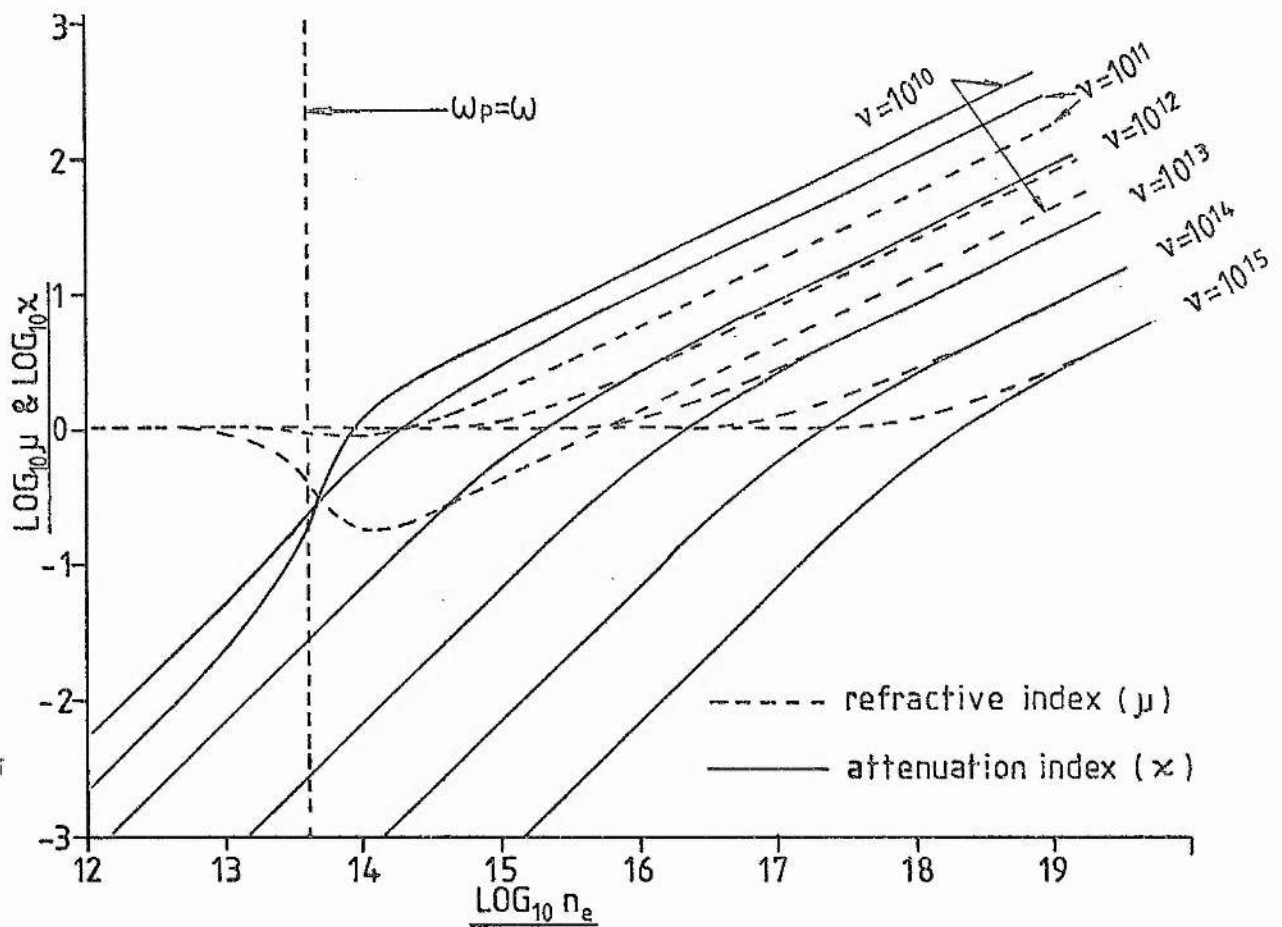


Figure 4.2 Refractive index ( $\mu$ ), attenuation index ( $\chi$ ), and skin-depth ( $\delta$ ) vs electron density ( $n_e - \text{cm}^{-3}$ ). Microwave frequency 9 GHz.

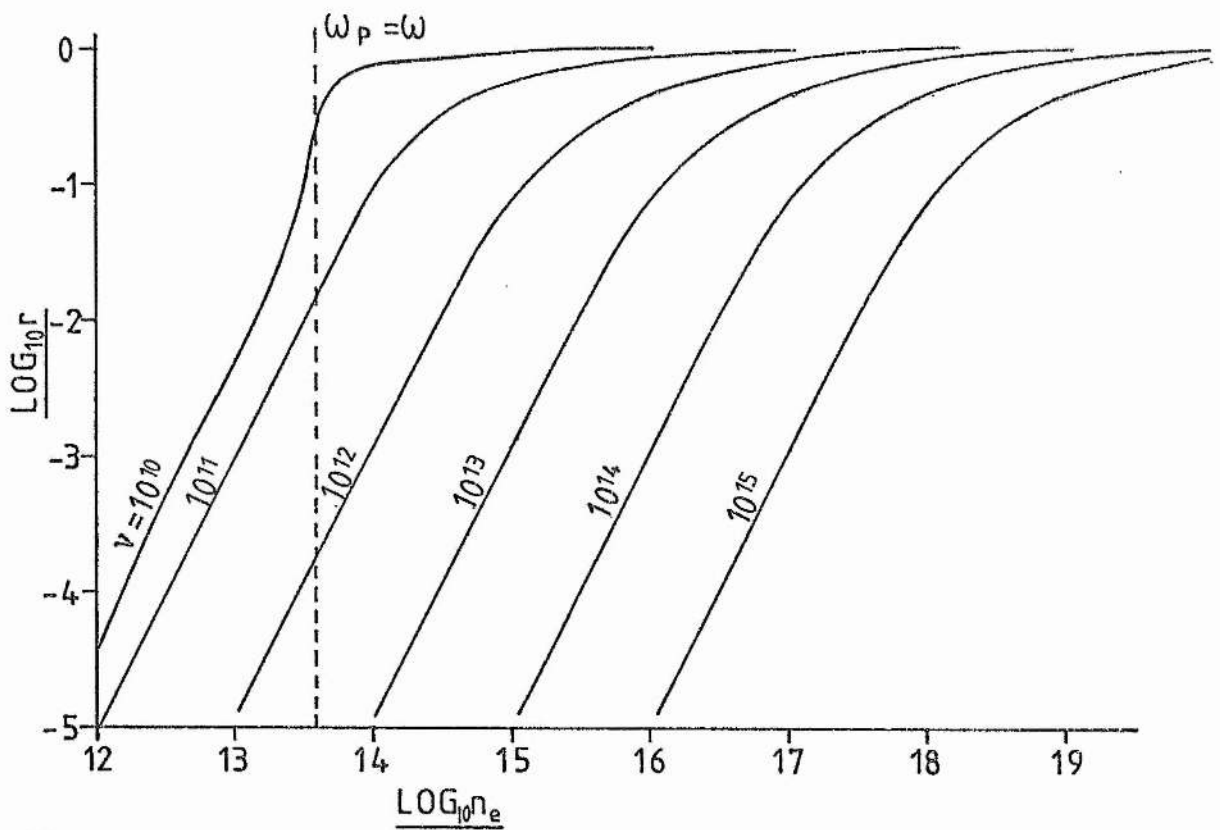


Figure 4.3 (a) Reflection coefficient vs electron density

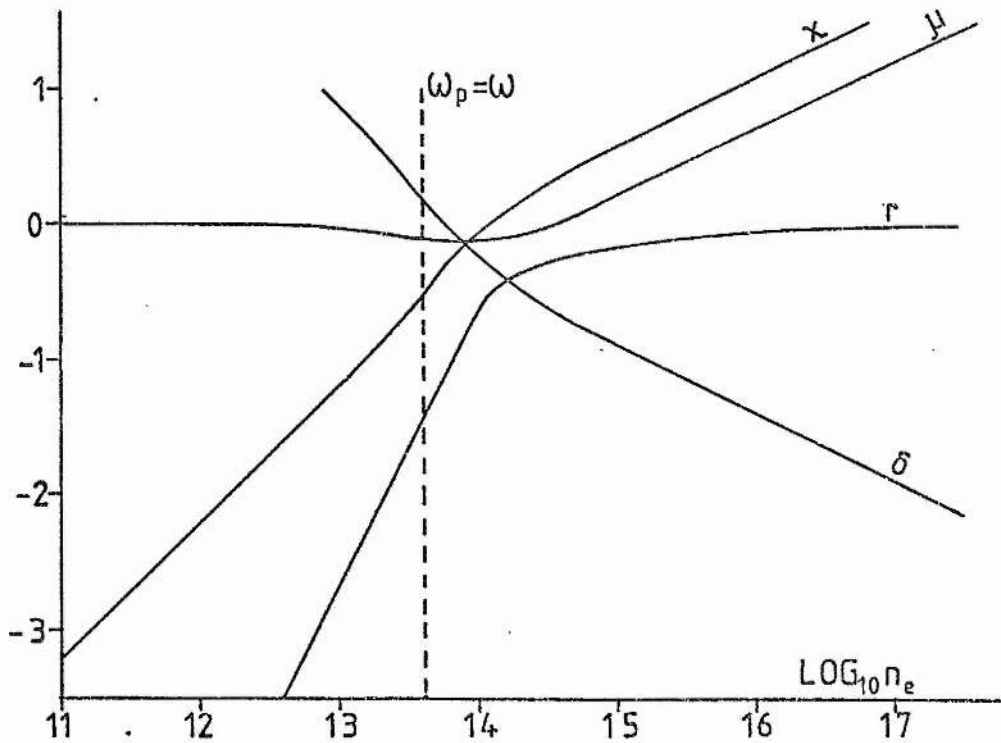


Figure 4.3 (b)  $\mu, x, \delta,$  and  $r$  vs  $n_e$ .  $\nu = \omega = 5.7 \times 10^{10}$



absorption was linear there would still be an exponential decay in the electron density in the microwave propagation direction. It is interesting to note that in the above context the electron density will automatically be near the critical value, in the discharge region, for low collision frequencies ( $\nu < \omega$ ). For the X-band radar frequency this gives  $n_e$  as around  $4 \times 10^{13} \text{ cm}^{-3}$ . At high collision frequencies ( $\nu > \omega$ ) the electron density will stabilise where the reflection coefficient approaches unity. This occurs when

$$\omega_p^2 \approx \nu \omega$$

as can be seen from equations (5) and (6). For an electron energy of 10eV and a gas pressure of 1 atm the collision frequency is about  $2 \times 10^{12} \text{ s}^{-1}$  for He and Ne and about  $1 \times 10^{13} \text{ s}^{-1}$  in Ar. The electron density value will therefore be approximately  $1.5 \times 10^{15} \text{ cm}^{-3}$  in He and Ne and  $7 \times 10^{15} \text{ cm}^{-3}$  in Ar.

The preceding paragraphs clearly demonstrate the fundamental difficulty of using microwaves to generate a long uniform discharge suitable for laser excitation. The manifestation of these difficulties in practical coupling structures are now discussed followed by some specific details of coupler design.

## 4.2 Microwave Discharge Couplers

### 4.2.1 The Coupling Problem

The microwave discharge coupler has to provide efficient and uniform coupling of the microwave power to the discharge. In addition to this the discharge must be initiated and this rather separate problem is discussed first. The problem exists because of the difference between the electric field required to cause breakdown and that required to maintain it, the latter being the smaller. The reason for the difference is that at high electron densities (above  $10^{-4}$  times the critical density (see MacDonald 1966)) ambipolar diffusion dominates and reduces the electron diffusion and therefore the electron loss rate. In the absence of sufficient seed electrons the breakdown field will become very high, there will be statistical delays in the occurrence of breakdown, spatial uniformity may develop slowly, and the growth of electron density will be slow. These problems will be particularly important where short repetitive pulses are used, as in the case under consideration here. It was explained in Section 4.1.2 that the ultimate uniformity of a pulsed microwave discharge is self establishing and not dependent on preionisation. However even if fields well above the maintenance fields are used, preionisation will still be of value in removing statistical pulse variations and lowering the discharge formation time. The latter improvement should increase the efficiency since there will be less wasted energy in the early part of the pulse. Systematic studies of

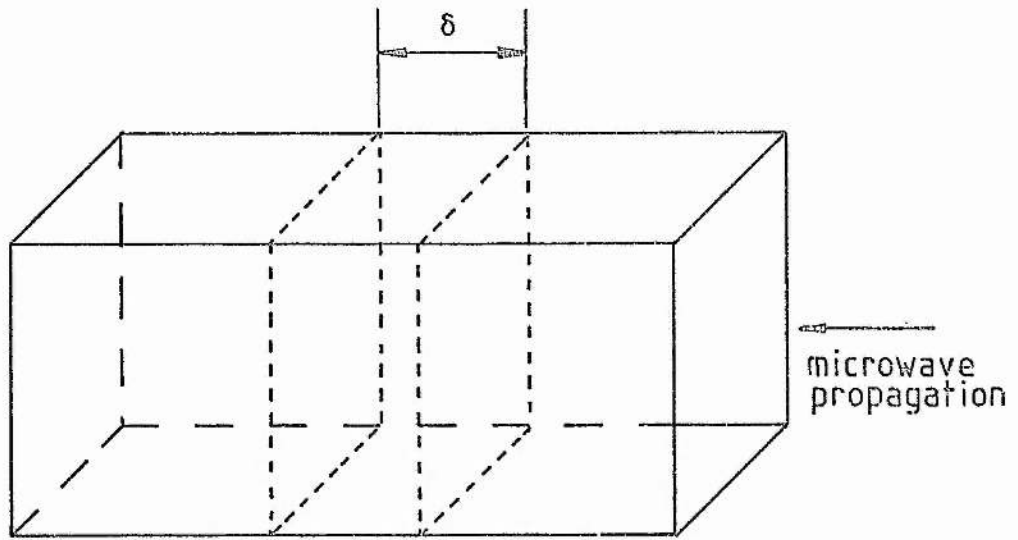
the use of preionisation in a high power microwave discharge have not been carried out although Mendelsohn et. al. (1981) reported greater stability and reproducibility with its use. It is difficult, therefore, to be conclusive about the level and uniformity of preionisation required. In addition it is noted that for the rapid repetitive pulses of the experimental work the ionisation surviving the inter-pulse period may be significant. Therefore preionisation may be much more effective for the first pulse than for the following pulses. Practical suggestions for preionisation methods are given in the next section.

The difficulties of using a microwave system to excite a laser discharge stem from the non-linear absorption effects described above and the fact that the microwave radiation is delivered by a waveguide of small dimensions (23mm x 10mm, X-band) while the active laser volume needs to be long ( $>200$ mm). The first observation to make is that the waveguide must, in effect, have only a small fraction of its aperture filled by the plasma. This is to prevent the occurrence of a short, high density, one skin depth plasma, localised at the microwave source end of the gas volume and creating a waveguide short-circuit with high reflection. Such a requirement is not particularly inconvenient since, as has been shown, small discharge volumes are required in order to obtain high pump power densities. Therefore practical discharge tube dimensions will probably be 1 - 5mm in diameter and 200 - 400mm in length and the discharge tube can be conveniently placed within the waveguide or in some kind of waveguide structure. Clearly then the skin depth does not have to be greater than the tube length but must be rather greater than the tube

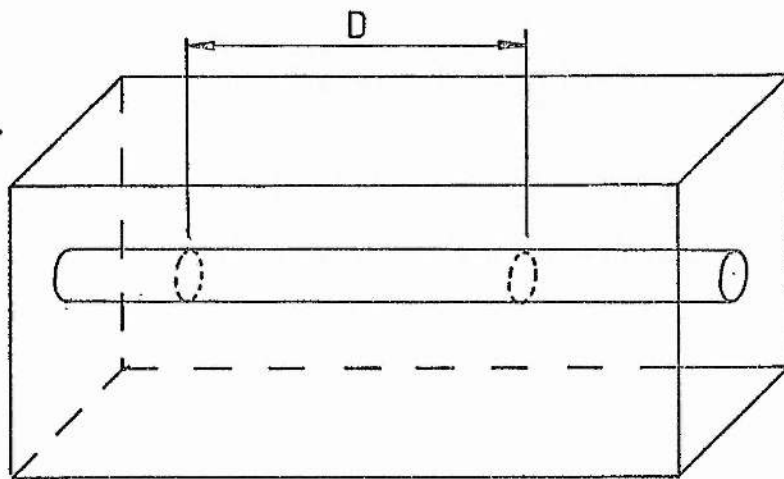
diameter to ensure transverse uniformity. It will be useful to refer to a longitudinal skin depth, in the following, as the characteristic absorption length along the discharge tube. This length will be related to the ordinary skin depth by a function involving the ratio of the discharge cross-sectional area to the waveguide cross-sectional area. A further explanation is given in Fig 4.4 which provides a diagrammatic representation of the longitudinal skin depth.

In terms of microwave engineering the discharge has to act as a matched load. That is it must behave as a lossy dielectric of sufficient extent to give total absorption and it must not unduly alter the waveguide impedance, otherwise reflections will occur. Such a load would consist of a wall of resistive material placed across the waveguide interior. In order to obtain impedance matching, the wall must be inclined to lie at a small angle to the guide axis. A discharge tube within the guide would have to be inclined to the axis for the same reason.

Consider now a waveguide terminated by a plane end wall perpendicular to the axis with a discharge tube entering the guide through a hole in the end wall centre and leaving the guide through the side wall some distance away along the guide. The RMS field (in the absence of a discharge and without reflection from the end wall) along the tube axis will vary as a quarter sine-wave with a maximum at the end wall and a minimum at the short wall. This is simply the projection of the transverse field profile in the guide for the  $TE_{01}$  mode. In this configuration the decrease in power along the guide,



Skin depth ( $\delta$ ) in a plasma filled waveguide ,cross-section A



Skin depth ( $D$ ) in a plasma filled tube ,cross-section a

$$D = f(\delta, a/A)$$

Figure 4.4 Longitudinal skin depth ( $D$ ) in a partially filled waveguide.

due to absorption by the discharge, may be compensated by the effect of the inclination of the tube towards a position of higher field. In a practical device the discharge tube entry points may be more conveniently placed at waveguide bends (as in the device used during the experimental work) so that unabsorbed energy may pass to a matched load and thus prevent the occurrence of reflection and standing waves. There will most certainly be a region of relatively low pressure ( $<0.5$  atm) where this arrangement will give good uniformity, perhaps at the expense of efficient absorption. At higher pressures, however, it can be expected that decay to a localised high density plasma will still occur.

It would be desirable to find an alternative to the 'tube in guide' coupling structure so that uniform high pressure discharges may be obtained. An ideal structure would distribute the microwave power in such a way that the field in the active discharge was constant at all points, and would give efficient coupling, over a range of plasma conditions. One approach to such a system, that of placing the discharge tube in an auxiliary guide and coupling via discrete elements graded so as to give constant power coupling through each element, is described in detail in the next section. Of the remaining possibilities, slow-wave structures are perhaps the most promising. The other major coupling method is to utilise a resonant structure, a method frequently encountered in the literature. This method is given no further attention here as the indications in the literature suggest that these devices are best suited to low densities and short tube lengths, and are rather sensitive to discharge conditions.

There are two kinds of slow-wave structure that may be of interest for the present application; open periodic arrays and the helical structure that is used in travelling-wave-tube amplifiers. Open slow-wave structures, such as the linear strapped bar described by Bosisio(1972) and the meander line used by Goldsbrough(1966) provide a strong fringe field adjacent to the structure. The discharge tube can be placed in this field with suitable inclination to improve uniformity. Bosisio(1972) used two structures in parallel but with opposed propagation directions to give improved uniformity. The travelling-wave-tube helix consists of a helical wire suspended within a conducting tube. The device is open-ended allowing a discharge tube to be placed axially within it. Unfortunately the radial field variation is quite complicated and inclining the tube to the helix axis may not be a particularly successful way to obtain a uniform discharge. An interesting possibility with these slow-wave structures would be to vary a suitable dimension of the structure gradually along its length in order to give a uniform discharge. This could be achieved most readily in the helix system by a gradual reduction in the helix pitch or diameter. A final observation concerning these two types of slow-wave structures is that while the 'open' system may require shielding in high power work, it does provide an excellent system for experimental work with ease of access and an unimpeded view of the discharge.



#### 4.2.2 Microwave Discharge Coupler Design

In this section the design details are derived for a coupler in which the discharge tube is placed in an auxiliary guide coupled by apertures to the primary guide. (It is pointed out that this coupler was designed and constructed towards the end of the experimental work and was used for a small number of the experiments only.) The basic concept behind this design is that the fraction of the main waveguide power coupled by each successive aperture can be made to increase so that equal powers are coupled by each element. Thus the discharge will be excited by equal intensities at a series of points along its length. If these points are close, compared with the longitudinal skin depth, a high degree of uniformity may be achieved. This can be expressed in a different way. If the discharge tube is simply placed axially in the main waveguide, uniformity can only be approached for longitudinal skin depths somewhat greater than the tube length. If, however, the power is divided and the tube excited in many short sections the longitudinal skin depth need only be greater than the spacing of these sections. Another aspect of this design is that because the power is divided the discharge cannot decay to the condition where all the power interacts with a very small high density plasma. The conditions where this decay does occur in each section will be those of higher power and/or pressure compared with the simple tube-in-guide structure.

A schematic diagram of the coupling device is shown in Fig 4.5(a) and the three ways in which the main and auxiliary guides may be joined is shown in Fig 4.5(b). It can be shown that where a coupling element between guides is perfectly matched (no reflection takes place) the radiation into the auxiliary guide is purely directional (Harvey 1963). Therefore, since good matching is required, the coupling device is simply a multi-element directional coupler. Many designs exist for such directional couplers but with equal sized elements rather than the graded sized elements required here. Coupling elements are usually round holes or slots, the latter having broader frequency characteristics. Slots were therefore chosen for the coupling elements because they would be less sensitive to dimensional irregularities. The waveguide configuration chosen was that of Fig 4.5(b)(iii). This is the form of the Schwinger reverse directional coupler for which design information is readily available ('The Microwave Engineers' Handbook' 1962). A useful feature of this design is that the auxiliary guide may be constructed in two halves allowing simple disassembly and access to the discharge tube. This possibility arises because in the  $TE_{01}$  mode the wall currents in the broad wall do not cross the longitudinal centre line and radiation will not occur at a joint along this line. Since this joint is adjacent to the discharge tube, as shown in Fig 4.5(b)(iii), small spacers in the joint will allow the active discharge to be observed with only slight radiation leakage.

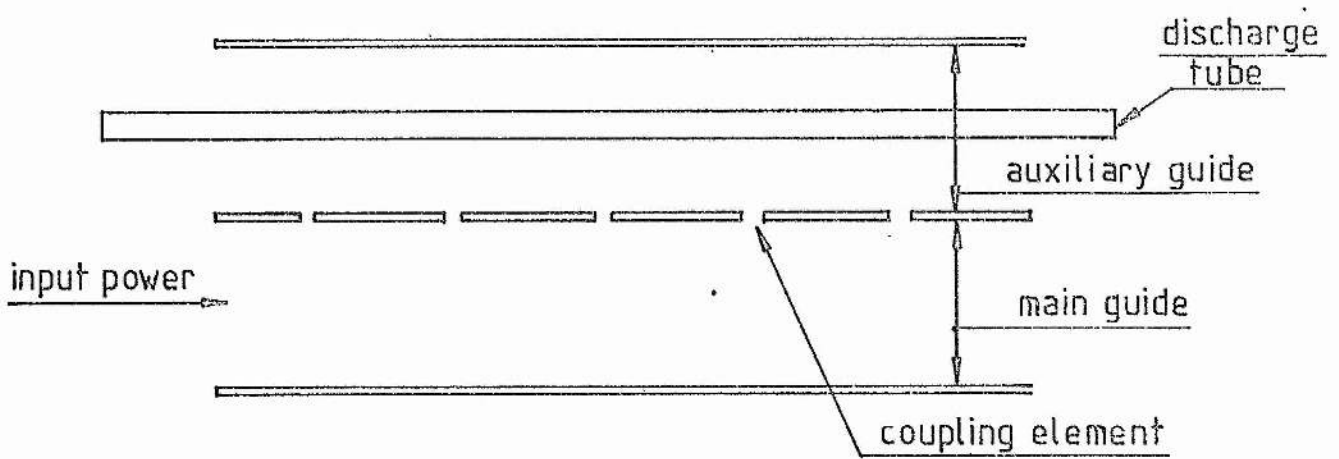


Figure 4.5 (a) Coupler schematic.

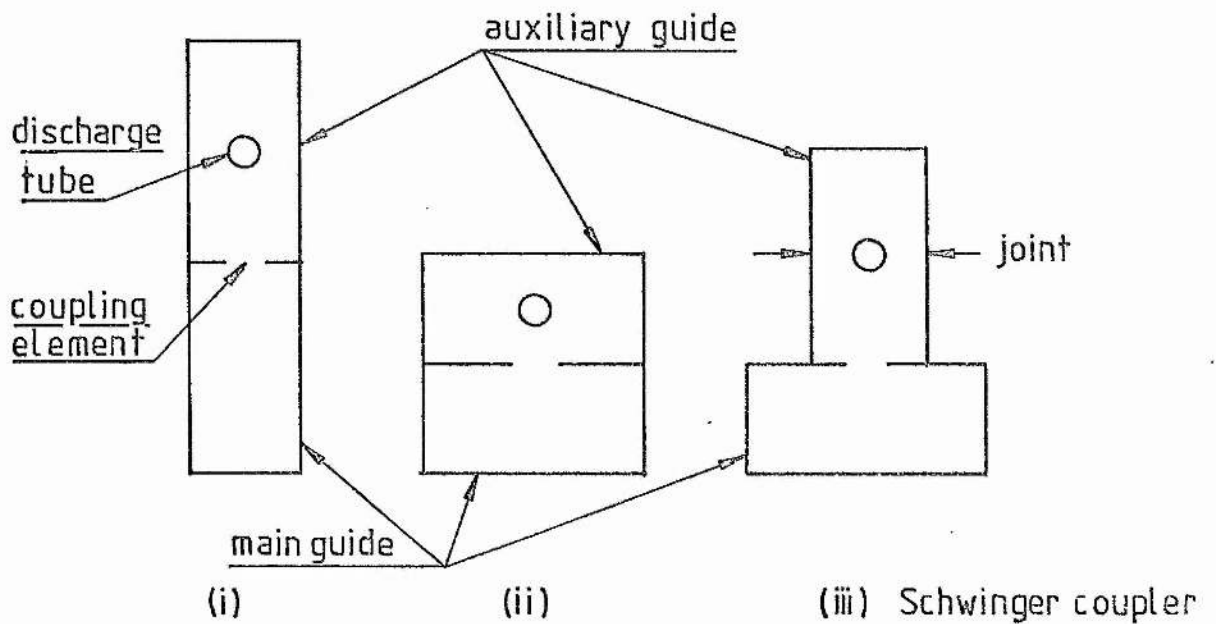


Figure 4.5 (b) Waveguide configurations

In multi-element directional couplers the elements have to be spaced by an odd number of quarter-wavelengths for the array to be directional and well matched. The elements in the Schwinger coupler are longitudinal slot pairs and the coupling factor is related to the length by design curves given in 'The Microwave Engineers' Handbook' (1962) and reproduced in Fig 4.6 which also contains all the remaining design details.

A formula is now derived which will enable the coupling factor for each element to be calculated. The following list defines the quantities and symbols to be used;

$F$  - coupling factor - coupled power/uncoupled power

$P_I, P_R$  - input power, residual power, respectively (main guide)

$p$  - power coupled by each element

$r, n, T$  - subscripts denoting  $r$ -th and  $n$ -th elements and total

The highest coupling factor, that of the last element, is limited by the longest slot that can be accommodated and cannot be infinite. Therefore there is a limit to the total coupled power since there will be an unavoidable residual power in the main guide. Using the above definitions we can write

$$F_n = p/P_R \quad \text{and}$$

$$F_T = np/P_R$$

**SCHWINGER REVERSED DIRECTIONAL COUPLER**  
**ASPECT RATIO 2 : 1**

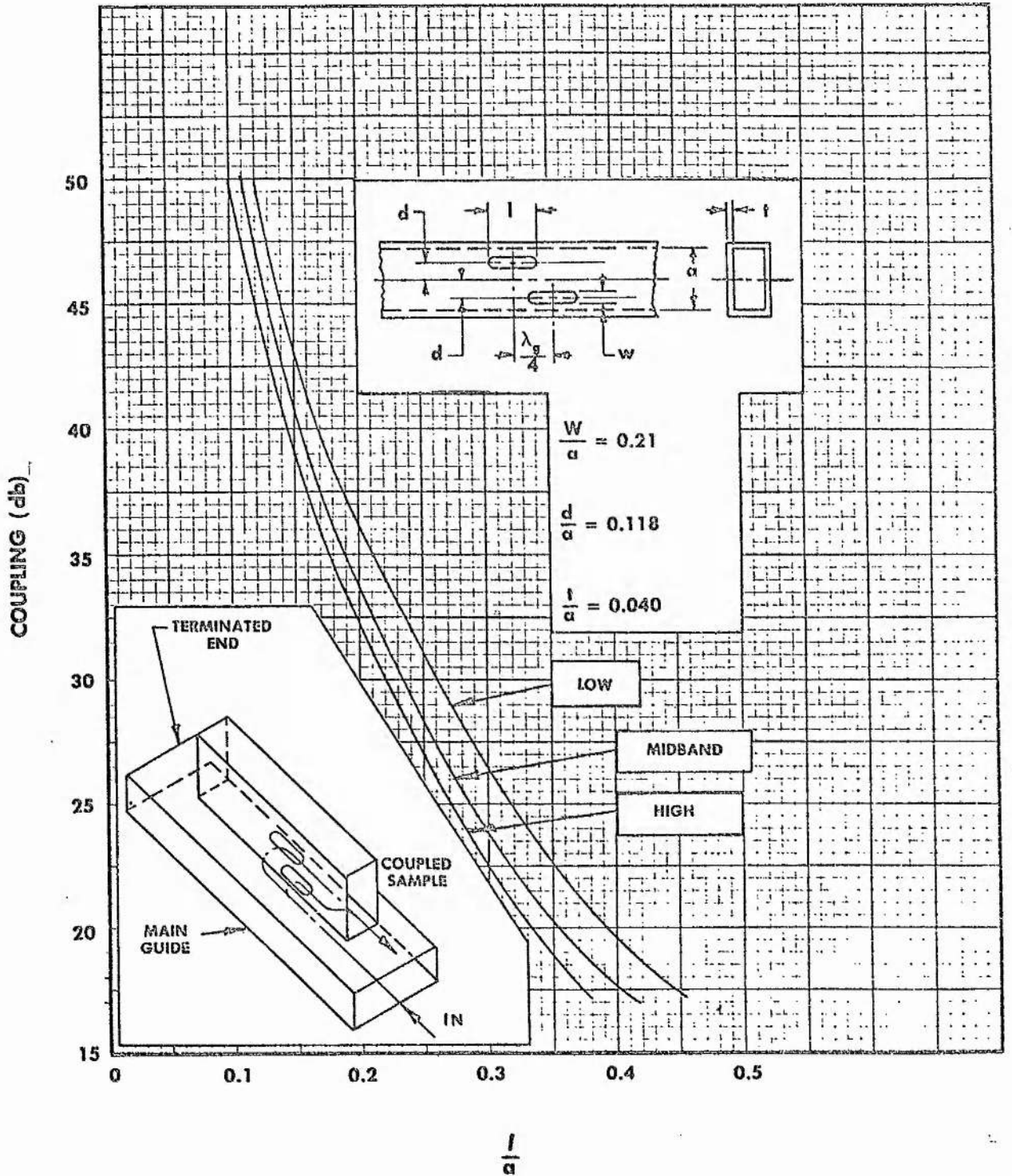


Figure 4.6 Coupler design data (from The Microwave Engineers' Handbook 1962)



which give the relation

$$F_T = nF_n \quad (1)$$

The coupling factor of the r-th element is given by

$$F_r = p/(P_I - rp) \quad .$$

Using

$$P_I = np - P_R$$

and the first equation above gives

$$F_r = F_n/(F_n(n - r) - 1) \quad . \quad (2)$$

Equations (1) and (2) give the basis of the design procedure. That is, the total coupling factor can be set by consideration of the coupling factor of the last element, the number of elements appropriate to the discharge tube length, and the element spacing. The coupling factors of the remaining elements are found using equation (2). These equations can be applied to any kind of multi-element directional coupler. The approximate conditions for uniformity are that the element spacing be somewhat less than the total length. The unabsorbed power in both guides should be carried to matched loads to prevent reflection and standing waves occurring. The physical dimensions of the Schwinger reverse directional coupler that was constructed during experimental work are given with its constructional details in Section 5.3.

#### 4.2.3 Preionisation Methods

It has been pointed out in section 4.2.1 that preionisation in the high pressure microwave discharges of interest may lead to greater pulse to pulse uniformity and improve the spatial uniformity of the discharge. In addition to this the discharge formation time may be reduced leading to improved efficiency. Since the detailed level and uniformity of preionisation are unlikely to be critical, simple methods need only be considered. Methods requiring electrodes in the discharge volume or utilising separate discharge circuitry are therefore not discussed. Thus an auxiliary low power discharge driven by the microwave pulse is likely to provide the most useful method although the use of a radio-active source may also be of interest.

The utilisation of a radio-active source has certain clear attractions. In particular, since the source strength can be accurately measured and its irradiance of the discharge tube carefully controlled, it could be very useful in experimental investigations. In addition to this the problem of timing the preionisation relative to the microwave pulse is completely absent. Clearly these attractions have to be weighed against the handling and management problems of using radio-active sources. The major practical problems are the difficulty of preventing the occurrence of a discharge within the waveguide, external to the discharge tube, and of placing the source so that it does not perturb the the microwave transmission.

An auxiliary discharge obtained in a quartz tube adjacent to the main tube can be simply provided. This discharge will have to cause little perturbation in the guide and absorb a small amount of power so that overall efficiency is not unduly reduced. In addition the UV production efficiency will need to be high. A small bore ( $\leq 1\text{mm}$ ) quartz tube containing xenon at low pressure will provide considerable UV radiation. The best pressure for rapid breakdown and the most favourable location for the tube may be found experimentally. If the tube is shorter than the main discharge tube and placed at the end opposite to that at which the microwave radiation is incident it is possible that the auxiliary discharge will extinguish as the main discharge becomes fully developed. That is the absorption of the microwave power by the main discharge may result in a field in the vicinity of the auxiliary tube that is below its maintenance threshold. Under these circumstances a higher power absorption by the auxiliary discharge may be permitted since it will be active only briefly.

The notion of a priming discharge that becomes screened by the main discharge leads to a preioniser design of great simplicity where the auxiliary discharge takes place across the waveguide interior. The formation of this discharge is stimulated by placing a spike or series of spikes, inside the waveguide, that cause a discharge to form between a waveguide broad wall and the spikes and pass over the surface of the discharge tube. This discharge would have to be located well away from the microwave input end so that subsequent extinction would be ensured. This method and the method utilising an

auxiliary discharge tube were used in the experimental work although systematic evaluations were not carried out. Details of the physical construction of the preionisers appear in Section 5.3.

#### 4.3 Comparison of Microwave and DC Discharge Apparatus

As a conclusion to the present chapter the differences between a microwave discharge apparatus and a DC discharge apparatus, suitable for pumping excimer lasers, are highlighted. For convenience the apparatus will be divided into five sections. These are the power supply and pulse forming circuit, the pulse transmission system, the discharge container, the optical components, and the gas handling system.

There is no particular distinction to be made between the power supplies for the two systems. However, it has been pointed out that pulse rise times have to be very short ( $\leq 10\text{ns}$ ) in DC systems whereas the absence of the tendency to form filaments in a microwave discharge means that rise times of around  $50\text{ns}$  will be adequate. This difference is critical since the switching time of simple gas discharge switches is limited to around  $15\text{ns}$ . Therefore for efficient DC systems rail-gap switches or hydrogen thyratrons have to be used for switching. The impedance of the pulse forming network has to match that of the discharge in DC systems or the magnetron in microwave systems, the latter being about an order of magnitude larger than the former. The existence of the switching element in this impedance adds considerably to the design difficulties in DC

systems.

Connections between the pulse forming network and the discharge electrodes in DC systems have to maintain the low source impedance. In particular, the transmission system (and switch) have to be of a low inductance to permit rapid current rise times. This requires that current loop areas be as small as possible. However, the use of high voltages and high gas pressures means that the electrodes in the discharge head have to be separated by substantial insulators so that the requirement for small current loops has to be compromised. These difficulties are completely absent in a microwave system where the high frequency modulation allows the use of simple and cheap waveguide transmission systems. It is an outstanding feature of a microwave system that the use of waveguide allows great flexibility in the placing of the discharge relative to the power supply and pulse forming network. In DC systems the pulse forming network and laser head are intimately connected forming a relatively immobile structure.

It is possible that the ultimate advantage in using a microwave discharge for pumping an excimer laser will derive from the use of a dielectric tube for the containment of the discharge. Thus a low level of contamination may be realised and with increased effective gas life the cost of gas replacement reduced. It should be noted that this possibility has not been investigated in depth though the work of this thesis allows certain limited conclusions to be drawn for a quartz discharge tube. In DC systems the contamination due to the electrodes and insulating material that form the discharge



chamber may reduce the gas life to just a few pulses. To combat this difficulty special materials are required such as monel for the electrodes and PTFE for the insulator. Both of these materials are expensive. In order to give long tracking distances the insulator has to be large. In addition to this the electrodes and insulator have to be securely bolted together against the gas pressure with no possibility of leaks. The final structure is thus inevitably bulky and expensive in materials and manufacturing costs.

The optical components and gas handling systems will be similar in the two systems except that when fast gas flows are required the small bore of the discharge tube in the microwave apparatus will create a severe limitation. One final point of comparison is that the exposure of the laser head in a DC system compared with the well contained tube in the microwave system means that in the former there is a hazard due to the presence of high voltages and that high levels of radiated radio noise will be emitted. The laser head and its attached circuitry have therefore to be contained in a large metal box adding considerably to the bulk and inconvenience of the structure.

To summarise, if it can be shown that a microwave discharge can drive an excimer laser successfully, the use of a small discharge tube within a waveguide offers an apparatus which is outstandingly compact and simple compared with a DC system. The additional possibility of low contamination adds much to the importance of investigating microwave discharge pumping for excimers. In addition to this the high uniformity possible with a microwave discharge

should give high beam quality and may therefore make the system useful as an oscillator producing radiation for amplification in by conventional DC pulsed discharges. The additional cost that has to be considered for a microwave system is that of the magnetron and of providing a pressurised waveguide. Finally it is pointed out that notwithstanding the success or failure of the microwave system in relation to excimer laser pumping, the advantages of the microwave apparatus make it a strong contender for use in a wide variety of high power gas discharge applications. In particular such a system would be highly suitable for use as a spectral source providing high energy pulses at high repetition rates.

## 5 MICROWAVE APPARATUS

### 5.1 The Radar Set

#### 5.1.1 General Description

The radar set that was subsequently adapted for the generation of microwave discharges was obtained from the Royal Navy (ASWE - Portsmouth) as redundant equipment. It had been used for indoor laboratory testing only and was brought into service in about 1964. (The design of this model may precede this date considerably). It operates in the X - band of frequency and was intended as a navigation aid for small ships with an ultimate range of 48 miles for large features. Several manuals were obtained with the set but these were mainly concerned with operational instructions, installation instructions, and parts lists. The brief section describing the internal operation of the system contained no diagrams of parts or wiring. It seems likely that detailed information would reside with the manufacturers (Hughes) but whether they would provide such information was not investigated. General specifications of the set are given in Table 5.1 which includes some dimensions to give an indication of the size of the system.

Frequency/Wavelength	9410MHz / 3.186cm
Power Output	50kW (peak)
Pulse Repetition rate	1100 Hz
Pulse Length	170 or 320 ns
Intermediate Frequency	60 MHz
Receiver Bandwidth.	12MHz
Power Requirement	220V DC , 2kW
<u>Components</u>	
Transmitter - Receiver	40x46x23 (cm) , 42kg
Azimuth - Range Indicator	56 x 43 x 69 , 50
Indicator Control Unit	43 x 36 x 19 , 20
Power Supply	36 x 31 x 13 , 10
Motor Generator	30 x 30 x 90 , 132
Aerial	200 cm long , 51
Motor Starter	40 x 35 x 20 , 16
Interconnecting Cables	

Table 5.1 Radar set specification

The components of the system are interconnected with heavy, screened, multi-wire cables plus some coaxial signal cable. The connecting arrangements for the fully operational system are shown in Fig 5.1. The functions of each component are as follows :-

Transmitter - Receiver Generates microwave pulses which are fed to the waveguide. Contains a high voltage generator, pulse generator, magnetron, transmit - receive cell, and detection system.

Azimuth - Range Indicator Radar display with radially swept signal line.

Indicator Control Unit Acts as a central terminal block and has a facility for switching between two display units.

Power Supply Provides nearly all of the DC voltage requirements of the system and is an interconnection point between the indicator control and the display. The operational switches are installed on this unit.

Motor Generator This is a 220V DC motor in tandem with an AC generator and converts the DC supply to 180V, 1100Hz, AC.

Motor Starter Three operational units are housed within this unit; (a) a switching system to prevent the DC power supply being presented with a very low impedance when switching on, (b) switching which prevents the output AC from being connected to the radar load until the motor generator has reached at least half speed, and (c) a regulator for the AC output.

Aerial Comprises a six foot end-fed shunt slotted waveguide in a perspex housing, aerial rotation motor, activity sensor, and a rotary waveguide joint.



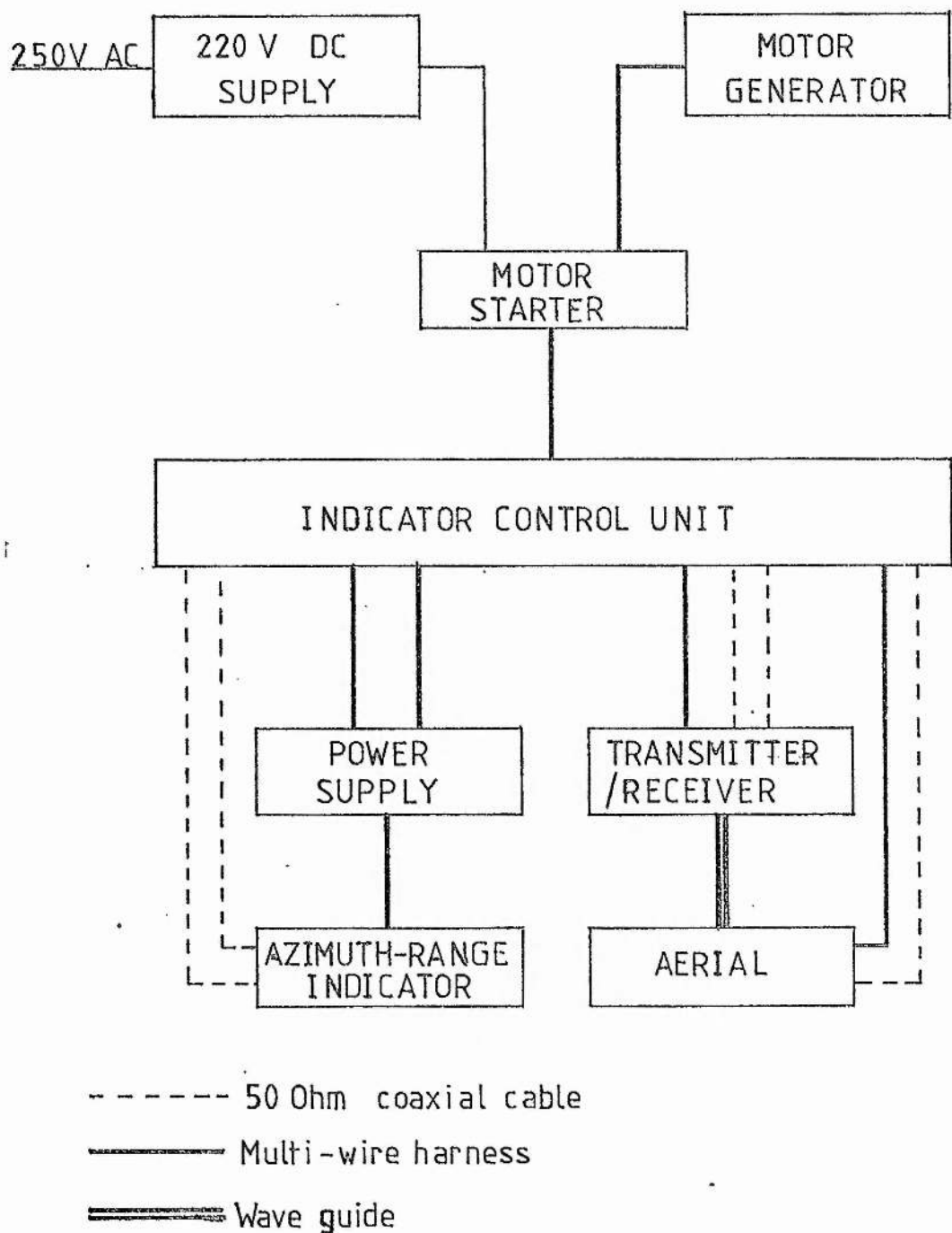


Figure 5.1 Connection diagram

220V DC Supply

The rectifier for converting single phase mains to 220V DC was not part of the supplied system. The 220V DC supply has to provide a 9A running current and 21A during the motor generator starting period. A DC supply (Service Trading Co. London) was used with a current capacity of 10A. It was a type of variable supply that has to be increased from zero to the operating voltage after connection to the load; the reverse procedure being followed when switching off. It was found that by carrying out this procedure slowly the supply current during the starting period of the motor generator could be kept below 10A.

As a preliminary to adapting the radar set to the function of driving a discharge the system was set up and tested for normal functioning. The set was found to be in good working order with the exception of a single fault. This was found to be due to faulty operation of the indicator selection switch and, although the fault was trivial, considerable difficulty was encountered in tracing it. Had circuit diagrams been available this task, and the problems of understanding the operation of the system, would have been simplified considerably. The testing showed that the whole system was quite cumbersome and noisy, and generated heat to the extent that operation in a small laboratory was quite unpleasant. It therefore seemed desirable to remove as much of the unwanted parts of the system as possible as described in Section 5.2 below.

### 5.1.2 Safety

In working in close proximity to microwave radiation careful attention has to be paid to the hazards of the radiation. The hazard warnings contained in the radar set manuals were very brief, consisting of the following two sentences:-

Radiation hazards may result from exposure to the main beam of the radar aerial at a distance of six inches (15.24cm) or less from the central front perspex face of the aerial.

Never look down a waveguide from which power is being radiated.

Since a long period of working in close proximity with the apparatus was envisaged, more detailed information on microwave radiation hazards was sought. Harvey (1963) discusses microwave radiation hazards and gives many references. The standards adopted in the USSR are quite detailed, giving consideration to frequency band and exposure time. At 9410MHz the limits are  $10\mu\text{W}/\text{cm}^2$  (continuous exposure during an average working day),  $100\mu\text{W}/\text{cm}^2$  (for 2 hours exposure per day), and  $1\text{mW}/\text{cm}^2$  (15 - 20 minute exposure per day). These, together with the widely accepted short period maximum of  $10\text{mW}/\text{cm}^2$ , were adopted as the maximum values during experimental work.

The microwave radiation was completely contained in a waveguide structure except at the two apertures that carried the discharge tube. In order to check for leaks at waveguide joints and to measure the extent to which a discharge could couple radiation out through the tube apertures a microwave detection diode in a quarter wavelength short-circuit mount was utilised. No leaks at any joint could be detected giving more than a thousandth of the power intensity within the waveguide. However, it was found that at low pressure (<10Torr) the luminous gas discharge extended a few centimetres along the discharge tube outside the waveguide. Under these conditions the maximum detected intensity close to the discharge was about a twentieth of the waveguide intensity. Using the mean microwave output power of 7W and the inverse square law, the minimum safe distance for a radiation intensity of  $10 \text{ W/cm}^2$  (the continuous exposure limit) is 53cm.

In practice, safe conditions were assured during experimental running for two reasons. Firstly, the operator was able to control the apparatus and take measurements at a distance of over 2m from the discharge tube. Secondly, in all experiments the microwave power was used in short bursts (often 1 second) with long periods (about 1 minute) between bursts. During the few experiments when longer 'on' times were used the automatic recording facility enabled the operator to stand 5m from the apparatus or leave the room.

### 5.1.3 Details of the Magnetron Circuitry

The parts of the radar set of principal interest for the microwave discharge application were the magnetron and the surrounding circuitry. The following description of these and their operation is derived from the scant details given in the manuals and may therefore be inaccurate in certain details. However, the basic principles are clear and could be applied to a separate purpose built system.

A likely arrangement for the magnetron circuit and the waveforms at various points in it are shown in Fig 5.2. The 180V RMS supply, after passing a filter, potentiometer, and transformer is rectified to give  $\sim 8.2\text{kV}$ . This charges one section (short pulse) or two sections (long pulse) of a delay line. The 180V supply is also fed to a pulse generating circuit. During the early part of the positive half cycle the saturable reactor exhibits a high impedance and allows the capacitor to be charged. When the reactor current reaches a critical value the reactor impedance drops and the capacitor is discharged through the transformer primary. The high voltage pulse appearing on the transformer secondary acts as the trigger pulse for the trigatron valve which then discharges the delay line through a pulse transformer generating  $17\text{kV}$  at the magnetron cathode. Charging of the delay line takes place in the negative half cycle of the supply during which circuit operation is prevented by the diode in the pulse circuit. The magnetron heater current is supplied via the bifilar secondary of the pulse transformer.

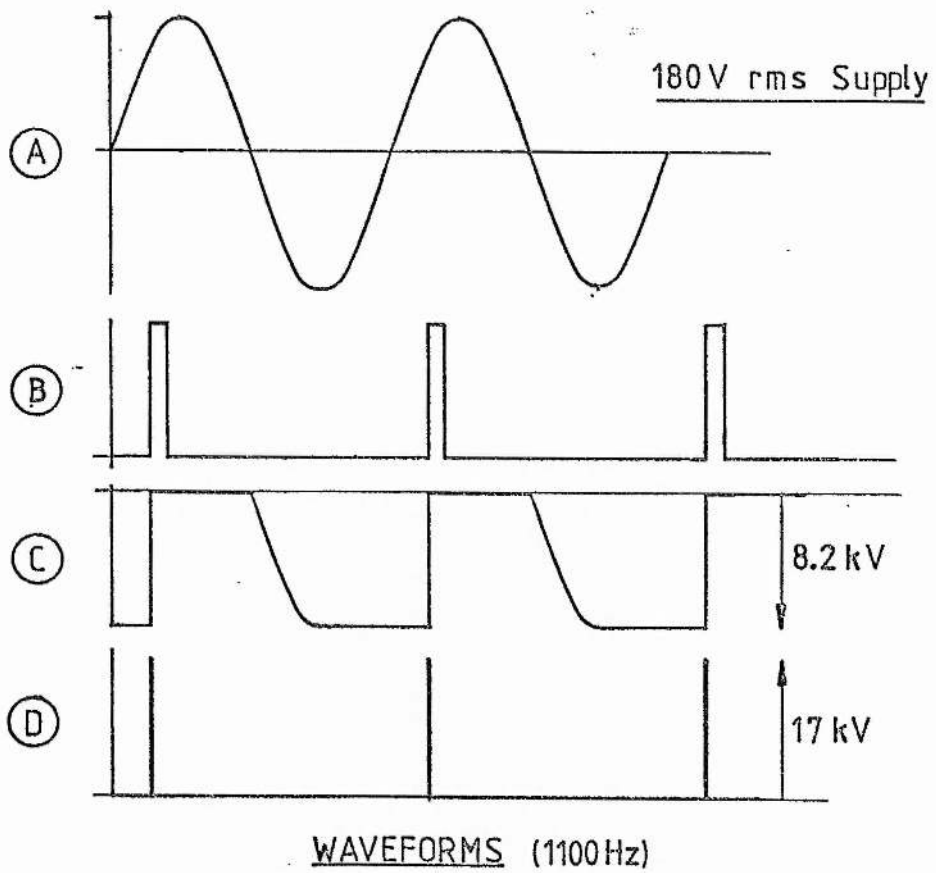
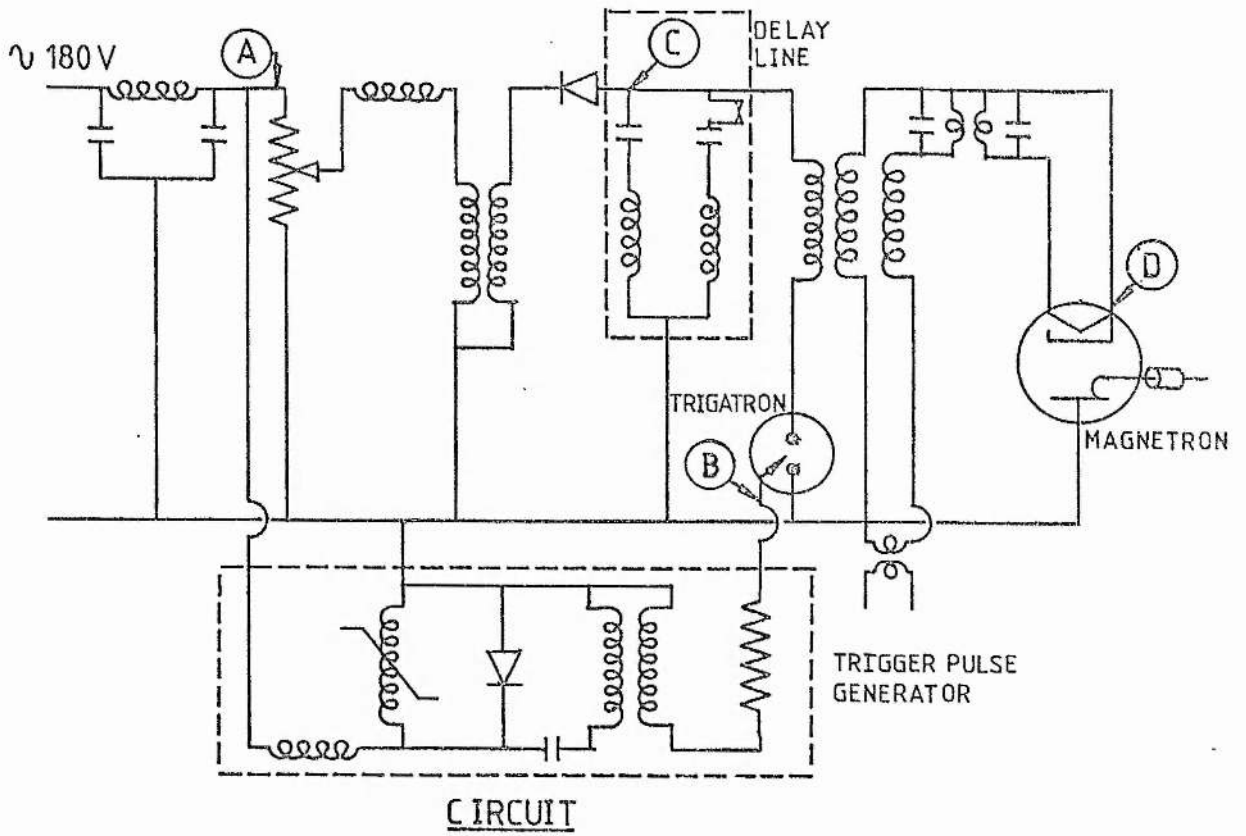


Figure 5.2 Magnetron circuit (modulator)



In providing a high repetition rate this system enabled the investigations of gas life-times to be carried out in short periods of time. In addition the ionisation surviving the inter-pulse period at a high repetition rate is sufficient to give effective pulse preionisation. However, if greater flexibility of pulse timing is required there are three main ways in which the present system could be adapted;

- (a) The magnetron could be driven from a separate system entirely.
- (b) The delay line could be charged from a negative DC supply connected to point C in Fig 5.2. The pulse circuit could be fed with a positive (perhaps slowly rising) pulse at its input.
- (c) The 180V input, or perhaps just the input to the trigger pulse generator, could be interrupted by circuitry that would enable connection to be made for single whole cycles. This would be achieved using thyristors (or a triac) and an integrated circuit zero voltage switch.

The advantage of using (c) would be that a minimum of additional equipment would be required while (b) would enable the system to be operated without the encumbrance of the radar power generating system and the other parts and cables required for interconnection.

## 5.2 Radar Set Adaptation

### 5.2.1 Alterations and Additions

The radar aerial was not required for experimental work and was therefore disconnected at the first waveguide joint on the outside of the transmitter unit. The electrical connections to the aerial consisted of the motor supply, connections for the radar activity detector and a direction sensor, and an electrical output from the aerial motor. This output, obtained from an additional winding on the motor armature, was of 115V, 3-phase, 50Hz and was used to drive the display sweep in synchronism with the aerial and to feed a cooling fan in the transmitter unit. In order to maintain the operation of this fan the motor was extracted from the aerial assembly and allowed to run during operation of the system. Disconnection of the remaining wiring had no deleterious effect on the functioning of the system.

The radar display was also not required and was removed. Disconnection of the wiring harness connecting it to the system had no undesired effect on the generation of radar pulses. However, the display unit housed the range change switch which gave a choice of microwave pulse lengths of 170ns or 32ns. Since it was desirable to retain these two possible pulse lengths the wiring for the switching was traced. It was found that switching took place by momentary contact of a live wire to one of two other wires depending on the

pulse length required. Terminals for these three wires were found in the power supply unit and a separate non-latching, single pole change-over switch was connected to them to replace the switch on the display unit.

After removal of the aerial and the display, the transmitter was attached to a robust but movable table. This enabled the discharge apparatus to be operated in a remote and variable position relative to the remaining radar equipment. To complete this flexibility it was desirable to allow the operator to switch the microwave power on and off from anywhere in the vicinity of the apparatus. The operational switches were housed on the power supply unit and were used with the 220V DC supply in the following way. The run/stop switch on the power supply was left permanently in the 'run' position and the operation of the system initiated by turning the DC supply slowly up to 220V as described in Section 5.1.1. After this, generation of microwave pulses is inhibited for two minutes until the on/standby switch on the power supply becomes effective and allows the microwave pulse generation to be switched on and off at will. Thus it was required to connect a switch in parallel to the standby switch at the end of a long cable so that remote switching would be permitted. In addition to this it was required that the microwave pulses could be switched on for bursts of a constant duration of about 1 second. This was achieved by use of a monostable circuit that could be triggered by a push-button switch, also at the end of a long cable. A complete diagram of this switching arrangement is shown in Fig 5.3.

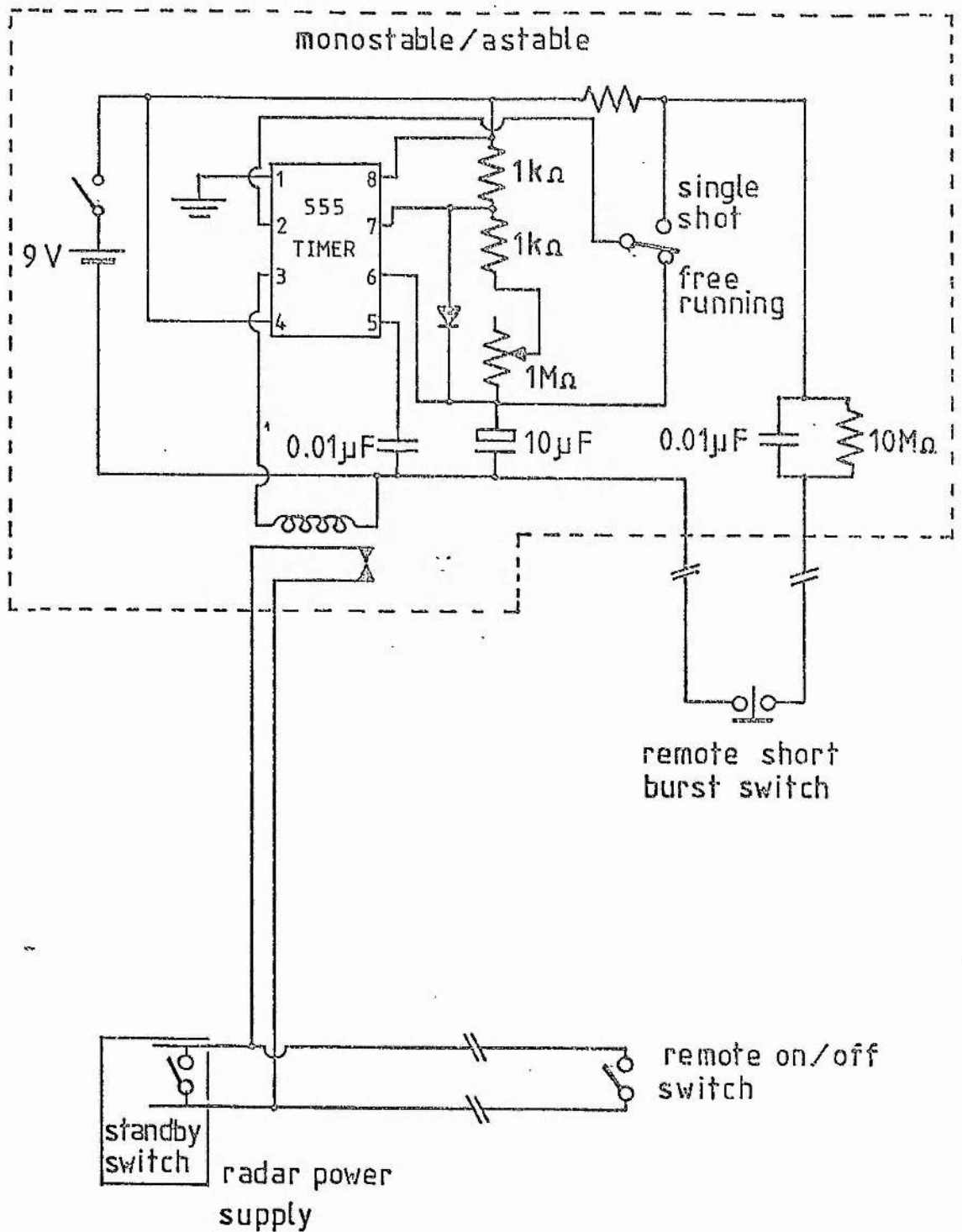


Figure 5.3 Additional radar set switching

### 5.2.2 Waveguide Assembly

The radar transmitter output waveguide was connected to the microwave discharge coupling device with a waveguide structure that incorporated several components interconnected with standard waveguide type WG16 (internal dimensions 0.9x0.4 inches). The whole assembly is shown schematically in Fig 5.4, missing out the bends and twists required to place the coupler and discharge tube in a convenient position.

The isolator was used in this assembly to prevent large reflected signals returning to the magnetron. Any residual returning signal could be detected at detector 1 and removed by adjustment of E - H tuner 1. Reflection from the coupler, whose magnitude could be used to judge the degree to which microwave power was being absorbed in the discharge, was indicated by detector 2 after reduction by the attenuator preceding it. The reflection from the discharge could be minimised by adjustment of E - H tuner 2 or by the adjustable short circuit.

### 5.3 Microwave Discharge Couplers

Three microwave discharge couplers were used during experimental work. During preliminary trials and development of the apparatus a transverse-tube coupler was used while the main body of experimental work used a longitudinal-tube coupler. For some of the concluding experimental work a coupler based on the Schwinger reverse

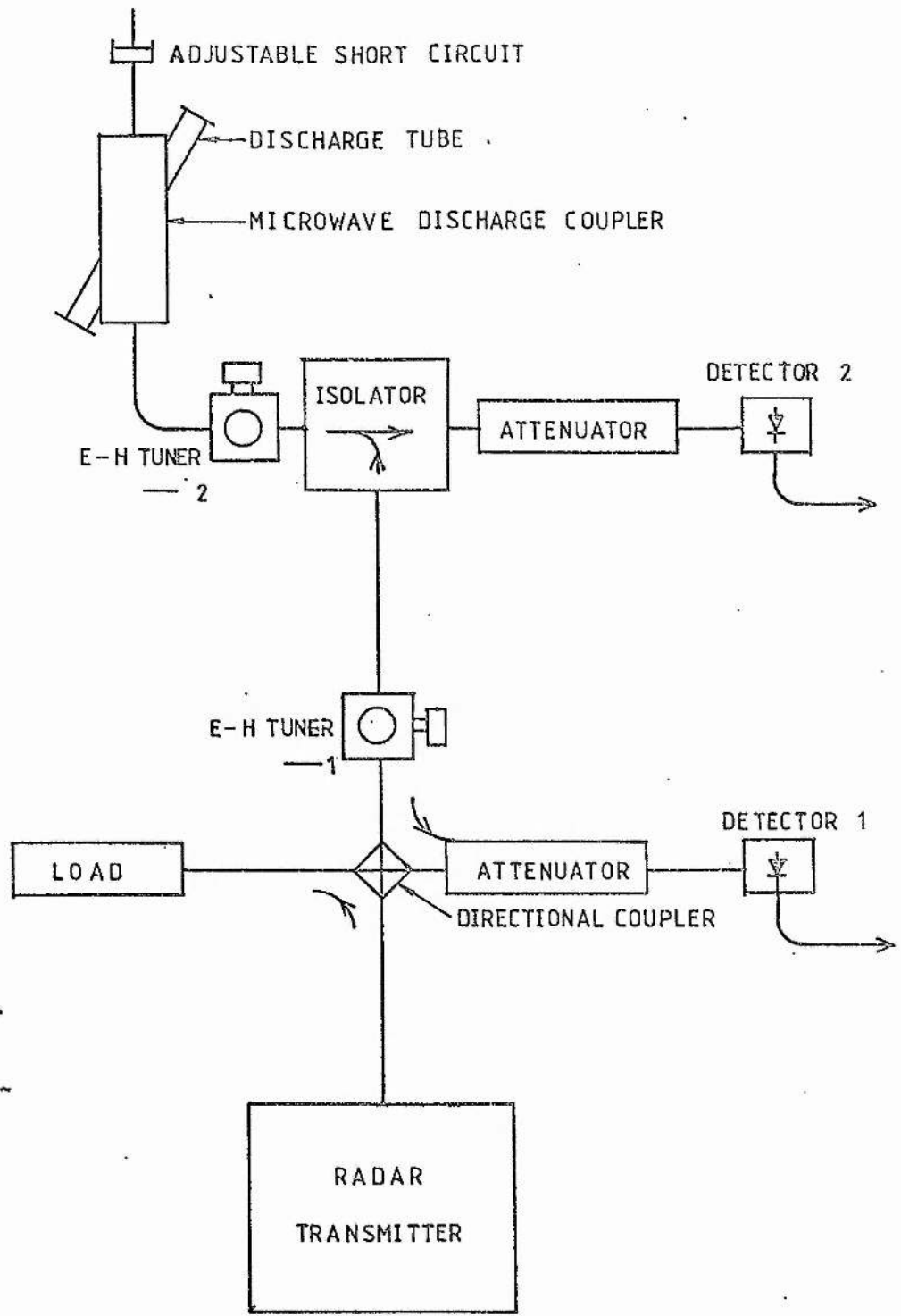


Figure 54 Waveguide assembly



directional coupler was used. Since the theoretical aspects of coupler design were discussed in Chapter 4 above, the descriptions below will be limited to the physical aspects with a brief summary of the performance of each device.

### 5.3.1 Transverse-Tube Coupler

A cross-sectional view of this coupler is shown in Fig 5.5(a). The quartz discharge tube passes centrally through the narrow walls of the waveguide, perpendicular to the waveguide axis. Soldered onto the waveguide are two screening tubes through which the discharge tube passes. The 2mm ID discharge tube carried two stubs for gas connection and had two rough windows formed on the ends. Completion of the tube had to take place with the tube in place in the waveguide. The coupler was connected to the assembly shown in Fig 5.4.

The physical construction of this coupler, though quite straightforward, caused two main difficulties. Firstly, the assembly in situ of the quartz glassware was quite difficult. A demountable waveguide allowing easy replacement and inspection would have been preferable. Secondly, the tube was connected to the halogen compatible gas handling system by lengths of viton (a halogen compatible elastomer) tube which is quite stiff. This meant that great care had to be taken to prevent the discharge tube from being broken either during connection of the viton tube or by some movement of the viton tube at a later date.

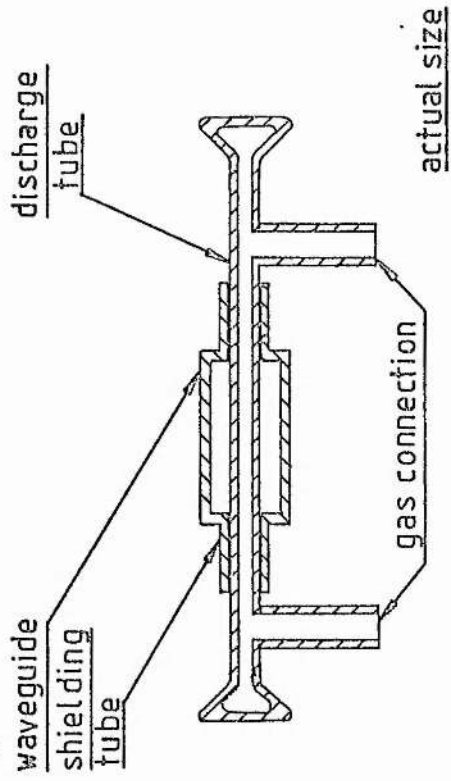
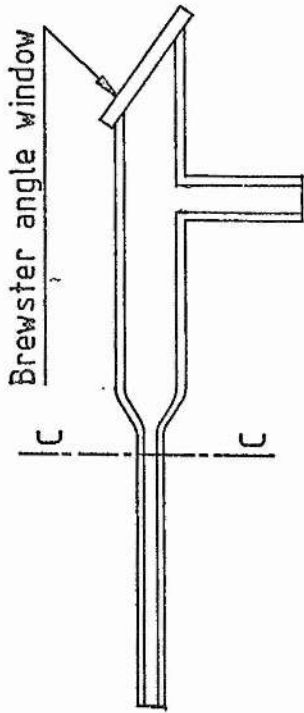


Figure 5.5 (a) Transverse-tube coupler.



tube ends attached at C-C

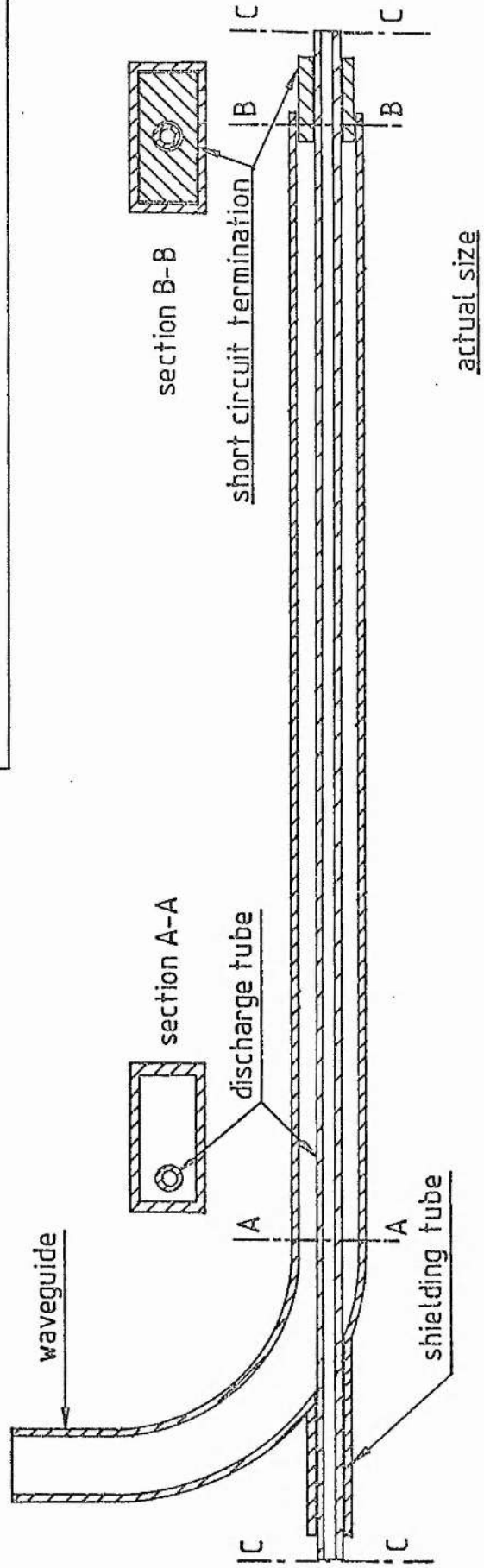


Figure 5.5 (b) Longitudinal-tube coupler

This discharge tube arrangement was not employed for the principal experiments, for the reasons given below, but it did provide the first demonstration that excimer spectra could be obtained with microwave pulses obtained from the adapted radar set. The intensity of emission and its time behaviour enabled the setting up of the optical recording system and the formulation of experimental procedures. Also the full requirements for the gas handling system were established and the apparatus developed accordingly.

In terms of discharge performance the transverse tube coupler was inferior to later designs in almost all respects. It was most noticeable that a discharge occurred spontaneously for just a narrow range of mixtures and pressures. However, the discharge could often be initiated by means of a Tesla coil. The range of conditions where this method was successful was wider than those for spontaneous breakdown initiation, indicating that sufficient ionisation can survive the inter-pulse period to allow spontaneous breakdown to occur.

Observations of the output of the reflection detector (detector 2 in Fig 5.4) were used to indicate the absorption performance of the discharge. Despite the lack of calibration, the absorption could be judged to be considerably poorer in the transverse coupler than in the longitudinal couplers. The apparatus of Fig 5.4 could not be used to distinguish between reflections from the discharge and reflections from the adjustable short. However, it was found that

the positions of the short were different for optimum ease of initiation and optimum absorption. The position of the short also had to be adjusted for optimum absorption when the total pressure was changed. This requirement for retuning meant that if intensity measurements were made relating to gas life, two gas samples were required at each experimental pressure; one to optimise matching (absorption) and one for the intensity/lifetime measurement.

Finally it was observed that as the pressure was increased above half an atmosphere the discharge became increasingly localised on the input side of the discharge tube, and that this was accompanied by a continuous increase in the reflection signal. This observation, and the others above, are broadly consistent with the discussions of Chapter 4.

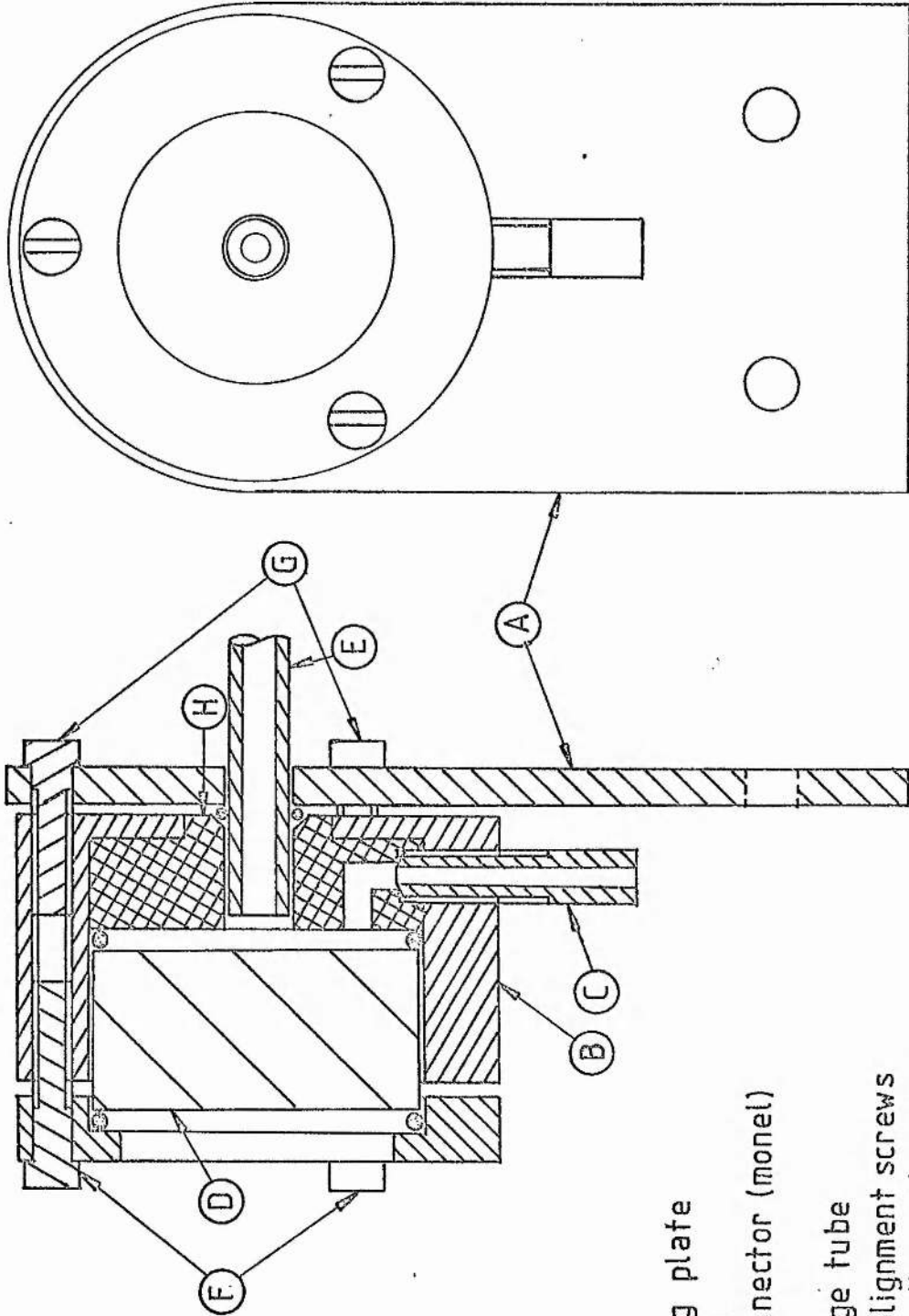
### 5.3.2 Longitudinal-tube Coupler

The longitudinal-tube coupler is shown in Fig 5.5(b) in a cross-section taken along the discharge tube axis. Two transverse sections are shown in order to indicate the inclination of the tube to the waveguide axis. The discharge tube enters the guide at the bend and at the short-circuit termination (which is adjustable). By this means the length of inactive gas on the optical axis is kept small. The microwave leakage at the entry points was found to be small but could be reduced further by wrapping the entry areas in aluminium foil. Observation holes were drilled at 2cm intervals on the narrow wall centre line and the radiation leakage was checked and

found to be undetectable.

Although the majority of the experimental work was concerned with excimer fluorescence emission, some concerted efforts were made to obtain excimer laser action using this coupler. Two types of low loss cavity were used for these attempts, one utilising Brewster angled windows, the other placing the laser mirrors in direct contact with the gas. In the Brewster window system the discharge tube, windows, and gas connections formed a single quartz glass structure which had to be completed in situ. The tube ends for this case are shown in Fig 5.5(b). In the windowless system laser mirror mounts, shown in Fig 5.6, were constructed so that the mirror surfaces were as near to the discharge tube ends as possible in order to minimise the length of inactive gas in the optical path. Mirror alignment is adjusted in this mount by means of screws and compressible 'o'-rings. The materials in contact with the gas were chosen for halogen compatibility. In the majority of the experiments, where laser mirrors were not required, the same mirror mounts were used but with calcium fluoride windows instead of laser mirrors.

The good performance of this coupler was demonstrated during the experimental programme where discharges were obtained from pressures below 0.01 atm up to over 2 atm depending on the mixture used. In most gas mixtures high absorption could be obtained over at least 70% of the pressure range for which a discharge was present. However, at the lower pressures in a range, retuning (using E - H tuner 2 of Fig 5.4) was required to obtain good absorption following a change in total pressure. Good uniformity was limited to a much narrower



- A - mounting plate
- B - housing
- C - gas connector (monel)
- D - mirror
- E - discharge tube
- F - mirror alignment screws
- G - housing alignment screws
- - o'-rings (viton)
- H - PTFE liner

scale :twice full size

Figure 5.6 Mirror mount.

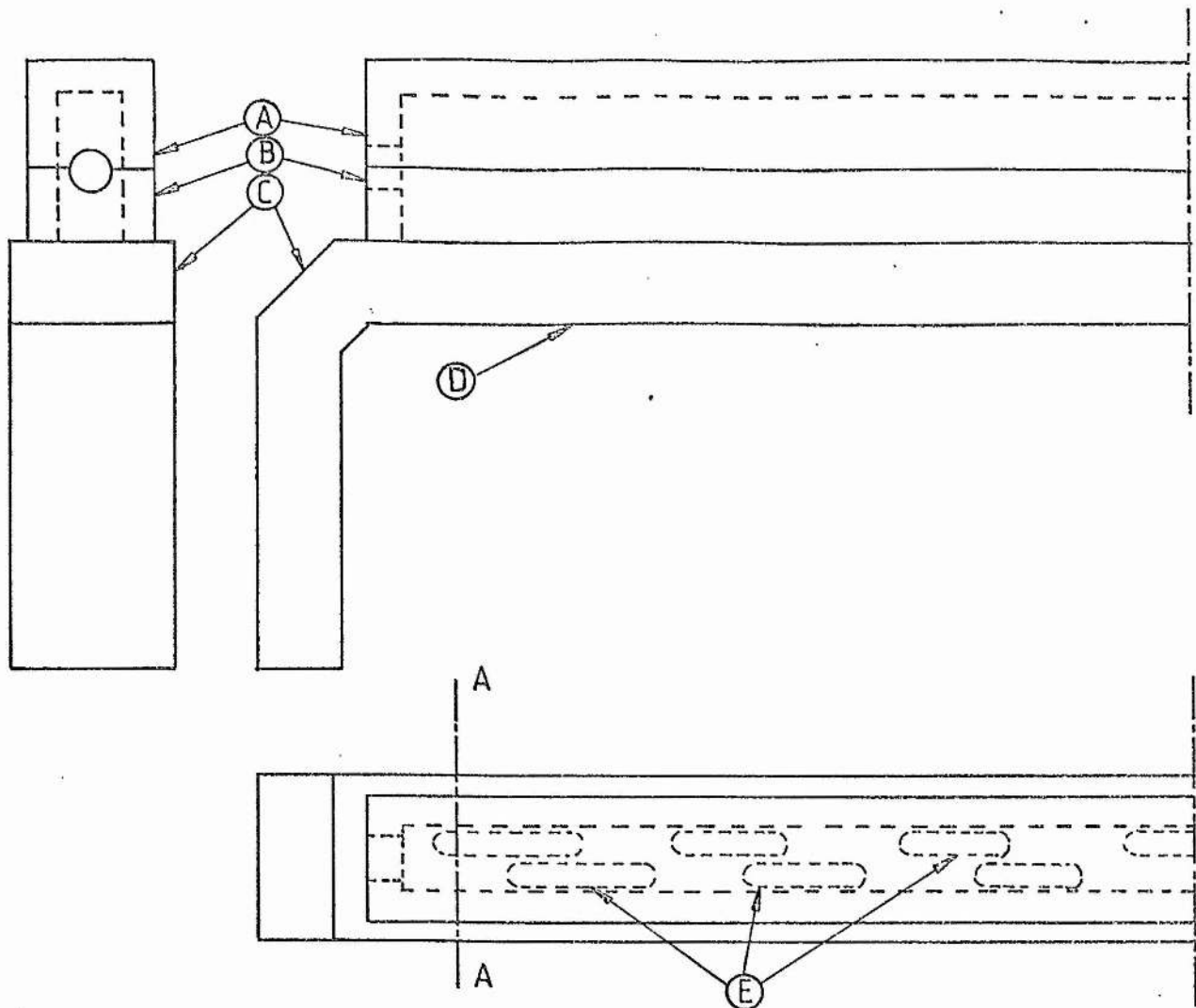


pressure range, perhaps 30% of the total pressure range. Particularly noticeable was the increasing localisation of the discharge, at the microwave input end of the discharge tube, as the pressure was increased. It was this observation that demonstrated the need for further coupler development which resulted in the Schwinger coupler being designed and constructed.

During the use of the longitudinal tube coupler the preionisation method using an auxiliary discharge tube was developed. It consisted of a quartz tube 1mm in internal diameter and 10cm in length which entered the waveguide through the short-circuit termination. Flexible plastic tubing was used to connect the discharge tube to a small gas handling system that allowed the tube to be evacuated and filled with xenon. The position of the tube and the xenon pressure were varied to find conditions of reliable operation but with small power absorption. Xenon pressures in the range 1 to 5 Torr were found to be satisfactory. It was found that at low pressures (<100Torr) discharges were initiated with less tendency for a delay while the high pressure limit for discharge formation was extended slightly.

### 5.3.3 Schwinger Coupler

A discharge coupler based on the Schwinger reverse directional coupler was constructed using the design details given in Section 4.2.2. A simplified diagram of the coupler is shown in Fig 5.7. For the sake of simplicity the diagram shows only half of the coupler, the other half being identical except for the coupling slots, and also does not show fixing screws, waveguide joints or the mirror mounting brackets. The main waveguide and bends were constructed from standard waveguide and the auxiliary guide was machined from brass. The lower half of the auxiliary guide was soldered onto the main guide while the upper half was fixed to the lower half by removable screws. The coupling slots were milled in the common wall between the two guides using dimensions derived from Fig 4.5 with the guide dimensions 10.16mm by 22.8mm and the guide wavelength as 44.6mm. Each coupling element is a pair of slots of equal length staggered by a quarter wavelength along the guide. The spacing between elements is three-quarters of a wavelength. Seven coupling elements were used and, in order to give 95% coupling, the total coupling factor was set at 20. The coupling factors, calculated using equations (1) and (2) in Section 4.2.2, were 2.857, 0.7407, 0.4255, 0.2985, 0.2299, 0.1869, and 0.1575. The slot lengths obtained by using these values in Fig 4.5 were (in mm) 23.43, 18.35, 16.58, 15.53, 14.80, 14.25, and 13.80.



A and B - auxiliary guide,

A removable.

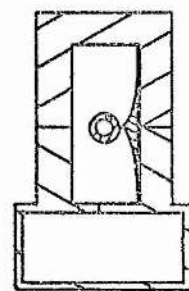
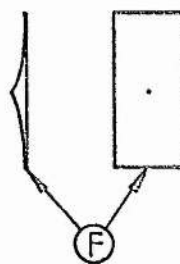
C - mitred bends (details from Harvey 1963).

D - main guide.

E - coupling slots.

F - preioniser, front and side view.

G - section at A-A with discharge tube and preioniser present.



G

full size

Figure 5.7 Schwinger coupler (half view).

The assembled coupler could be used with the Brewster window discharge tube or the mirror mounts, described above. It was connected to the waveguide assembly of Fig 5.4 and used during the final phases of the experimental work.

Without the use of a preioniser, the performance of the Schwinger coupler was similar to the longitudinal coupler in terms of the pressure range over which a discharge could be obtained. When the spike type preioniser shown in Fig 5.7 was introduced the pressure range was extended slightly for the extreme cases. However, for high halogen donor - low buffer gas mixtures, which have a low upper pressure limit for discharge formation, the upper pressure limit was increased considerably by the preioniser. The range of pressure over which high absorption occurred was marginally wider than with the longitudinal coupler. In contrast with the longitudinal coupler, however, the Schwinger coupler required very little retuning, after pressure changes, to maintain high absorption. In comparing the two couplers for uniformity, judged visually, in a pure helium discharge, the Schwinger coupler gave a better performance than the longitudinal coupler, the upper pressure limits for uniformity being about 1.5 atm and 1 atm respectively. At higher pressures, the Schwinger coupler gave a discharge which was divided into seven sections each located in the vicinity of a coupling element. For increasing pressure the loss of uniformity occurred before the high pressure fall in power coupling but nearer to it than with the longitudinal coupler.

This final observation indicates that a further improvement may be possible if the elements of the coupler could be more closely spaced. It is recalled that to obtain directionality and matching in a multi-element coupler the element spacing must be an odd number of wavelengths. Thus the only possibility in this case is to reduce the spacing from three-quarter wavelength to one-quarter wavelength. This would require about 300 elements and a discharge coupling region of over 3m in length for the slots to be short enough to prevent overlapping. Therefore to obtain the benefit of quarter wavelength element spacing, a different design for coupling elements should be sought. Data for round hole elements and 'T' slots are given in 'The Microwave Engineers' Handbook 1962'.

## 6 OTHER APPARATUS

### 6.1 Optical Spectrum Analyser

The production of a large quantity of experimental data during the investigation of excimer molecule formation was made possible by the use of an optical spectrum analyser (OSA) (B & M Spectronic WP1). The complete instrument consisted of a monochromator, vidicon tube camera, and a processing unit with a control panel and cathode-ray tube display. The provision of an X - Y recorder with a time sweep option was all that was required for a fully operational recording system. A Bryans 26000 A4 recorder was used connected directly to terminals on the OSA processing unit.

The monochromator was compact and utilised an arrangement of a plane reflection diffraction grating and a parabolic mirror. Wavelength scanning was by rotation of the grating using a manual sine-drive with a revolution counter to give an approximate reading proportional to wavelength. Furthermore, the grating could be located on the rotation table in one of three angular positions so that three scanning ranges were available. The UV grating used had 2400 lines per mm and was blazed in the range 3000 - 6500 Å. In operation the output slit of the monochromator was removed so that a band of the spectrum under study was resolved at the output focal plane.



The vidicon camera optical detection was by a photodiode array preceded by an image intensifier tube. The camera was attached to the monochromator so that the front surface of the image intensifier was at the monochromator focal plane. As well as giving a high sensitivity, the image intensifier could be used as an electronic shutter. The diode array was 2cm wide which, with the UV grating, collected a spectrum about  $170\text{\AA}$  wide. It contained 20000 diodes arranged in 500 columns, with 400 diodes in each column. An electron scanning system was used to interrogate the diode columns and produce a signal proportional to the optical intensity.

The intensity information from the camera was passed to the processing unit and stored in 500, 16-bit registers, each corresponding to a diode column, and updated about 30 times a second. This set of registers will now be referred to as the real time register with data stored in the 500 'channels'. Two additional memories, memory A and memory B, were provided to allow accumulation of the real time data. The number of accumulation scans could be set on the control panel.

The output and display signals were obtained from a single register via a digital to analogue converter. For any channel the output could be set to give the real time value, either of the memory values, or the difference between the memory values. The screen display consisted of 500 points, representing the 500 channels, which gave the appearance of a continuous intensity - wavelength curve. This was generated by a cyclical transfer of the channel data, in the

real time register or the memories, to the display register.

The Y - terminal of the X - Y recorder output could be set, using the control panel, for any desired channel. In practice a channel was chosen on the peak of the excimer emission which, in conjunction with the recorder time sweep, gave temporal intensity records when the system was set to real time functioning. In memory mode the X - Y recorder could be used to obtain a copy of the spectrum presented in the display. To do this the X - signal was used which gave a voltage proportional to the channel number. An output sweep from channel 1 to channel 500 took about 80 seconds.

The facility for recording two spectra and subtracting them in the display (and chart record) had several uses including the subtraction of a background spectrum and the photodiode dark current from weak spectra and the recording of spectrum changes. The particular OSA used during the experimental work had an excessive dark current signal over the centre of the diode array. Therefore whenever a spectrum was accumulated for a certain number of scans, the dark current signal, with the source switched off, had to be accumulated for the same number of scans and subtracted from the spectrum.

Initial, rough, wavelength calibration of the revolution counter on the monochromator was carried out using small, quartz tube, neon and mercury lamps. However, it was found that the spectra of excimer mixtures which had been subject to several minutes of discharge at pressures below 0.1 atm were rich in silicon lines. These lines are

plentiful throughout the U - V spectral region of interest and were frequently utilised for accurate wavelength determination.

The response time of the OSA - recorder system was assessed by rapidly interrupting an emission giving a real time intensity record. Examination of the recording showed that the characteristic rise and fall times were in the region of 0.3s. This was due mainly to the X - Y recorder response since the OSA output was found to have a slightly faster response than this, of about 0.1s. The observation that the pulsed nature of the source was not apparent in this output, and the fact that the photodiode scanning frequency was 30 scans per second, indicated that accurate averaging and integration of the pulses was taking place.

## 6.2 Gas Handling System

The gas handling system, shown in Fig 6.1, was designed to be flexible in use, maintain high gas purity, and to be compatible with halogen gases. In addition to this the system had to give safe operation at several atmospheres pressure and had to facilitate controlled gas supply and mixing with as little gas wastage as possible. To give halogen compatibility monel pipes, joints, and valves were used with viton tube for flexible connections and viton 'o'-rings used at sealing joints. The other materials in contact with the gas were stainless steel in the pressure gauges, aluminium in the storage tank and the quartz of the discharge tube. The meters and storage tank could be replaced by components with monel

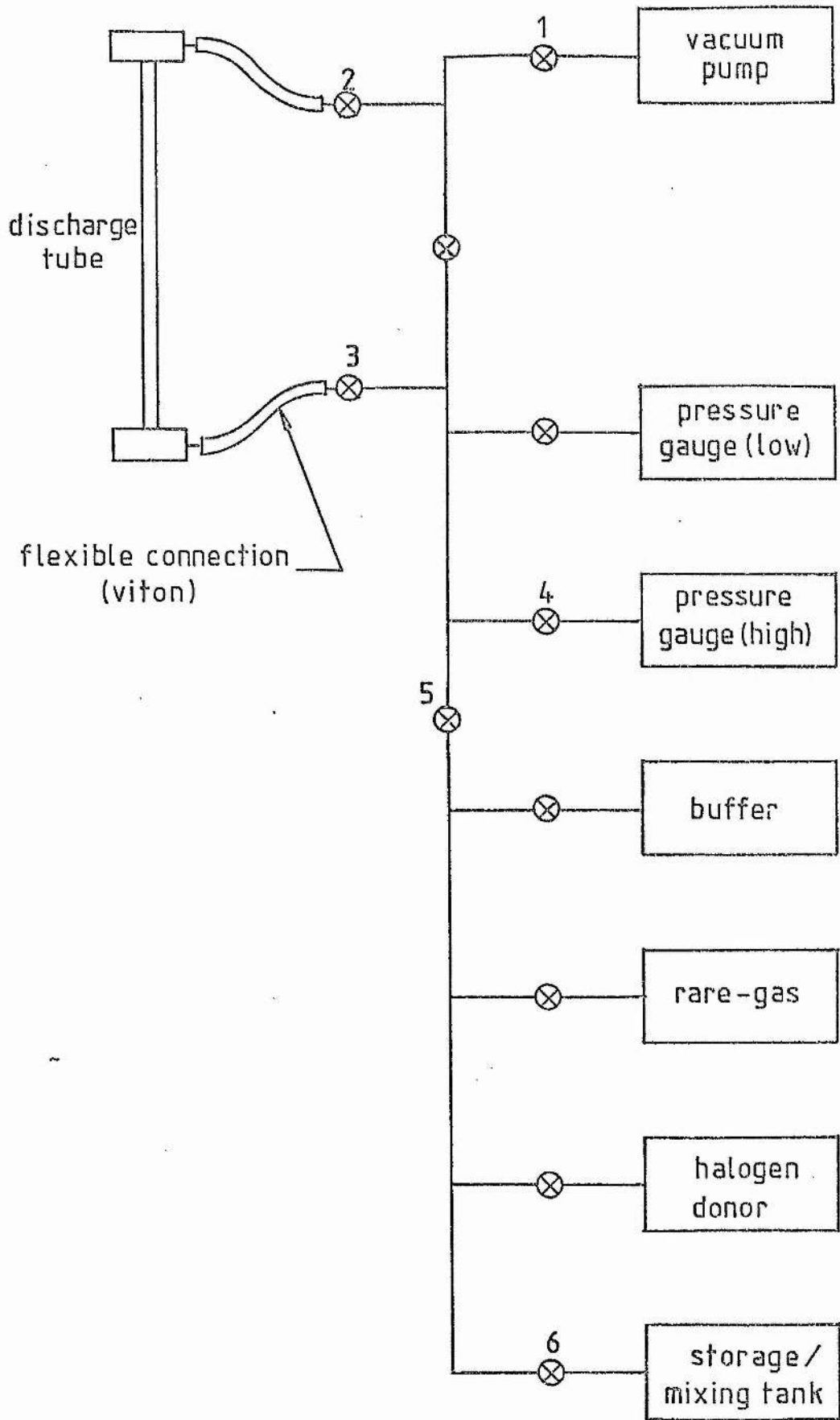


Figure 6.1 Gas handling apparatus

gas - contact surfaces if necessary (if it was required to use fluorine as a donor gas, for example).

Gases were supplied direct from the bottles obtained from suppliers via standard control valves. Mixing was carried out, following a period of degassing, by passing the required quantities of the minority gases into the storage tank using partial pressure indications. The majority gas was then let in, up to the required total pressure, as rapidly as possible. In this way mixing could be ensured by the action of turbulence within the mixing tank.

It was found during experimental work that the section of pipe between the discharge tube and the storage tank was sufficiently long to enable it to be used as a secondary gas store. This allowed an experimental routine to be used that had very little gas wastage. As described in Chapter 7, for a given set of three gases for an excimer mixture (rare-gas, halogen donor, buffer) it was desired to investigate the excimer emission intensity in terms of the full range of mixture ratios and total pressures for which a discharge occurred. For a given mixture ratio a spectrum recording and temporal recording were obtained at about eight pressures in the operational range using the sequence; tube evacuation - fill to new pressure - spectrum recording - tube evacuation - fill to same pressure - temporal recording. It was usually found that the gas stored in the pipework was sufficient for all the measurements for a given mixture if this sequence was used with measurements taken in the order of decreasing pressure. For a given ratio of donor to rare-gas the first mixture tested was always that with least buffer

gas. Since it was generally found that the maximum discharge pressure increased with the buffer fraction, buffer gas could simply be added to the tank between each run to change its fraction in the mixture and no more rare-gas and donor gas were required for the whole experimental run at that particular donor to rare-gas mixture ratio.

It was possible, using the gas handling system, to obtain discharges in flowing gas. This was done by careful adjustment of the valves in Fig 6.1 so that gas flowed from the storage tank, through the discharge tube to the vacuum pump. To achieve this valves 1 and 6 in Fig 6.1 were carefully adjusted with valves 2 - 5 open and the remainder closed. This technique was used simply to increase the recorded intensity of a spectrum that was weak due to a short gas life. It was not used in any of the routine experiments and so no attempts were made to measure the flow rate or pressure in the discharge tube.

### 6.3 Pulse Recording System

The temporal recording system based on the OSA had two major limitations deriving from the long response time in that variations during a single optical pulse and variations between pulses could not be observed on a timescale of less than the OSA response time (0.1s). To make these observations possible a separate system was developed using the same monochromator as before with a fast photomultiplier and a storage oscilloscope. The monochromator was used with its output slit in place and set to pass the peak of the



excimer emission. The discharge apparatus remained undisturbed for the pulse recording experiments.

To record single optical pulses, the fast photomultiplier output was displayed using a Tetronix 7834 storage oscilloscope. In this oscilloscope the signal is transmitted through a delay line between the point at which the trigger signal is obtained and the Y - amplifier. This enables the leading edge of nanosecond risetime pulses to be viewed and therefore internal triggering was satisfactory for recording the optical pulses. However, a variable delay could be applied to the trigger signal so that the displayed pulse could be a chosen number of pulses after the first pulse. In addition to this a second trigger pulse with variable delay is derived from the initial trigger signal and can be used to trigger a second input to the oscilloscope. It was therefore possible to obtain a pair of traces on the oscilloscope storage screen showing two optical pulses, each pulse occurring after a chosen number of pulses had elapsed following the first pulse of the sequence. In the experimental work, records of these pulses were made by taking tracings from the oscilloscope screen.

It was realised that during a typical one second burst of microwave pulses the optical pulse intensity might build up during the first few pulses and be subject to other variations too rapid to be revealed by the OSA system. It was therefore desirable to display a succession of pulses together on the oscilloscope. It was not possible to do this simply by using a slow sweep rate because with a pulse width to pulse interval ratio of 1 : 3000 the pulses became

extremely narrow. Although the vertical lines of the pulses could be recorded quite easily by the oscilloscope storage screen, they were swamped by the base line between pulses. Even with the base line shifted to a position below the screen, internal scattering still saturated the storage screen when sensitivities sufficient for recording the pulses were used. As a consequence of this a system was developed to cause blanking of the oscilloscope trace between pulses.

The control of the Tetrnix oscilloscope blanking was straightforward and required the intensity control to be fully down and a -2V rectangular signal to be fed to the Z - modulation input in coincidence with the pulse to be observed. A Venner TSA628 pulse generator was used to generate this unblanking signal. This device could be triggered externally and adjusted to give a -2V pulse equal in duration to the optical pulse. It was found that the optical signal could not be used to trigger the pulse generator because the inherent delay in the generator caused the unblanking to occur some 100ns too late. Therefore the radar set sync pulse, the earliest pulse in the system, was used together with a delay introduced between the photomultiplier and oscilloscope by means of 20m of 50ohm coaxial cable. The complete system for multiple pulse recording is shown in Fig 6.2

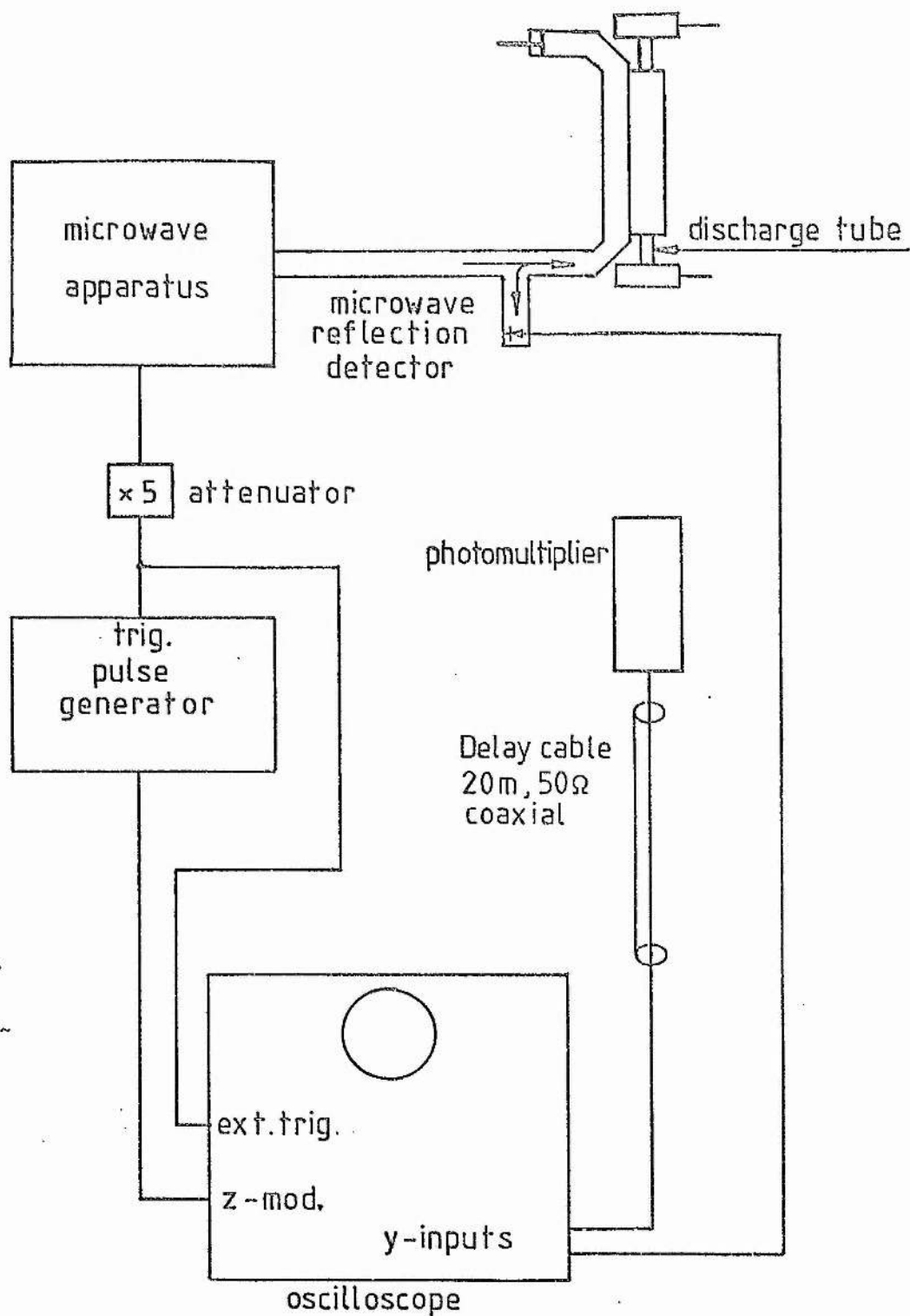


Figure 6.2 Pulse recording system

## 7 EXPERIMENTS

This chapter is concerned with the procedures that enabled results to be obtained using the apparatus described above and with giving the details of the range of the investigations. The raw data from the experiments were in three forms. Firstly the B - X excimer emission bands were obtained on spectrum records approximately  $170\text{\AA}$  wide with linear intensity and wavelength scales. Secondly, time records of the emission peak were obtained on linear intensity and time scales. Since averaging of the 1100pps pulse frequency was inherent in these records, a system with a fast response time (described above) was developed so that single pulse and multiple unaveraged pulse behaviour could be observed. The raw data obtained using this technique were in the form of photographs or tracings of a storage oscilloscope display. Data records, especially the first two types, were obtained for a very wide range of gas mixtures and total pressures during the execution of a lengthy experimental programme. The procedures that were developed allowed this programme to be carried out in a realistic period of time while maintaining consistency of experimental conditions and minimising the use of the expensive gases.

## 7.1 Experimental Methods

### 7.1.1 Intensity vs Time Recording

By setting the OSA recorder output to give the intensity at the maximum point of an excimer B - X spectrum in real time mode, recordings of intensity vs time were obtained which gave the basis for assessments of relative peak fluorescent output and effective gas life in terms of mixture ratio and pressure. To produce these records the X - Y plotter was set for a linear time sweep and triggered by means of a push button just before switching on the microwave source. Scaling of the intensity coordinate could be altered, according to the strength of emission expected, by the plotter gain control and a range facility on the OSA. For cases where saturation of the vidicon camera might occur, glass filters were placed between the discharge tube and the monochromator. The fractional loss introduced by a filter was simply obtained by using the same experimental arrangement but with a slow gas flow in the discharge tube giving a constant optical output. The loss was found by inserting the filter during the X-Y recorder sweep in order to produce a step in the record. The linearity of the vidicon response allowed the fractional fall in intensity shown in the record to be taken as the fractional loss introduced by the filter.

Two routines were used for gas replacement during experiments yielding intensity vs time records:

Method 1 Following preparation of the current gas mixture and evacuation of the discharge tube and pipe network, a first sample was let into the discharge tube. The microwave source was then switched on and optimum tuning set for the highest pressure at which a discharge could be struck. The discharge tube was then evacuated, refilled with fresh gas to the same pressure, and temporal intensity recording initiated. The system was then left undisturbed until the intensity had fallen by about 70%, at which point the pressure was reduced by an increment as rapidly as possible using the gas tap between the discharge tube and the vacuum pump. This process was repeated until extinction of the discharge occurred. If at any time an increase in the reflected microwave signal occurred, the E - H tuner was readjusted for optimum tuning before the next pressure step. As has been mentioned earlier, sufficient gas for a run such as this was usually present in the pipework between the discharge tube and the storage tank.

Examples of records obtained by this technique are shown in Fig 7.1. Each time the total pressure is reduced, which gives simultaneous gas replacement, a new intensity peak results. The rising edge of the peaks occur during the pressure change which was generally rapid at first but slower as the new pressure was approached. The falling edges of the peaks occur at the constant pressures indicated on the horizontal(time) axis and reveal the gas life. It can be seen that for a given mixture ratio peak intensity



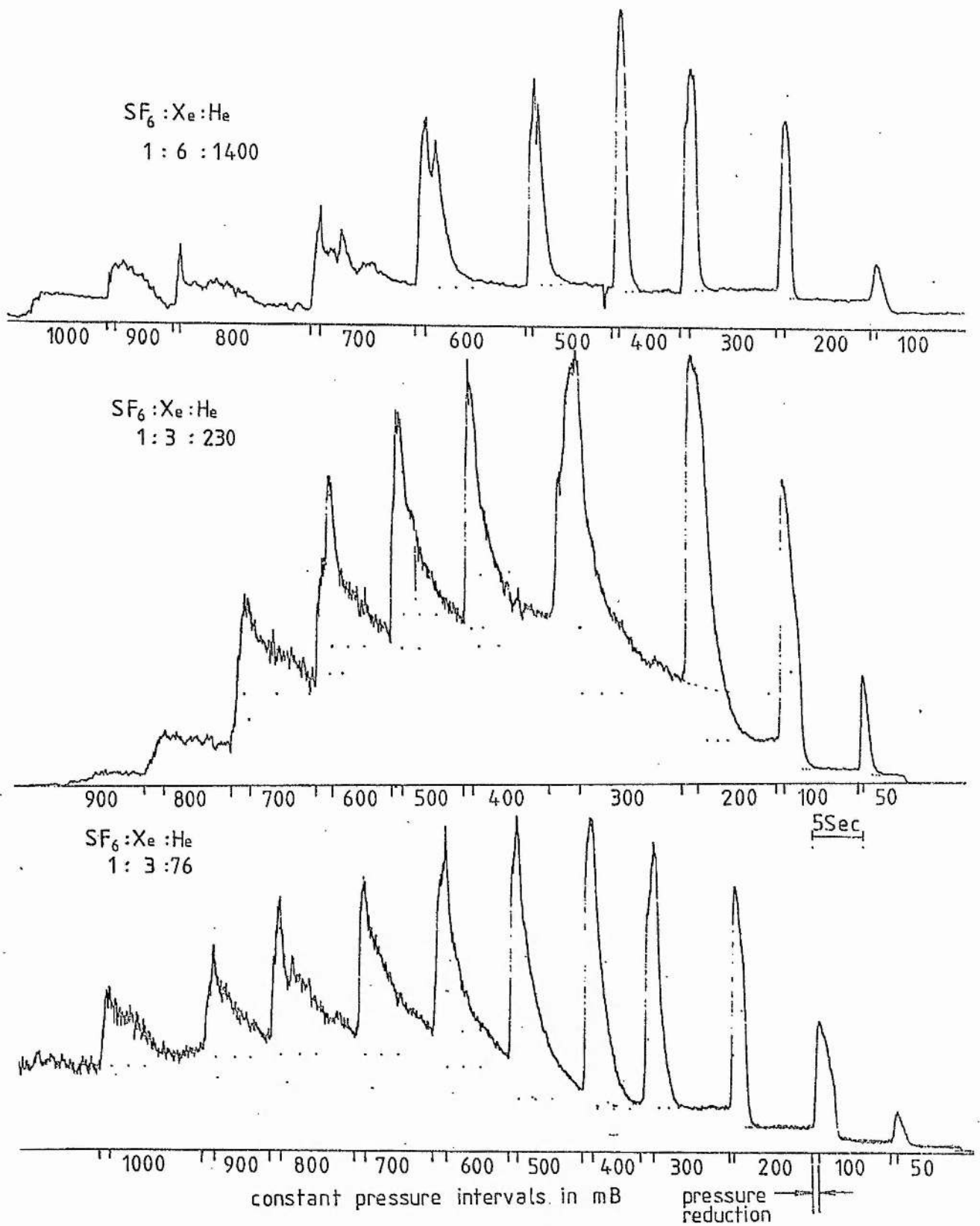


Figure 7.1 Temporal records by method 1

vs total pressure curves can be drawn immediately. It can also be seen that gas life increases with total pressure but in these cases quantification is difficult due to complexities in the curve shapes in the regions of falling intensity. These results clearly demonstrate a major difficulty with method 1 in that gas lives equal to or less than the time required for pressure changes (1 - 1.5 s) are present at the lower pressures. Under these conditions gas will be effectively used up during its passage into the discharge tube, effectively reducing the peak value obtainable. While this method was used for all the XeF experiments, a different technique (method 2) was evolved and used for all remaining experiments.

Method 2 In this method an entirely fresh gas sample was used at each pressure and the microwave source was switched off during pressure changes. An intensity - time plot was obtained at about eight different pressures for a given mixture ratio using the following routine.

1. Gas placed in tube to maximum discharge pressure, tuning optimised.
2. Tube evacuated and allowed to cool, refilled to maximum pressure.
3. Chart recorder sweep on, microwave source on, microwave source off after about 70% fall in optical output.
4. Tube evacuated, fresh gas introduced to new pressure, coupling retuned, tube evacuated and allowed to cool.
5. Gas replaced to new pressure.

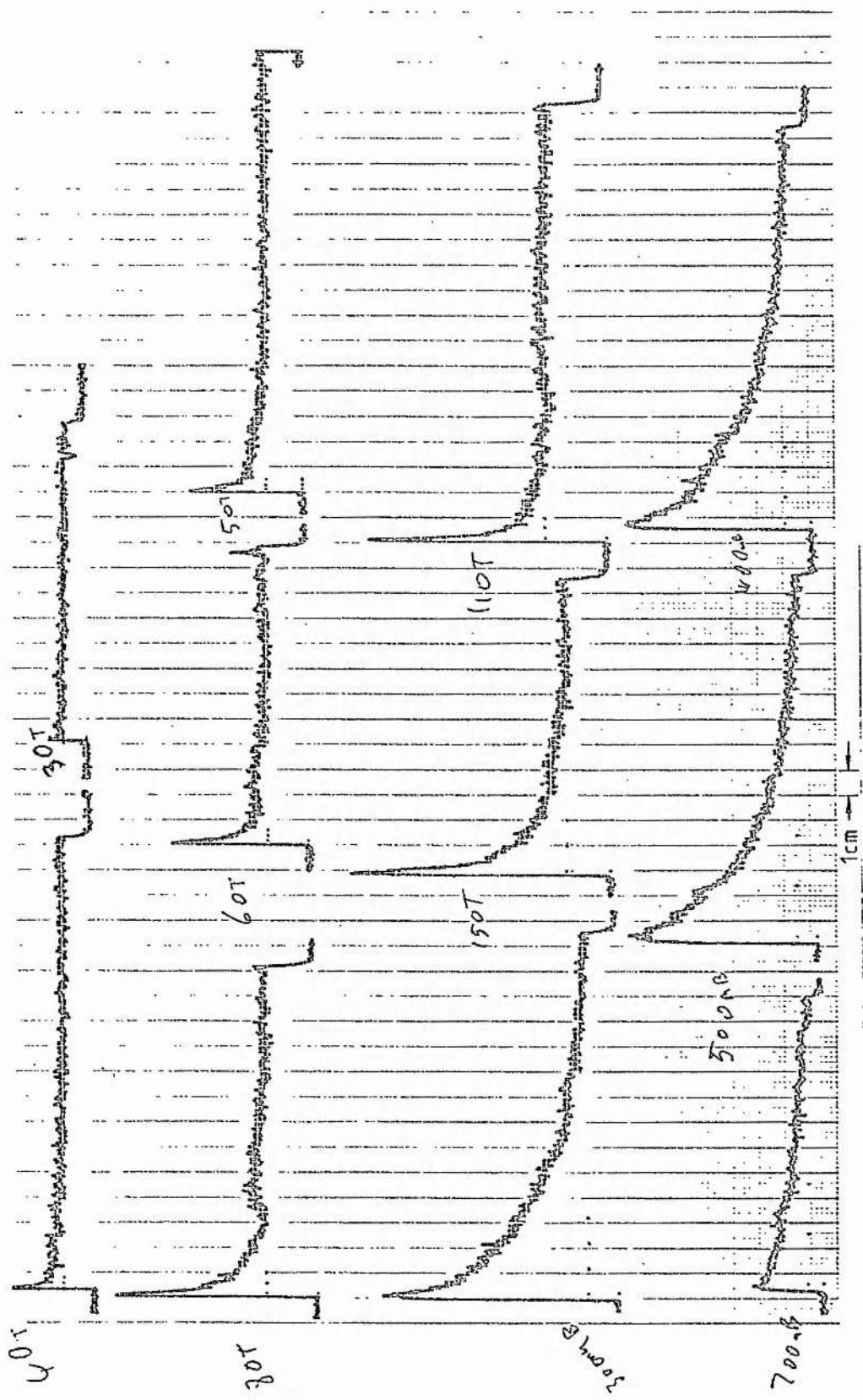
[Routine continued from step 3.]

This method provided greater consistency of conditions than method 1 but was much more time consuming and used a greater quantity of gas for each result. Examples of records using method 2 appear in Fig

7.2. In this case intensity/time records were obtained at eleven total pressures for the mixture indicated. Each record shows the characteristic rapid rise to a maximum intensity at the initiation of the discharge and the subsequent decay (perhaps to a constant level) from which gas life measurements were obtained.

### 7.1.2 Spectrum Recording

Spectrum records were obtained using the OSA for several purposes. Primarily a spectrum was obtained for every gas mixture and pressure that was used in the temporal recording experiments. In every case care was taken to ensure that fresh gas was used, that the discharge tube had cooled, and that tuning was optimum. The OSA was used in memory mode so that the spectrum was accumulated over a number of internal data transfer cycles. The number of cycles (scans) chosen was such that the microwave source could be switched on and off within the period during which accumulation was taking place. For the main bulk of the experimental work, spectra were obtained during a one second burst from the microwave source using the monostable switch described in Section 5.2.1. Therefore, the recorded spectra represented the integrated spectra of 1100 pulses. These recordings could then be used as an alternative method for relating intensity to mixture ratio and pressure but only for the cases where gas lifetimes were known to be considerably greater than one second. However, the main purpose in obtaining the spectrum records was to find if variations occurred in the intensity distribution of the spectra and to demonstrate how the variations



SF<sub>6</sub>:Kr:Ne 1:3:30 TIME → 5sec cm<sup>-1</sup> INTENSITY (arbitrary units)

Figure 7.2 Temporal records by method 2.

depended on buffer gas type and total pressure.

In addition to the records obtained during the main experimental programme, spectra were obtained at the outset of the investigation of any particular excimer molecule for the purposes of identification and to identify the OSA data channel lying nearest to the spectrum peak. The other outstanding reason for obtaining spectrum records occurred during the attempts to obtain lasing described below. In both of these cases the number of accumulation scans was set to encompass the operational period of the discharge which was set to a variety of values depending on the requirements.

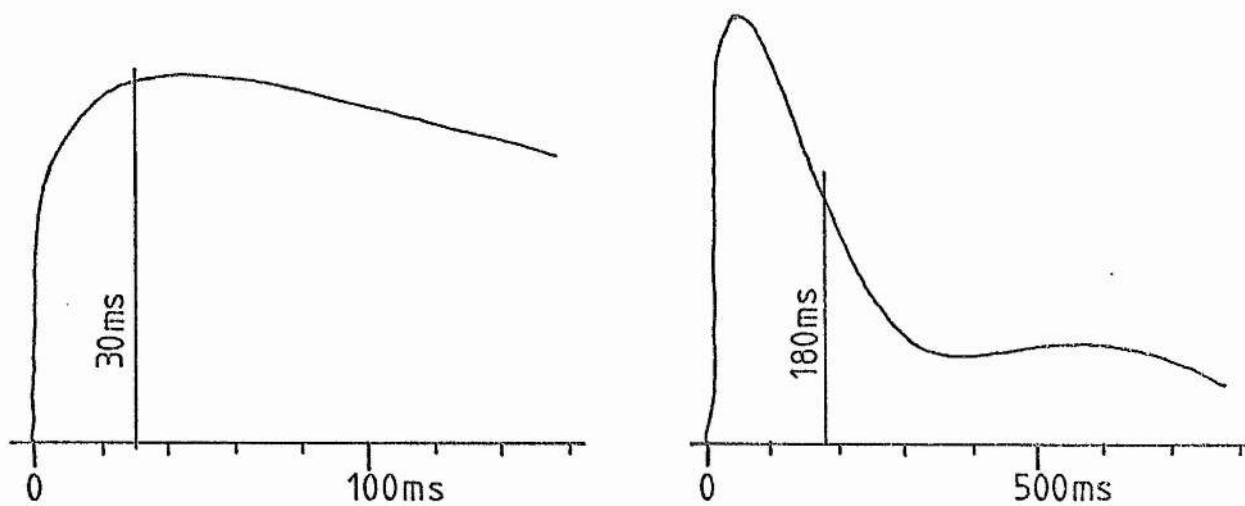
### 7.1.3 Pulse Recording

The pulse recording apparatus was devised so that variations within single optical pulses could be displayed and to record any pulse-to-pulse variations that were too rapid to be detected by the OSA system. In addition it was found that corresponding optical and microwave reflection pulses could be obtained for consecutive gas samples of the same mixture and pressure. The reflected microwave pulse was recorded so that correlations between the temporal behaviour of the optical pulse and microwave pulse could be revealed. These recordings also allowed a check to be kept on the overall efficiency of the tuning for each optical pulse record. Results were obtained using the pulse recording system for the same mixtures and pressures used in a small fraction of the KrF experiments as indicated in Section 7.2 below. The gas handling

procedures were as described for method 2 above.

Some examples from the pulse recording technique are shown in Fig 7.3. This figure was produced by taking the original oscilloscope screen tracings, which were on acetate, and retracing them and adding the scales in detail. During the retracing the optical and microwave reflection pulses were superimposed since they were obtained on the same time scale. To obtain this set of records four samples of fresh gas were required. The first two samples were used to obtain the optical pulse amplitude envelopes, shown in (a), which differ only in the time base setting. In the 20ms/div trace the closely spaced vertical lines of the individual pulses were discernable on the oscilloscope screen but were not copied onto the record. With the time base set at 100ms/div, individual pulses were not discernable and the area under the curve was uniformly bright. The third gas sample was used to produce the two optical pulse records using the oscilloscope dual beam facility. The oscilloscope was set so that the first optical pulse was recorded after a 30ms delay from the first discharge pulse. The second pulse was recorded after a 180ms delay from the first discharge pulse. Since the pulse rate is 1100 per second, the two recorded pulses represent the 33rd and 198th pulses of the train of pulses. The positions of the selected pulses are shown on the pulse envelope records. The microwave reflection records were obtained with the fourth gas sample using the same method as that used for the two optical pulse records simply by connecting the signal cable from the detection diode in place of the photomultiplier cable.

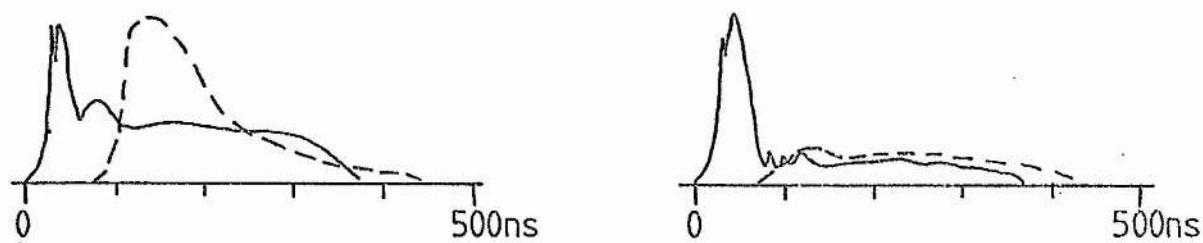




(a) Pulse amplitude envelopes

20ms/div

100ms/div



(b) Single pulses. - - - - optical, ——— microwave reflection

Delay 30ms (ie. 33rd pulse)

Delay 180ms (ie. 198th pulse)

All records  $\text{NF}_3 : \text{Kr} \quad 1:3$ , total pressure 30 Torr

↑ Intensity      — Time

Figure 7.3 Examples of pulse records.

## 7.2 Experimental Programme

The experimental work consisted of preliminary development followed by the execution of an extensive programme in which the main body of data were collected. Although this programme took the form of a sequential routine in which each excimer was studied in turn, it will be more useful to classify the experimentation in terms appropriate to the presentation of data rather than adhere to the chronology of the work. Therefore the experiments are divided into three broad sections; spectrum identification, investigation of mixture ratios and pressures, and various miscellaneous experiments. This breakdown is shown in Table 7.1 which also indicates the methods used and the main experimental variables. Table 7.2 presents the full range of mixture ratios that were tested and the approximate pressure range for which a discharge was obtained for each mixture.

EXPERIMENT	METHOD
<u>Spectrum identification</u> $X_eF$ $K_rF$ $ArF$ $X_eCl$ $K_rCl$ $ArCl$ [not found] $X_eO$	As in Section 7.1.2 or similar.
<u>Experimental programme  for mixture ratios and  total pressure(see Table 7.2)</u> $X_eF$	Spectra - 7.1.2 , intensity vs time -method 1 in 7.1.1,pulse records 7.1.3.(5 mixtures).
$K_rF$	7.1.2 ,method 2 in 7.1.1, 7.1.3(3 mixtures).
$X_eCl$	7.1.2 ,method.1-7.1.1.
$ArF$ (weak spectra only)	
$K_rCl$ 2 mixtures	7.1.2
<u>Variables</u> Buffer and donor type ,mixture ratio, total pressure.	
<u>Miscellaneous</u> 1.Lasing attempts in $X_eF$ , $K_rF$ , and $X_eCl$ . 2.High and low pressure spectra in $K_rF$ . 3.Comparison of two tube diameters , $K_rF$ . 4. Effect of tube cooling, $K_rF$ .	7.1.2 ,method 1-7.1.1.  7.1.1

Table 7.1 Principal classification of experiments.

	DONOR		BUFFER			$P_L$	$P_H$	DONOR		BUFFER			$P_L$	$P_H$	
	SF <sub>6</sub>	NF <sub>3</sub>	GAS	He	Ne			Ar	SF <sub>6</sub>	NF <sub>3</sub>	GAS	He			Ne
	KrF						XeF								
1	1		1			26	200	P1	1	6	460		50	900	50
2	1		1	1		13	220	1		6	1400		50	1000	51
3	1		1	5		13	220	1		6	3000		50	900	52
4	1		1	33		40	400	1		3	76		50	500	53
5	1		1	100		50	700	1		3	230		50	800	54
6	1		1	500		500	1200	1		3	680		50	1100	55
7	1		3			7	210	P1	1	0.75	57		50	800	56
8	1		3	4		13	300	1		0.75	170		50	1000	57
9	1		3	16		26	500	P1	1	3		76	50	900	58
10	P1		3	100		200	800	1		3		230	50	1200	59
11	1		3	500		500	1000	P1	1	3		76	50	900	60
12	1		3	1000		400	1400	P1	1	3		230	50	800	61
13	1		10			13	240	P1	1	3	76		50	1000	62
14	1		10	10		66	500		1	3	680		50	500	63
15	1		10	30		66	700		1	3		76	50	600	64
16	1		10	100		300	1200		1	3		230	50	1000	65
17	1		10	300		600	1000	HCl	XeCl						
18	1		30			13	260	1		0.5			13	110	66
19	1		30	30		26	400	1		1			13	200	67
20	1		30	100		80	500	1		3			7	210	68
21	1		30	300		130	600	1		10			7	120	69
22	1		30	1000		400	1400	1		30			7	120	70
23	1		30	2000		500	1300	1		100			7	79	71
24	1		100			26	400	1		300			7	79	72
25	1		100	100		53	500	1		3	100		100	350	73
26	1		100	300		110	500	1		3	300		200	800	74
27	1		100	1000		200	1300	1		3	1000		100	800	75
28		1	0.5			13	79	1		20	200		100	900	76
29		1	1			26	66	1		20	1000		100	1000	77
30	P1		1	3		40	110	1		20	2000		300	1100	78
31		1	10			40	180	1		100			40	120	79
32		1	30			13	250	1		100	100		66	170	80
33		1	100			26	300	1		100	300		100	300	81
34		1	300			26	400	1		100	1000		100	900	82
35	P1		1	3	100	100	800	1		20		80	100	900	83
36	P1		3	100		100	1000	SF <sub>6</sub>	NF <sub>3</sub>	ArF					
37	1		3			13	170		1	30		30			84
38	1		3			3	13	210		1	30		60		85
39	1		3			10	13	250	1		3	250			86
40	1		3			30	40	300	1		100				87
41	1		3			13	170	1		100	100				88
42	1		3		3	13	250	1		100	200				89
43	1		3		10	26	500	1		30					90
44	1		3		30	40	900	1		30					91
45	1		3		100	110	1300		1	30					92
46	1		3		300	300	1500	HCl	KrCl						
47	1		3		1000	400	1700	1		50	1000				93
48	1		3			7	180	1		50	3000				94
49	1		3		100	200	1000	P1-Also used in pulse experiments							

$P_L, P_H$  - Lowest, highest pressures of discharge in mB.

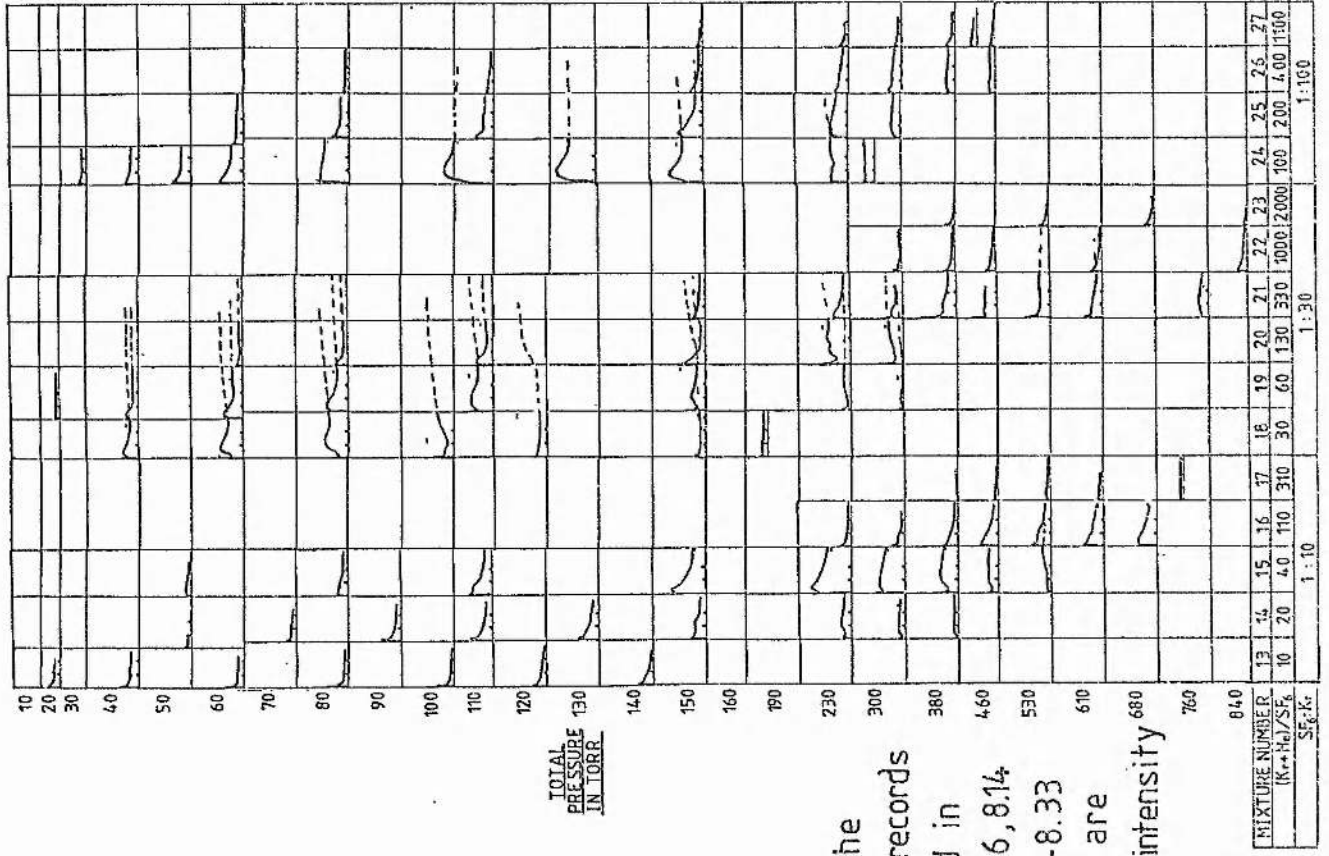
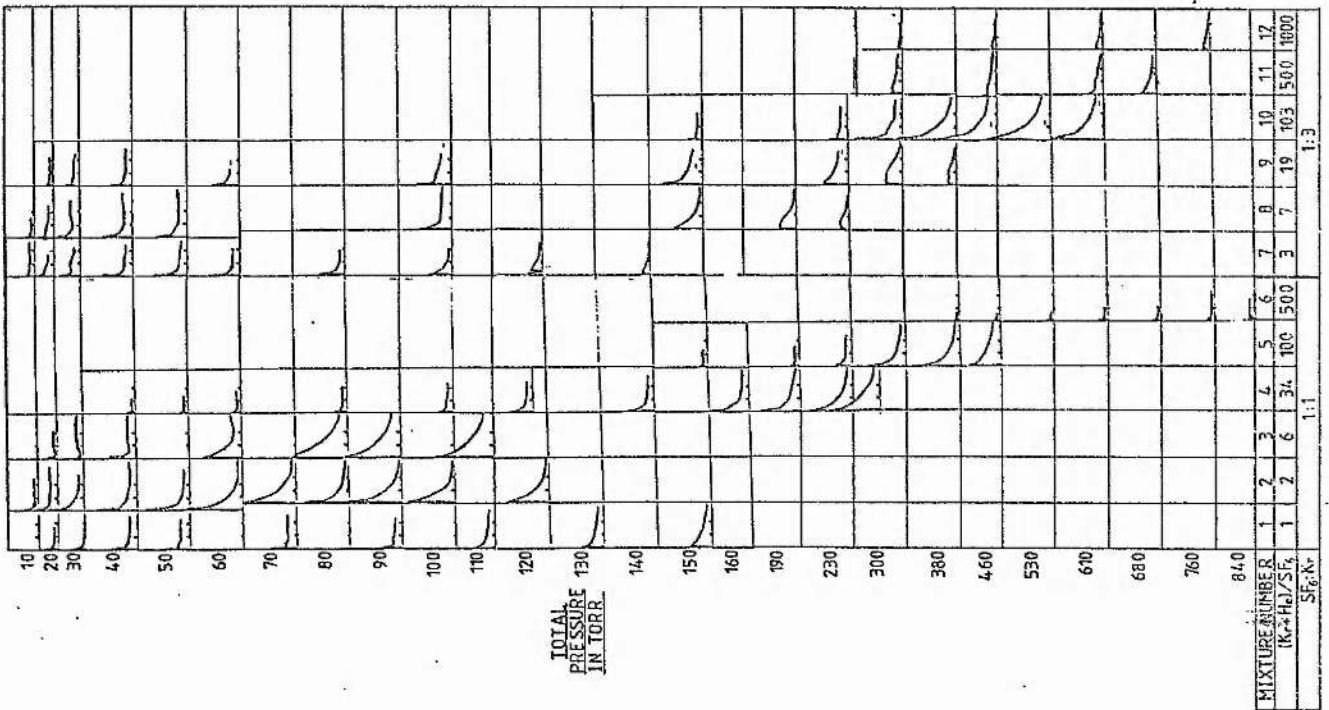
Table 7.2 Experimental programme - mixture ratios and pressure ranges.

## 8 RESULTS

The results appearing in the figures of this chapter are either traced copies of the raw data or graphs produced from measurements taken from the raw data. They are presented first on an empirical basis giving as much of the data as possible in a condensed form. Following this is a series of sections in which the data are selected from the raw results according to various analytical topics. Each section contains a discussion of the outstanding features of the graphs presented.

### 8.1 Empirical Presentation of Results

The data shown in Figs 8.1 to 8.6 are tracings of the intensity vs time records for nearly all of the KrF mixtures (1-47 in Table 7.2). In all of these figures the recordings are arranged in vertical columns of increasing total pressure with a constant mixture ratio within each column. Figures 8.2(a) and 8.2(b) are the same as Fig 8.1 but on a larger scale. These results are for SF<sub>6</sub>:Kr:He mixtures number 1 to 27. The 27 mixtures (columns) are placed in five groups, each group having a particular SF<sub>6</sub>:Kr ratio. Within each group the columns are in order of increasing dilution described by the partial pressure ratio of the total rare-gas content to the SF<sub>6</sub> content.



**Note**  
 In all of the individual records contained in Figs 8.1-8.6, 8.14-8.17, 8.30-8.33 the axes are relative intensity vs time

Figure 8.1 KrF intensity vs time records, SF<sub>6</sub>:Kr:He mixtures (1-27 in Table 7.2) reduced by 0.09. Time scale 10 sec per division.



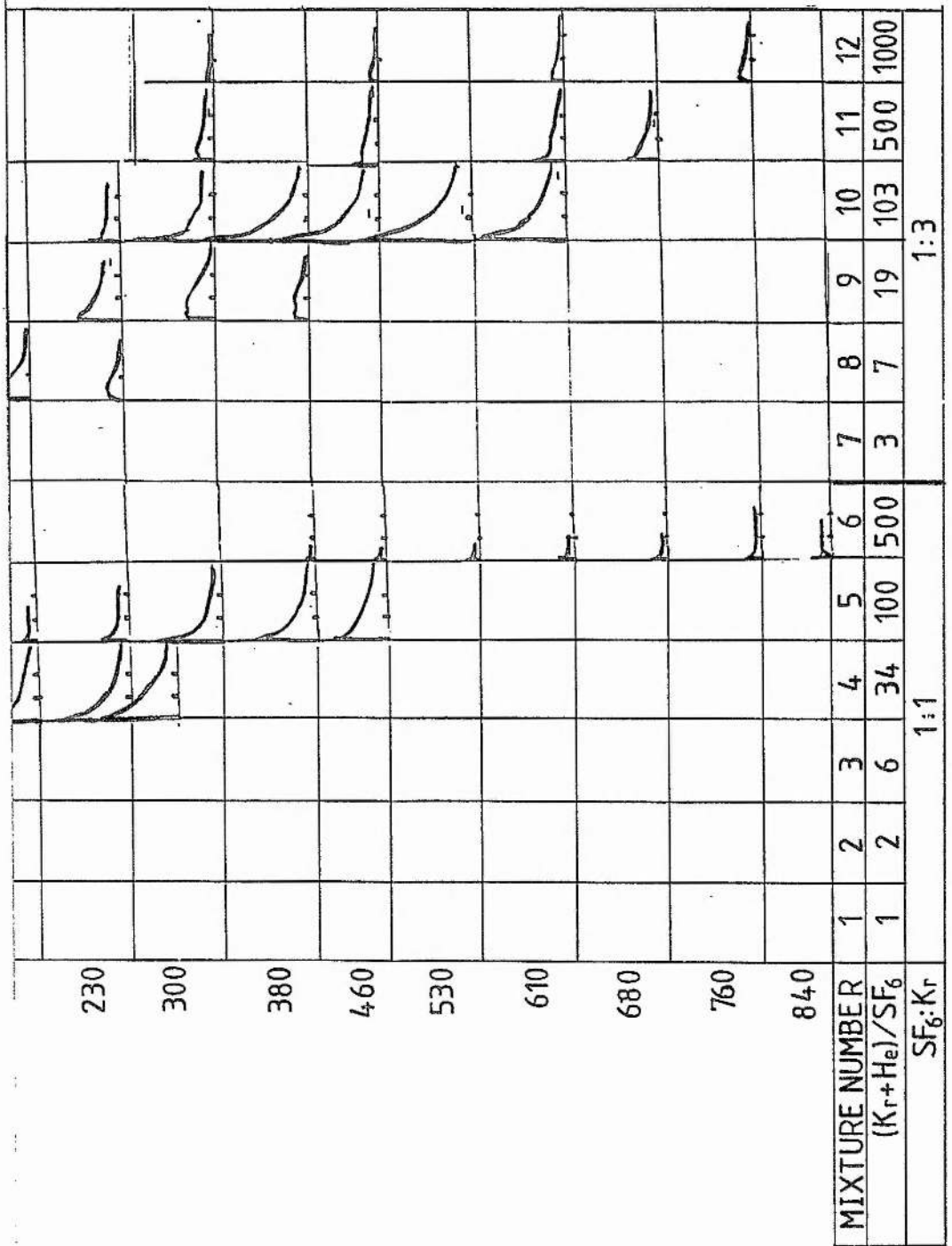


Figure 8.2 (a) As Fig.8.1, 0.18 reduction  
(continued in Fig.8.2 (b)).

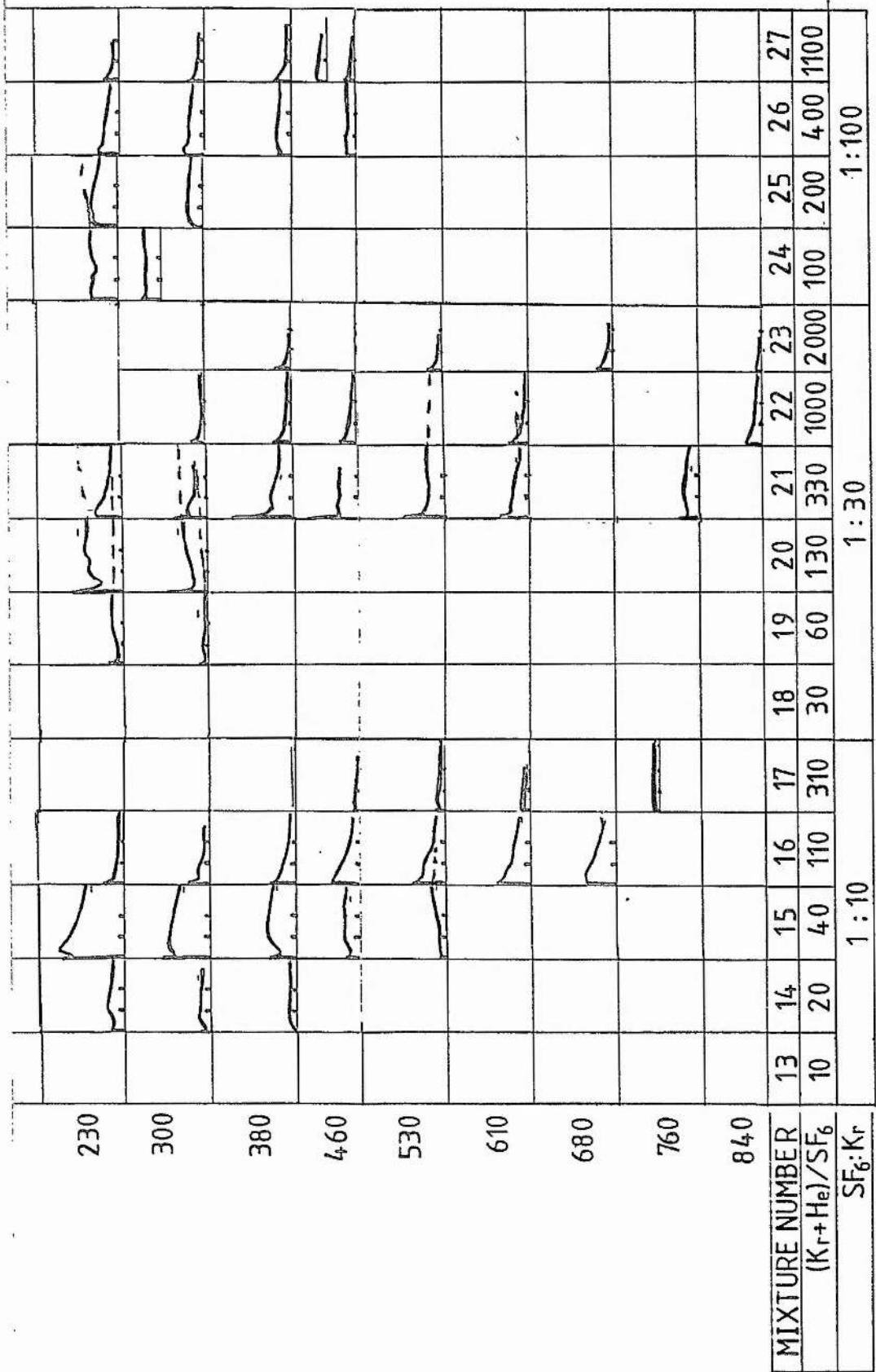


Figure 8.2 (b)



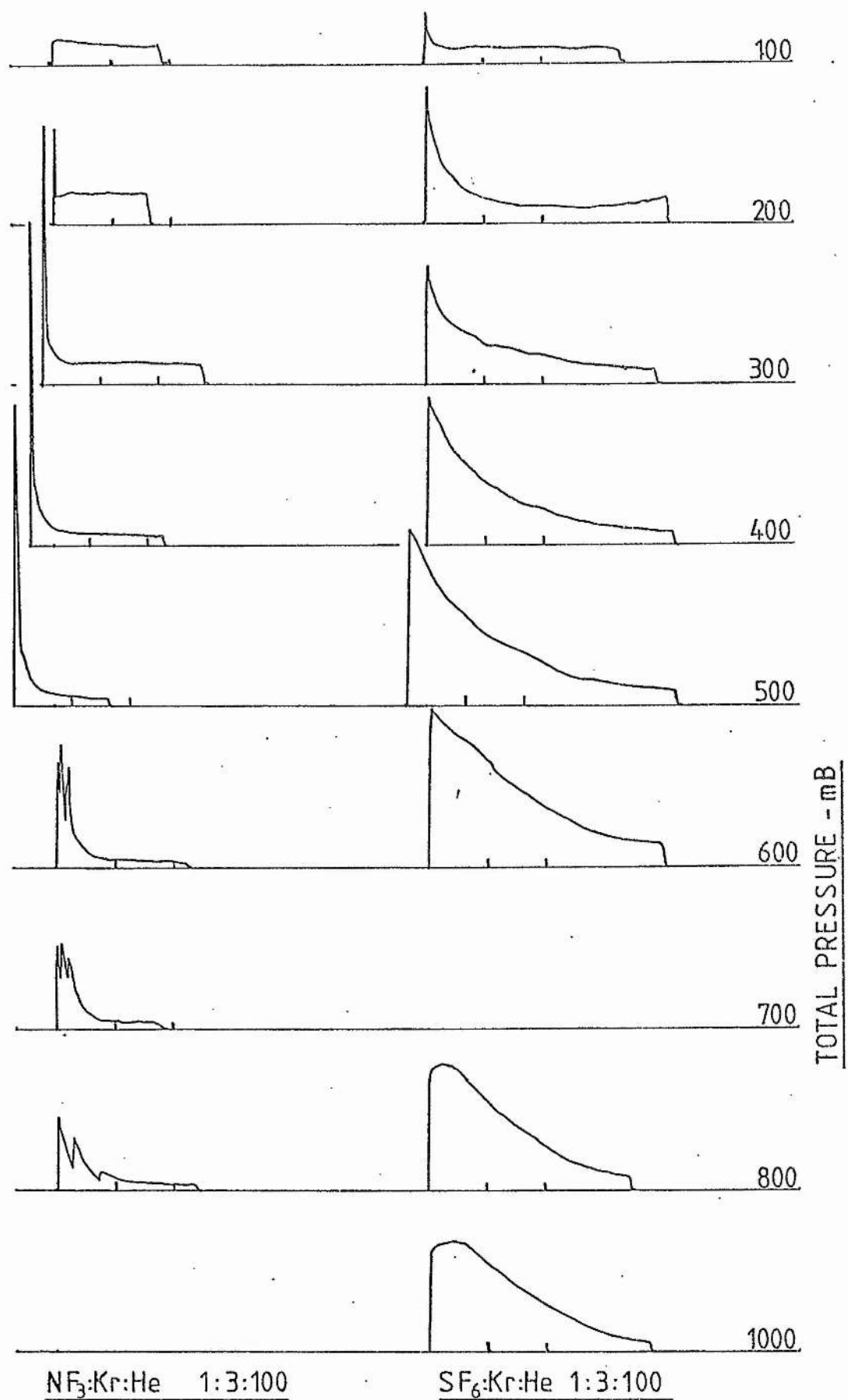
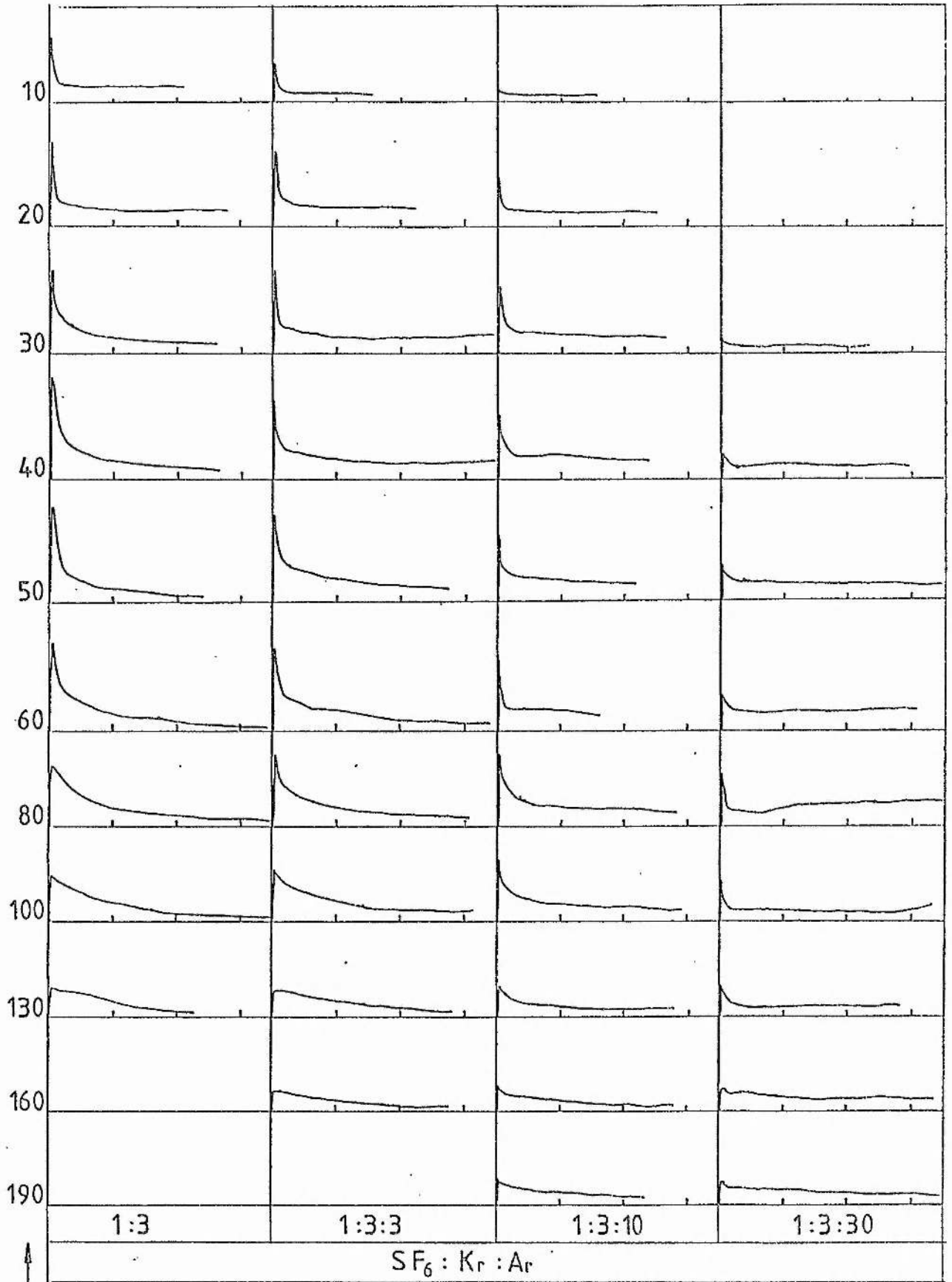


Figure 8.4 KrF Intensity vs time records, donor comparison (35,36).  
10 sec per division.



TOTAL PRESSURE - TORR

Figure 8.5 KrF Intensity vs time, Ar buffer (37-40). 10sec per div.

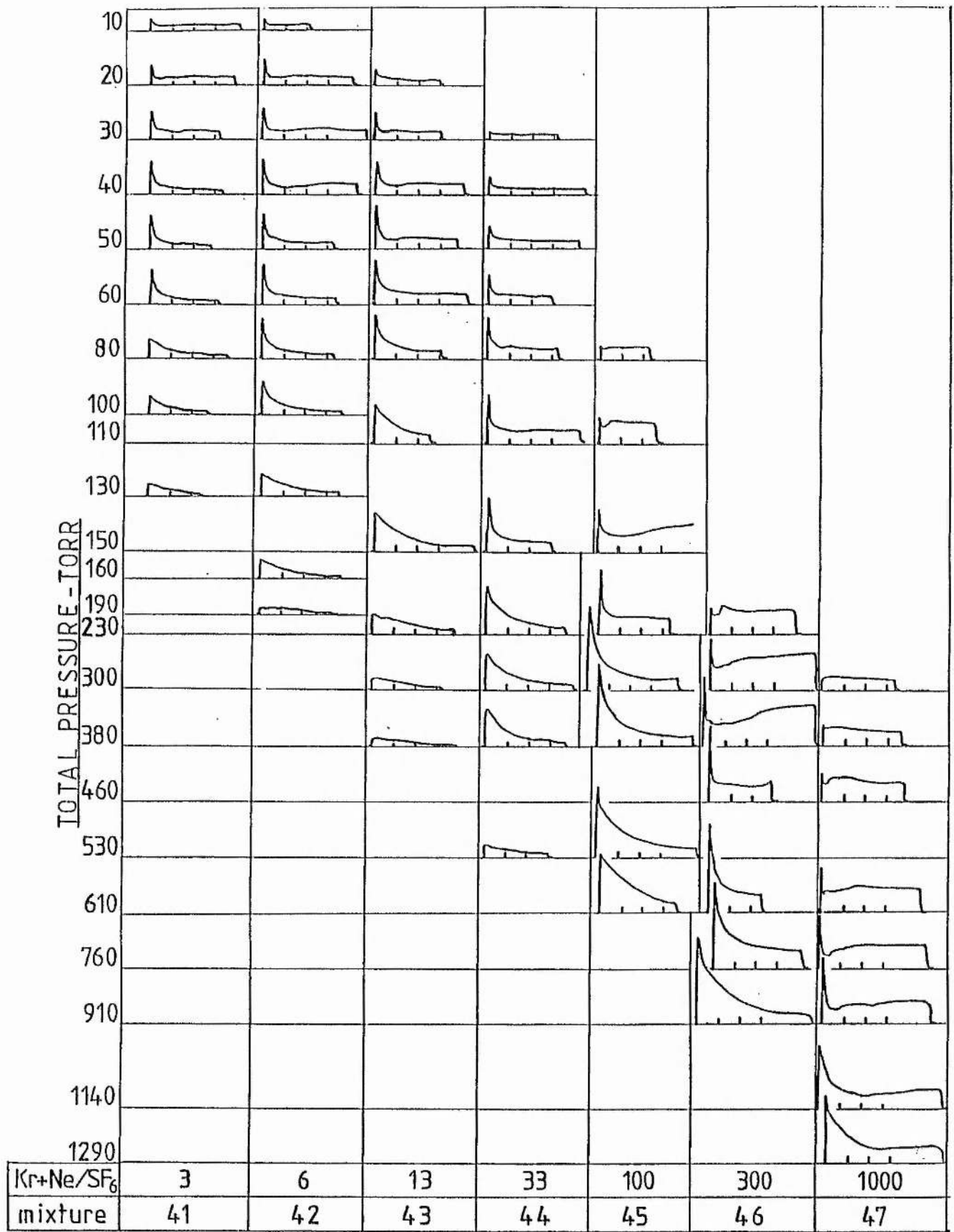


Figure 8.6 KrF Intensity vs time records, Ne buffer. (41-47).  
10 sec per division.



Figure 8.3 contains the records for the binary  $\text{NF}_3$ :Kr mixtures (28-34) with columns arranged in the order of increasing dilution. Figure 8.4 shows the records for the two mixtures (35-36) where  $\text{SF}_6$  is compared with  $\text{NF}_3$ . Records for the mixtures of  $\text{SF}_6$ :Kr:Ar (37-40) are shown in Fig 8.5 where the  $\text{SF}_6$ :Kr ratio was constant at 1:3 and the columns are in order of increasing dilution. The records shown in Fig 8.6 are similar to those of Fig 8.5 only here the buffer gas is Ne.

The data shown in Figs 8.7 to 8.13 were obtained from peak intensity and intensity half life measurements of the raw data as described in Table 8.1. The appropriate methods and mixture ratios can be found in Tables 7.1 and 7.2. Figures 8.14 to 8.17 show the results obtained using the pulse recording system and are copies of the raw data. Tables 8.1, 7.1, and 7.2 give the details of these records.

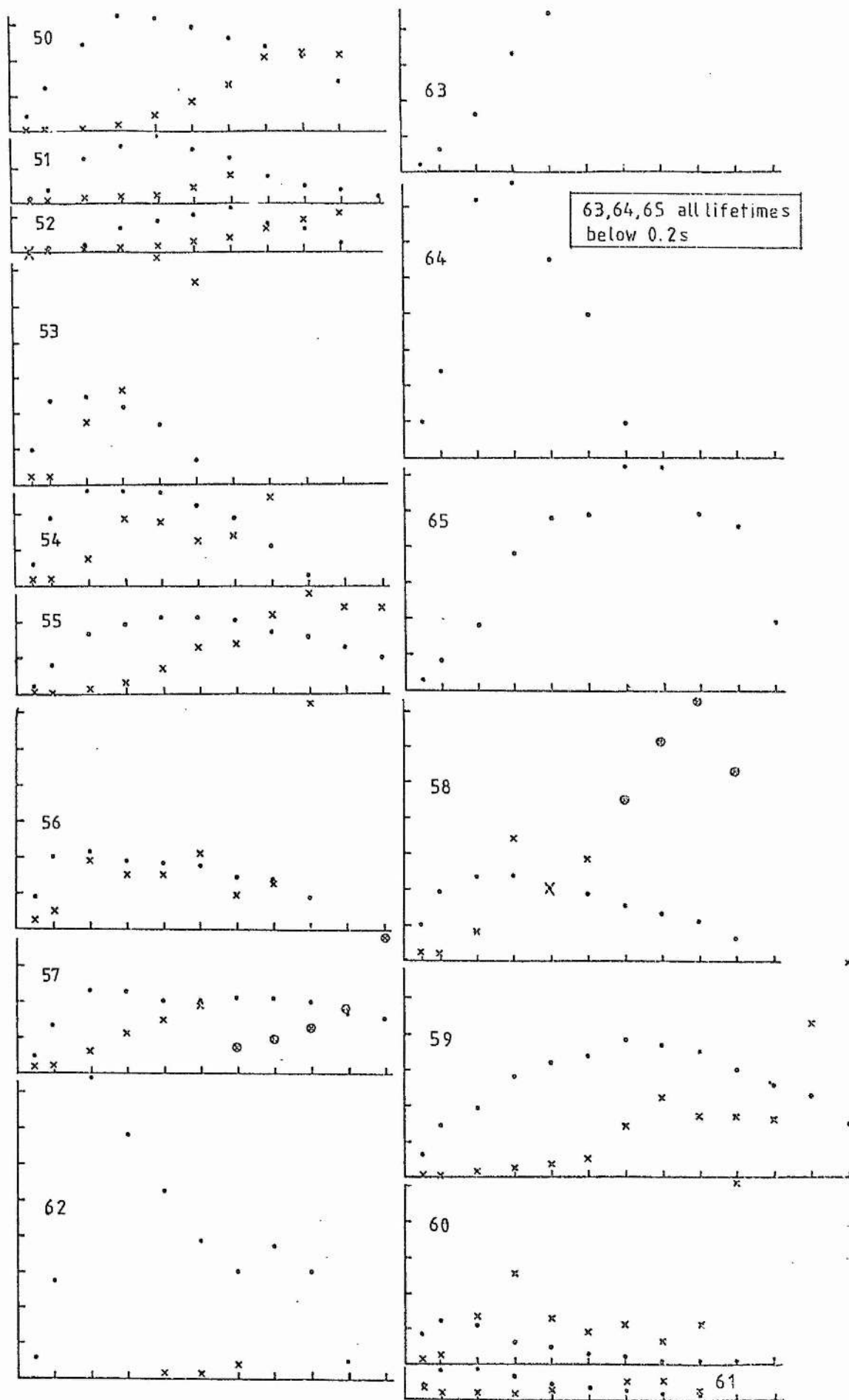


Figure 8.7 Empirical presentation,  $X_{eF}$ . Explanation - Table 8.1 and 7.2.

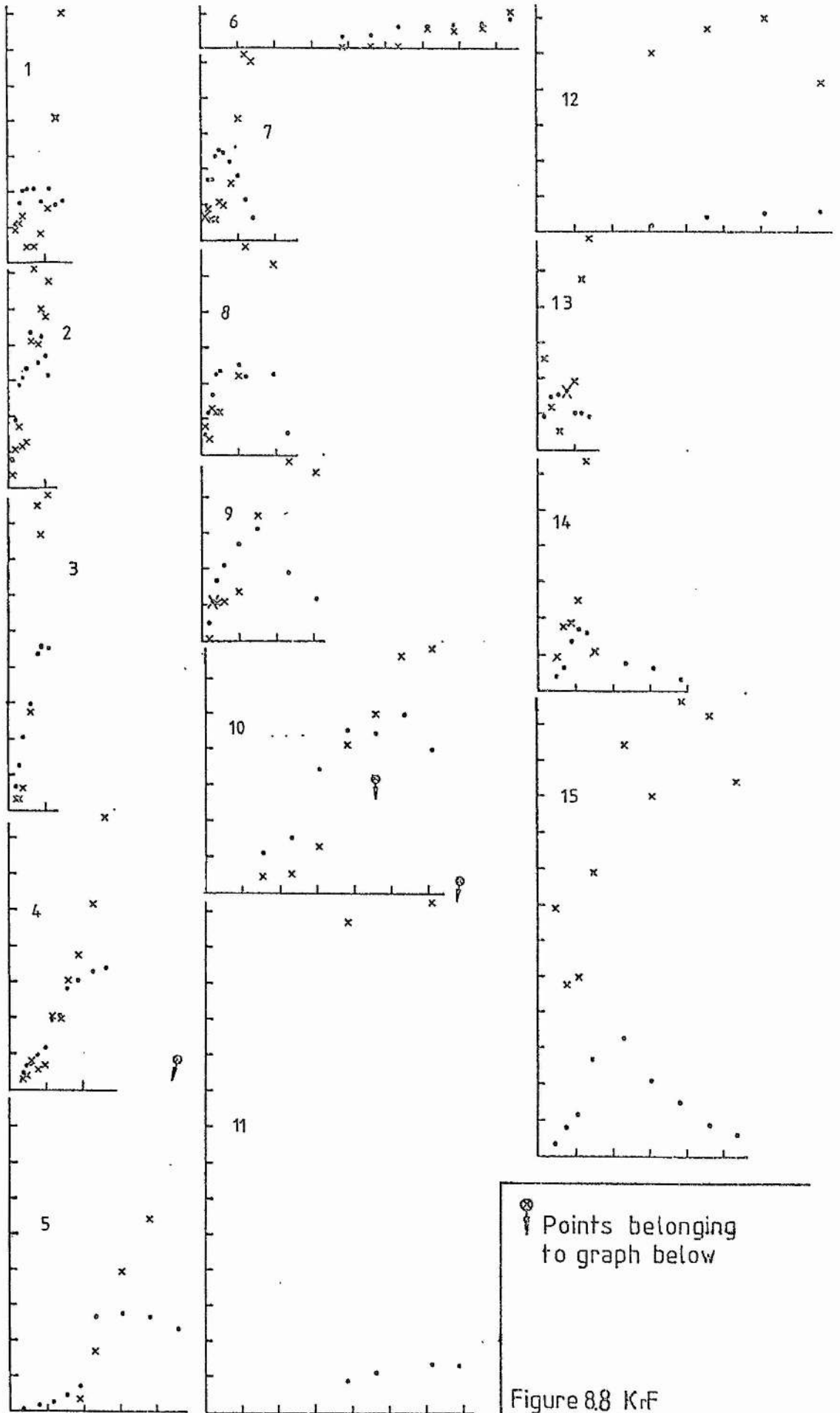


Figure 8.8 KrF

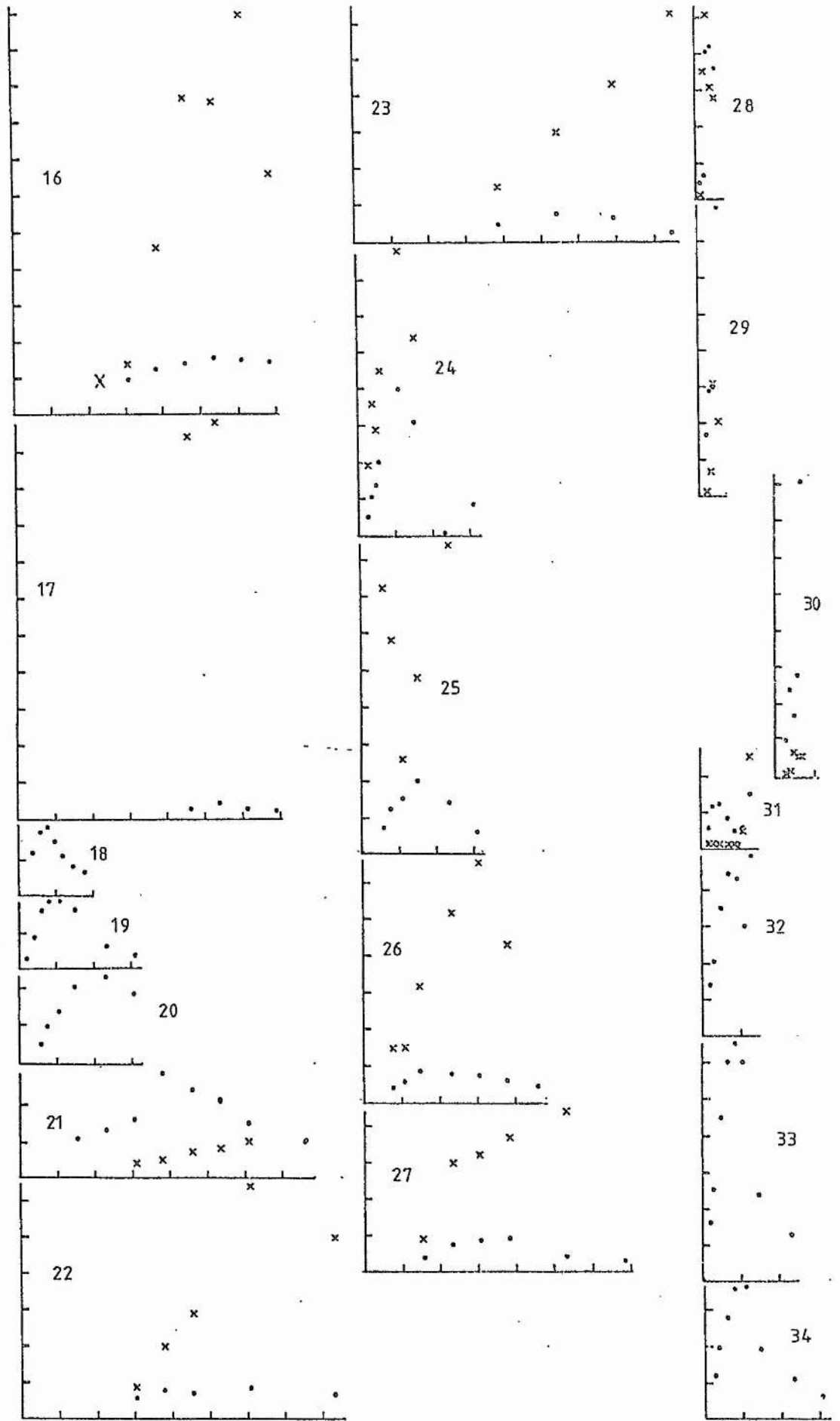


Figure 8.9 KrF

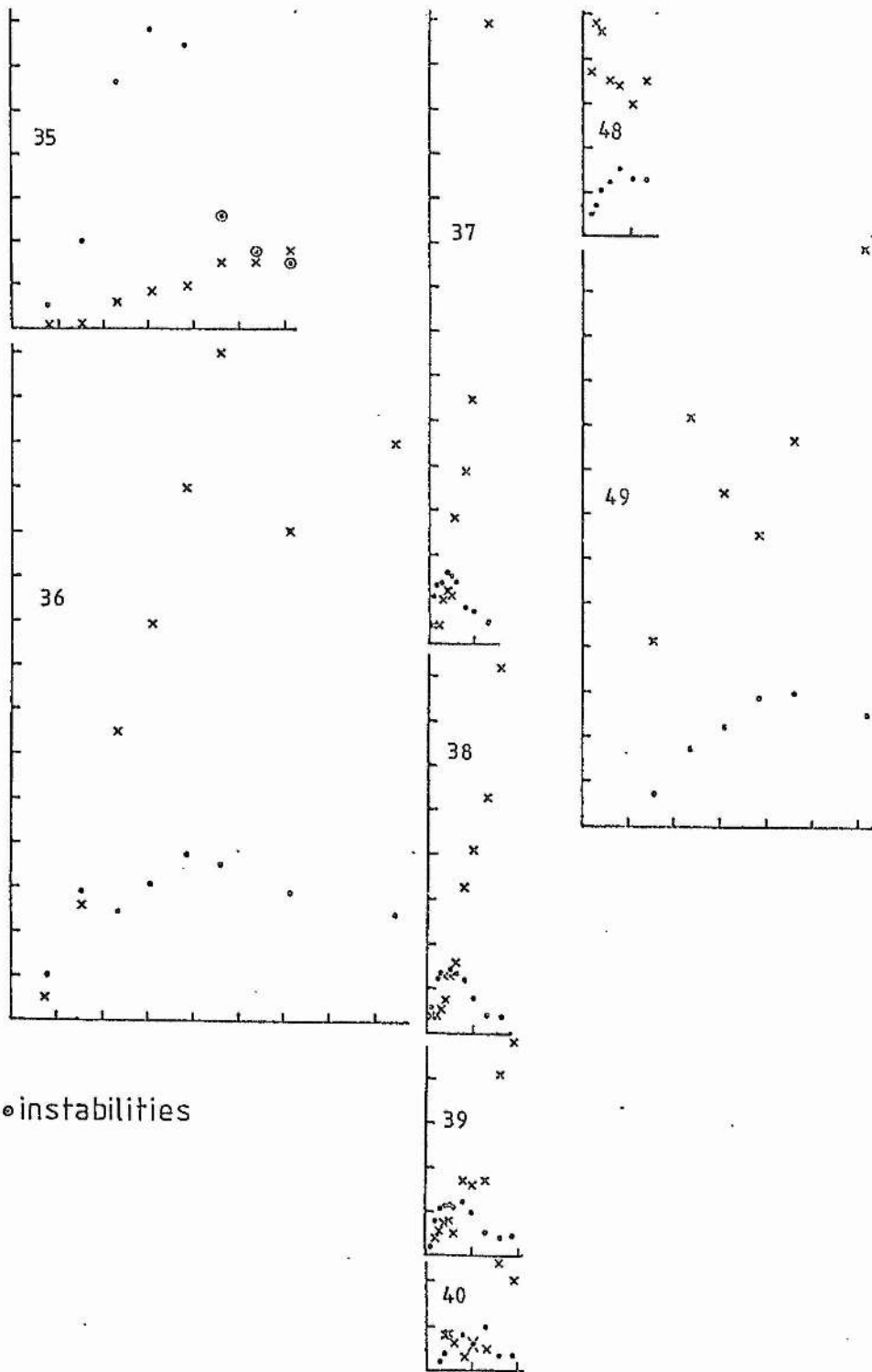


Figure 8.10KrF

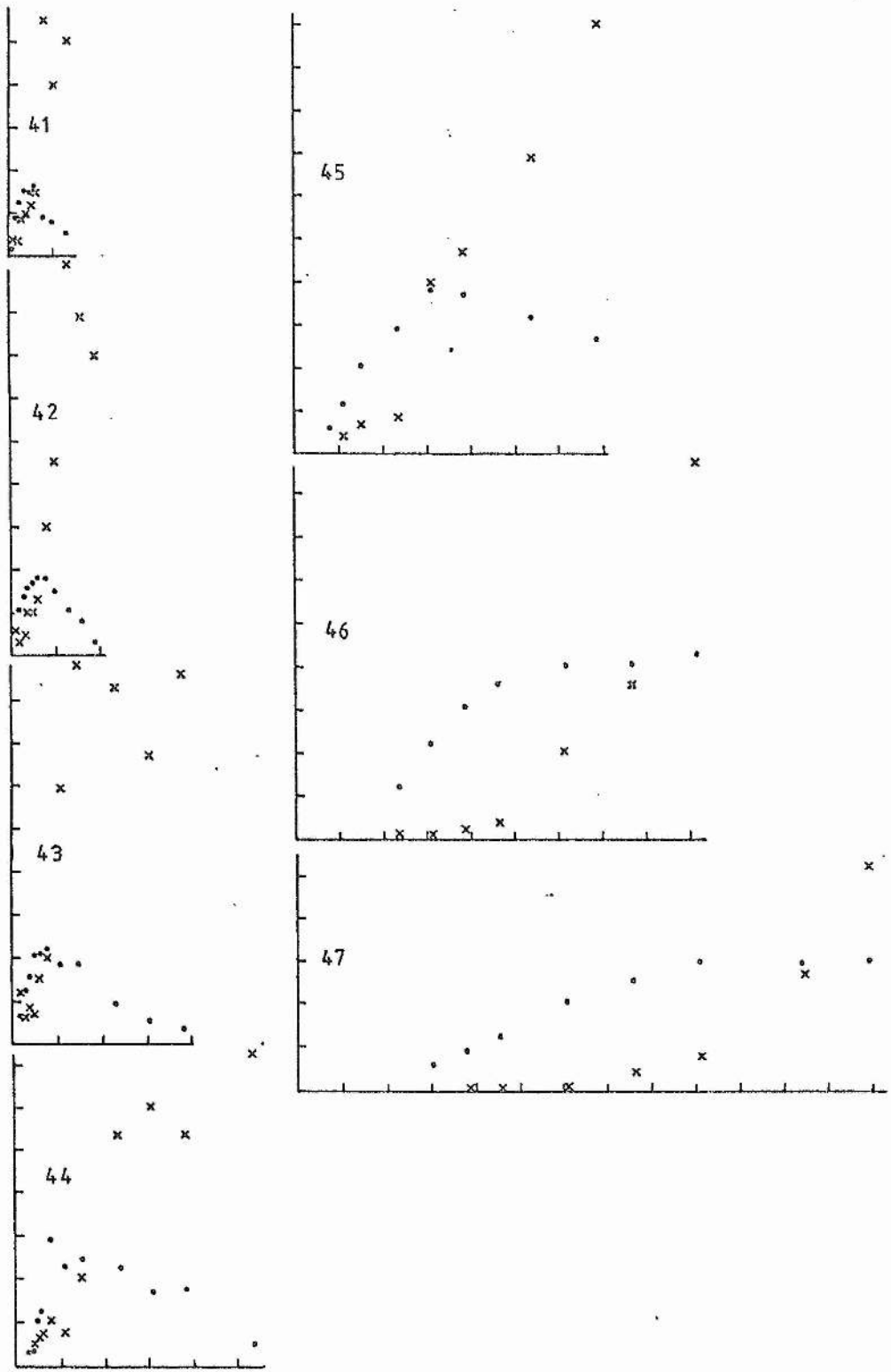


Figure 8.11K-F



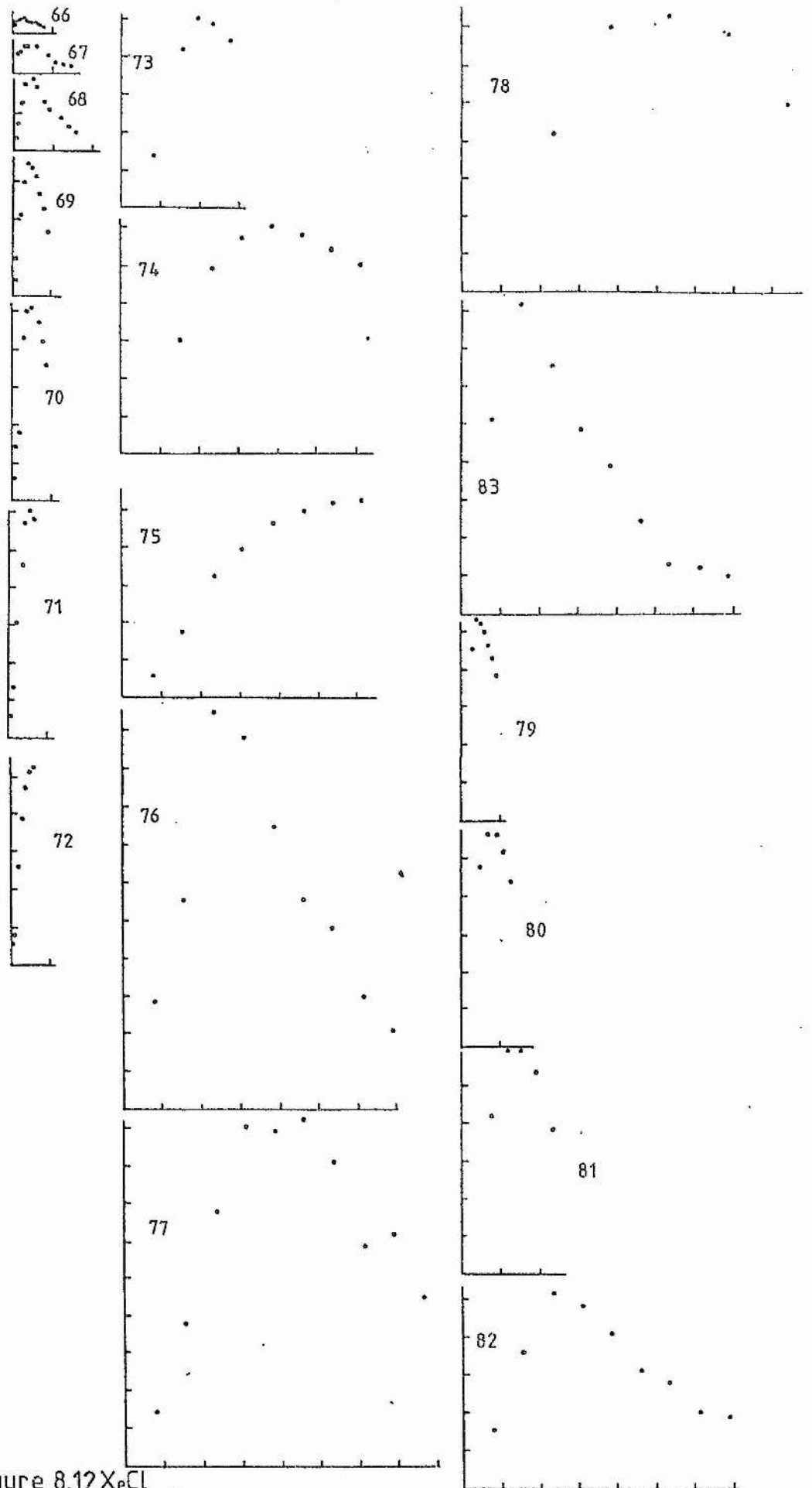


Figure 8.12 XeCl

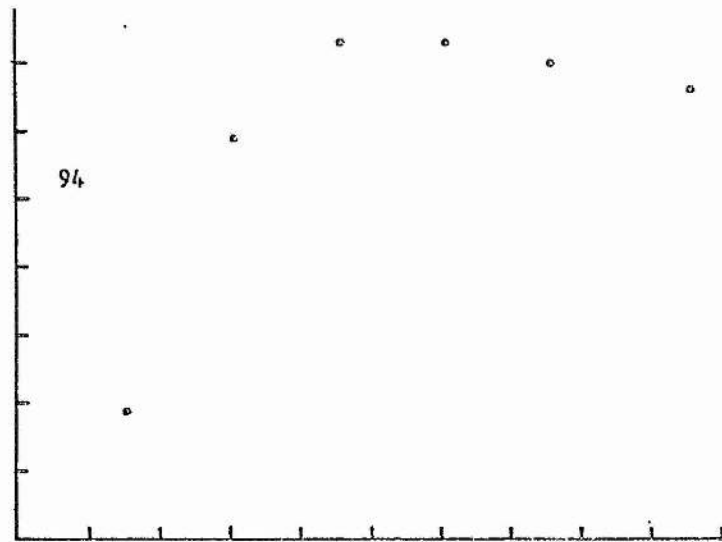
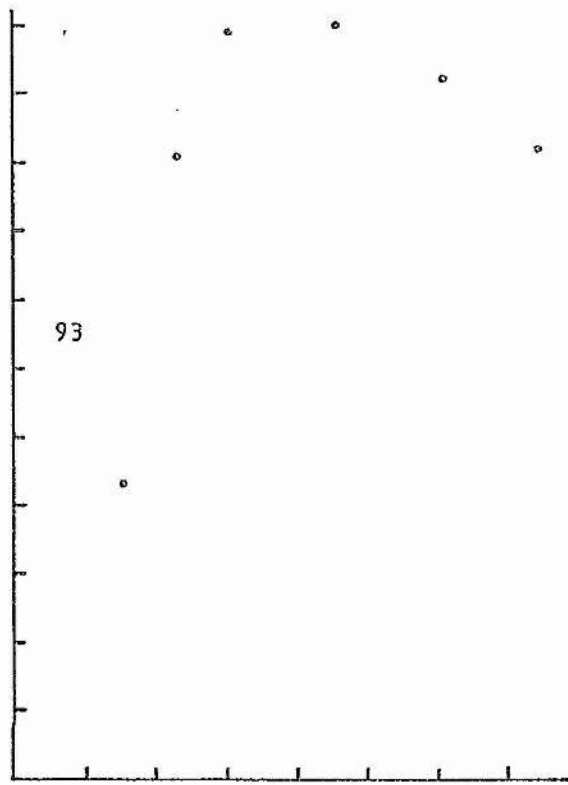


Figure 8.13KrCl

Peak intensity and intensity half-life vs pressure. (Derived from spectrum, and intensity vs time, records).

Figure	Excimer	Mixtures (Table 7.2)	Horizontal Axis Pressure Scale	Vertical Axis	
				Relative Intensity •	Half Life ×, ⊙
8.7	XeF	50-65	100mB/div	•	1sec/div
8.8	KrF	1-15	100Torr/div	•	
8.9	KrF	16-34		•	
8.10	KrF	35-40		•	
		48-49		•	
8.11	KrF	41-47		•	
8.12	XeCl	66-75		•	
		76-78		•	
		79-83		•	
8.13	KrCl	93-94		•	

× exponential fit  
⊙ linear fit

Relative intensity only comparable within each set of mixtures except KrF where the four sets are intercomparable.

Multiple pulse and single pulse intensity vs time. (Assembled from oscilloscope tracings). See also Figure 7.3.

Figure	Excimer	Column (a)	Column (b) and (c)
8.14	KrF	Multiple pulse amplitude envelopes. —fast, - - - -slow time base - ms/div indicated.	Single delayed pulse
8.15	KrF		—microwave reflection - - - -optical. Delay shown in ms. 100ns/div.
8.16	KrF	Multiple pulse amplitude envelopes.	
8.17	KrF		

Table 8.1 Key for Figures 8.7 to 8.17. (Data presentation on an empirical basis.)

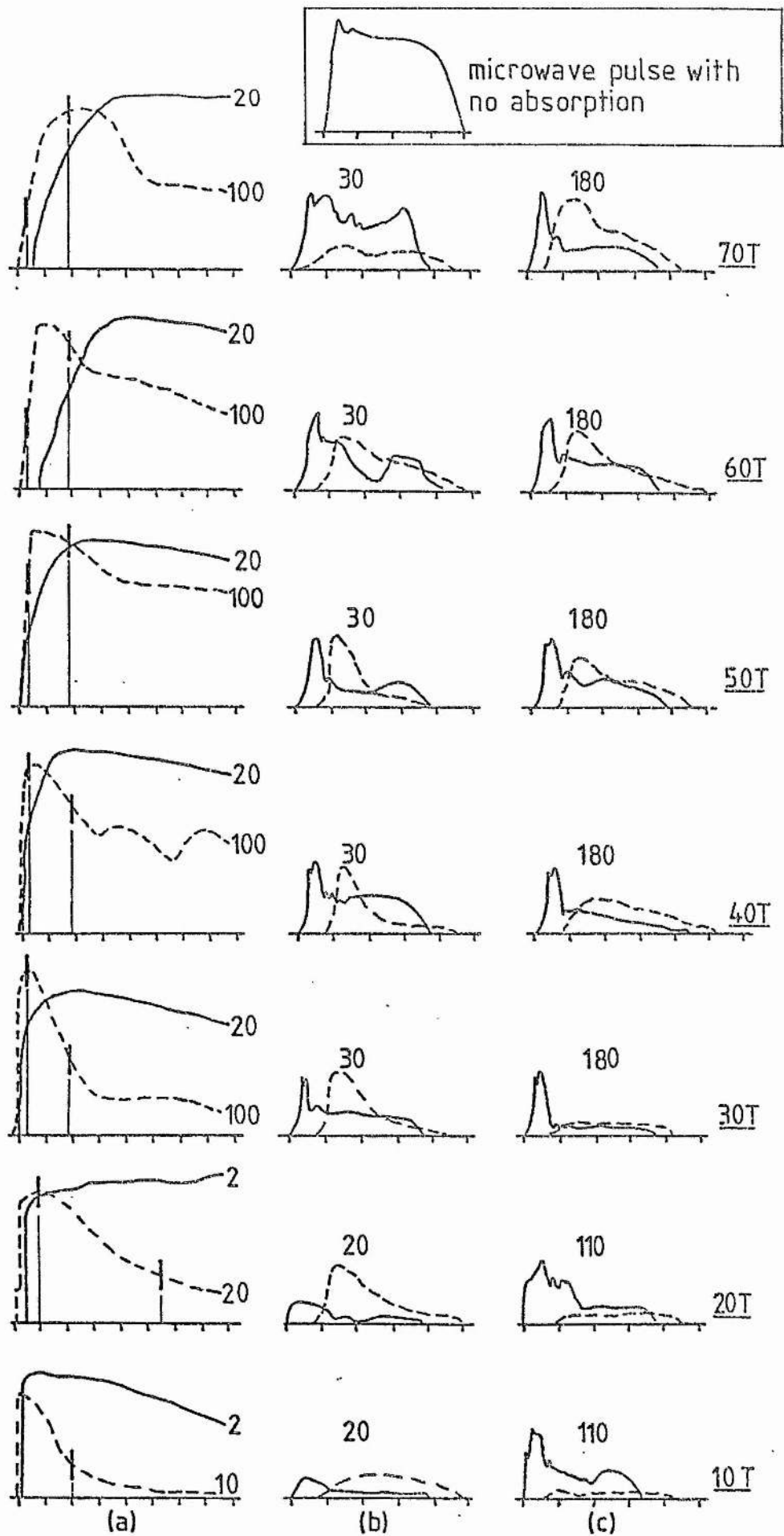


Figure 8<sup>14</sup>KrF NF<sub>3</sub>:Kr 1:3 (30). Explanation - Table 8.1

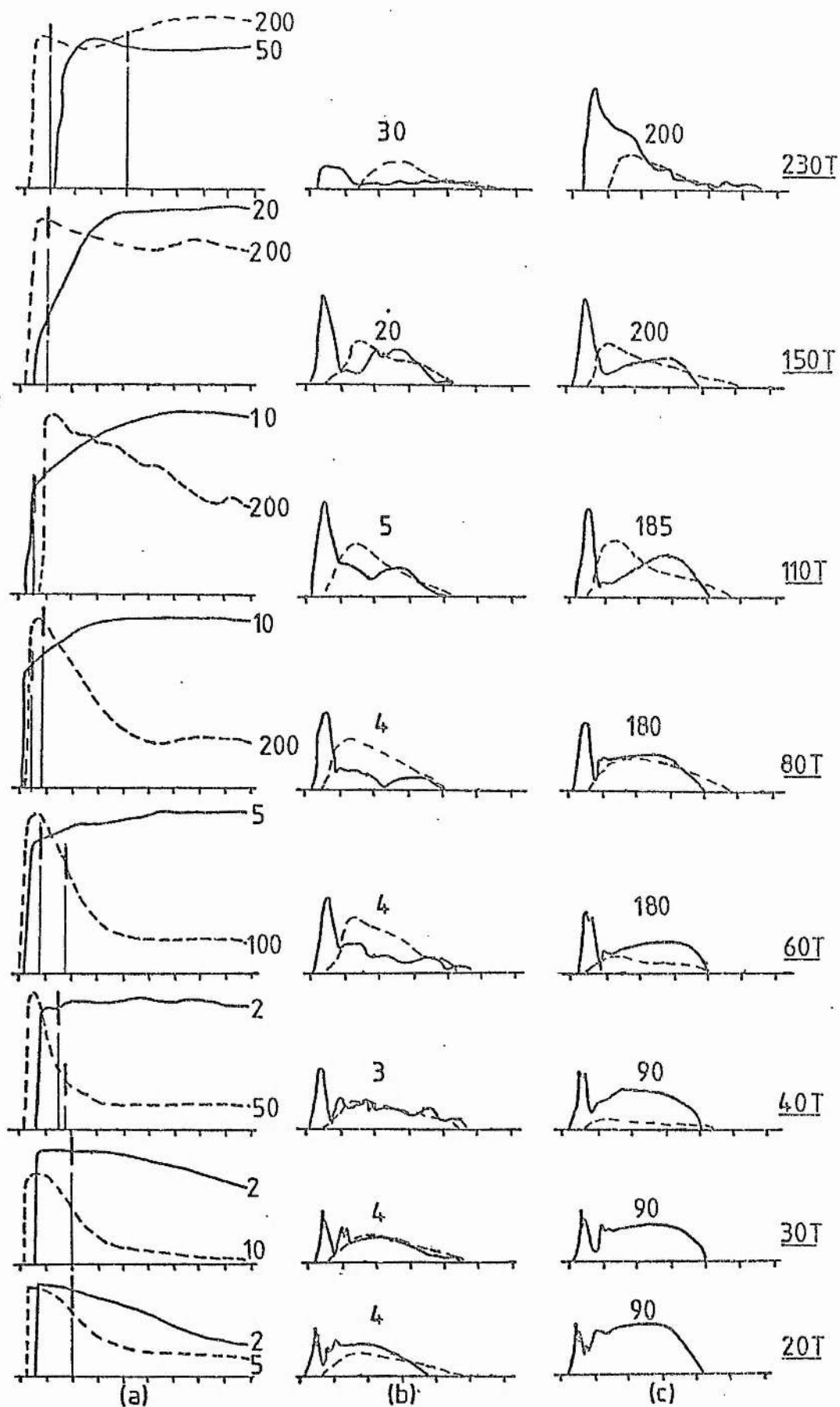


Figure 8.15KrF  $\text{NF}_3:\text{Kr}:\text{He}$  1:3:10

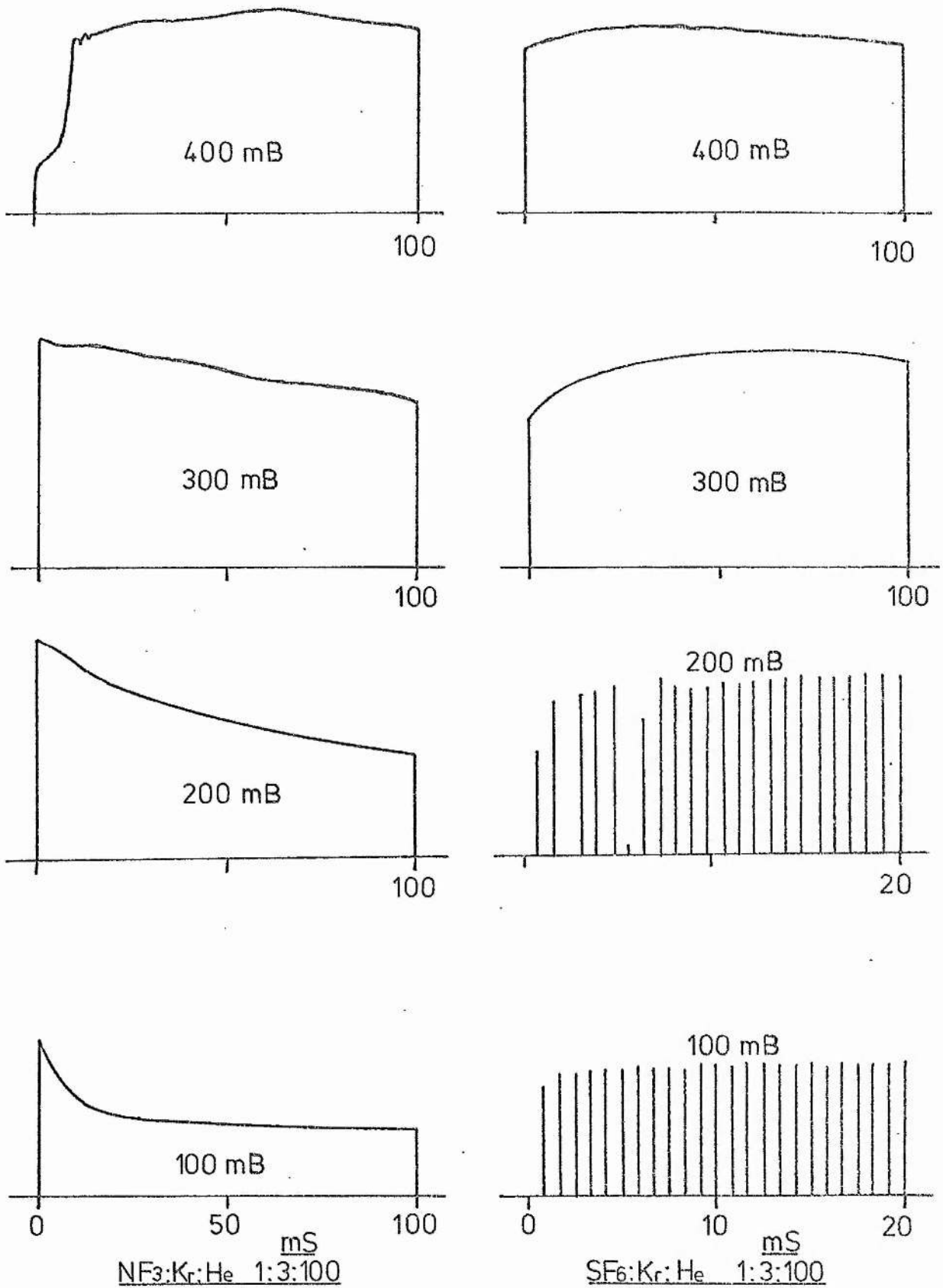
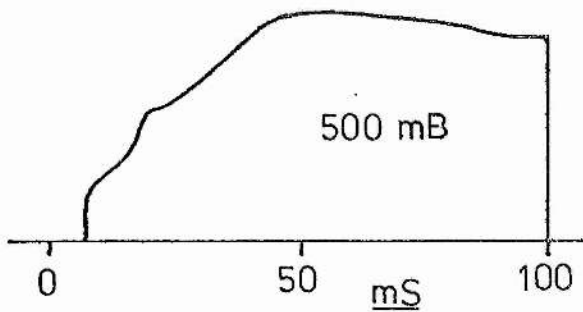
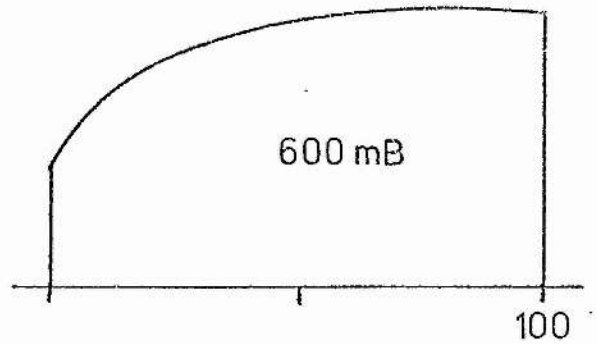
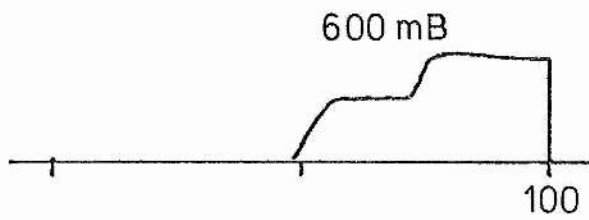
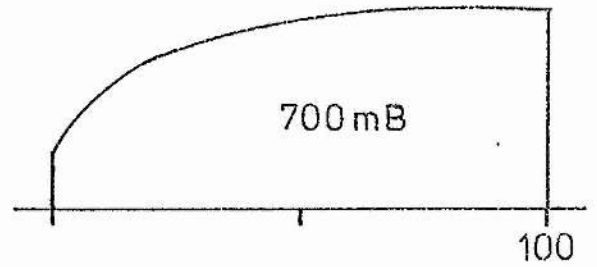
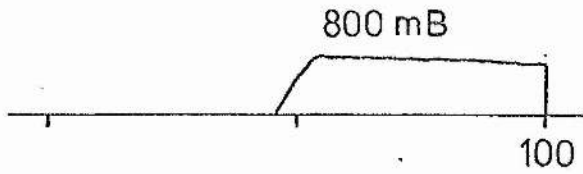
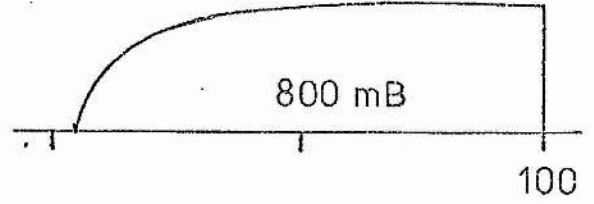
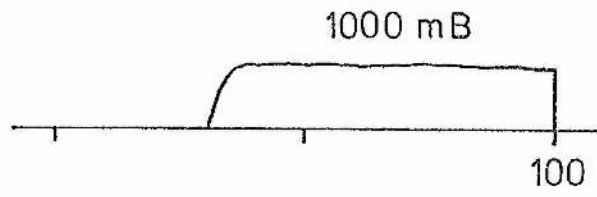
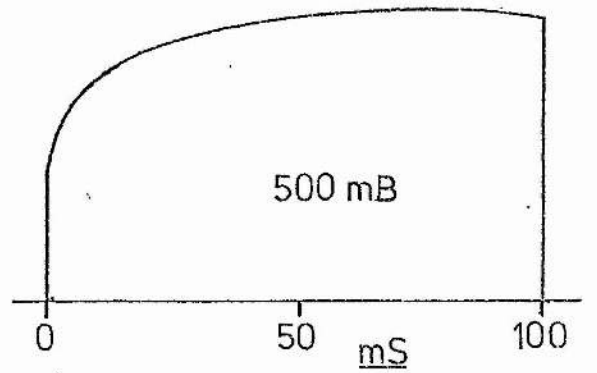


Figure 8.16 KrF Amplitude envelopes (cont. Fig 8.17) (35,36).





NF<sub>3</sub>:Kr:He 1:3:100



SF<sub>6</sub>:Kr:He 1:3:100

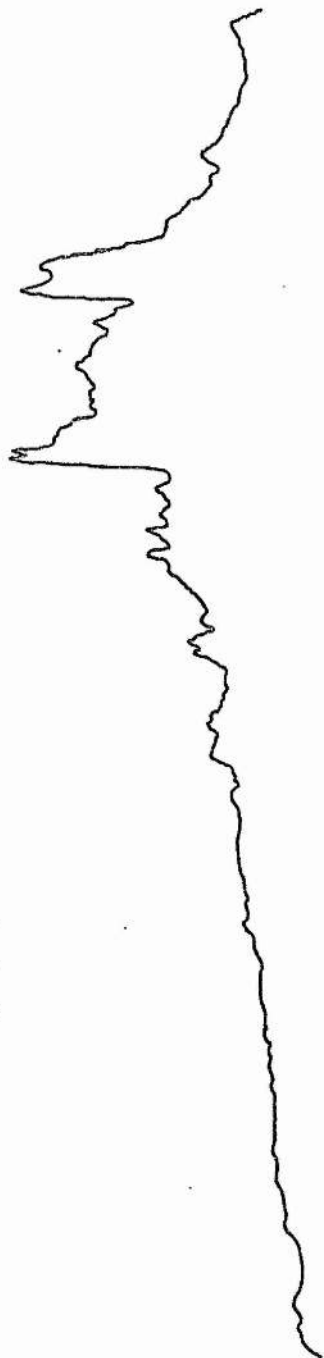
Figure 8.17KrF

## 8.2 Excimer Spectra

The B - X emission spectra of all the rare-gas halide molecules observed (XeF, XeCl, KrF, KrCl, and ArF) are presented in Figs 8.18 to 8.22 with the vibrational assignments given in the literature for XeF and XeCl. In order to demonstrate the effect of the total gas pressure on the emission profile, a low pressure spectrum is included for XeF, XeCl, and KrF. The spectrum of ArF (Fig 8.22) was weak and therefore quite difficult to obtain. To produce a spectrum with a low background spectrum, long integration times and fast gas flow rates were required to compensate for the short emission lifetime. Because of these difficulties, ArF was not studied in detail in this work.

Attempts were made to study the spectrum of the XeO excimer. However, this emission proved to be very difficult to obtain and identify in the present apparatus. The clearest result recorded is shown in Fig 8.23 and was obtained using a long integration time with fast gas flow. Despite this, numerous background lines are present. A mercury spectrum was superimposed on this record by switching off the discharge and allowing the emission of a mercury lamp to pass along the discharge tube axis. The small spectrum in Fig 8.23 is reproduced from Kenty et. al.(1946) and demonstrates clearly that the XeO spectrum is present in the record.

NF<sub>3</sub>:Xe:He 1:3:76 30mB



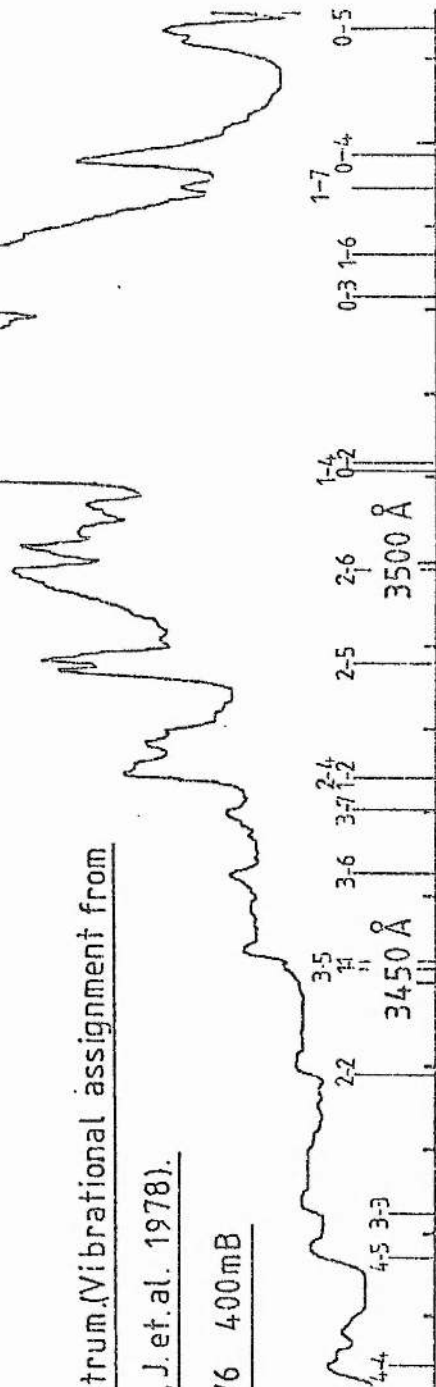
3450 Å

3500 Å

Figure 8.18 Xe F-B-X spectrum (Vibrational assignment from

Tellinghuisen, J. et. al. 1978).

SF<sub>6</sub>:Xe:He 1:3:76 400mB



4-4

4-5

3-3

2-2

3-5

1-1

3-6

3-7

1-2

2-4

2-5

2-6

1-4

0-2

0-3

1-6

1-7

0-4

0-5

3500 Å

3450 Å

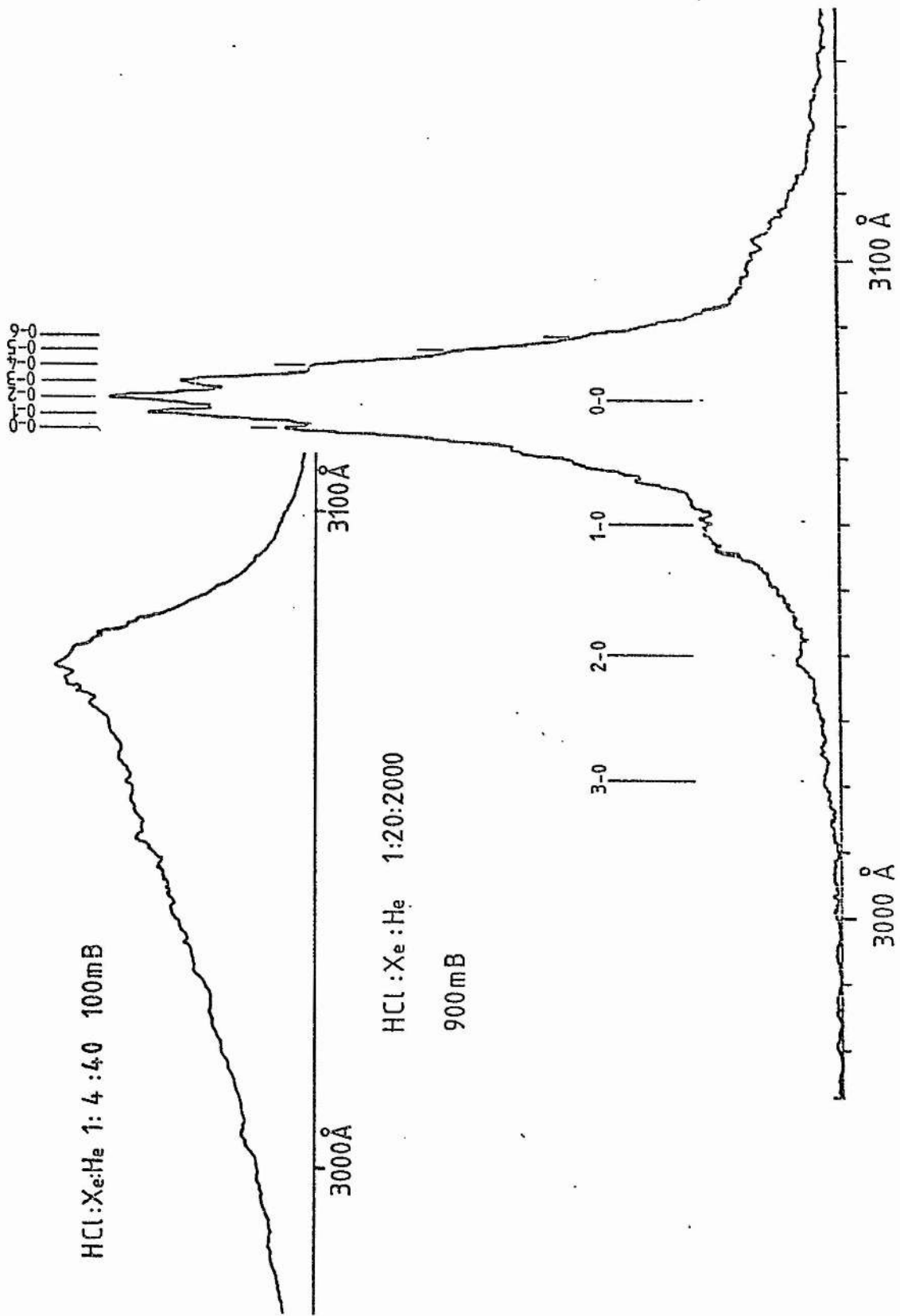


Figure 8.19 XeCl B-X spectrum. (Vibrational assignments from Tellinghuisen et al. 1976)

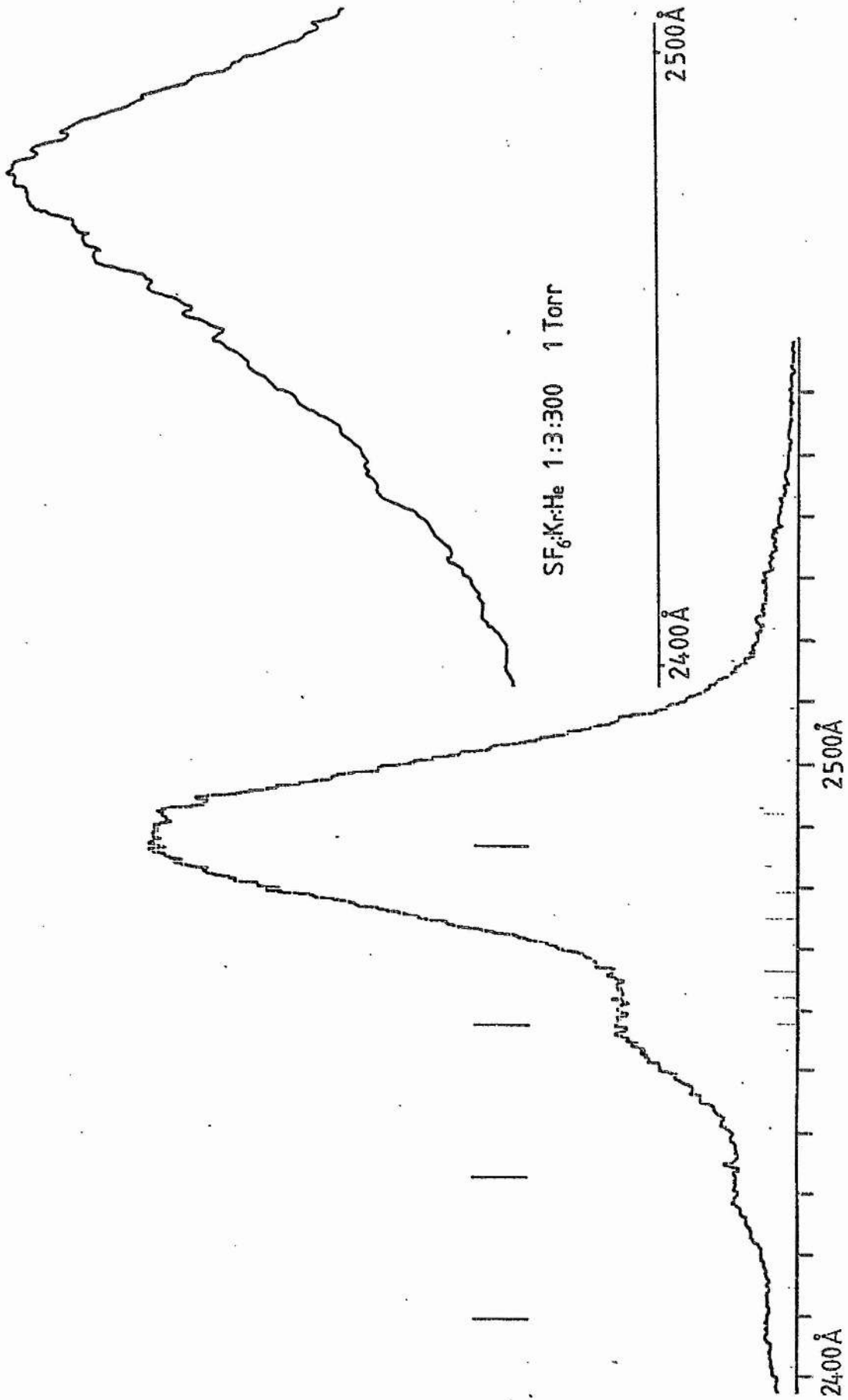


Figure 8.20 KrF B-X spectrum. SF<sub>6</sub>:Kr:He 1:3:100 400mB

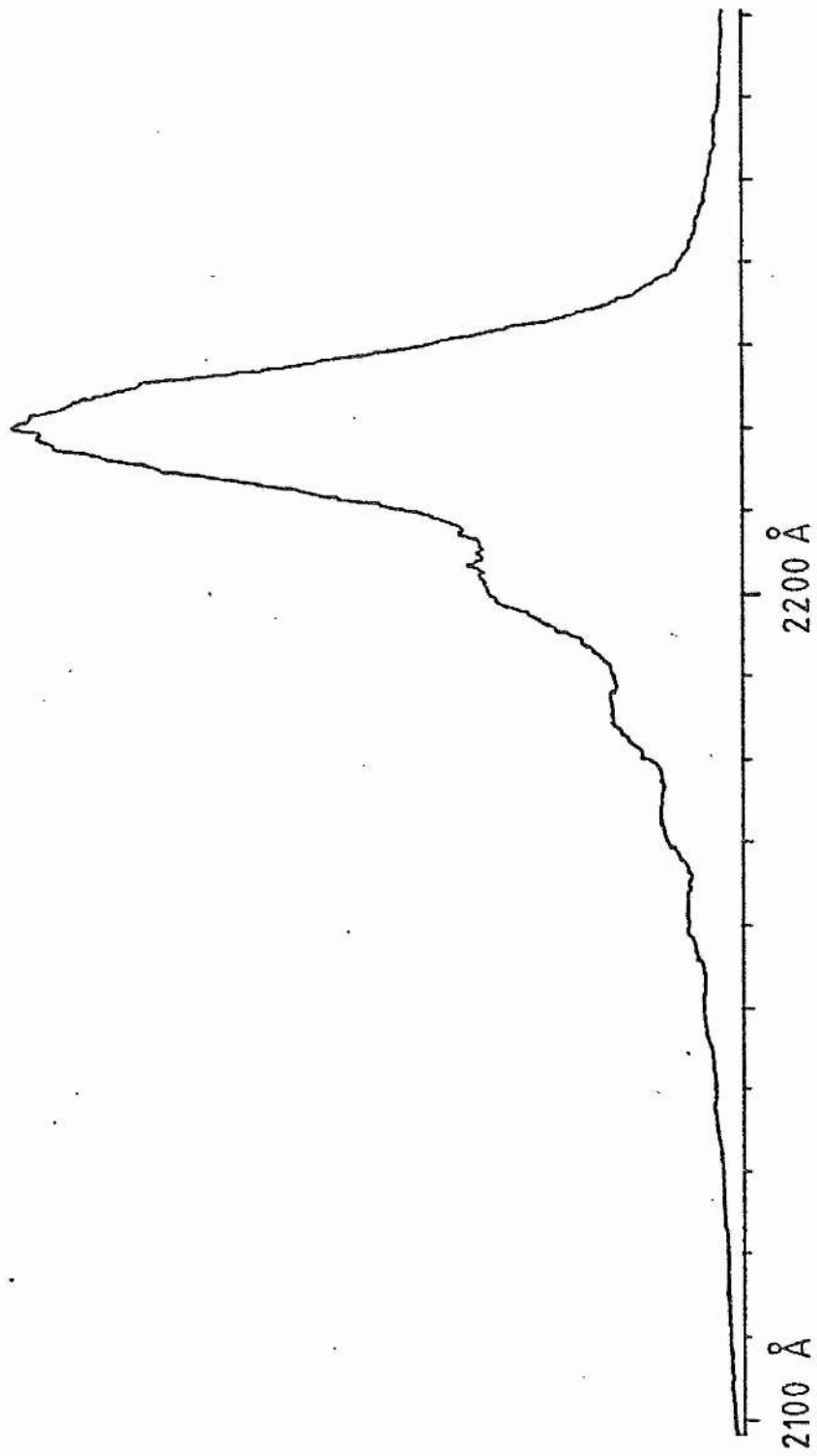


Figure 8.21 KrCl B-X spectrum. HCl:Kr:He 1:50:1000 500mB



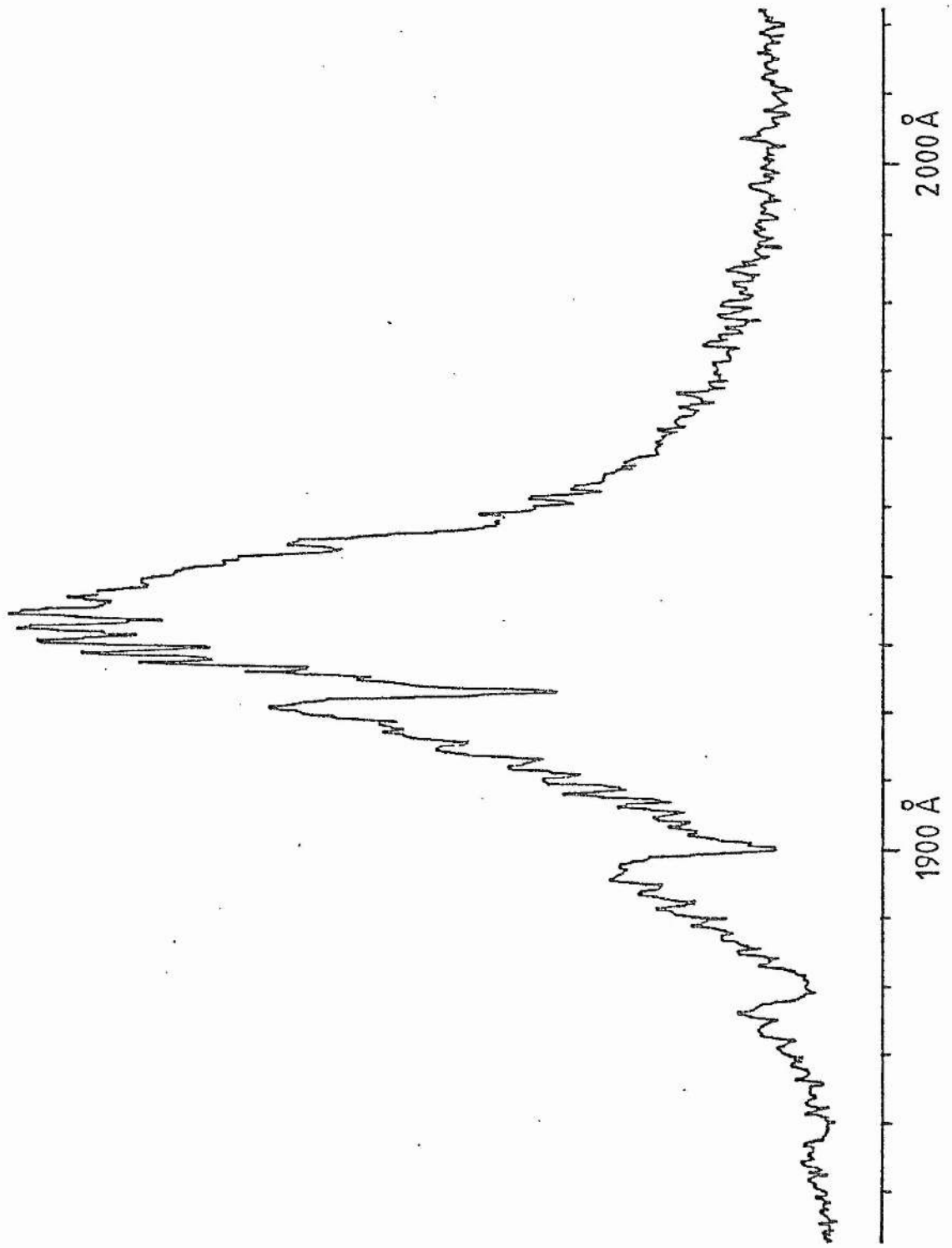
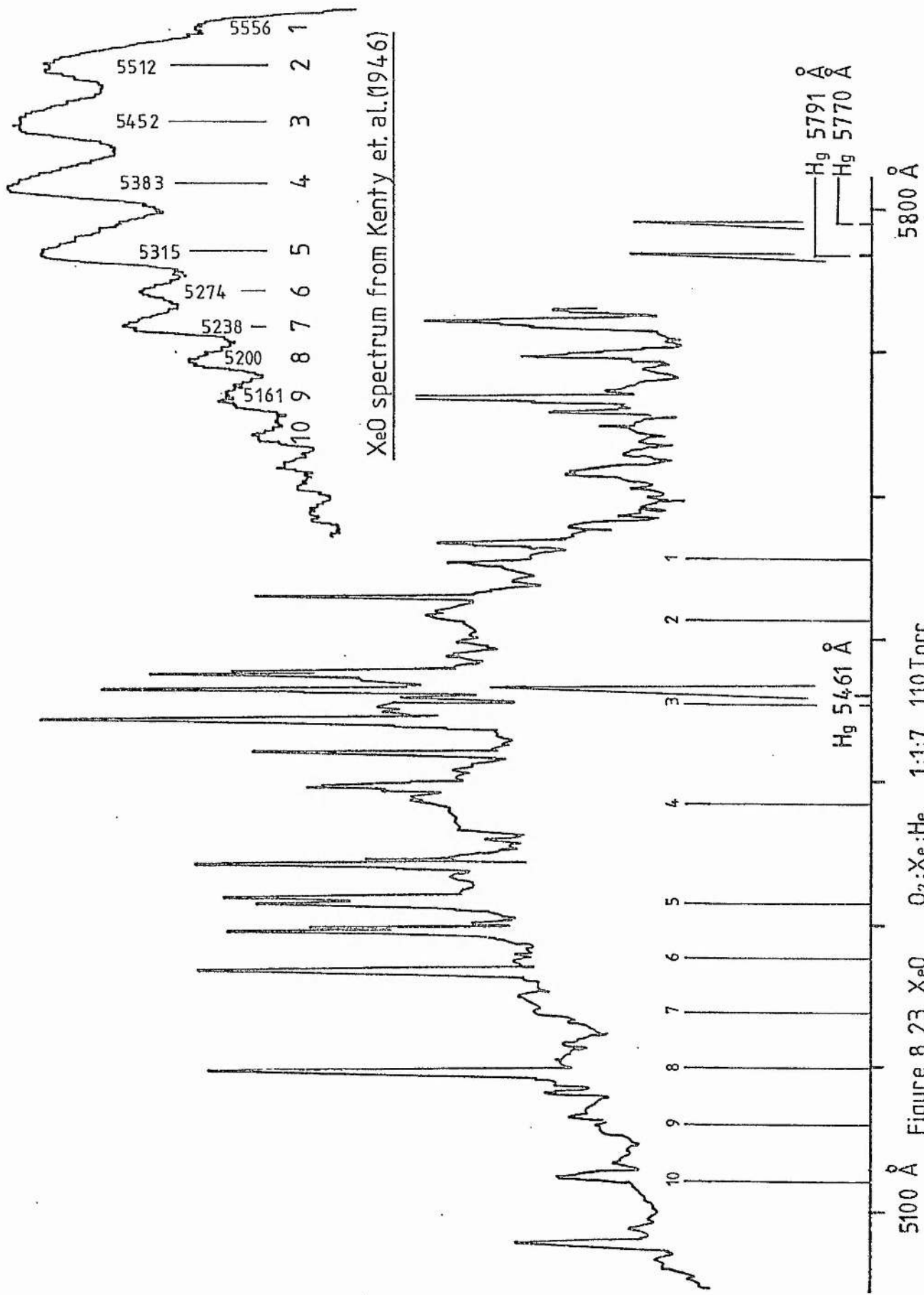


Figure 8.22 ArF B-X spectrum. SF<sub>6</sub>:Ar 1:30 20mB



### 8.3 Mixture Ratios and Total Pressure

One of the aims of the present investigation was to find, empirically, the mixture ratios and total pressure for which the fluorescent emission, for any given excimer system, was a maximum. These ratios and pressures could then be used as a starting point in attempts to obtain lasing.

#### 8.3.1 XeF Mixtures

For XeF the results in Fig 8.7 give an indication of the trends in output accompanying variations in mixtures. In some cases, most notably the mixtures with  $\text{NF}_3$  donor, the emission lifetimes are short, being well below the 0.3 second response time of the recording system over the whole pressure range. For these cases a higher relative intensity than that recorded would be obtained if operation over a small number of pulses had been feasible. Within each of the three groups of the mixtures of  $\text{SF}_6:\text{Xe}:\text{He}$  (50-52, 53-55, 56-57 in Table 7.2 and Fig 8.7), the peak intensity occurs at higher total pressure as the mixture becomes more dilute and also the gas lifetime rises rapidly with total pressure. Comparing these three groups, the general effects of increasing the donor fraction are to shift the peak emission to lower total pressure and give increased gas lifetimes. Within the limitations set by the response time of the apparatus, it seems that, for  $\text{SF}_6:\text{Xe}:\text{He}$  mixtures, the smaller donor fraction may be more suitable. Mixtures approximating 1:6:500, for example, may be optimum for peak output for small numbers of pulses.

The results for mixtures 62-67 in Fig 8.7 show that a much higher output is obtained with  $\text{NF}_3$  as donor, despite the reduced signal occurring through very short lifetimes. Results using argon buffer show a small output only. Thus it seems that for high intensity for small numbers of pulses in XeF emission,  $\text{NF}_3$  should be used as donor and, since greater intensities are seen for mixtures 58 and 59 than for 53 and 54, neon should be used as the buffer. The optimum ratios for fluorescent emission are difficult to assess but may not be particularly critical. Thus  $\text{NF}_3$ :Xe:Ne mixtures in the approximate range 1:3:100-1000 may suffice. It may be that the higher dilution, while giving less fluorescent emission, could give better laser operation due to relaxation of the B state. For long life,  $\text{SF}_6$  is superior to  $\text{NF}_3$  but laser operation may be much harder to achieve with  $\text{SF}_6$ . Therefore in applications where long gas life is of primary importance it may be possible to use  $\text{SF}_6$  instead of  $\text{NF}_3$  if reduced laser output is acceptable.

### 8.3.2 KrF Mixtures

The KrF results (1-49 in Table 7.2) were the most detailed of the experimental sequence, especially 1-27 for  $\text{SF}_6$ :Kr:He mixtures. These may be examined in Figs 8.1, 8.2(a) and 8.2(b) and also in Figs 8.8 and 8.9 where the groups 1-6, 7-12, 13-17, 18-23, and 24-27 correspond to a progressive decrease in donor fraction, while within each group a range of dilution by the buffer is tested. In the majority of cases the gas lifetime is longer than 0.3 sec. It is

most noticeable that changes in the peak intensity with changes in mixture ratios are not particularly sharp. This is shown more clearly in Fig 8.24 where the peak intensity and the absolute pressure at which it occurs are plotted against donor fraction on a negative log scale. The donor:rare-gas ratio is constant within each graph. The broad trend is to a maximum with donor:rare-gas ratios in the range 1:1 to 1:3 with donor:total gas content ratios in the range 1:5 to 1:300. However, in the extreme case of SF<sub>6</sub>:Kr in the ratio 1:1 the maximum occurs at about 5 Torr where the B - X emission band is still rather broad. For high relaxation higher total pressures are preferred and for peak emission above say 500 Torr total pressure, ratios in the region of 1:3:100 may give the optimum lasing mixture.

### 8.3.3 XeCl Mixtures

The results for XeCl (Fig 8.12) give only a rough basis for choosing an optimum mixture since the behaviour shows no sharp features and the ratios were not tested in great detail. Figure 8.25 presents the variation of peak intensity, and the pressure it occurs at, against donor fraction in the same fashion as Fig 8.24. These results suggest an optimum mixture of HCl:Xe:He in the approximate ratio 1:20:200.

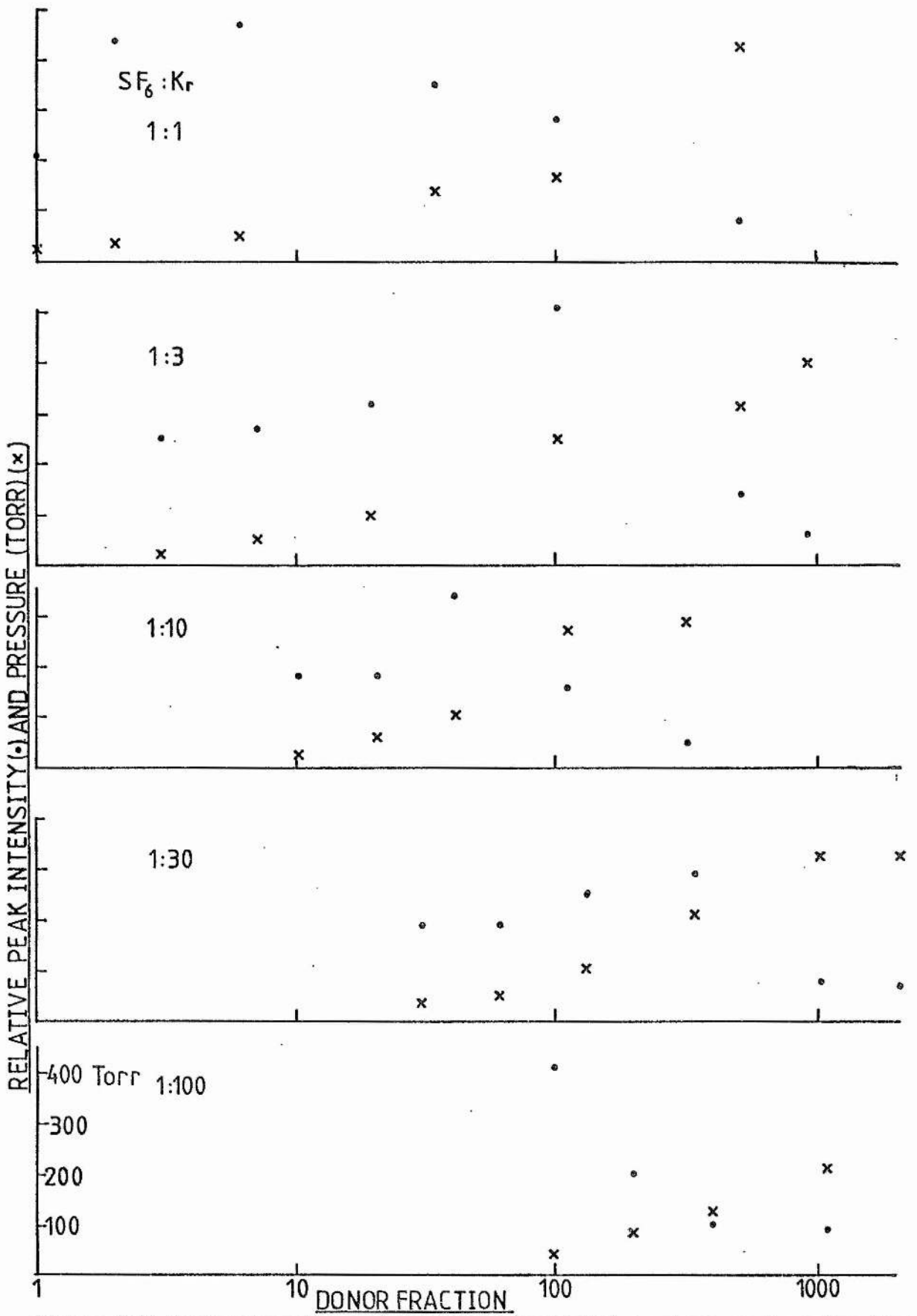


Figure 8.24 Peak intensity and corresponding total pressure vs donor fraction.  
KrF with helium buffer.



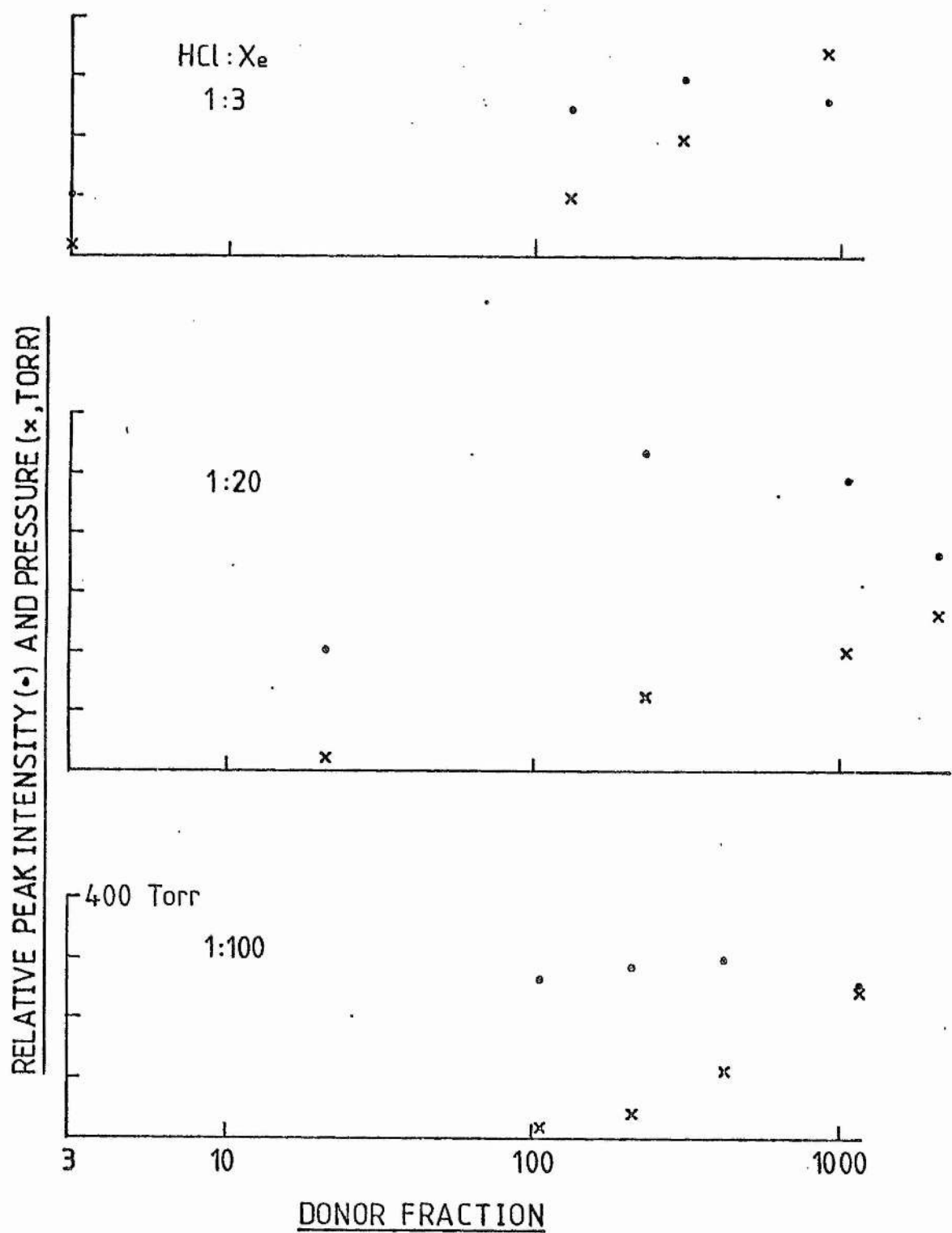


Figure 8.25 Peak intensity and corresponding pressure vs donor fraction. X<sub>2</sub>Cl with helium buffer.

#### 8.3.4 Lasing Attempts

Attempts were made to obtain laser operation in XeF, KrF, and XeCl using ranges of mixtures in the vicinity of those mentioned above. The low optical loss arrangements described in Section 5.3.2 were used with the most highly reflective dielectric mirrors available (about 98%). Since apparatus for the measurement of optical absorption and gain at the lasing wavelength was not available, the emission spectrum was examined for indication of increased intensity at the emission band centres. Static mixtures were tested over a wide range of total pressures. Following this attempts were made with flowing gas using flow rates up to the fastest that could be produced in the apparatus. This was particularly effective in increasing the integrated (1 sec) intensity of mixtures containing  $\text{NF}_3$ . However, no evidence was found in any of the tests of net gain at the emission band centres. The discussions of Section 2.3 indicated that the pump power density in the present apparatus is likely to be insufficient for laser operation. This seems even more likely when it is considered that the microwave pumped excimer laser reported by Mendelsohn et. al. (1981) used a microwave pulse power of 600kW, while the pulse power used here was only 50kW. In addition they reported an efficiency of 0.01% whereas in the calculations of Section 2.3 an overall efficiency of 0.084% was used to give the most optimistic threshold pump power density of  $10\text{kW cm}^{-3}$ .

### 8.3.5 Mixtures With No Buffer Gas

It can be seen in Table 7.2 that some mixtures were tested in which no buffer gas was present, namely  $\text{SF}_6$ :Kr,  $\text{NF}_3$ :Kr, and HCl:Xe. Peak intensities and the pressures that they occur at are shown against the donor fraction (inverse) in Fig 8.26. It is noted that high relative intensities are possible with no buffer gas. The graph for XeCl is smooth with an optimum ratio of about 1:100 for HCl:Xe. The graph for KrF with  $\text{SF}_6$  as donor is rather irregular and a choice of an optimum mixture would be meaningless. Where  $\text{NF}_3$  is used for the donor, the results are highly irregular. In all cases the peak intensity occurs at a pressure of between 30 and 100 Torr.

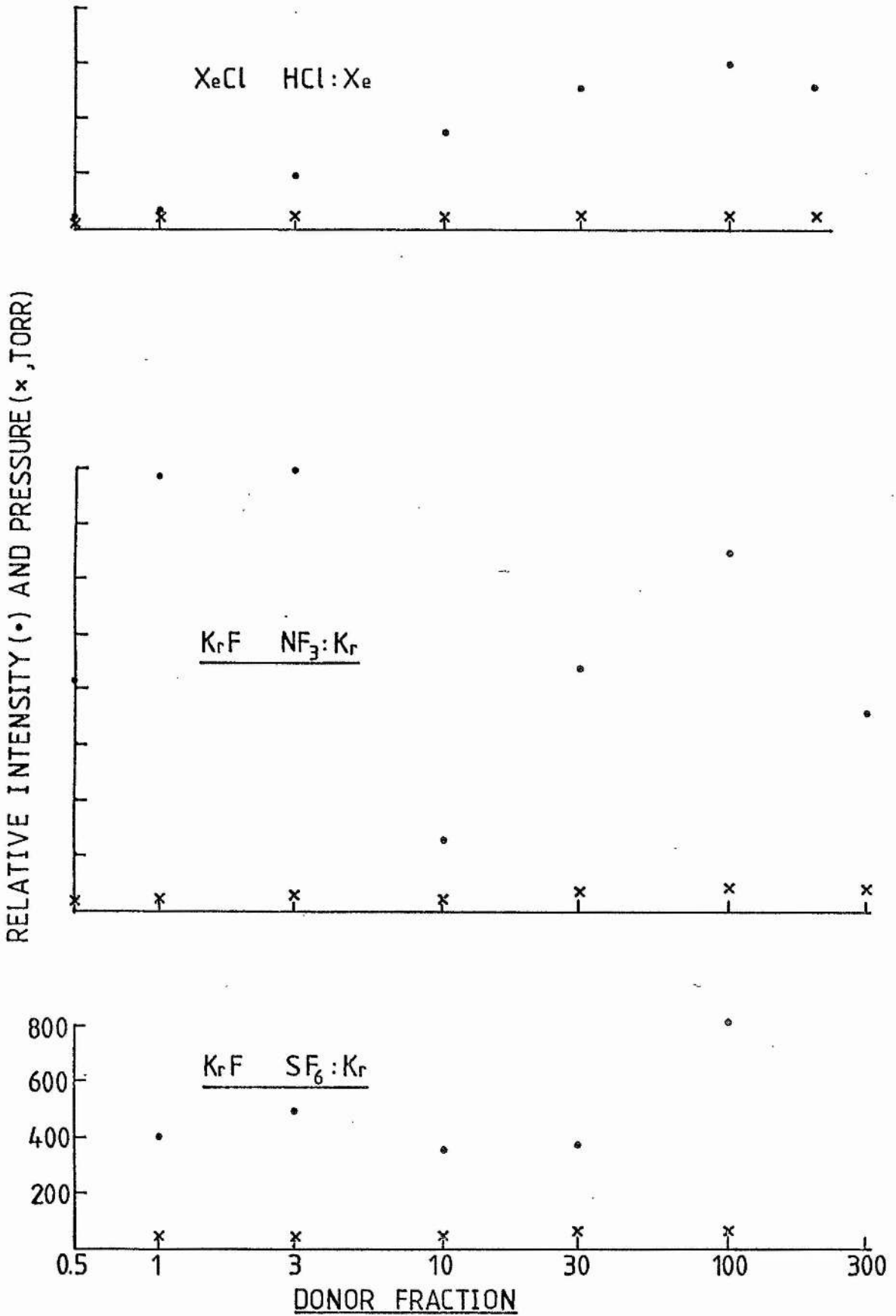


Figure 8.26 Mixtures with no buffer. Peak intensity and corresponding pressure vs donor fraction.

#### 8.4 Temporal Behaviour

In excimer lasers, gas mixtures have a limited useful life. Generally the laser output for a single gas fill decreases with time until lasing no longer occurs. This means that excimer lasers suffer the inconvenience and expense of frequent gas replacement. For this reason a major part of the present study involved temporal recordings of the excimer emissions from which gas lifetimes could be measured. However, the intensity follows a simple exponential decay to zero in very few cases and generally an interesting and complex time behaviour is displayed. The details of this behaviour are described in this section in terms of the various parameters that affect it. The results reviewed are all those where temporal recording by Method 2 and the pulse recording method (see Chapter 7) were used, that is, all the KrF results. The raw data for these results have already been presented in Figs 8.1 to 8.6 for the intensity-time records and in Figs 8.14 to 8.17 for the pulse recording method.

It is pointed out here that the small discharge volume and high repetition rate afforded by the microwave apparatus provides a unique opportunity for accelerated gas lifetime studies. The active gas volume in DC discharge pumped excimer lasers is usually about 1 litre while repetition rates are usually about 1pps. In the microwave apparatus the volume was about  $0.5\text{cm}^3$  and the repetition rate was 1100pps. Thus the experiments that were carried out would take between  $10^3$  and  $10^6$  times longer using a conventional excimer laser. (The uncertainty in this scale factor arises from uncertainty in the role of the different gas volumes: the power density is comparable in

both cases).

Where lifetimes are quoted, and expressed in seconds, multiplication by 1100 will give the lifetime in numbers of pulses. For comparison with gas lives in other systems, the gas lives measured in this work should be normalised for gas volume and the donor partial pressure. The discharge volume was about  $0.63\text{cm}^{-3}$  so that multiplication of a lifetime by  $1.6 \times 10^3$  gives the lifetime per litre of gas. Normalisation for donor partial pressure requires dividing a lifetime by the corresponding donor partial pressure. However, since there appears to be a non-linear and inconsistent relation between donor partial pressure and gas lifetime through the results normalisation for donor fraction is not possible.

#### 8.4.1 Single Pulse Behaviour

Single optical pulses were recorded as described in Chapter 7 and appear in the dashed curves of columns (b) and (c) in Figs 8.14 and 8.15 on a time scale of 100ns/div. The continuous curves in these records are of the simultaneous output from the detection diode in the microwave apparatus and give a rough indication of the microwave absorption. The microwave pulse with no absorption taking place is shown in Fig 8.14. The numbers appended to each record give the delay in ms between the first microwave pulse and the recorded optical pulse (and microwave pulse). The instants of the recordings are indicated on the pulse amplitude envelope records in column (a) where the numbers represent the ms/div for the two time-bases used.



Before interpreting these records it should be noted that no attempt was made to obtain a calibration of the optical intensity scale or of the microwave signal strength; the microwave signal scale especially may be non-linear (in power) due to the high powers involved. In addition to this the temporal superposition of the microwave and optical signals has some uncertainty, probably of around 10ns. The microwave signals show, typically, an early spike followed by a rough plateau which is due to low absorption at first, with reflection from the short circuit termination, followed by absorption during the remainder of the pulse. The degree to which the reflected (unabsorbed) signal, after breakdown, is due to the waveguide termination (ie. transmission through the discharge), rather than reflection from the discharge, cannot be determined from these records.

The peak in the optical signal occurs in most cases about 50ns after the principal increase in microwave absorption. The optical peaks are between 100ns and 200ns wide and the width bears little or no relation to the microwave absorption. Also there is no clear relation between the optical pulse width and the total pressure. In shifting from the early pulses to later pulses, the main change is the loss of the intense peak. Generally all the results with a buffer gas in the mixture have a wider optical pulse than those without.

With the exception of the (perhaps spurious) result at 230Torr in Fig 8.15, breakdown is more rapid at low pressures for early pulses in the train of pulses. Below about 30Torr breakdown occurs before the microwave pulse has risen to its maximum. However, the opposite appears to be the case for later pulses (column (c)) in the unbuffered mixture (Fig 8.14).

The most outstanding feature of these records is the lack of any strong dependency of the single optical and microwave pulse features on total pressure or the presence of a buffer gas. The buffer gas seems merely to permit operation at higher pressure. It must be concluded then that the optical pulse intensity and width is not limited by the number density of the donor gas. The observation that the fluorescent output decreases during the second half of the pulse even though, in many cases, the microwave absorption remains high, is of considerable importance. However, there is no clear indication of the source of this decrease. There are perhaps two general areas from which a cause may be sought; growing discharge inefficiency (less metastable excitation) and quenching by a species generated in the reaction. For example, the electron energy distribution may have passed through the optimum for metastable production by the second half of the pulse.

#### 8.4.2 Pulse Envelope Records

Records showing the envelopes of optical pulses appear in Figs 8.14 and 8.15 column (a) and Figs 8.16 and 8.17. The number of pulses in a record ranges approximately from 20 to 2000. These results are particularly important for indicating pulse-to-pulse variations on a timescale below the 0.3 sec limit of the OSA apparatus. It is immediately seen that there is still a lack of strong variation in peak intensity with total pressure. The curves at the lower pressures in Figs 8.14 and 8.15 and for the  $\text{NF}_3$  mixture in Fig 8.16 can be described quite well by a rapid rise to a maximum followed by an exponential decay. The time taken for the intensity to fall to half of its peak value is plotted against total pressure (on log-log scales) for these cases in Fig 8.27. Other features, such as the gradual rise to maximum that occurs at higher pressures, the long term plateau, and instabilities, are also present in the OSA time records. It will therefore be appropriate to discuss these features in conjunction with the consideration of the OSA temporal records that now follows.

#### 8.4.3 Temporal Records

The OSA temporal records for  $\text{SF}_6$ :Kr:He mixtures appear in Figs 8.1 and 8.2. Other results appear in Figs 8.4, 8.16 and 8.17 for donor comparison, Fig 8.3 for unbuffered mixtures using  $\text{NF}_3$ , and Figs 8.5 and 8.6 for Ar and Ne buffers, respectively. Some of these records display an approximate rapid rise - exponential decay curve

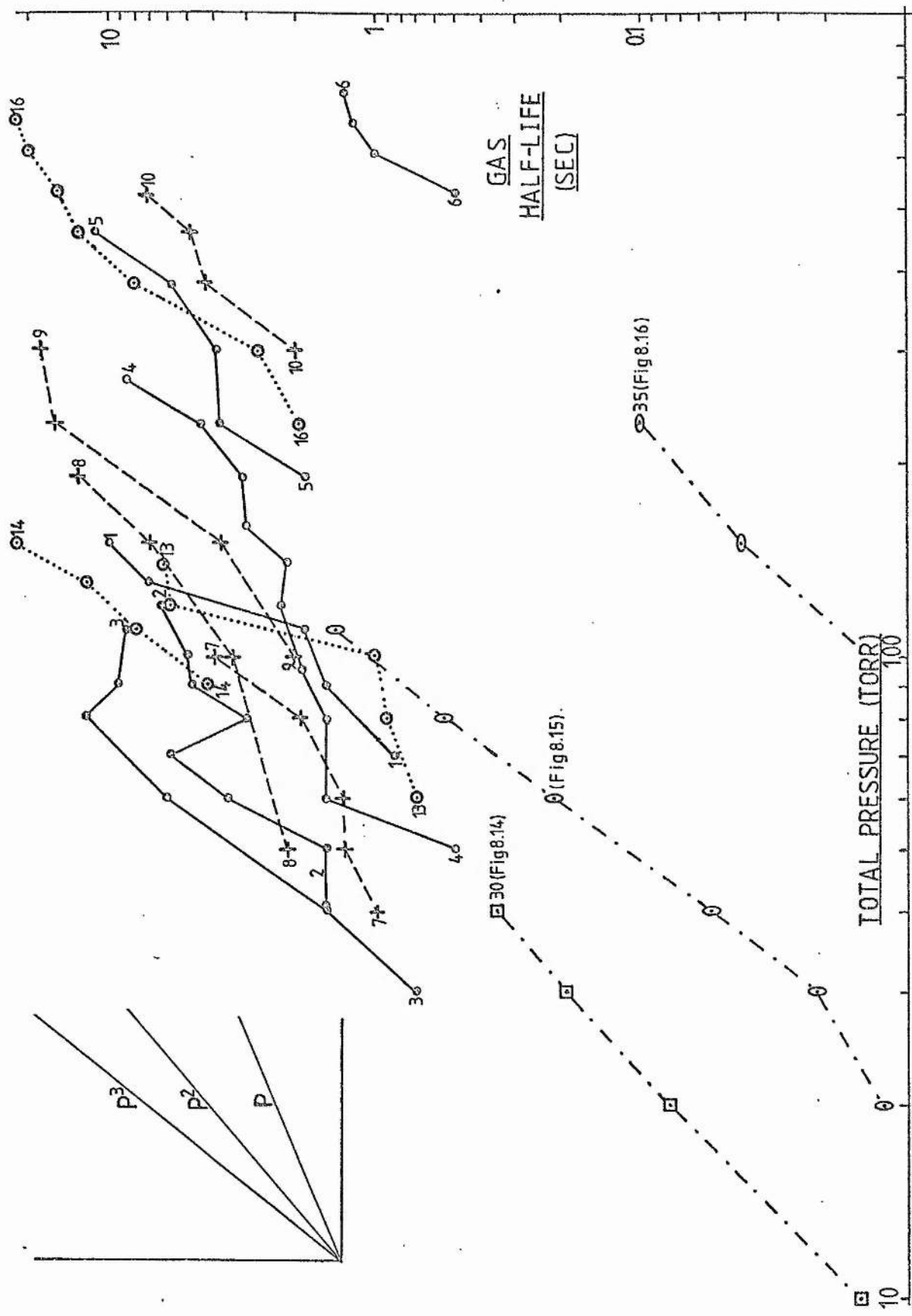


Figure 8.27

so that the intensity half-life may be measured and plotted against total pressure. This is shown (on log - log scales) in Figs 8.27 and 8.28 where the numbers appended to the diagrams refer to the mixtures in Table 7.1. Points are marked and joined by lines using the same style if they share the same donor:rare-gas ratio (eg. crosses linked by dashed lines in Fig 8.27 are for SF<sub>6</sub>:Kr at 1:3 mixtures). Both figures include an indication of the straight line gradients corresponding to variation of the half-life with pressure cubed, pressure squared, and pressure directly. These are provided in order to indicate departures from the direct dependency of lifetime on total pressure that a simple model of a finite reservoir of donor molecules would predict. A possible mechanism for such departures is the existence of secondary donors of short lifetime. The probability of excimer formation from such molecules would then increase with collision frequency and therefore total pressure.

Many of the OSA temporal records and pulse envelope records do not conform to a rapid rise - exponential decay model and the various features of this departure are categorised and described below.

#### 8.4.4 Constant Intensity

In all of the intensity - time records the intensity becomes approximately constant during the measurement period. The duration of the records (30sec) was increased in some cases (see the dashed lines in Figs 8.1 and 8.2 mixtures 18-24) to investigate the decay of the constant level. It was found that the intensity could remain

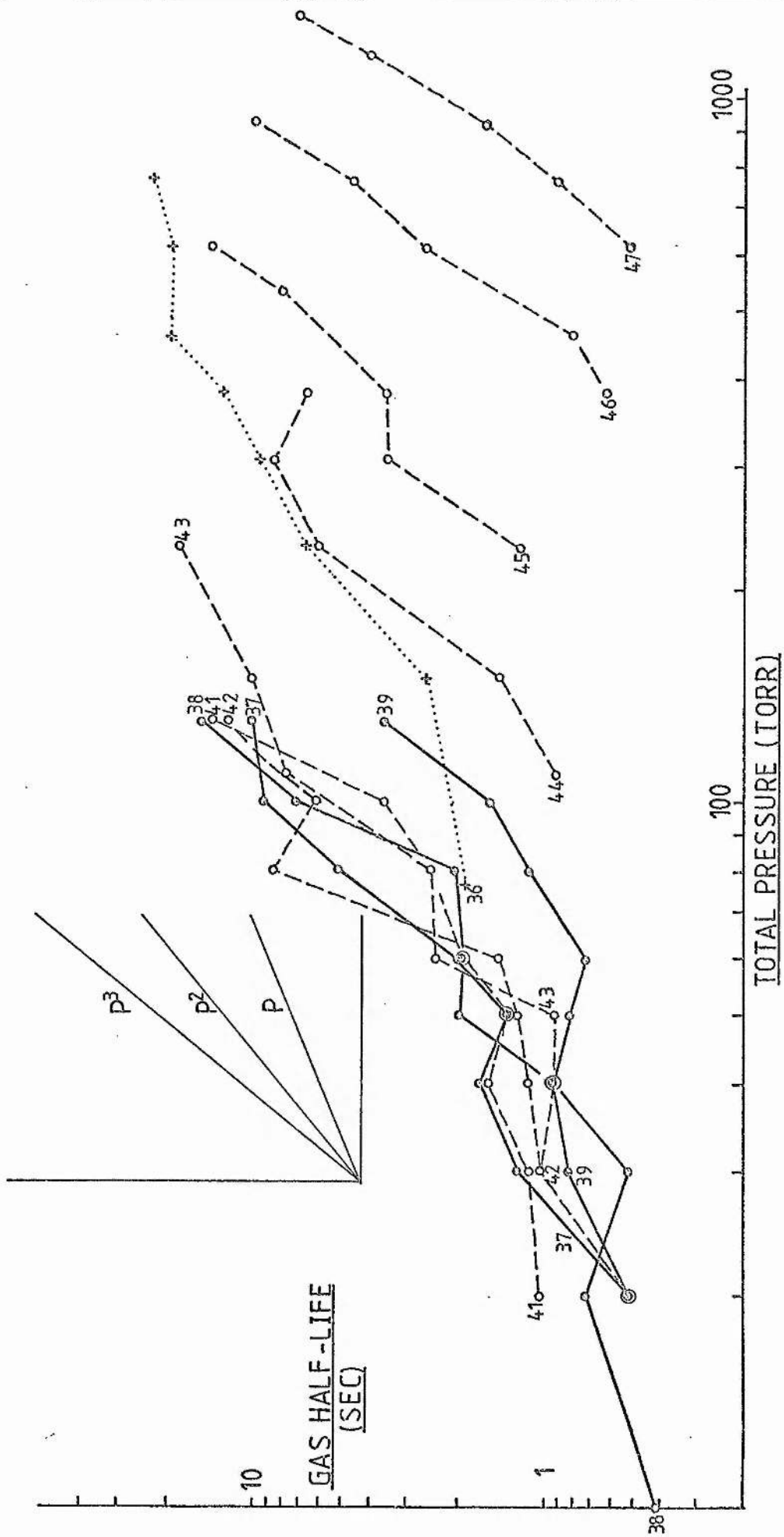


Figure 8.28

constant or perhaps increase slightly over several minutes (ie. for over 100,000 pulses). This is an important observation for which no explanation is offered, although it is clear that a stable donor population is involved. It suggests that gas lifetimes, in excimer lasers, very much greater than those achieved at present may be possible. This would, of course, be dependent on achieving laser action under non-optimum conditions where the fluorescent emission is relatively low.

#### 8.4.5 Three Process behaviour

The record in Fig 8.2(b) for mixture 19 at 110Torr has three maxima; one short duration spike ( $<1\text{sec}$ ), one of about 20sec, and one for the eventual constant level of many minutes duration. This suggests that for mixtures with  $\text{SF}_6$  donor a model based on three processes for the determination of the excimer fluorescent emission intensity may be appropriate. The processes responsible for the short duration spike, which in many cases may be present in the emission but too short in duration for recording by the OSA system, may represent the most efficient use of the donor. This would involve the harpoon reaction or the ionic reaction. Termination of this process would occur as the original donor molecules were used up or as a strongly quenching species (eg.  $\text{F}_2$ ) was generated. The intermediate process may involve some temporary product of the halogen donor, while the long term process must utilise a stable end product for halogen donation. This may be a molecule deriving from the original donor molecule or, more likely, a molecule formed from



the halogen and impurities, especially from the wall material (SiF for example).

The degree to which any one of these hypothetical processes are present in the temporal records depends on the mixture ratio, the total pressure and the gas types. Generally, the initial spike becomes wider with increased total pressure as is shown above. Also, increasing the dilution decreases the spike width at a constant total pressure except at the lowest dilution levels. The intermediate and long term processes both become stronger as the donor fraction decreases, while the intermediate process seems to decrease, relative to the long term process, at high total pressure.

#### 8.4.6 Intensity During Early Pulses

Certain OSA temporal records and pulse envelope records indicate that the initial rise in pulse intensity to the first peak (spike) could take place over many pulses. The most striking cases occur for mixture 24 ( $\text{SF}_6$  donor) in Fig 8.2(b) and mixture 32 ( $\text{NF}_3$  donor) in Fig 8.3. These mixtures are similar in that neither has a buffer gas and the donor:rare-gas ratios are quite close, being 1:100 and 1:30. However, a spike is just discernable in Fig 8.3 at 110 and 130Torr, and may well be present at other pressures and the mixture in Fig 8.2(b), but is of too short a duration to be recorded clearly. The peak in these cases is therefore likely to be due to the second hypothetical process mentioned above. The slow rise-time for this process is apparent in many records. Thus the only cases where a

discernable rise-time is present for the early peak (first process) are those of the pulse envelope records of Figs 8.14 to 8.17. At the lowest pressures these records show that the peak intensity may be reached by the first pulse. In general as the pressure is increased the intensity of the first pulse decreases and the number of pulses taken to reach maximum increases. When Figs 8.14 and 8.15 are compared the pattern of behaviour is seen to shift to higher pressure when buffer gas is present. Conversely, the rise-time at a given total pressure is less in the more dilute mixture. Clearly then, the more donor gas there is present in the discharge, the longer the time taken to reach the maximum. This suggests that a secondary donor molecule is being generated which permits greater fluorescent efficiency than the primary donor.

Possible candidates for secondary donor molecules were suggested in Section 2.2.3. It was pointed out that where  $\text{SF}_6$  or  $\text{NF}_3$  are used as donors,  $\text{F}_2$  will be produced and may lead to greater efficiency if quantities are sufficient. This is because the excimer formation reaction with  $\text{F}_2$  is rapid (see Table 2.3). For  $\text{NF}_3$  donor the production of  $\text{NF}_2$  may give increased efficiency due to a fast excimer formation reaction (Chow 1977). It is not known whether any of the products from  $\text{SF}_6$ , such as  $\text{SF}_5$ ,  $\text{SF}_4$ , etc., have fast excimer formation rates.

#### 8.4.7 Unbuffered Mixtures of Nitrogen-Trifluoride and Krypton

The results of Fig 8.3 for KrF in the unbuffered  $\text{NF}_3$ :Kr mixtures are perhaps the most interesting results obtained in this work. Particularly outstanding are the results for intermediate pressures in the more dilute mixtures where the emission is both of high intensity and very long duration. In addition to this, the overall results may be described in terms of the three processes, as outlined in Section 8.4.5, by observing that the first process is strongly represented at high donor fractions whereas the second and third processes are strong or even dominant in the more dilute cases. These two regions appear to be separated by a region of instability (ratio 1:3) and low intensity (1:10). If the entire results for KrF with  $\text{SF}_6$  as donor are examined (Figs 8.1 and 8.2(a) and (b)) there are slight indications that the same behaviour is present with the additional possibility that the buffer gas tends to shift the behaviour to higher total pressure.

Clearly the life-times shown in the results of Fig 8.3 cannot be explained in terms of the donor molecules being used up, since for a single total pressure, the lifetime is generally greater when the donor fraction is less. It is difficult to speculate on the process responsible for the behaviour observed because of the rather broad range of possibilities. Further measurements would be required to assess the relative importance of the ionic and metastable channels and to record the evolution of various reaction species. In addition, it would be helpful to obtain pulse envelope results (short timescale) and extend the long term recording for all the mixtures.

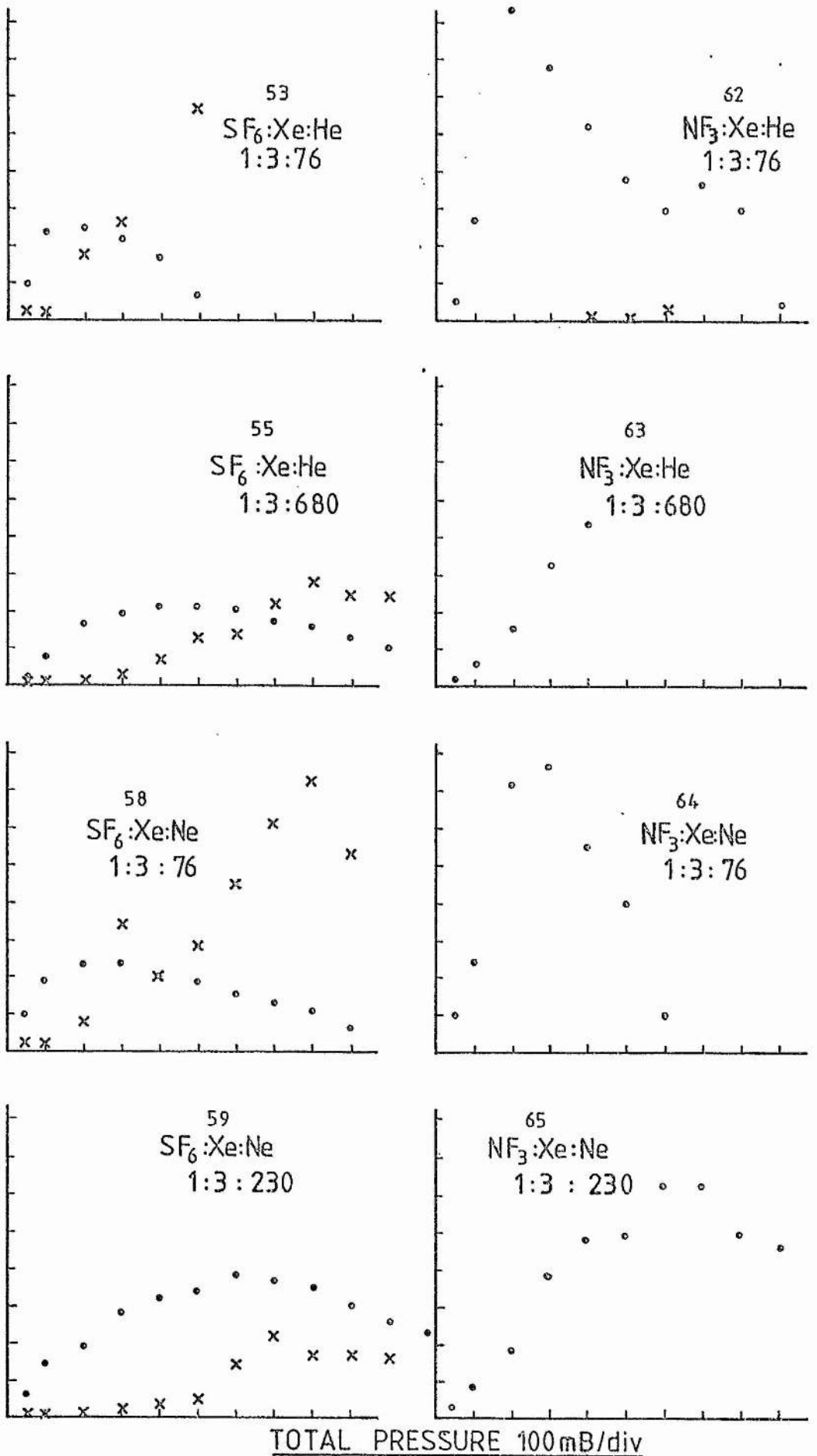
A fairly precise indication of the total microwave power absorption and optical power emission would be also be most useful if reasons for the behaviour observed were to be sought.

### 8.5 Donor Comparison

The relative performance of  $\text{NF}_3$  and  $\text{SF}_6$  can be demonstrated by selecting comparable pairs of results from the main body of data. Results selected from the XeF experiments are chosen from Fig 8.7 and presented in Fig 8.29. As mentioned before, the experimental method (method 1) used for XeF is likely to give depressed intensities at the shorter gas lifetimes and therefore the results of Fig 8.29 may be distorted. This means that corrected results would probably give some considerable increase in intensities at the lower pressures. Such a correction would be greater for the  $\text{NF}_3$  results since the gas lifetimes are so short. Therefore it can safely be concluded that far greater intensities are obtained when  $\text{NF}_3$  is used as the donor in XeF mixtures but that the gas lifetime is much less than for mixtures with the  $\text{SF}_6$  donor. This is corroborated by Fig 8.30 which shows some XeF results using the OSA recording method 2.

Donor performance in KrF experiments is shown in Fig 8.31 (compiled from Figs 8.2 and 8.3) which contrasts mixtures with no buffer gas. Mixtures 35 and 36 where He was used as the buffer, are compared in Figs 8.16 and 8.17 for pulse envelope records and in Fig 8.4 for OSA temporal records. The latter results are similar to the XeF results, showing greater peak intensities and shorter lifetimes

• RELATIVE INTENSITY, × GAS HALF-LIFE 1sec/div



SF<sub>6</sub> Donor

NF<sub>3</sub> Donor  
(gas life-times < 0.3 s)

Figure 8.29 XeF Donor comparison

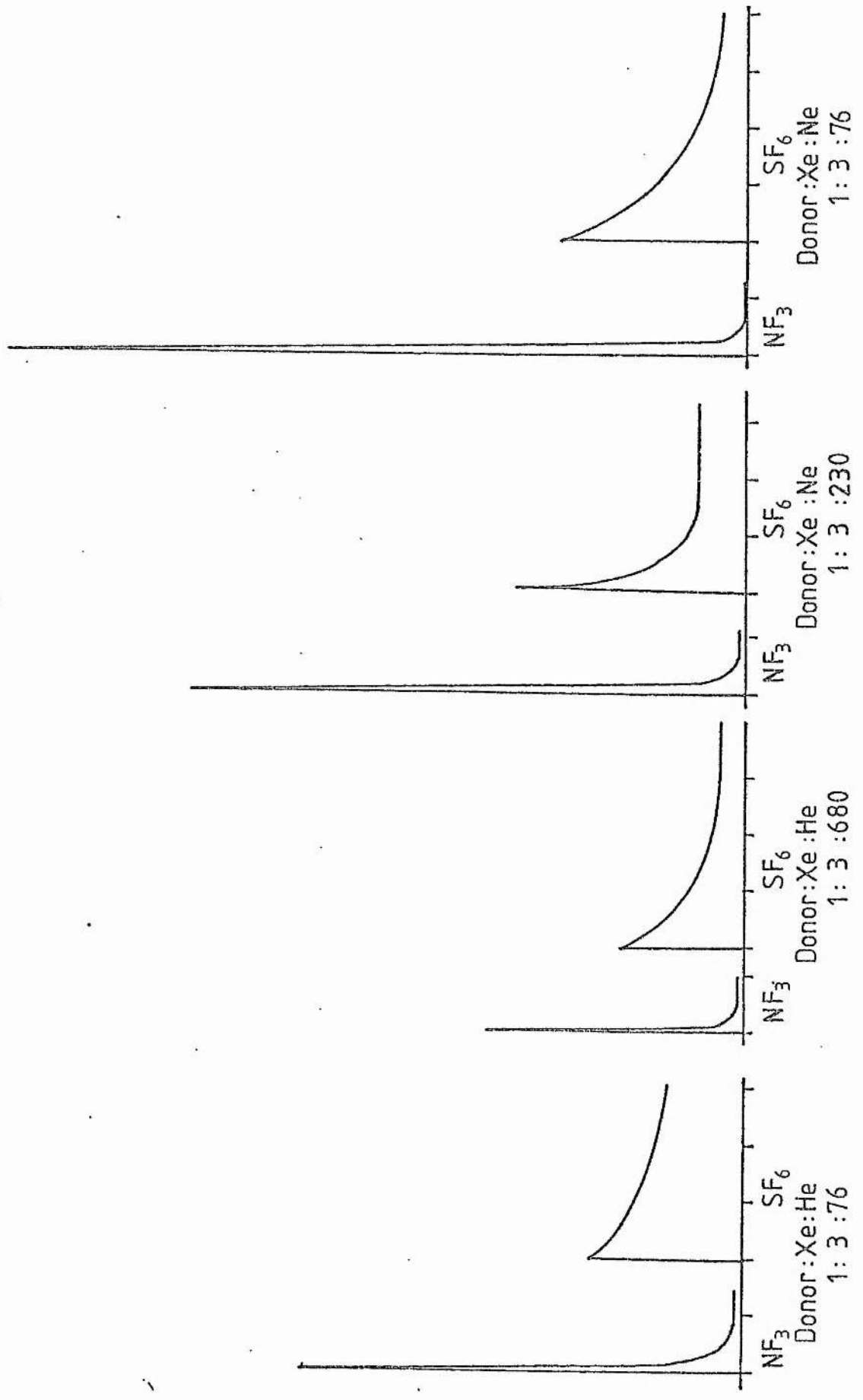


Figure 8.30 XeF Intensity vs time records, 3 sec/div, 300mB total pressure.

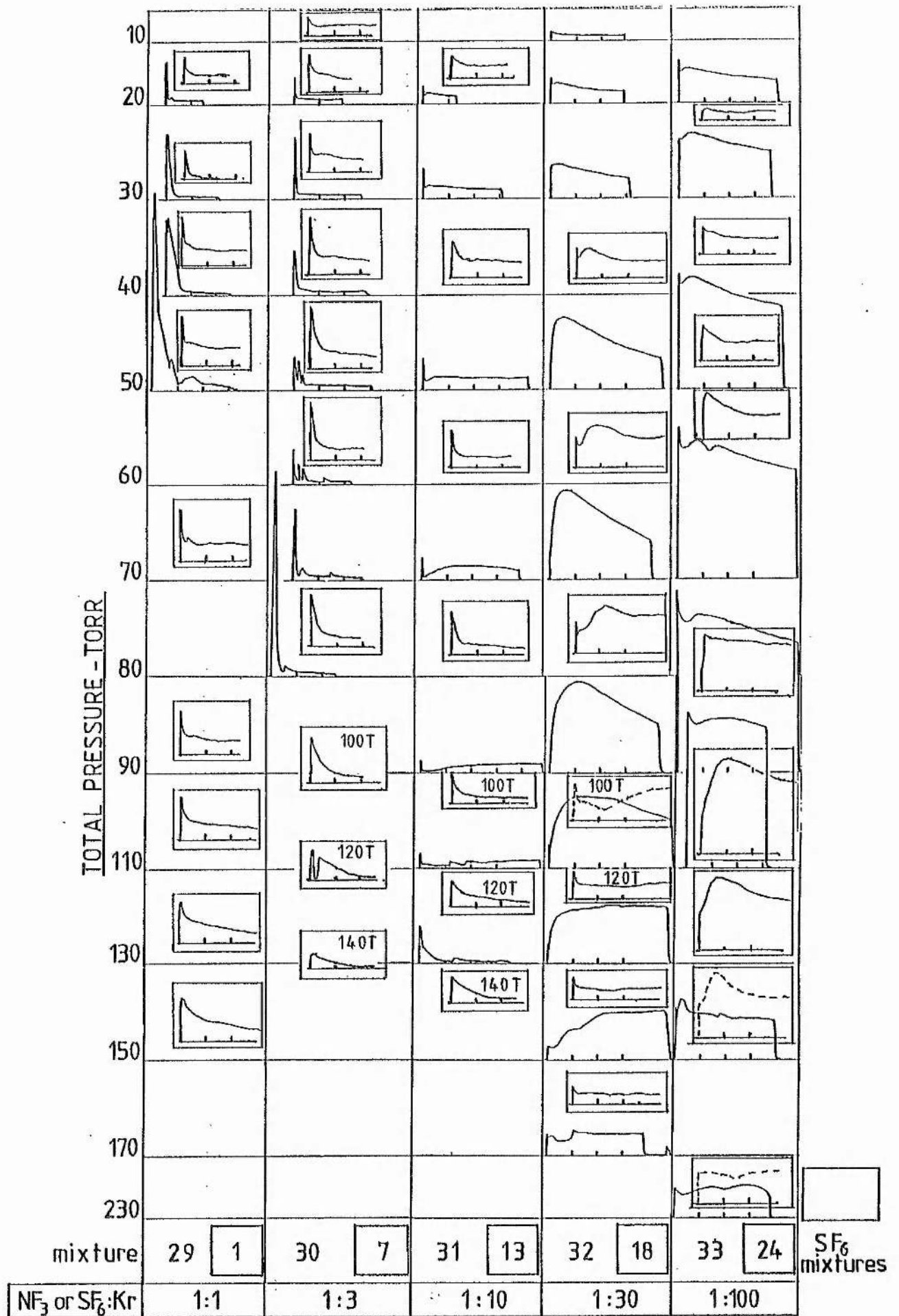


Figure 8.31 Donor comparison, Intensity vs time records.

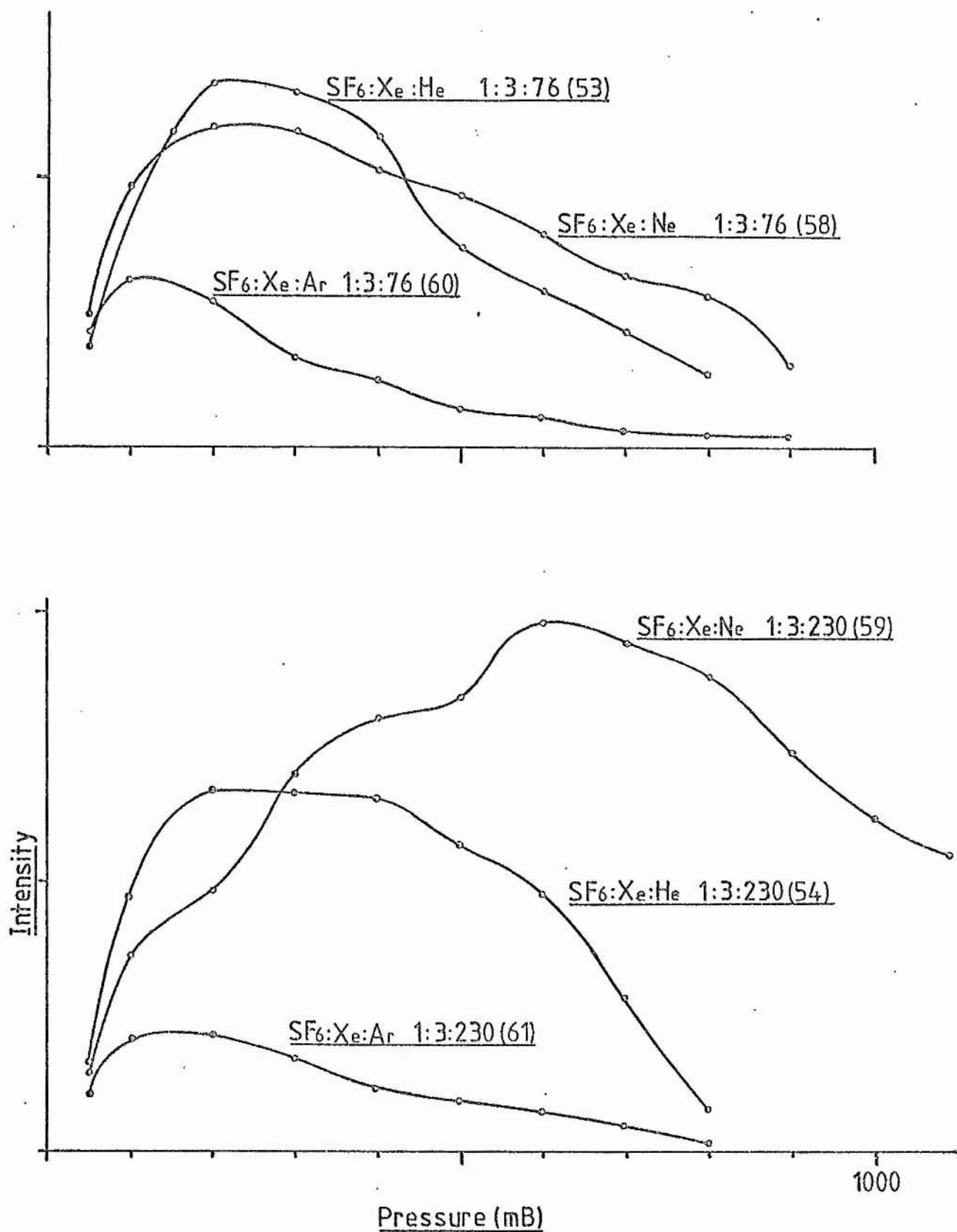


for  $\text{NF}_3$ , except that the discharge shows an oscillatory instability at higher pressures with  $\text{NF}_3$  as donor. The results of Fig 8.31 (no buffer gas) are quite complicated. In the richer mixtures (1:1 to 1:3), the  $\text{SF}_6$  mixtures have a lower peak intensity but longer lifetimes and a greater constant level in the long term. Also the  $\text{NF}_3$  mixtures show greater discharge instability and are confined to lower operating pressures than the  $\text{SF}_6$  mixtures. For the remaining more dilute mixtures, the  $\text{NF}_3$  results abruptly take on the intense, long duration behaviour described above. This behaviour appears also for the  $\text{SF}_6$  mixtures but is rather less marked. The intensities with  $\text{SF}_6$  are slightly less than with  $\text{NF}_3$  but the timescale of the measurements is too short to justify lifetime comparisons.

## 8.6 Buffer Gas Type

### 8.6.1 Buffers in XeF Mixtures

The results of Fig 8.7 allowing comparison of buffers in XeF mixtures are redrawn in Fig 8.32. It is clear that Ar gives much poorer results than He or Ne. The difference between He and Ne is not significant in the lower dilution case but, at the higher dilution, the intensity obtained with Ne increases considerably and gives a peak at higher total pressure than the He buffer. The gas lifetimes for these mixtures as they appear in Fig 8.7 are not significantly different. However, a difference in lifetime is revealed for the results obtained by the OSA temporal recording by method 2 which appears in Fig 8.33. Here, where the total pressure is 300mB, the peak intensity with He buffer is only marginally less than that with Ne buffer whereas the gas lifetimes are quite different. The half-lives are 2.5s and 9s at the lower dilution and 1s and 8s at the higher dilution for He and Ne respectively.



Relative intensities from intensity time record peaks as in Fig.8.7.

Figure 8.32 Buffer comparison -XeF mixtures.

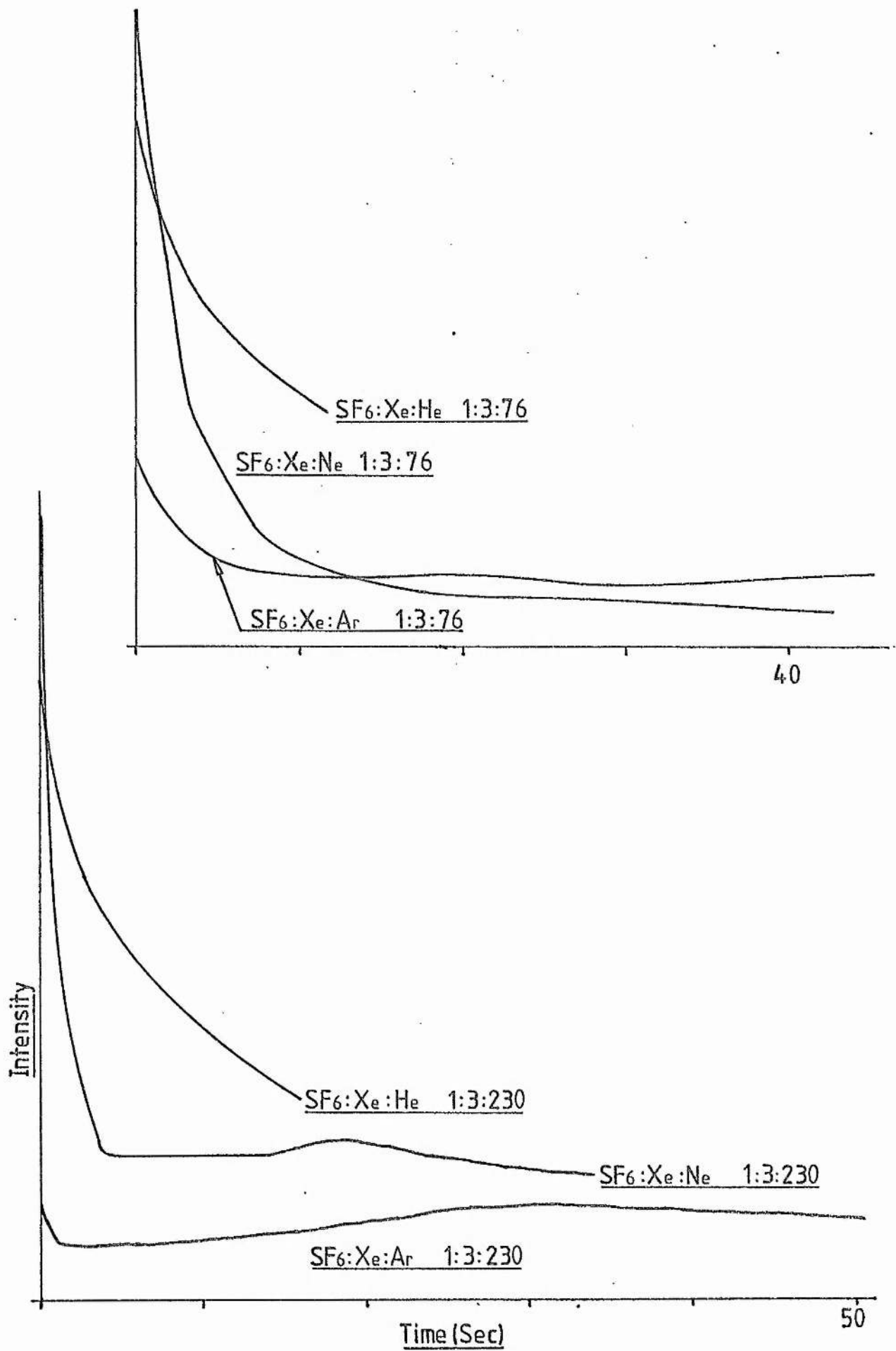


Figure 8.33 Buffer comparison in XeF mixtures. I vs t records by method 2.

### 8.6.2 Buffers in KrF Mixtures

The three buffers, He, Ne, and Ar are compared in their effects on intensity in Fig 8.34. This figure is compiled from Figs 8.8, 8.10, and 8.11 and so gives curves of peak intensities from OSA temporal records against total pressure.

Emission from the Ar buffered mixtures is considerably weaker than from the He and Ne buffered mixtures. In addition, operation with Ar buffer is confined to low pressure (below about 100Torr) and discharges could not be formed in mixtures more dilute than those tested.

In comparing He with Ne, no particular distinction is apparent in mixtures at the ratio 1:3:100 or any of the less dilute cases. At greater dilution, the He buffered mixtures give much reduced intensities while those with Ne continue to give high intensities even in the ratio 1:3:1000. It is also noticeable that the use of Ne buffer extends the high pressure operation beyond that for He buffer in the more dilute mixtures.

Gas lifetimes are compared for the three buffers in Fig 8.35 which gives the gas half-lives against total pressure on log-log scales. The results used for this figure correspond to those of Fig 8.34 except that lifetimes for mixtures 11, 12, and 40 could not be reliably measured in the OSA results and are therefore not included. These results indicate that the buffer type has little effect on lifetime in the less dilute mixtures. The lack of

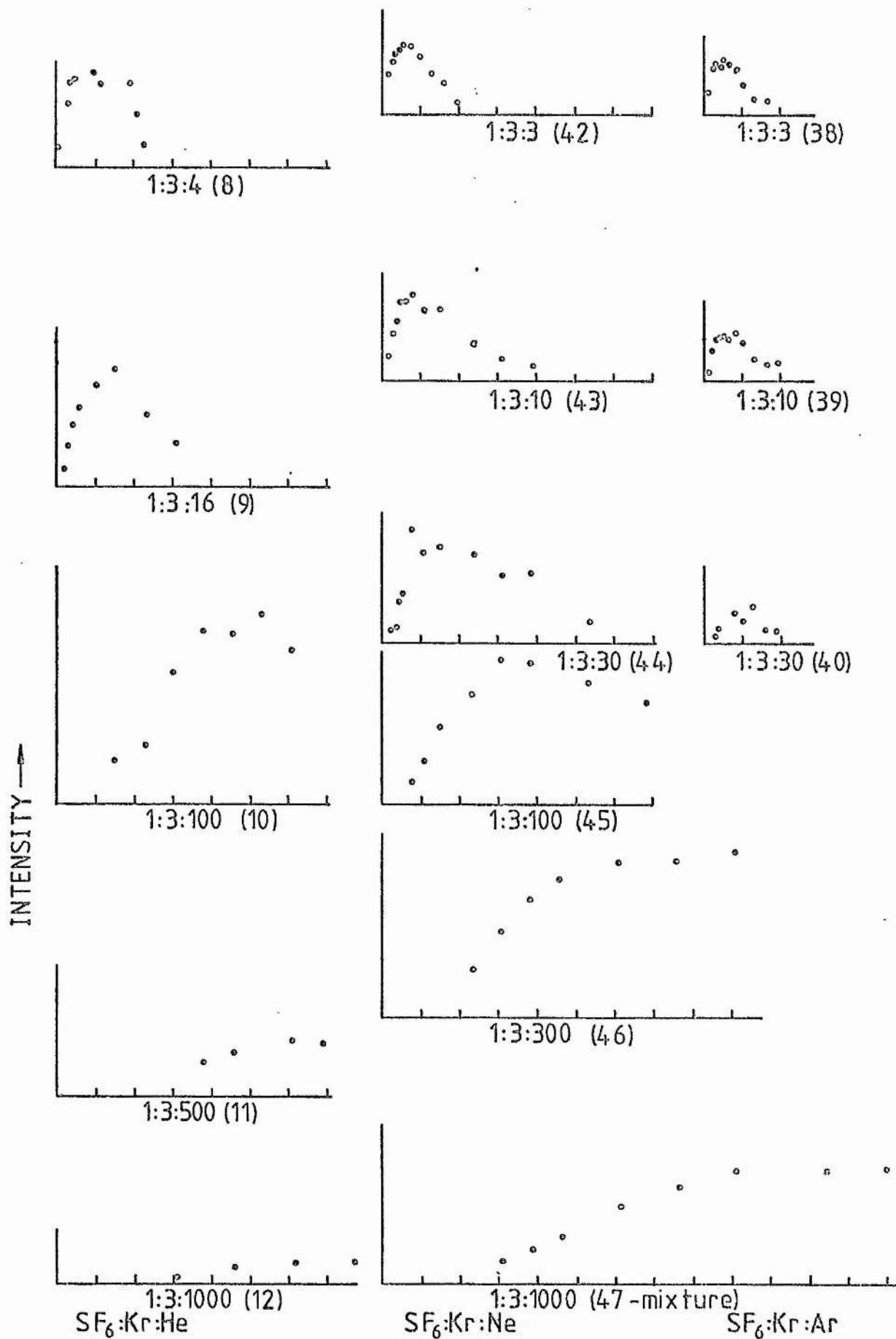


Figure 8.34 Buffer comparison. Intensity vs pressure (100 Torr/div). KrF.





measurement makes it difficult to ascertain whether there is a difference between He and Ne mixtures in the more dilute cases similar to that observed in the XeF mixtures.

In looking for an explanation for the low excimer emission when Ar is the buffer, it might be supposed that the effect simply accompanies the use of a heavier buffer gas. However, relatively high intensities were obtained in the unbuffered mixtures where, presumably, the rare-gas acts as the buffer gas. It seems likely that Ar is not a good buffer gas simply because the low metastable energy level results in a significant population of Ar metastables. Since, if Ar is the buffer gas, Ar will have a number density of 10 to 100 times the rare-gas (Kr or Xe) density, a large fraction of the available energy may be diverted away from the desired excimer formation channel. One possible mechanism for the loss of Ar metastables is the formation of ArF excimers.

The better high dilution performance with Ne buffer (compared with He) may be harder to explain. Some of the difference may be due to the reduced discharge efficiency resulting from momentum transfer from electrons to He when He is present in large quantities in the discharge.

### 8.7 Collisional Relaxation

The records of the excimer spectra obtained for most of the excimer mixtures are most useful in allowing investigations of the band profile to be carried out. The significance of the distribution of energy in the emission band was discussed in Section 2.1.3 where it was emphasised that rapid collisional redistribution of the vibrational-rotational manifold was a determinant of laser efficiency and the threshold pump power density. When collisional redistribution is slow the emission spectrum will be broader because the excimer is formed in a range of rotational and vibrational states. Observations of the variations in spectral content of the KrF excimer emissions are now described in detail.

A typical example of the emission band-spectrum for the B - X transition in KrF was shown in Fig 8.20. The main peak of this spectrum is due to a transition from the ground vibrational level of the bound (B) electronic state to the unbound (X) electronic state. Transitions originating from the first, second and third vibrational states (above the ground state) give rise to the three subsidiary peaks indicated on the short wavelength side of the main peak. In order to give a measure of the degree of collisional relaxation, the ratio ( $r$ ) of the central peak intensity ( $I_1$ ) to the first subsidiary peak intensity ( $I_2$ ) is used and provides a measure independent of the absolute intensity of the spectrum (The ratio is given by  $r=I_1/I_2$ ). Spectra were obtained for a range of total pressures for each of the mixtures in Table 7.2 and the intensity ratio was measured for all of these results.

In order to illustrate the general features of the relaxation process a selection of results covering a wide range of mixtures is given in Fig 8.36. The results are divided into three groups, according to the donor:rare-gas ratio, each with several mixtures (dilutions). In the results where the  $\text{SF}_6$ :Kr ratio is 1:1, the effect of increasing the dilution (using He) is to give markedly decreasing relaxation at any given total pressure. Another feature is that the results for a given mixture fall roughly on a straight line, the gradient of which increases as the mixture becomes more dilute. In the sets of results for  $\text{SF}_6$ :Kr ratios of 1:10 and 1:100, these trends become progressively less distinct. Clearly this lack of distinction accompanies a decrease in the fraction of Kr in the mixtures. These trends are consistent with the possibility that Kr itself is much more effective than He in causing vibrational relaxation in KrF.

In order to compare the differences in vibrational relaxation in KrF that occur when the different buffer gases are used, the intensity ratio was measured for an appropriate selection of mixtures. Figure 8.37 gives the intensity ratio plotted against total pressure in the same way as in Fig 8.36. It is recalled that when Ar was used as the buffer, discharges could only be obtained at fairly low pressures. Therefore Ar can only be compared with He and Ne below about 200Torr. Figure 8.37 indicates that relaxation is considerably greater with Ar buffer than with Ne for an equal mixture ratio. When Ne is compared with He, slightly greater relaxation occurs for the He buffer in both of the mixtures tested. Although

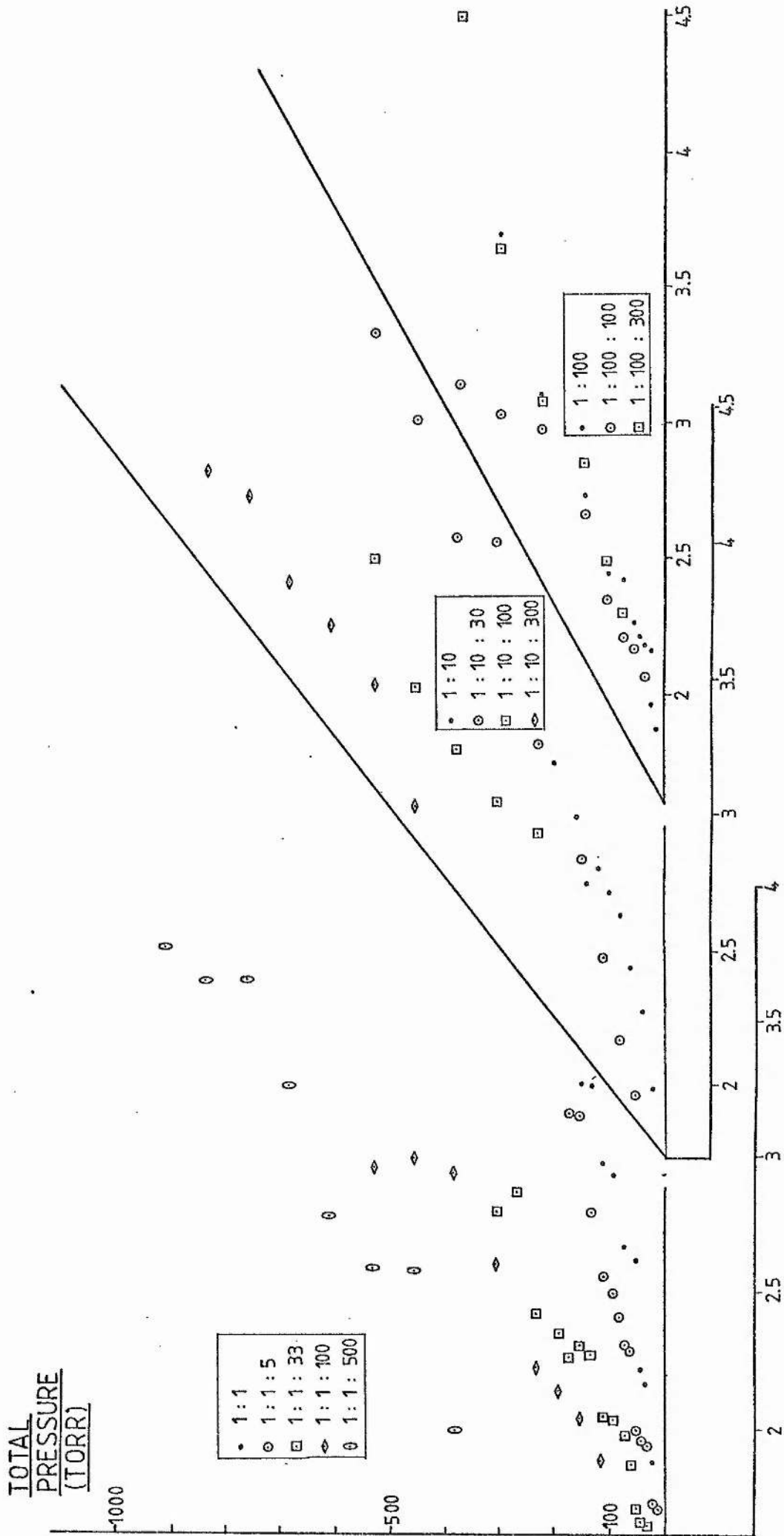


Figure 836KrF Relaxation of vibrational states in SF<sub>6</sub>:Kr:He mixtures.

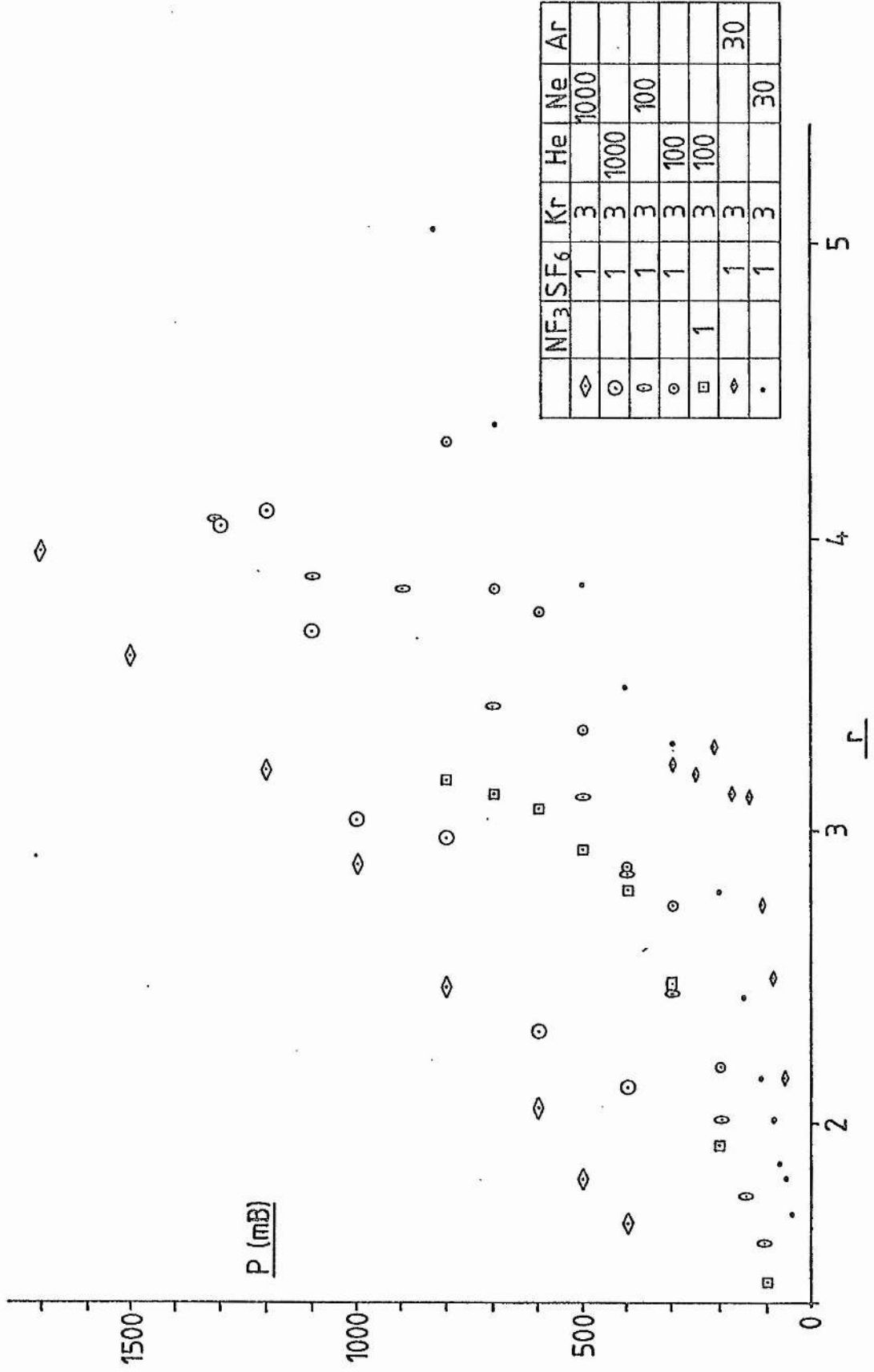


Figure 8.37 KrF Relaxation : buffer comparison.

the results for the buffer comparison show only marginal differences, a strong effect is seen in Fig 8.37 in that, at a given pressure, the higher dilutions display much lower relaxation, as was the case in Fig 8.36 at low Kr fractions.

There are three sources of error in measuring the vibrational peak intensities which may account for the scatter in the points of Figs 36 and 37. Firstly, the general noise in the spectrum recordings (to which may be added the occurrence of background spectra) made it difficult to measure the peak height accurately. Secondly, the spectrum base line position, as recorded by the OSA and chart recorder system, was subjected to slight variations. Both of these errors would be particularly disturbing where the intensities were small; ie. at the lowest and highest pressures. The third source of error arises from the difficulty of locating the position, on the wavelength scale, of the vibrational peaks. The technique used was to locate the centre of the main peak visually and measure the height of the second peak at a fixed distance from this centre. At small intensities, the peak centre could not be located accurately due to its flat shape and the higher proportion of noise in the recording. In order to test whether greater regularity could be achieved, the mixture  $\text{SF}_6:\text{Kr}:\text{He}$  at 1:3:100 was tested with more care. The spectra were collected by accumulation over several gas fills at each experimental pressure. This considerably reduced the scatter in the points as the plot in Fig 8.38 demonstrates. The experiment was repeated and the second results (also shown in Fig 8.38) were found to be significantly displaced from the first results though the scatter was still small. Figure 8.38 also

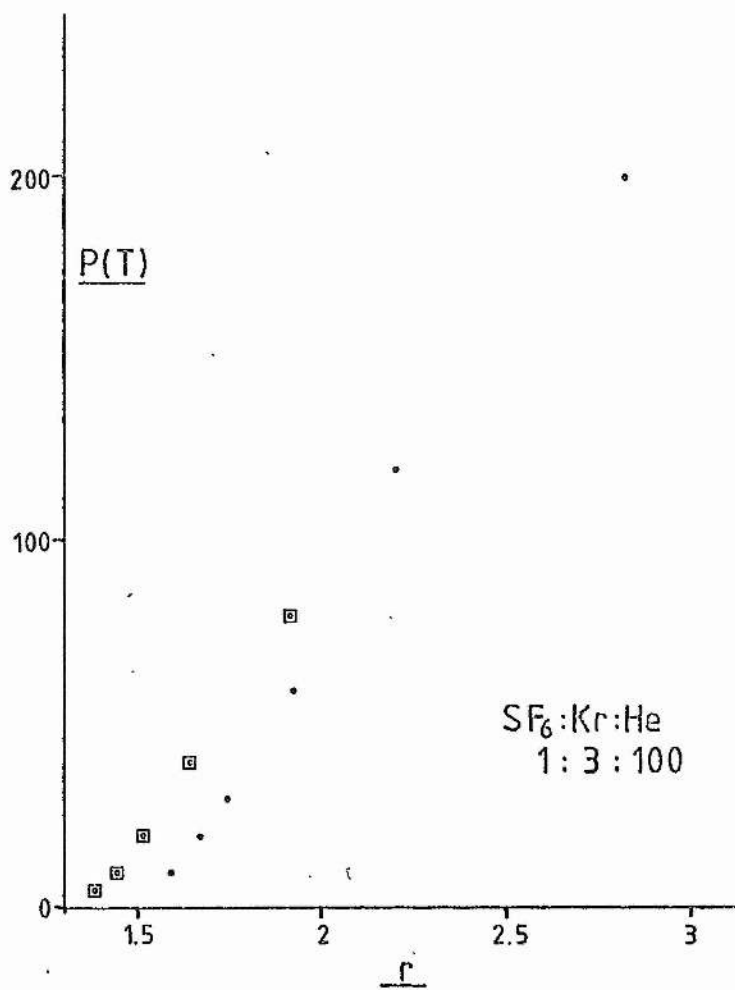


Figure 8.38 KrF Relaxation : large signal results.



indicates that the intensity ratio may approach a constant value (of about 1.4) as the pressure approaches zero.

Figure 8.37 contains a plot for a mixture containing  $\text{NF}_3$  which may be contrasted with the mixture using  $\text{SF}_6$  as donor. For the  $\text{SF}_6$  mixture the  $P - r$  relationship remains approximately linear while the  $\text{NF}_3$  mixture shows an approach to saturation for a value of  $r$  of around 3.2. However, this result arises from very few data points and may not be reliable.

For all of the above results the intensity ratio approaches a value which is between 1 and 2 as the total pressure, and hence the collisional relaxation, approaches zero. Since the spontaneous lifetime of the molecule is not dependent on the particular vibration state, this ratio also represents the ratio of both the formation rates and the populations of the two vibration states.

The ratio,  $r$ , of the populations of the two states in thermal equilibrium, with  $n_1$  and  $n_2$  as the particle densities, is given by

$$r = n_1/n_2 = e^{hv/kT} .$$

This value is appropriate at high pressure where the spontaneous emission rate is negligible compared with the collisional relaxation rate. In  $\text{KrF}$  the wavelength spacing between the first and second vibrational feature is about  $29\text{\AA}$  which gives a frequency spacing of  $1.42 \times 10^{13} \text{ Hz}$ . Using this and 300K for  $T$  in the previous equation gives a population ratio of 9.7. The maximum ratio observed in the

results was about 5 which suggests that thermal equilibrium was not established. Since the downward transition rate is considerably greater than the upward rate in this regime, the latter can be ignored and therefore the relation between the population ratio (and observed intensity ratio) and the downward transition rate will be linear. This rate will be directly proportional to the collision frequency, and therefore the total pressure, giving the linearity observed. It is clear that greater relaxation than that observed could be achieved by operation at higher pressures than those reached in the experiments.

It is interesting to apply this argument for increased relaxation with collision frequency to the effects of mixture variation. It might be expected that increases in the fraction of the lightest gas in the mixture (the buffer gas), or replacement of a heavier buffer gas by a lighter one, would give increased relaxation due to the higher collision frequency in the lighter gas. However, in all of the cases presented greater dilution gives greatly reduced relaxation (steeper gradients) at any given total pressure. In addition, as mentioned above, Ar gives greater relaxation than Ne but in the He, Ne comparison the lighter gas, He, does give better relaxation. From these results, rare-gases can be placed in order of effectiveness in relaxing the KrF vibrational manifold as Kr, Ar, He, Ne. It is likely that the collision frequency effect is suppressed in favour of a difference in collision cross-section for relaxation between these atoms. For example, the cross-section may be greater in the more reactive heavier atoms where the binding of the outer electrons is less. The relaxation may then involve an intermediate

triatomic species.

It is noted in conclusion that, in common with the results of other sections, the trends in the results that accompany changes in gas types, mixture ratio, or total pressure are somewhat surprising and complex. The relaxation process can be included in the several areas investigated where knowledge is lacking.

REFERENCES

- S.A.Ahmed and R.Kocher, Proc. IEEE, 1737(1964).
- L.Bertrand, J.M.Gagne, R.G.Bosisio, and M.Moisan, IEEE J. Quantum Electron., 14(1), 8(1978).
- R.G.Bosisio, C.F.Weissfloch, and M.R.Wertheimer, J. Microwave Power, 7(4), 325(1972).
- J.E.Brandelik and G.A.Smith, IEEE J. Quantum Electron., 16(1), 7(1980).
- C.A.Brau and J.J.Ewing, Appl. Phys. Lett., 27, 435(1975a).
- C.A.Brau and J.J.Ewing, J. Chem. Phys., 63(11), 4640(1975b).
- R.Burnam and N.Djeu, Appl. Phys. Lett., 29(11), 707(1976).
- H.S.Carslaw and J.C.Jaeger, Conduction of Heat in Solids, (Oxford 1959).
- W.Chow, M.Stuke, and F.P.Schafer, Appl. Phys., 13, 1(1977).
- C.P.Christensen and R.W.Waynant, Conference on Lasers and Electro-Electro-optics, Technical Digest, April 14-16, 1982, Page 16, (Optical Society of America).
- J.Crank, The Mathematics of Diffusion, (Clarendon, Oxford 1956).
- T.H.Dunning and P.J.Hay, J. Chem. Phys., 69(1), 134(1978).
- J.J.Ewing and C.A.Brau, Appl. Phys. Lett., 27, 350(1975).
- F.C.Fehsenfeld, J. Chem. Phys., 53(5), 2000(1970).
- C.H.Fisher and R.E.Centre, J. Chem. Phys., 69(5), 2011(1978).
- M.R.Flannery and T.P.Yang, Appl. Phys. Lett., 32(5), 327(1978).
- S.F.Fulghum, M.S.Feld, and Ali Javan, IEEE J. Quantum Electron., 16(8), 815(1980).
- M.F.Golde and B.A.Thrush, Chem. Phys. Lett., 29, 486(1974).
- J.P.Goldsborough, Appl. Phys. Lett., 8(9), 218(1966).
- M.C.Gower, R.Exberger, P.D.Rowley, and K.W.Billman, Appl. Phys. Lett., 33(1), 65(1978).

- K.G.Handy and J.E.Brandelik, *J. Appl. Phys.*, 49(7), 3753(1978).
- A.F.Harvey, Microwave Engineering, (Academic Press, London and New York 1963).
- P.J.Hay, W.R.Wadt, and T.H.Dunning, *Ann. Rev. Phys. Chem.*, 311-346 (1979).
- S.C.Haydon, Discharge and Plasma Physics, (Department of University Extension, The University of New England, Armidale, Australia 1964).
- M.A.Heald and C.B.Wharton, Plasma Diagnostics with Microwaves, (Wiley, New York, London, Sydney 1965).
- G.Herzberg, Molecular Spectra and Molecular Structure, Volumes 1 and 2, (Van Nostrand, New York 1950).
- F.G.Houtermans, *Helv. Phys. Acta.*, 33, 933(1960).
- J.C.Hsia, J.A.Mangano, J.H.Jacob, and M.Rokni, *Appl. Phys. Lett.*, 34(3), 208(1979).
- J.H.Jacob and S.A.Mani, *Appl. Phys. Lett.*, 26, 53(1975).
- T.H.Johnson and A.M.Hunter, *J. Appl. Phys.*, 51(5), 2406(1980).
- W.Jost, Diffusion in Solids, Liquids, Gases, (Academic Press, New York 1952).
- C.Kenty, J.O.Aicher, E.B.Noel, A.Poritsky, and V.Paolino, *Phys. Rev.*, 69, 36(1946).
- M.Krauss and B.Liu, *Chem. Phys. Lett.*, 44(2), 257(1976).
- J.I.Levatter and S.C.Lin, *J. Appl. Phys.*, 51(1), 210(1980).
- E.W.McDaniel and E.A.Mason, The Mobility and Diffusion of Ions in Gases, (Wiley, New York, London, Sydney, Toronto 1973).
- A.D.MacDonald, Microwave Breakdown in Gases, (Wiley, New York, London Sydney 1966).
- J.P.McGeehan, B.C.O'Neill, A.N.Prasad, and J.D.Craggs, *J. Phys. D:Appl. Phys.*, 8, 153(1975).
- A.J.Mendelsohn, R.Normandin, S.E.Harris, and J.F.Young, *Appl. Phys. Lett.*, 38(8), 603(1981).

- The Microwave Engineers' Handbook and Buyers' Guide, Page T-102, Horizon House - Microwave Inc., 1330, Beacon Street, Brookline 46, Massachusetts (1962).
- W.J.Moore, Physical Chemistry, (Longman, London 1972).
- S.F.Paik and J.E.Creedon, Proc. IEEE, 2086, November, (1968).
- H.Raether, Arch. Electrotech. (Berlin), 34, 49(1940).
- Ch.K.Rhodes, Excimer Lasers, Topics in Applied Physics, Volume 30, (Springer-Verlag, Berlin, Heidelberg, New York, 1979).
- M.Rokni, J.H.Jacob, J.A.Mangano, and R.Brochu, Appl. Phys. Lett., 30(9), 458(1977).
- M.Rokni, J.A.Mangano, J.H.Jacob, and J.C.Hsia, IEEE J. Quantum Electron., 14(7), 464(1978).
- D.E.Rothe and R.A.Gibson, Opt. Commun., 22(3), 265(1977).
- S.K.Searles and G.A.Hart, Appl. Phys. Lett., 29, 486(1974).
- M.J.Shaw and J.D.C.Jones, Appl. Phys., 14, 393(1977).
- G.P.Smith and D.L.Huestis, J. Appl. Phys., 52(10), 6041(1981).
- R.D.Suart, P.H.Dawson, and G.H.Kimbell, J. Appl. Phys., 43(3), 1022 (1972).
- R.C.Sze, IEEE J. Quantum Electron., Vol. QE-15(12), 1338(1979).
- K.Y.Tang, R.O.Hunter, and D.L.Huestis, J. Appl. Phys., 52(10), 6046 (1981).
- J.Tellinghuisen, J.M.Hoffman, G.C.Tisone, and A.K.Hays, J. Chem. Phys., 64(6), 2484(1976).
- J.Tellinghuisen, P.C.Tellinghuisen, G.C.Tisone, J.M.Hoffman, and A.K.Hays, J. Chem. Phys., 68(11), 5177(1978).
- P.C.Tellinghuisen, J.Tellinghuisen, J.A.Coxon, J.E.Velazco, and D.W.Setser, J. Chem. Phys., 68(11), 5187(1978).
- D.W.Trainor, J.H.Jacob, and M.Rokni, J. Chem. Phys., 72(6), 3646 (1980).
- J.E.Valazco and D.W.Setser, J. Chem. Phys., 62, 1990(1975).
- J.E.Velazco, J.H.Kolts, and D.W.Setser, J. Chem. Phys., 65(9), 3468 (1976).
- J.T.Verdeyen, Laser Electronics, (Prentice-Hall, Inc., Englewood Cliffs, New Jersey 1981).

- P.J.K.Wisoff, A.J.Mendelsohn, S.E.Harris, and J.F.Young, IEEE J. Quantum Electron., 18(11), 1839(1982).
- J.F.Young, S.E.Harris, P.J.K.Wisoff, and A.J.Mendelsohn, Laser Focus April (1982)
- M.W.Zemansky, Heat and Thermodynamics, (McGraw-Hill, New York, Toronto, London 1957).